

LAYERED SILICATE PARTICLES FILLED POLYMER NANOCOMPOSITE FOR
BARRIER APPLICATION

By

JINWOO KWAK

A DISSERTATION PRESENTED TO THE GRADUATE SCHOOL
OF THE UNIVERSITY OF FLORIDA IN PARTIAL FULFILLMENT
OF THE REQUIREMENTS FOR THE DEGREE OF
DOCTOR OF PHILOSOPHY

UNIVERSITY OF FLORIDA

2010

© 2010 Jinwoo Kwak

To my father, mother and my lovely wife for all devoted love and sacrifices they made
toward my education

ACKNOWLEDGMENTS

First of all, I am grateful to the late, Dr. Charles L. Beatty, my advisor, for his endless support. I would like to thank Dr. Matthew Siobhan, from SCF processing Inc., for her exceptional guidance and generous support throughout my doctoral studies. I will never forget her help and kindness. And, I would like to express my thanks to Dr. Bruce A. Welt for providing valuable comments and help in the progress of my research. I would like to extend my thanks to Dr. Valentin Craciun for his time and effort toward me as my co-chair.

My thanks also goes to Dr. Christopher Batich and Dr. Hassan El-Shall for serving on my committee. I would also like to express my gratitude to Sungwan Jeon for his thankful endeavor and assistance as a coworker. I also appreciate Tom Gasset, Aniket Selarka, Myong Hwa Lee and Dr. Junghun Jang for helping me in several ways. I would like to thank the faculty and staff in Department of Materials Science and Engineering at the University of Florida.

The financial support of the Kraft Foods, Inc. and the US Army Natick Soldier RD&E Center during my Ph.D. study is gratefully acknowledged. This research was possible with their enduring support and kind cooperation. Finally, I wish to thank all of my friends both near and far who have always encouraged me throughout my life.

TABLE OF CONTENTS

	<u>page</u>
ACKNOWLEDGMENTS	4
LIST OF FIGURES	9
LIST OF ABBREVIATIONS.....	15
NOMENCLATURE	19
ABSTRACT.....	23
CHAPTER	
1 INTRODUCTION	25
Polymer Clay Nanocomposite.....	26
Three Conventional Microstructures	26
Preparation of Polymer Clay Nanocomposite	27
The Fundamental Concept for Barrier Solutions.....	28
Barrier Mechanism in a Polymer Film	28
Basic Barrier Model for Polymer Clay Nanocomposite Materials	31
2 LITERATURE REVIEW ON MICROSTRUCTURE OF POLYMER CLAY NANOCOMPOSITE MATERIALS FOR BARRIER APPLICATIONS.....	37
Microstructures of Polymer Clay Nanocomposite	37
Microstructures in Practical Nanocomposite Materials	37
Roles of organic modifier for intercalation and exfoliation	37
Effects of processing parameters on intercalation and exfoliation	42
Formation of various microstructures	46
Interplay between clay orientation and segmental motion of polymer chains	53
Effects of Microstructures on Physical Properties	55
Mechanical property.....	55
Thermal property.....	57
Optical property.....	58
Barrier property	59
Effects of Microstructure on Barrier Property.....	59
Extended Barrier Model for Polymer Clay Nanocomposite	59
Practical Polymer Clay Nanocomposite for Barrier Applications	66
The effects of microstructure of clay platelets on barrier properties	66
The effects of processing and selection of matrix on barrier properties	68
The barrier properties based on geometry of clay platelets.....	73
Different types of barrier structure.....	75

3	POLYMER CLAY NANOCOMPOSITE COATINGS ON NON-POLAR POLYOLEFIN SUBSTRATE TO ENHANCE BARRIER PROPERTY.....	101
	Introduction.....	101
	Experiments.....	104
	Materials.....	104
	Step 1: Preparation of Polymer Clay Nanocomposite Solutions.....	104
	Step 2: Atmospheric Pressure Plasma Treatment.....	105
	Step 3: Coating Samples after APP Treatment.....	105
	Step 4: Drying PCN-Coated PP specimens.....	105
	Characterizations.....	105
	Results and Discussion.....	106
	Surface Modification by Atmospheric Pressure Plasma Treatment.....	106
	Clay Exfoliation.....	108
	Barrier Properties.....	109
4	EFFECT OF pH ON MICROSTRUCTURE OF LAYERED SILICATE AND BARRIER PROPERTIES IN NANOCOMPOSITE COATING SYSTEMS.....	124
	Introduction.....	124
	Experiments.....	127
	Preparation of Polymer Clay Nanocomposite Solutions at Various pHs.....	127
	Coating Samples After Atmospheric Pressure Plasma Treatment.....	128
	Characterizations and Analysis.....	128
	Results and Discussion.....	129
	A House of Cards Structure.....	129
	Effects of pH on the Clay Platelet Microstructure.....	130
	Barrier Properties.....	133
5	THEORETICAL ESTIMATION OF BARRIER PROPERTIES OF POLYMER CLAY NANOCOMPOSITE CONTAINING TWO CLAY TYPES "PC2N".....	149
	Introduction.....	149
	Experiments.....	150
	Preparation of PC2N Films.....	150
	Characterizations.....	151
	Discussion of Model and Results.....	151
	Derivation of Barrier Equation for PC2N.....	154
6	EFFECT OF POLY(ACRYLIC ACID) ON BARRIER PROPERTIES OF HIGHLY FILLED NANOCOMPOSITE FILMS.....	164
	Introduction.....	164
	Experiments.....	165
	Preparation of Highly Filled Nanocomposite Films.....	165
	Characterizations.....	166
	Results and Discussion.....	167

Variables Affecting Barrier Properties	167
Roles of Poly(vinyl) Butyral Layer	170
7 CONCLUSIONS	188
APPENDIX	
A CLASSIFICATION OF COMMONLY USED LAYERED SILICATES	194
B COMMERCIALY AVAILABLE ORGANOCCLAYS AND ORGANIC MOLECULES USED FOR THE MODIFICATION OF THE SURFACE OF NANOCCLAYS	195
LIST OF REFERENCES	196
BIOGRAPHICAL SKETCH	208

LIST OF TABLES

<u>Table</u>		<u>page</u>
2-1	Four different formulations to prepare polymer-clay composites (Demirkol et al., 2007)	78
2-2	Average spherulites radius (R _{sph}) and T _c crystallized from the melt as a cooling rate of 1°C/min (Yu et al., 2003).....	78
2-3	Oxygen permeability of HDPE/clay nanocomposites at different clay concentrations and ultrasonic amplitudes (Swain and Isayev, 2007).....	79
2-4	Processing conditions for blown film (Thellen et al., 2005).....	79
3-1	Specific data of PVA samples.....	111
3-2	Compositions of PCN solutions used for coating	111
3-3	Specific conditions of APP treatment	112
3-4	OTR results of PVA coated PP specimens	112
4-1	Specific conditions for the preparation of each specimen	135
4-2	EDS results for white unknown particles dispersed in clay composite solutions.....	135
5-1	Specific information of all clays used for the preparation of PC2N.....	159
5-2	Specific experimental conditions for the preparation of composite films	159
6-1	Corresponding relative amounts of clay and PAA for each sample	175

LIST OF FIGURES

<u>Figure</u>	<u>page</u>
1-1 Basic crystal structure of MMT	32
1-2 Evolution of morphologies of PCN from natural MMT to fully exfoliated PCN and corresponding general patterns of XRD; a more realistic microstructure which is a mixture of all structures and a corresponding TEM micrograph.....	33
1-3 Procedures for preparing PCNs	34
1-4 Permeability mechanism of gas molecules	35
1-5 Volume-temperature relationship for amorphous polymer	36
1-6 Effects of microstructures of clay platelets in polymer on barrier properties of PCNs.....	36
2-1 Phase diagrams of polymer-clay mixtures at $p_{gr}= 0.2$, $N_{gr}= 5$ (Ginzburg et al., 2000).....	80
2-2 Expectation of arrangements of modifiers in the intergallery regions.....	80
2-3 WAXRD patterns of the organically modified nanoclays and their nanocomposites and corresponding TEM micrographs	81
2-4 WAXRD Pattern of HDPE/MMT–Nanofil 15 and HDPE/HDPE–g-MA/MMT–Nanofil 15 nanocomposites.....	81
2-5 WAXRD Patterns of SAN/MMT and EVOH/MMT.....	82
2-6 Illustration showing distribution of organic MMT layers in a cross section of nylon-66/organic MMT nanocomposites. (Yu et al., 2003).....	82
2-7 Illustration of peeling mechanism for the exfoliation process (Borse and Kamal, 2009).	82
2-8 Shear-induced orientation of platelets with the flow (x), gradient (y) and vorticity (z) directions (Lin-Gibson et al., 2003).....	83
2-9 TEM micrographs showing PP/clay elongated at 150 °C.....	83
2-10 TEM micrographs for EVA/SIOM, EVA/DIOM, EVA/TRIOM.....	84
2-11 Illustration of the morphological hierarchy at different length scales extant in the PET/CL30B and TEM micrographs	84
2-12 Variation of d-spacings of the MAPE/CL20A and MAPP/CL20A nanocomposite fibers depending on volume fraction of clay	85

2-13	A beam configuration of SAXS measurement and resulting SAXS photographs of MAPE/CL20A nanocomposite fibers and MAPP/20A nanocomposite fibers	85
2-14	Y- and Z- beam configuration of SANS measurement and resulting SANS patterns of both configurations of films consisting of PEO/LRD with lower aspect ratio or PEO/CNa with higher aspect ratio	86
2-15	Schematic diagram to represent the procedure for the preparation of a cured epoxy-clay fabric film composite with with exfoliated clay nanolayers at the outer surfaces of the clay film	86
2-16	TEM of the nanocomposite viewed along x^{\wedge} showing layered-silicates oriented orthogonally to the BCP lamellae	87
2-17	Schematic picture to represent the fundamental concept for the use of anionic polymer as a binder additive to achieve a clay film of densely packed structures	87
2-18	TEM image of a cross section of the saponite film with 20 wt% of carboxymethyl cellulose sodium salt and corresponding schematic microstructure,	87
2-19	TEM image of the film with a polymer loading of 20 wt%, showing the c-axis direction (crosssection)	88
2-20	Schematic representation of the internal architecture of the PVA/MTM nanocomposite (Podsiadlo et al., 2007).	88
2-21	DSC crystallization exotherms plots of PE-g-MAN and I.44PA/PE-g-Man nanocomposites and XRD patterns for PE-g-MAN and I.44PA/PE-g-MAN systems.....	88
2-22	Optical micrographs and Hv patterns	89
2-23	TEM images of PUCCN with 5% C (a and b) and PULCN with 3% L (c and d), (I); AFM images of PUCCN and PULCN, (II) (Mishra et al., 2008).....	89
2-24	Bright field TEM images of the extruded polystyrene/montmorillonite pellet and corresponding in situ WAXD patterns.....	90
2-25	TGA result for normal PVA/organoclay PCN and crosslinked PET/CL30B PCN	90
2-26	Three common particles' geometries used in models.....	90
2-27	Theoretical effects of volume fraction on relative permeabilities	91
2-28	Theoretical effects of volume fraction on relative permeabilities	92
2-29	A unit of three silicate platelets representing the arrangement of platelets in whole system of idealized PCN structure	92

2-30	Effect of confinement of clay platelets on polymer chain-segment immobility and resulting relative permeability	92
2-31	Effects of lateral spacing on d-spacing and relative permeability at different aspect ratio of platelets; this plot is based on Equation (2-12) ($\phi= 0.05$)	93
2-32	Comparison of the changes in H spacing as b varies between larger and smaller platelets	93
2-33	Schematic figure to depict the variance of S values depending on platelets' orientations.....	94
2-34	Effects of volume fraction on R_p when fully exfoliated structure.....	94
2-35	Effects of volume fraction on R_p for present barrier models calculated at aspect ratio of 50 and 1000	95
2-36	Comparison of prediction for R_p as a function of aspect ratio; all curves were plotted based on the Equation 2-2, 2-3, 2-4, 2-5, 2-6, 2-11, and 2-13 at $\phi = 0.05$	96
2-37	Illustration of effective width and its effect on barrier property of PCN.....	96
2-38	OTR chart of a pure PET sheet and PCN sheets (left) and corresponding TEM micrographs of MMT-PCN).	97
2-39	TEM micrographs to represent the difference in tortuosity (refer to dot lines) between phase-separated microstructure of unmodified MMT-PCN and exfoliated one of modified MMT-PCN	97
2-40	Oxygen relative permeability of composite depending on clay content (wt%) and TEM micrographs of PU/CL-UE400S00.....	98
2-41	TEM micrograph of a compression molded specimen containing 5 wt% of clay filler dispersed in polyesteramide matrix	98
2-42	Oxygen permeability rate of various blown composite/neat film samples.....	99
2-43	Chemical structure of poly (vinyl alcohol-co-vinyl acetate-co-itaconic acid) where, x, y and z is 97, 2 and 1, respectively (Grunlan et al., 2004).....	99
2-44	Effects of PVA contents on oxygen permeability of neat polymer containing no fillers and effect of clay loadings on oxygen permeability of terpolymer/CNa composites.....	99
2-45	Concept of probability of a barrier cell using Kadanoff cell and Critical volume fraction versus aspect ratio of platelets with $S= 0$	100
2-46	TEM micrographs of various PI/clay hybrid films.....	100

2-47	Commercialized structural composite to enhance oxygen barrier property	100
3-1	SEM micrographs of Laponite JS powder.....	113
3-2	A chemical structure of PVA.....	114
3-3	Schematic mechanism showing the formation of ideally exfoliated PVA/Laponite JS nanocomposite solution through the ordered experimental procedures	114
3-4	Schematicly illustrated experiment procedures	115
3-5	Controllable variables when APP-treating the surface of i-PP.....	115
3-6	SEM micrographs taken at 6000X of untreated surface	116
3-7	3D surface and height images taken by AFM (contact mode) on a 20 x 20 μm^2 of untreated surface	117
3-8	Influence of the flow rate of nitrogen gas which is one of the APP parameters; 3D surface images taken by AFM.	118
3-9	Influence of the WD which is one of the APP parameters; 3D surface images taken by AFM.....	119
3-10	Influence of the flow rate of nitrogen gas which is one of the APP parameters on surface roughness.....	120
3-11	Influence of WD which is one of the APP parameters on surface roughness.	120
3-12	WAXRD patterns of the pure Laponite JS powder and several PCNs having exfoliated silicate layers in PVA matrix.	121
3-13	Difference in WAXRD patterns between LP20PVA PCN samples prepared with and without high shear process.....	121
3-14	WAXRD patterns of several PCN-coated surface containing various amount of silicate particles obtained at low angle range from 2 to 10 degree.....	122
3-15	Dependence of the content of clay loaded in PCN on OTR values.....	122
3-16	Effect of the flow rate of nitrogen gas on OTR values.....	123
3-17	Effect of the WD on OTR values.....	123
4-1	Structure of silicate layers, Laponite JS when dispersed in water phase.....	136
4-2	Schematic mechanism of ‘a house of cards’ structure.....	137

4-3	Schematic mechanism of ‘a house of cards’ structure through the diffusion of LMW anionic PAA chains into a clay structure and expected ideal barrier structure.	138
4-4	Schematicly illustrated experiment procedures	139
4-5	SEM micrographs of Laponite JS clay powder and corresponding clay aerogel	140
4-6	TEM micrographs of clay aerogel consisting of three structural features, edge-standing, tilted and paralleled as indicated as arrows	141
4-7	DRIFT results of composite samples of C5PA73 prepared at pH 2, 4, and 6	142
4-8	Photographs of the states of composite solutions prepared under different pH conditions	142
4-9	Picture of C5PA91IS solution after 2 weeks storage and SEM micrographs of its by-product, white particles dispersed in the solution.	143
4-10	Effects of the pH on the peak positions of XRD results depending on PAA contents. Red lines represent the positions of peaks for pure Laponite JS powder	144
4-11	Effects of the amount of PAA on the microstructure of PCN samples prepared at basic condition.	145
4-12	TEM micrographs of C5PA73BS and C5PA73AS	145
4-13	XRD results of clay composite powder and corresponding coated layer by a coating rod	146
4-14	Effect of clay platelet microstructure on barrier properties when the same amount of clay was arranged.....	147
4-15	SEM micrographs of nanocomposite-coated surfaces	147
4-16	Dependence of permeability on pH and the amount of PAA for highly filled PCN coating system.....	148
5-1	Schematic diagram showing a filled polymer with (a) one clay type and (b) two different clay types.....	160
5-2	Effect of the total volume fraction of clay ₂ on the relative permeability of PC ₂ N.....	161
5-3	Actual relative permeability of various composite films calculated from OTR values measured by MOCON	161
5-4	Optical transmittance of composite films at the visible wavelength range	162
5-5	Pictures of prepared transparent and translucent composite film samples	162

5-6	Parallel arrangement of two nanoclays in an effective volume.	163
6-1	Schematically presented experiment procedure for the preparation of PVB-coated PAA/CNa nanocomposite film	176
6-2	Schematic diagram of an intuitive curvature test to measure flexibility of obtained film specimens	177
6-3	OTR values of highly filled nanocomposite film specimens of different polymer loading.....	177
6-4	Schematic microstructure of clay platelets and PAA chains and corresponding SEM micrographs of prepared film specimen	178
6-5	SEM micrographs (x 5,000) of cross-section areas of obtained highly filled nanocomposite film specimens.	179
6-6	X-ray diffraction pattern for CN3P0, P10, P30, P50, P70, and P100; (b) a FWHM as a function of polymer loadings	180
6-7	DSC thermograms of highly filled nanocomposite films with various amounts of polymer	181
6-8	SEM micrographs (x 5,000) of surface areas of obtained highly filled nanocomposite film specimens.	182
6-9	Dependence of RMS on the amount of polymer in highly filled nanocomposite films. .	183
6-10	An expected schematic picture of protruded curved edge of tactoids from the surface of CN3P70..	183
6-11	3D height contrast images taken by AFM	184
6-12	Power spectral density diagrams of highly filled nanocomposite samples.....	185
6-13	Curvature of highly filled nanocomposite films with various amounts of polymer and a picture of a flexible film specimen CN3P50)	186
6-14	TGA thermograms of highly filled nanocomposite films with various amounts of polymer	187

LIST OF ABBREVIATIONS

AFM	Atomic Force Microscopy
APP	Atmospheric Pressure Plasma
BCP	Block Copolymer
BOPP	Biaxially Oriented Poly(propylene)
CBMC	Carboxymethyl Cellulose
CEC	Cation Exchange Capacity
CED	Cohesive Energy Density
CL	Cloisite (CL15A, CL20A, CL25A, CL30B: refer to Table.2-1)
CNa	Cloisite Na ⁺
DDAB	Dimethyl Distearyl Ammonium Bromide
DGEBA	Diglycidyl Ether of Bisphenol-A
DIAB	Dioctadecyldimethyl Ammonium Bromide
DP	Degree of Polymerization
DRIFT	Diffuse Reflectance Infrared Fourier Transform
DS	Degree of Saponification
DSC	Differential Scanning Calorimetry
DTA	Dodecyl Trimethyl Ammonium
EDS	Energy Dispersive X-ray Spectroscopy
EG	Ethylene Glycol
EVA	Ethylene Vinyl Acetate
EVOH	Ethylene Vinyl Alcohol
FDA	The United States Food and Drug Administration
FE-SEM	Field Emission Scanning Electron Microscopy
FWHM	Full-Width at Half Maximum

GA	Glutaraldehyde
-g-MAn	Maleic Anhydride Grafted
GRAS	Generally Recognized As Safe
HDPE	High Density Polyethylene
HMW	High Molecular Weight
IEP	Isoelectric Point
LBL	Layer-By-Layer process
LMW	Low Molecular Weight
LP	Unmodified Laponite
LRD	Laponite RD
MAPE	Maleated Poly(ethylene)
MAPP	Maleated Poly(propylene)
MC	Modified Clay
MDEA	N-methyl Diethanol Amine
MMA	Methyl Methacrylate
MMT	Montmorillonite
MRE	Meal-Ready-to Eat
NBR	Acrylonitrile-Butadiene Copolymer
OAC	Organic Ammonium Chloride
OTR	Oxygen Transmission Rate
PAA	Poly(acrylic acid)
PALS	Positron Annihilation Lifetime Spectroscopy
PC2N	PCN consisting of two clay types
PCL	Poly(ϵ -caprolactone)
PCN	Polymer Clay Nanocomposite

PDMS	Poly(dimethyl siloxane)
PEG	Poly(ethylene glycol)
PEO	Poly(ethylene oxide)
PET	Poly(ethylene terephthalate)
PI	Poly(imide)
PMMA	Poly(methyl methacrylate)
PP	Poly(propylene)
PS	Poly(styrene)
PSD	Power Spectral Density
PU	Polyurethane
PUCN	Thermoplastic Polyurethane Clay Nanocomposite
PVA	Poly(vinyl alcohol)
PVB	Poly(vinyl butyral)
PVC	Poly(vinyl chloride)
RH	Relative Humidity
RMS	Root Mean Square
SAN	Styrene Acrylonitrile Copolymer
SANS	Small Angle Neutron Scattering
SAXS	Small Angle X-ray Scattering
SBR	Styrene Butadiene Rubber
SBS	Styrene-Butadiene-Styrene
scCO ₂	Supercritical Carbon Dioxide
SEM	Scanning Electron Microscopy
SIAB	Octadecyltrimethyl Ammonium Bromide
SPA	Sodium Polyacrylate

TEM	Transmission Electron Microscopy
TGA	Thermal Gravimetric Analysis
TPU	Thermoplastic Polyurethane
TRIAB	Tricetadecylmethyl Ammonium Bromide
TSE	Twin Screw Extruder
VA	Vinyl Alcohol
VAc	Vinyl Acetate
WAXRD	Wide Angle X-ray Diffractometer
WD	Working Distance

NOMENCLATURE

Chapter 1

J	diffusive flux of gas through film
Q	the amount of gas passing through a surface of certain area
A	surface of area
t	time
D	diffusion coefficient for a gas molecule through the film
S	solubility coefficient
C	concentration of gas molecules
C_1	concentration of gas molecules inside film (one side)
C_2	concentration of gas molecules outside film (counter side)
l	thickness of the film
p	partial pressure of gas
p_1	partial pressure of gas inside film (one side)
p_2	partial pressure of gas outside film (counter side)
P	permeability
π	permachor parameter
a	a constant based on gas molecules (Equation (1-7))
s	a constant based on polymers (Equation (1-7))
ρ	material density
T_g	glass transition temperature
V_f	average free-volume fraction of a polymer
α	diffusion jump length
ω	effective jump frequency

Chapter 2

ρ_{gr}	grafting density
N_{gr}	grafting length
Φ	volume fraction of fillers (clay particles)
X	polymer-clay pair-wise interaction
A_c	area of an alkylammonium ion of a 2:1 phyllosilicate
A_e	area of a half unit-cell of a 2:1 phyllosilicate
T	optical transmittance
C	the dependent on the the ratio of the refractive index of clay and matrix
d	d-spacing (Equation (2-1))
f_w	weight concentration of clay particle per unit volume
R_c	average aspect ratio
m	Rayleigh scattering factor
n_m	refractive index of matrix polymer
λ	wavelength of incident light
R_p	Relative permeability
P	permeability of polymer clay nanocomposites
P_o	permeability of matrix polymer without nanoclay
α	aspect ratio
t	thickness of a clay platelet (refer to Figure. 2-26)
d	diameter of a clay platelet (refer to Figure. 2-26)
L	length of a clay platelet (refer to Figure. 2-26)
ξ	reduction parameter of permeability
ξ_1	polymer chain-segment immobility factor
ξ_2	detour factor

H	face-to-face distance between two clay platelets (refer to Figure. 2-29)
b	edge-to-edge distance between two clay platelets (refer to Figure. 2-29)
S	orientation parameter
Θ	angle between direction of orientation and sheet normal (refer to Figure 2-33).
P_c	critical value of clay platelets for minimum permeability
Φ_c	critical volume fraction
L/w	degree of exfoliation (length/thickness)

Chapter 3

R_a	surface roughness calculated as average roughness
R_{max}	maximum height
R_q	root mean square value
L	Evaluation length
$Z(x)$	profile height function

Chapter 5

Clay 1	Clay type 1 with large aspect ratio
Clay 2	Clay type 2 with smaller aspect ratio than Clay 1
L_1	lateral length including edge-to-edge distance of clay 1, (l_1+b_1)
L_2	lateral length including edge-to-edge distance of clay 1, (l_2+b_2)
H_1	vertical length occupied by Clay 1 per unit volume, (h_1+w_1)
h_1	face-to-face distance of clay 1
h_2	face-to-face distance of clay 2
w_1	width of clay 1
w_2	width of clay 2
l_1	length of clay 1
l_2	length of clay 2

b_1	lateral edge-to-edge distance of clay 1
b_2	lateral edge-to-edge distance of clay 2
N_1	number of clay 1/unit volume within effective volume of clay 1
N_2	number of clay 2/unit volume within effective volume of clay 1
v_T	total volume of two clay types
v_1	volume of clay 1
v_2	volume of clay 2
V_{eff1}	effective volume of clay 1
V_{eff2}	effective volume of clay 2
ϕ_T	volume fraction of two clay types
ϕ_1	volume fraction of clay 1
ϕ_2	volume fraction of clay 2
$\phi_{polymer}$	volume fraction of polymer
n	total number of clay 2 occupying in a layer in the unit cell
l	the number of layers in the unit cell
d	the shortest tortuous path through unfilled polymer
d_a	lateral tortuous path
d_{a2}	additional lateral tortuous path by clay 2
d'	tortuous path
Chapter 6	
k	local curvature
r	radius of curvature

Abstract of Dissertation Presented to the Graduate School
of the University of Florida in Partial Fulfillment of the
Requirements for the Degree of Doctor of Philosophy

LAYERED SILICATE PARTICLES FILLED POLYMER NANOCOMPOSITE FOR
BARRIER APPLICATION

By
Jinwoo Kwak

May 2010

Chair: Charles L. Beatty
Major: Materials Science and Engineering

A polymer clay nanocomposite (PCN) system for barrier applications has been studied and various materials have been utilized to achieve a better barrier solution. This study aims at making progress in the packaging industry toward super barrier materials by tailoring processing parameters to the creation of new barrier solutions and also by systemizing theoretical background knowledge. Comparisons of several barrier models were made in order to develop a new model and to assist with material selection and experimental design.

PCN consisting of synthetic layered silicate (Laponite) in polyvinyl alcohol (PVA) was applied to atmospheric plasma treated, semi-rigid polypropylene (PP) samples. PCN coating bonded to polyolefins offers a simpler method to achieve higher barrier properties without modifying commodity materials.

Highly filled PCN coating layers, with parallel arranged dense structures of Laponite were studied. An investigation on effects of pH of poly(acrylic acid) (PAA) on PCN coating system performance suggested that enhanced barrier properties were achievable with the aid of positively charged poly(acrylic acid) and a shear coating processes. This work also suggested another PCN coating system that incorporates a dense stratified structure of silicate platelets using a polymer as a linkage molecule.

Benefits of dispersing smaller nanoparticles between larger ones in a polymer matrix (PC2N) were explored and a barrier model to estimate relative permeability of the PC2N system was proposed. It was demonstrated that total volume fraction of particles determined barrier properties and this was confirmed by experiment. No significant difference in oxygen transmission rate of three composite films was found. A film containing only Cloisite had a lower oxygen transmission rate than that of Laponite and PC2N films because of the relatively larger aspect ratio of Cloisite; however Laponite and PC2N films had better optical transmittance due to the smaller aspect ratio resulting in lower numbers of scattering events.

Achieving good flexibility and high barrier properties was possible with PAA negatively charged organic molecules as linkage molecules and poly(vinyl butyral) (PVB) exterior layers. Unlike the observed 'house of cards' structure formed in Laponite aqueous solution, the large aspect ratio of Cloisite Na⁺ (CNa) clay platelets resulted in parallel arrangement as observed by scanning electron microscopy (SEM). Result showed that the layered structures had various features depending upon the amount of linkage polymer applied. In addition, enhancement of barrier properties and flexibility was achieved after PVB coating. A barrier model based on Nielsen's detour theory or Beall's filling void theory predicted overall barrier properties experiments.

CHAPTER 1 INTRODUCTION

Microstructures of clay platelets in polymer matrices have been widely studied in order to better understand relationships between physical structures of polymer clay nanocomposites (PCN) and resulting properties. A variety of applications such as material reinforcement [1-5], gas barrier and membrane separations [4-15], advanced electronic devices [16-20], and biomedical applications [21-23] have shown great potential of PCN materials. These studies help to elucidate characteristics of filler particles and polymers as well as mutual interactions between components. Because of differences between conventional composites with macro-sized filler and PCN, new approaches are required to better understand features of nano-fillers in polymer chains. Study of orientation and dispersion of nano-sized inorganic platelets in polymer and effects on physical properties have shown differences that suggest potential for better designs of PCN materials compared to previously proposed systems.

Commonly used filler particles for PCN are phyllosilicate. The classification of commonly used phyllosilicate for PCN is listed in Appendix A. The basic crystal structure of Montmorillonite (MMT), which is one of the more commonly used silicates under the smectites group is shown in Figure 1-1. An octahedral sheet is between two tetrahedral silica sheets and oxygen atoms in these sheets are common to both layers. Resulting three-layer units are aggregated together showing negative surface charges with positive ions between units that neutralize the whole structure. The weak bond between the cation and negative surface allows diffusion of water and other polar molecules into this interplanar space, intergallery region inducing an expansion of the mineral structure. In general, separation of clay platelets via this expansion process and insertion of polymer chains into the intergallery region has proven to offer enhancement of physical properties such as barrier, flame retardant, mechanical, optical and

membrane properties. Understanding mechanisms of changes from micron-sized particles to nano-sized particles and correlations to changes in physical properties are key aspects to the nanotechnology required for the preparation of PCN materials.

This study has made progress in the area of packaging films regarding enhanced gas barrier properties. Through the literature study, various practical PCN systems and several barrier models to estimate theoretical permeability have been reviewed. Based on this theoretical background, four barrier structures have been developed for study. In this chapter, three typical microstructures of PCN, generalized preparation methods for PCN, and fundamental mechanism of barrier performance in a polymer film as well as in a nanocomposite structure are reviewed.

Polymer Clay Nanocomposite

Three Conventional Microstructures

Degree of dispersion and dissociation of clay platelets by diffusion of polymer chains into interlayer spacing determines the microstructure of PCN. In fact, the term 'PCN' only can be used for the morphologically ideal case, when particles are exfoliated. Exfoliation means that clay nanoplatelets are uniformly dispersed in the polymer matrix. When polymer is inserted into the intergallery of the mineral making a regularly enlarged spacing, an intercalated microstructure is achieved and separation of platelets causes an increase in surface area, resulting in modified physical properties. However, poor separation leads to local morphologies, a phase-separated, micro-sized morphology with aggregated stacks dispersed in polymer matrix, forming a microcomposite resulting in slightly modified properties compared to both the intercalated and exfoliated. Figure 1-2 illustrates the evolution of morphologies of clay platelets in the polymer matrix from their initial state of aggregated stacks to fully exfoliated one. X-ray diffractometry (XRD) and transmission electron microscopy (TEM) have been used in combination to identify microstructures. According to Bragg's law, d-spacing calculated from a characteristic peak in

XRD is usually used to determine separation of interspacing due to polymer chains, and this is a descriptor used to analyze intercalated morphology (blue curve in Figure 1-2). When an intercalated morphology is achieved, a shift to lower 2θ (2 theta) angles of a characteristic peak (a shift from the black curve to the blue curve) is observed. Further increase in both the d-spacing and random orientations of clay platelets caused by diffusion of polymer chains results in an exfoliated morphology. Lack of regularities from platelets results in no peak as shown by the red curve in Figure 1-2. Small “humps” may appear instead of strong peaks suggesting the possibility of remaining tactoids. However, discrepancies can arise in analyzing XRD patterns because a peak can appear from a unit cell of crystallized polymer matrices or from additives added during the process of preparation of PCN. Thus, interpretation of XRD requires care and consideration about variables that can affect positions of peaks. More definitive tools such as TEM are also used to analyze PCN structures. Because of differences in atomic configuration between polymer and platelet, contrasts from different diffractions appear in TEM micrograph as shown in Figure 1-2. Figure 1-2 represents a general realistic microstructure of PCN material consisting of intercalated and exfoliated regions. Clay platelets appear as dark lines and some gradient around the dark lines illustrate interfacial regions between clay and polymer.

Preparation of Polymer Clay Nanocomposite

Even though some differences in final morphologies of PCN may depend on selection of materials and processing parameters, processes for preparation of PCN can be classified into three categories with resulting microstructures shown in Figure 1-3.

In solution mixing, when clay platelets are added to an aqueous phase, clay powder is in the form of aggregated nanoparticle stacks. Stacks may be separated by hydration of cations. Cations may be exchanged with organic modifiers with alkyl chains in order to modify the hydrophilic nature of inorganic platelets and to open intergallery regions. Diffusion of polymer

chains into intergallery regions is usually accomplished by high shear forces. For intercalating polymerization, monomer diffuses into the intergallery space homogeneously, and then polymerization occurs in the inner and outer regions resulting in intercalated morphology of PCN. In melt process, shear and crystallization significantly effect on final morphologies of PCNs.

The Fundamental Concept for Barrier Solutions

Barrier Mechanism in a Polymer Film

Permeation of a gas molecule through neat polymers, without fillers is well known. Gas molecules are adsorbed on the surface and diffuse into and through the interior of a film and finally desorbed from the opposite side of the material. Diffusion of a permeant, such as a gas molecule, conforms to the Fick's law and sorption and desorption of gas molecules follow Henry's law as shown in Figure 1-4 (I).

Steady state diffusion of gas across a film results in mass flux (J) across the film described by Equation (1-1)

$$J = \frac{Q}{At} \tag{1-1}$$

Where, 'Q' is the amount of gas passing through a surface of area (A) normal to the flowing direction and 't' is duration during which the diffusion occurs. According to Fick's first law, flux, J is also expressed as Equation (1-2)

$$J = -D \frac{\partial C}{\partial x} = \frac{D(C_1 - C_2)}{l} \tag{1-2}$$

where, 'D' is the diffusion coefficient of a gas molecule through the polymer film, and C_1 and C_2 represent the concentration of gas molecules at each side of the film, respectively, and l is the thickness of the polymer film.

Combining Equation (1-1) and (1-2) results in Equation (1-3).

$$Q = \frac{D(C_1 - C_2)At}{l} \quad (1-3)$$

Since Henry's law applies for typically low concentrations of gas; thus C can be expressed as

$$C = Sp \quad (1-4)$$

Where S is the solubility coefficient and p is the partial pressure of gas. Therefore, Equation (1-3) can be rewritten as the following Equation (1-5)

$$Q = \frac{DS(p_1 - p_2)At}{l} \quad (1-5)$$

Permeability (P) is defined the combined coefficient of D and S (P=DS), also known as DS, where D is the diffusion coefficient, and S is the solubility coefficient, P can be estimated from the following Equation (1-6)

$$P = \frac{Ql}{At(p_1 - p_2)} \quad (1-6)$$

Therefore, knowing the partial pressures of gas on both sides of the films, the amount of gas diffused, and dimensions of the film allows us to estimate the permeability of a polymer film sample.

Koros [24] reports that permeability is related to diffusion and solubility as mentioned above (P=DS) and hence permeability, P may either decrease or increase with increasing molecular weight of the penetrant depending upon which factor dominates. Therefore, the permeability of a polymer is a function of both the diffusion and solubility coefficients which are mainly determined by the chemical and structural properties, such as polymer polarity and

degree of crystallinity. Salame [25] proposed a comprehensive semi-empirical correlation of polymer structure and gas permeability based on the Permachor parameter (π).

$$P = as^{-3\pi} \quad (1-7)$$

where a and s are constants based on the permeant gas and polymers. And this Permachor parameter is based on the molecular forces holding the polymer together, cohesive energy density (CED), material density (ρ), and average free-volume fraction (V_f) of the polymer. Therefore, the Permachor value of a polymer can be calculated using Equation (1-8), which is based on the ratio of amorphous and crystalline regions [24-26].

$$Permachor(\pi) = 71 \left[\ln \left(\frac{CED - \rho^2}{v_f} \right) - 5.7 \right] \quad (1-8)$$

Therefore, the choice of a polymer for a high barrier property could be based on the Permachor value. Equation (1-8) suggests that the higher Permachor value, the higher the barrier property.

Increasing barrier properties of polymer materials can be realized in several ways. A polymer generally consists of crystalline and amorphous regions as shown in the simple fringed micelle model of semi-crystalline polymer of Figure 1-4 (II). Gas molecules diffuse into amorphous regions with lower packing densities because crystalline regions effectively block diffusion due to higher packing densities. Small intermolecular pores, which are called 'excess free volume hole,' introduced by random entanglements of polymer chains in amorphous regions allow gas molecules to diffuse through the film by a mechanism known as vacancy hopping diffusion [27]. Excess free volume hole is caused by differences in specific volumes of polymer in different equilibrium states as shown in Figure 1-5. Generally, the temperature called " T_2 " is the point where a real discontinuity in specific volume occurs and T_2 is generally $T_g - 50^\circ\text{C}$ for a

glassy polymer. For instance, in the case of PE, the average size of free holes is below 1 nm above T_g , with concentration of about $10 \times 10^{21}/\text{cc}$. The Van der Waals diameter for oxygen is 0.375 nm [28,29]. Permeant gas molecules usually stay longer in free volume holes and occasionally hop into neighboring holes by the formation of a channel as shown in Figure 1-5. Therefore, the number and size of holes, which is called ‘static free volume’ determines the permeability of a polymer. Static free volume included within a polymer is related to solubility (S) and dynamic free volume, and it determines diffusivity (D) with diffusion jump length (α). This relation regarding diffusivity was reported by the following Equation (1-9) [30].

$$D = \frac{1}{6} \omega \alpha^2 \quad (1-9)$$

Where, ω is the effective jump frequency.

Basic Barrier Model for Polymer Clay Nanocomposite Materials

Increasing crystallinity is the most effective way to lower permeability of a polymer material. However, flexibility, cost, optical properties under certain circumstances often deteriorate in sympathy with increasing crystallinity. Artificially increasing apparent crystallinity may be accomplished with uniformly dispersed and exfoliated clay platelets that are impermeable to gas molecules. Neilsen’s detour theory [31] suggested this fundamental concept of enhancing barrier properties in PCN materials and based on this model, a variety of studies have been conducted. As shown in Figure 1-6, the detour path would be increased significantly when a fully exfoliated microstructure (c or d) is achieved when compared to those of others (a and b). In this way, the microstructure of PCN has significant effects on barrier properties governed by factors such as aspect ratio and orientation of clay platelets. Aspect ratio, volume fraction, orientation and other factors have been involved in approximating the actual permeability in various barrier models.

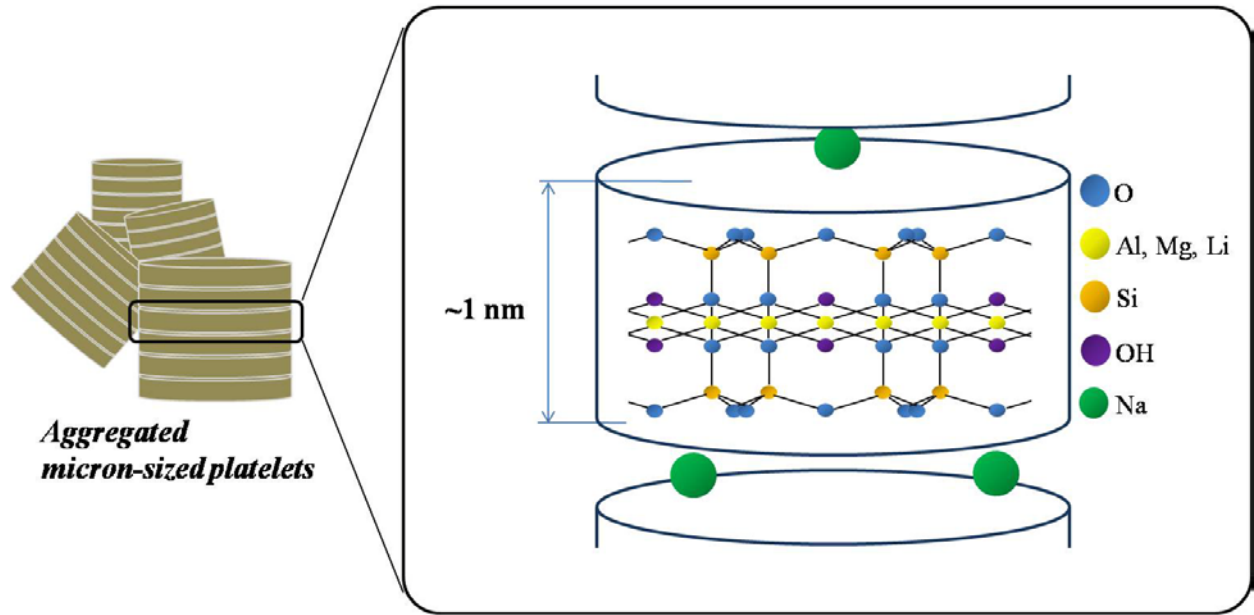


Figure 1-1. Basic crystal structure of montmorillonite

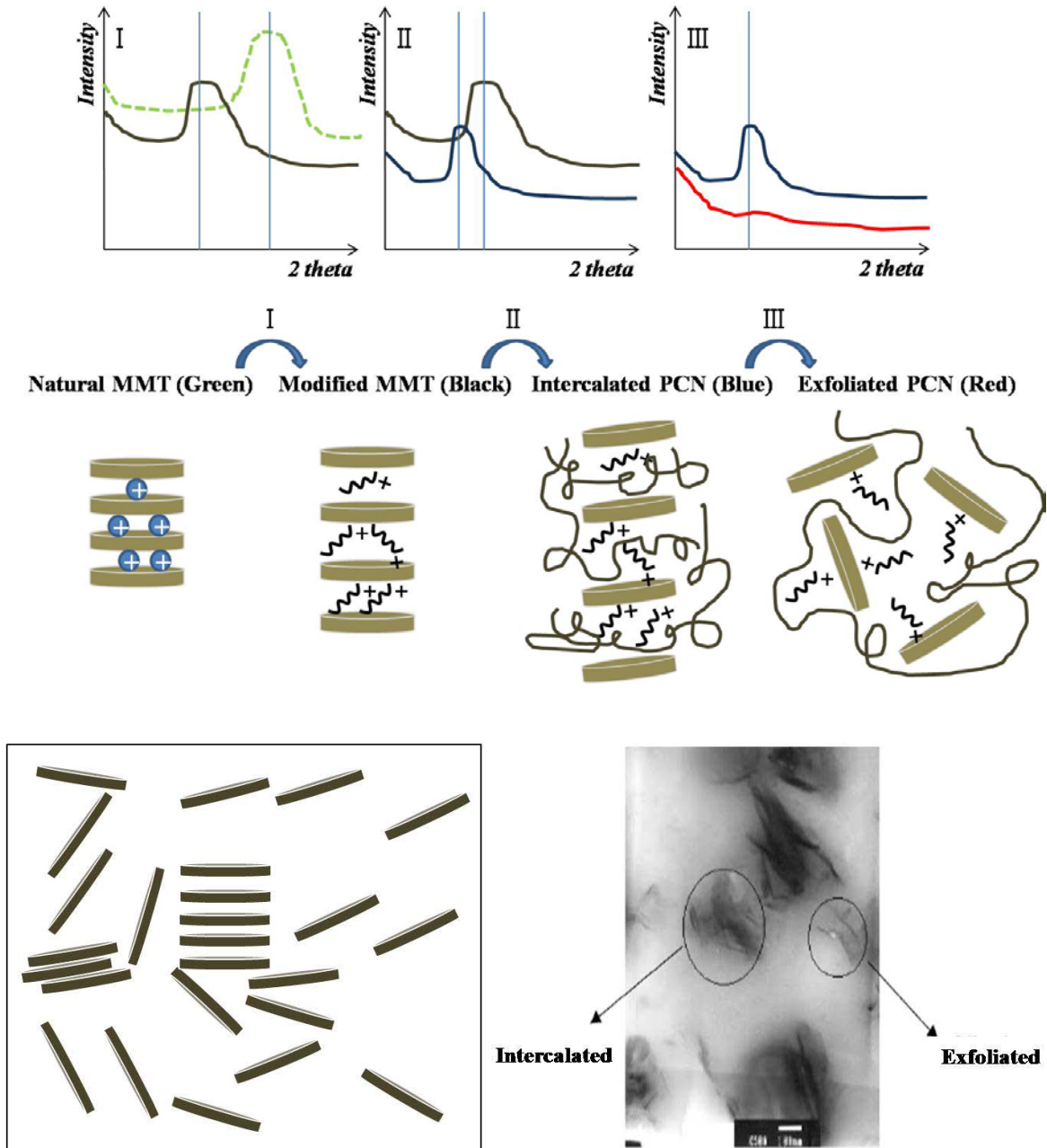


Figure 1-2. Evolution of morphologies of PCN from natural MMT to fully exfoliated PCN and corresponding general patterns of XRD; a more realistic microstructure which is a mixture of all structures and a corresponding TEM micrograph [32]

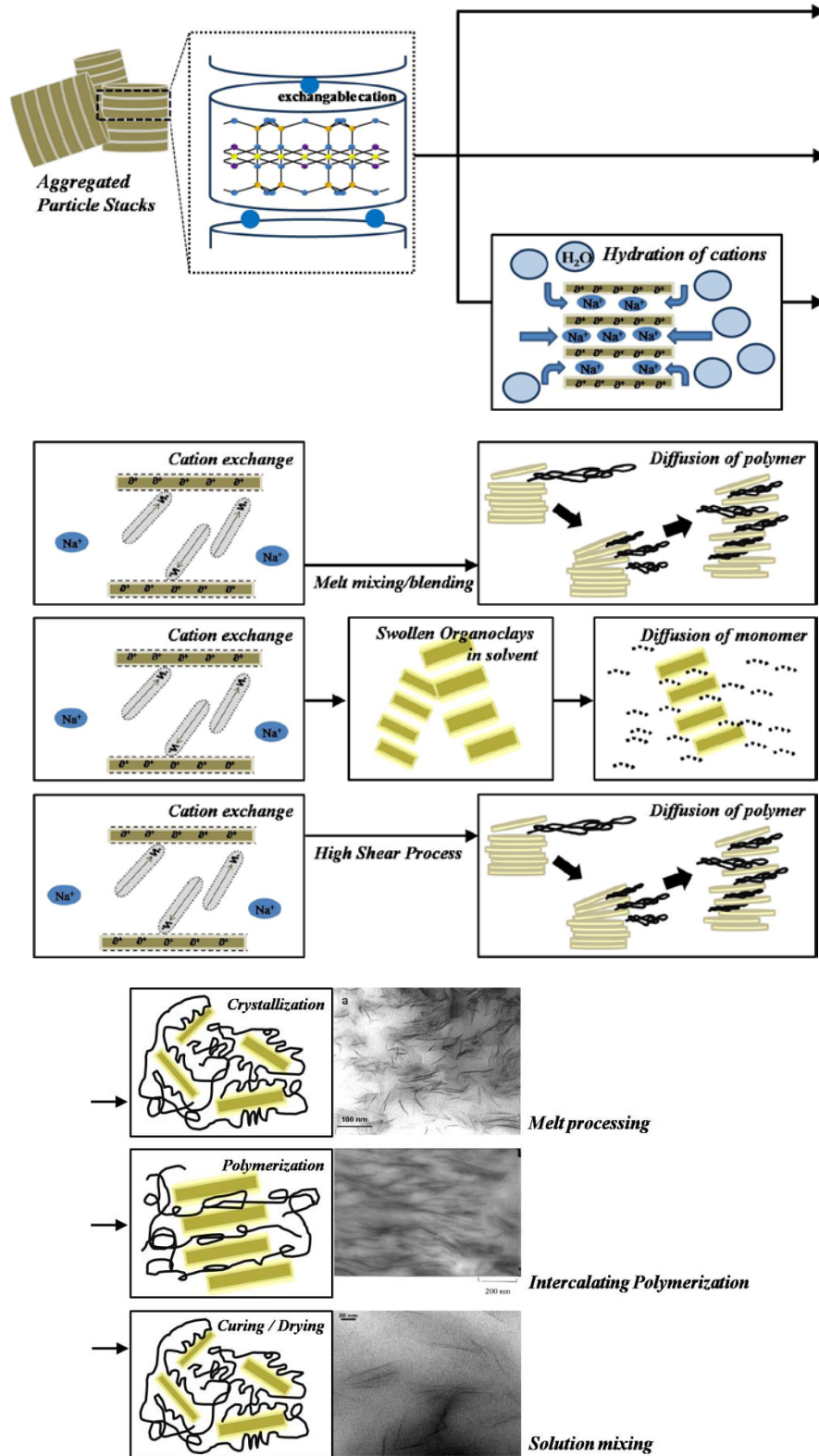


Figure 1-3. Procedures for preparing PCNs

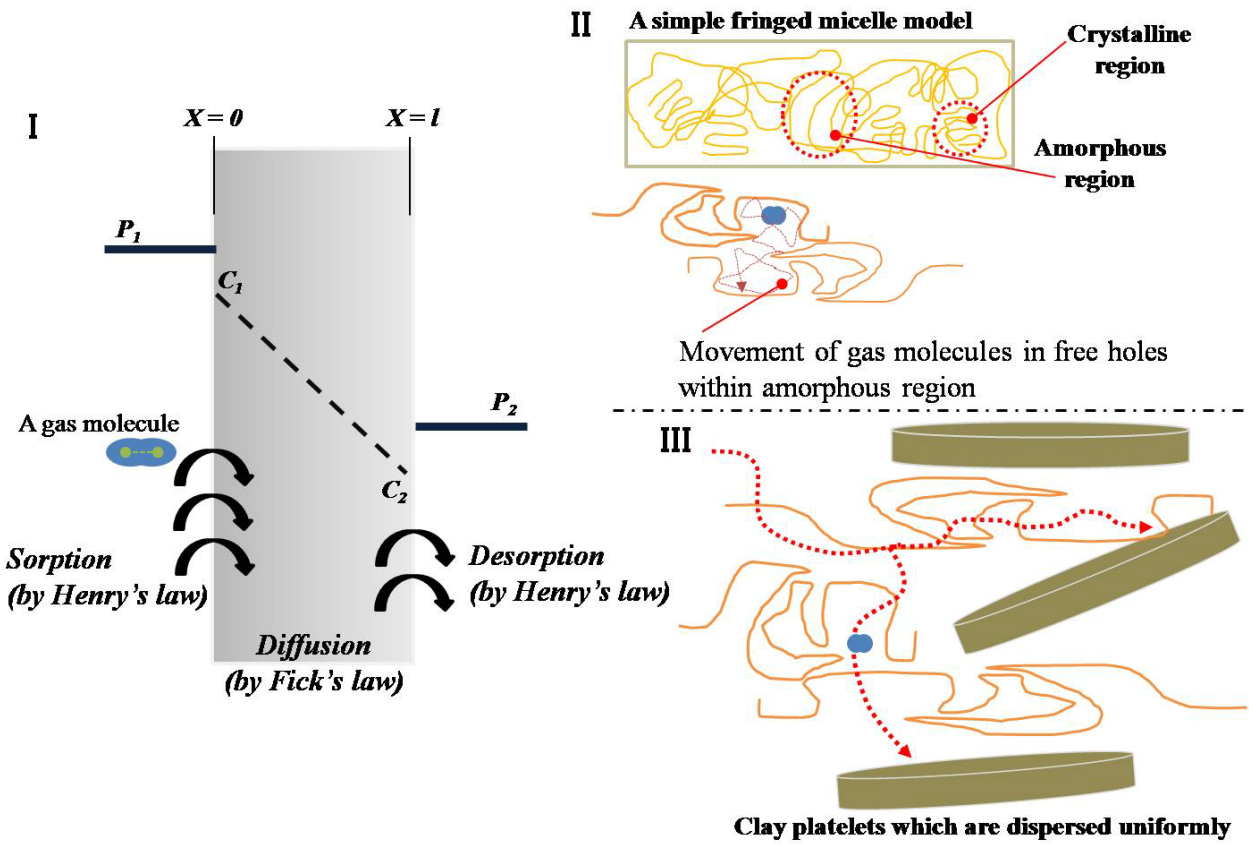


Figure 1-4. Permeability mechanism of gas molecules through polymer film, I; Diffusion motion of gas molecules in free holes within the amorphous region of the neat polymer, II; Motion of gas molecules to avoid impermeable clay platelets in PCN materials, III.

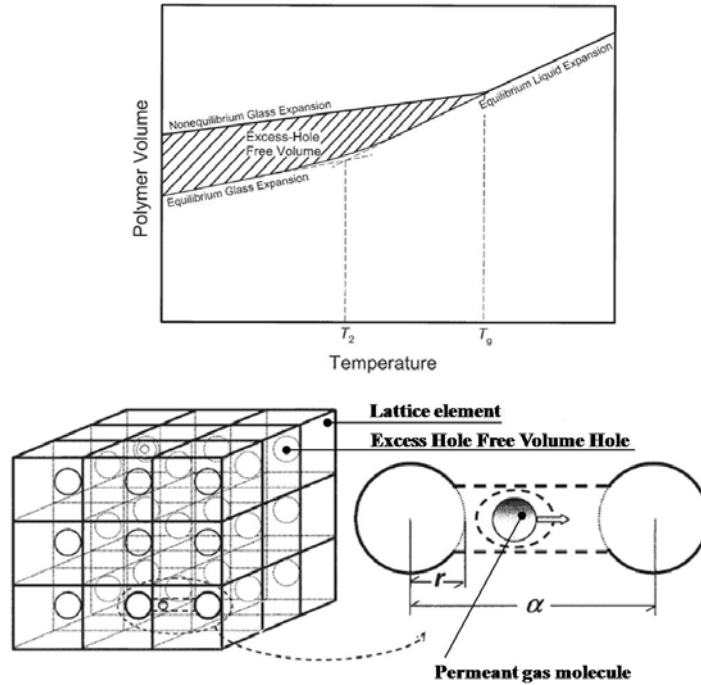


Figure 1-5. Volume-temperature relationship for amorphous polymer (upper). Lattice holes in polymer and vacancy-hopping diffusion model of gas molecules (lower) [27]

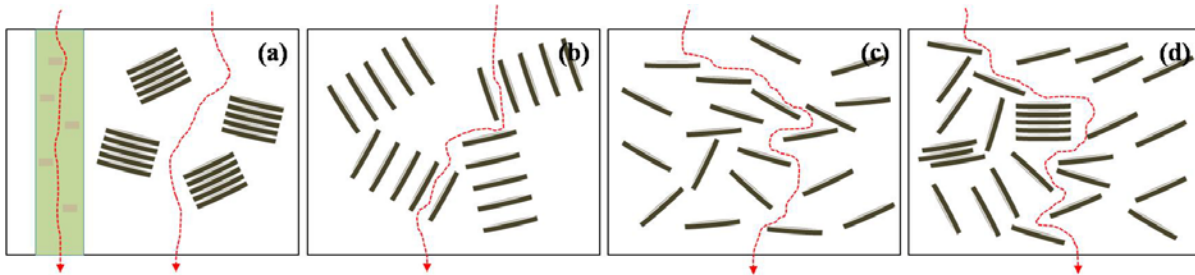


Figure 1-6. Effects of microstructures of clay platelets in polymer on barrier properties of PCNs. (a) Phase-separated (inset figure shows relatively shorter detour path through the neat polymer), (b) intercalated, (c) fully exfoliated and (d) more realistic exfoliated structure (arrow lines represent the diffusion path of gas molecules and the direction of diffusion is perpendicular to the surface of the PCN layer)

CHAPTER 2
LITERATURE REVIEW ON MICROSTRUCTURE OF POLYMER CLAY
NANOCOMPOSITE MATERIALS FOR BARRIER APPLICATIONS

Microstructures of Polymer Clay Nanocomposite

Unlike three typical microstructures, practical polymer clay nanocomposite (PCN) have shown diverse microstructures such as wedged, preferentially oriented nematic phase, densely stratified and others. A general microstructure of PCN in real composite systems can be described as a mixture of intercalated and exfoliated structures. Interplay among polymer matrix, nanoclays, organic molecules covering nanoclays and processing parameters leads to a structure representing the whole composite system. This chapter reviews variables that affect formation of certain microstructures of layered silicate particles from the stage of material selection to processing parameters.

Microstructures in Practical Nanocomposite Materials

Roles of organic modifier for intercalation and exfoliation

Achieving a complete exfoliation involves matching surface energy between matrix polymer chains and organic modifiers of nanoclays in order to increase interactions between nanoparticles and polymer. A theoretical phase diagram of PCN was suggested [33] to explore the role of grafted organic modifier to prove the importance of compatibility and interactions between nanoclay particles and polymer matrix in determining an average microstructure of PCN. Density function theory for the ordering of nanoclay particles and self-consistent field approximation for long-range order interaction between nanoclay layers covered with certain types of modifiers are used to realize phase-behavior of modeled polymer-clay mixtures. The resulting phase diagram is shown in Figure 2-1.

Phase-behaviors of a PCN can vary depending on grafting density (ρ_{gr}), grafting length (N_{gr}), volume fraction (ϕ), polymer-clay pair-wise interactions (χ) and whether it is located in an

isotropic or nematic phase. This theoretical development agrees well with recent experimental results [7,34-37,39]. Increases in ρ_{gr} and N_{gr} improve miscibility between nanoclays and polymer matrix with lower χ values. Thus, it can be demonstrated (Figure 2-1) that the equilibrium phase behavior at short grafting length is in the immiscible region. This suggests that there should be a strong attractive force between polymer and graft chains (lower χ value) to obtain an exfoliated structure (isotropic or nematic phase) when grafting length is short.

Organic modifiers serve to (a) increase intergallery space to prevent platelet–platelet cohesion and (b) match polarity to accelerate favorable interactions between polymer and modifier chains. It can be deduced that the crucial factor for obtaining high degree of exfoliation at small volume fraction is increased affinity of polymer chains to nanoclay surfaces as a result of the increased intergallery distance. These functions of organic modifiers are highly dependent on arrangements of modifier molecules which give rise to different particle surface properties. Subsequently, modified surface properties have a significant effect on the final morphology during swelling and shear processes.

Arrangements of organic modifiers depend on chains characteristics in low-charge 2:1 clay minerals. Depending on difference between areas of alkylammonium ions, A_c , and areas of a half unit-cell of a given 2:1 phyllosilicate, A_e , arrangements of organic modifiers in the intergallery regions are determined. As shown in Figure 2-2 (IV), when A_c is equal to A_e , the monolayer of alkylammonium ions is close-packed (Figure 2-2 (II), a). As chain length increases above monolayer coverage, alkylammonium ions adapt bilayer morphology (Figure 2-2 (II), c) resulting in some increases in d-spacing by insertion of one more layer. When the area for close-packed morphology is more than twice the area available for each monovalent cation ($A_c > 2A_e$), the transition from a complete bilayer to a pseudotrimolecular layer occurs and alkylammonium

cations will form paraffin-type structures in higher-charge 2:1 clay minerals (Figure 2-2 (II), b). When paraffin-type microstructures form, tilting angle shows changes that are sensitive to layer charge as shown in Figure 2-2 (III) [40]. Measurement of tilt angle was suggested by Usuki et al [41] as illustrated in Figure 2-2 (I). Therefore, cation exchange capacity (CEC) value of clay, amount of organic modifier, length of alkyl chains, and dimension of clay particles are critical to understanding arrangements of organic modifiers. Approximation of molecular length and the spacing from X-ray diffractometer (XRD) using the equation suggested by Usuki allows reasonable estimation of average tilting angle and it may be possible to study whether modifier molecules are inclined to the silicate layer surface. Adsorption of modifier onto the layer surface would be in monolayer if the ratio of the amount of modifier for cation exchange reaction to clay's CEC approaches to unity.

Organic modifiers (also referred to as “surfactants”) with long alkyl tails have been used for exfoliation, and a variety of commercially available modified nanoclays (organoclays) can be used depending on the types of processing and matrices. Appendix B lists commonly used commercial organoclays and modifiers used. Organoclays have also been prepared by the cation exchange reaction by many research groups and effects of surfactant molecules on the final morphology of PCN have also been reported. Effects of modifier molecules arrangement on characteristics of intergallery regions were investigated [42]. Results from thermal and XRD analyses of different grades of organoclays provided understanding of the ordered state of grafted alkyl chains. Water desorption from or through surfaces of organoclays decreased order of Nanofil 804 bearing hydroxymethyl group, Nanofil 919 containing one tallow and one benzyl methyl, and ditallow chain attached Nanofil 15. Endothermic peak area for melting tallow chains of Nanofil 15 was much larger than the other two Nanofil grades. This suggested that benzyl or

hydroxyl group interrupted formation of ordered structures of alkyl chains with higher packing density. The fact that the basal spacing mainly depends on length of alkyl chains attached to surfaces of nanoclays was confirmed by the result that well-stacked alkyl chains of Nanofil 15 had the higher d_{001} than others in XRD.

Polymer matrices bearing hydrogen bonding such as polyamide and poly(vinyl alcohol) (PVA) usually have a good affinity for surfaces of nanoclays because of the hydrophilic nature of the intergallery zone. When considering two functions of the organic modifier for good exfoliation, single long alkyl cations are required to be exchanged with cations in the gallery to make this space larger without distorting the polarity of the hydrophilic polymer chains. As vinyl acetate (VAc) content increases in ethylene vinyl acetate (EVA), intensity of intercalating peak became larger in XRD patterns because the higher the polarity caused by VAc groups in backbone chains, the more easily polymer chains diffused into interlayer regions. Single alkyl chain modifier molecules could not render enough space for full exfoliation by EVA chains even with higher VAc content resulting in a intercalated morphology [43]. Terpolymer, modified PVA consisting of 97 wt% of vinyl alcohol (VA), 2 wt% of VAc and 1 wt% of itaconic acid showed a strong interaction with organic modifier molecules because of the stronger hydrogen bonding by $-\text{COOH}$ on the itaconic acid unit than normal $-\text{OH}$ bonding [44].

PCNs based on polyurethane (PU), which has both lower and higher polarity at the soft and hard segment, respectively, revealed various interactions at the interface area between PU and organoclays. Non-polar hydrocarbon attached to Nanofil 15 filled PCN formed a phase-separated morphology because of the poor attractive force between organoclays and polar PU matrix. In this case, electrostatic force between nanoclays tended to squeeze polymer out, which confirmed expectations based on the function of grafted organic modifier. However, the case of

hydroxyethyl-attached Nanofil 804 deviated from the expectation in that increased interactions between organoclays-bearing polar groups and polar PU results in steric hindering of platelet–platelet cohesion by tethering polymer chains to surfaces of clay. Based on results of XRD and transmission electron microscopy (TEM) (Figure 2-3), the author concluded that there was little or no reaction with the suggested reasons of deactivation of OH groups through hydrogen bonding to the aluminosilicate surface or shielding effects by long alkyl chains [7].

Effects of adding maleic anhydride-grafted-high density polyethylene (HDPE-g-MA) as interfacial agent between organoclays and HDPE phases on morphology were investigated as shown in Figure 2-4 [42]. Due to the function of HDPE-g-MA, which is a polar copolymer used as an interfacial agent, organoclays were dispersed well when using HDPE-g-MA. On the other hand, TEM images of HDPE/Montmorillonite (MMT)-Nanofil 15 showed micro-sized agglomerates, suggesting that HDPE chains could not enter into the interlayer spacing. Wide Angle (WA) XRD (WAXRD) of HDPE/MMT-Nanofil 15 also confirmed this by showing intercalated peaks at around 3.1 degrees, suggesting no increase in d-spacing caused by insertion of polymer chains. Effectiveness of interfacial agents for better dispersion worked well for polypropylene (PP)/MAPP/MMT systems as shown in TEM micrographs of Figure 2-4 (II, III)[45,46].

Strong interaction energy between polymer chains and organoclays does not guarantee a large amount of polymer penetrating into the interlayer spacing. This was confirmed by XRD and boundary region between polymer and clay particles in TEM micrographs [47]. While styrene acrylonitrile copolymer (SAN)/MMT shows a discrete boundary region with poor interfacial affinity, ethylene vinyl alcohol (EVOH)/MMT revealed a tightly associated feature. The feature of the quite diffused boundary region represents a stabilized boundary due to strong

interaction energy. However, dissociation of organoclays was better developed in SAN/MMT composite. More polymer penetrated into the intergallery resulting in well-exfoliated structures. In Figure 2-5, the intercalating peak after 5 min in the case of EVOH/125C composite is much more intense than that of SAN/125C. Therefore, initial diffusion rate of guest polymer molecules depends on polarity of the polymer.

Increasing modifier sometimes decreases ability of polymer molecules, especially those with low molecular weight such as an oligomer, to penetrate into the clay. In other words, oligomer molecules prefer to penetrate into the intergallery space of MMT when the surface of this clay is partially covered with a modifier [48].

Bonding between delocalized π -quadrupolar of a benzyl group in organic modifier and/or epoxy resin induces strong Van der Waals attractions. This interaction is enhanced by the preferential parallel orientation of benzyl groups with surfaces of nanoclays. Therefore, when epoxy resin is used as polymer matrix, use of modifier containing long alkyl chains and benzyl groups will assist exfoliation by increasing d-spacing and facilitating penetration of polymer. Addition of hydroxyethyl group to the chemical structure of a modifier will further promote tethering of chains to the silicate surface. However, some criteria were required for selection of modifier in epoxy/MMT composite system. Long alkyl chain masked -OH group may hinder the reaction with epoxy resin and excess number of -OH groups were sometimes counterproductive [49].

Effects of processing parameters on intercalation and exfoliation

Various processing methods including in-situ polymerization, solution, and melt process have been suggested to be capable of producing a complete exfoliated system. Among various ways, melt processing is the most common method and has been widely used in the industry because of its ease of operation and flexibility. Many benefits can be realized because melt

processing usually utilizes commercially available facilities and materials. Such processes make it possible to vary formulations easily. Four different formulations with different facilities and materials were built as shown in Table 2-1. Microstructures were examined to investigate effects of processing parameters [45].

When nonpolar polymer was used such as F1 and F3, intercalation or exfoliation could not be attained by batch mixing or twin screw extruder (TSE) because of poor interaction between clay platelets and polymer. Moreover, this drawback cannot be improved by controlling processing parameters. In this case, using polar groups attached to interfacial agents is an efficient way to achieve intercalation or exfoliation. Dynamic properties such as shear viscosity and elasticity could be used to judge microstructural state during processing. A phase-separated structure, with particle size larger than 1 μm , generally shows decreased shear viscosity and elasticity with increasing mixing time and intensity. However, completely exfoliated or intercalated systems, which can be regarded as colloidal suspensions, show a counter behavior because of the enhanced interactions between matrix and particles. Sonication and TSE processes with use of modified poly (dimethyl siloxane) (PDMS) with a polar moiety as matrix in F2 showed a typical colloidal dynamic behavior of a well-exfoliated microstructure. F4 showed some sensitivity to processing conditions. While increasing specific energy input for mixing increased basal spacing, an intercalated structure was found at relatively short mixing times and low specific energy input [45].

Lee et al. proved that ultrasonication is most effective for dispersion of nanoparticles in low molecular weight (LMW) polymer matrices [46]. In-situ ultrasonication at elevated temperature was successfully used to enhance clay dispersion and exfoliation in LMW PP/CL20A without any mechanical shear or aid of interfacial agent. Increase in ultrasonic energy

promised increased interlayer spacing with enhanced shear thinning behavior as well as increased shear viscosity due to formation of gel-like structures. This can be explained in the same manner as with other works [50-55] such that larger input energy resulted in well exfoliated structures with randomly dispersed clay platelets consisting of edge-to-edge and edge-to-face contacts. The efficiency of ultrasonication to obtain well-exfoliated structures was shown with TEM for features of much smaller particle size and dispersed single platelets (Figure 2-4 (II)). However, ultrasonication was not an efficient candidate for exfoliated PCN when high molecular weight (HMW) PP was used as matrix, showing only modest increases in the interlayer spacing.

A masterbatch process consisting of two steps, in-situ intercalative polymerization and melt intercalation, was used to obtain a poly(ϵ -caprolactone) (PCL)/MMT PCN. Polymerized masterbatches showed intercalated/exfoliated microstructures and these masterbatches were dispersed into molten PCL and Poly(vinyl chloride) (PVC) matrices. As a result, intercalated/exfoliated PCL or PVC PCNs, which could not be obtained by direct melt blending, were successfully prepared [56]. Highly concentrated PCN (above 20 wt%) with an intercalated microstructure was achievable by overcoming challenges of high-viscosity using supercritical carbon dioxide ($scCO_2$) as a solvent for the intercalating polymerization of methyl methacrylate (MMA). $scCO_2$ was effective in distributing MMA monomer homogeneously prior to polymerization [57].

Injection molding induces different orientations of clay platelets between the region near the flat surface regions and the bulk regions of bar-shaped composite samples (Refer to Figure 2-6). Figure 2-6 shows spatial distributions of clay platelets dispersed in Nylon 66 in a cross section normal to the injection molding direction. While predominantly parallel orientation of platelets to the surface of bar-shaped sample were observed near the flat surface, orientation in

the bulk regions rotated themselves about the injection molding direction as indicated as an curved arrow in Figure 2-6. Differences in orientation between these regions may effect on crystallization [58].

Selection of mixing method and extrusion is a key factor for melt processing to attain uniformly dispersed and dissociated clay platelets. In other words, shear stress and residence time in the extruder have to be considered. Hamaker [59] made it possible to estimate adhesive energy and force between clay platelets during extrusion theoretically [50]. According to this work, unmodified clay requires much higher shear stress because of considerably higher attractive interaction between clay platelets with shorter interlayer spacing. Small tactoids also requires high shear stress.

During melt processing, the fundamental mechanism of size reduction for clay platelets is based on erosion and surface peeling as shown in Figure 2-7. Peeling angle, θ , determines the stress required for peeling of platelets and there is a critical angle for the initiation of polymer intercalation process. Different clay interlayer characteristics such as aspect ratio, d-spacing and initial affinity of polymer chains are key factors in determining mixing method and estimates for energy required.

Inducing a preferential orientation of clay platelets in a PCN system also requires appropriate shear rates [39,60,61]. A critical shear rate was found for the formation of a macroscopic domain pattern with preferential orientation of clay platelets in the polymer matrix when a PCN was obtained from solution process [61].

Randomly oriented platelets at equilibrium showed isotropic small angle neutron scattering (SANS) patterns in the x-z and y-z planes, resulting in a physical gel structure by diffusion of polymer chains. When shear rate is above a critical value, flow induced by shear rate disrupts the

transient physical network formed in equilibrium state and clay platelets move faster than polymer can diffuse, thus fragmenting the network into macroscopic domains. Macroscopic domain patterns accompany flow-induced nanoscale heterogeneities with structural connectivity in a macroscopically homogeneous system. Orientation of clay platelets shows anisotropic SANS pattern proving a shear-induced orientation as shown in Figure 2-8 (II) [61]. Similarly, flow induced microstructures with different features were also found in PP with maleic anhydride grafted PP (PP-g-MAn)/MMT PCN obtained by melt extrusion process. In this work, flow-induced internal structural change occurred in both shear and elongational flow and changes were very different from each other in that shear-induced change involved an extremely long relaxation time. As shown in Figure 2-9 (a) and (b), coherent order of the orientation was lower in (b) and this suggested that slow elongation flow leads to formation of ‘a house of cards’ structure. Results of this study also showed that strong strain-induced hardening originated from the microstructure with preferential perpendicular orientation of clay platelets to the stretching direction [62].

Formation of various microstructures

Several morphological features that are different from the three typical microstructures have been observed under various conditions. The physical properties from these microstructures are known to be substantially different from normally well-intercalated/exfoliated structure in nano scale. Fully exfoliated structures can be realized when two conditions of sufficient interlayer spacing and strong interaction between polymer chains and nanoclays. A wedged structure can be formed due to lack of interlayer space of nanoclays and/or polarity of polymer chains at certain condition. EVA/MMT nanocomposite is an example showing a wedge structure. VA content in EVA polymer chain determines polarity of this polymer. Therefore VA content and three organic modifiers containing different lengths of alkyl chains resulted in different

interlayer gaps that were controlled to investigate the effect on morphological features of prepared PCN materials [43]. The organic modifiers used were octadecyltrimethyl ammonium bromide (SIAB), dioctadecyldimethyl ammonium bromide (DIAB) and tricetadecylmethyl ammonium bromide (TRIAB). The higher number of long alkyl chains the modifier possessed, the larger interlayer spacing was obtained, as shown in WAXRD pattern of Figure 2-10 (II). Cross-checking TEM micrographs and a WAXRD pattern of corresponding PCN materials shows that partially exfoliated, intercalated, and a mixture of partially intercalated and exfoliated structures were obtained for EVA/SIOM, EVA/DIOM and EVA/TRIOM, respectively.

A partially exfoliated structure referred to as a ‘wedge structure’ of EVA/SIOM occurred because the basal spacing of SIOM is not enough to insert polymer chains and VA content is also not enough to induce strong interaction between the chains of EVA and SIOM. Therefore, only some portion of EVA chains was wedged into the sheets of clay so, the ordered structure of SIOM is damaged, showing an exfoliated feature in WAXRD pattern. When the number of alkyl chains attached to the modifier molecules was enough to increase the basal spacing for EVA chains to enter, intercalated PCN was obtained as shown in Figure 2-10 (b).

A tactoid, which is also termed a ,‘stack’, consisting of several sheets stacked face-to-face with an interlayer charge and an agglomeration of these tactoids is a micron-sized particle which is a main component in phase-separated structures. It is possible to form individually dispersed aggregates of completely delaminated sheet throughout the system. Different types of exfoliated structures were introduced in cross-linked polyethylene terephthalate (PET)/CL30B nanocomposites system [63]. Two situations of exfoliated structure were observed in PET/CL30B. First, a long-range ordered exfoliation in which clay sheets are completely delaminated and homogeneously dispersed throughout the matrix (Figure 2-11 (c)). Second, a

short-range ordered exfoliation which contains localized regions of exfoliated sheet dispersed throughout the matrix (Figure 2-11 (a) and (b)). This short range, ordered exfoliation is useful to envisage macroscopic physical behaviors.

Volume fraction and orientation of nanoclays in polymer are key factors in the formation of various microstructures in PCNs. MAPE/CL20A and MAPP/CL20A with incorporation of various concentrations of nanoclays were prepared to address morphological evolution from high volume fraction condition to dilute condition [60]. Volume fraction of clay is a major consideration in determining specific microstructures when other factors are optimized. Volume fraction controlled morphologies were classified into four distinct stages as shown in Figure 2-12. At high concentrations, stage IV, silicate particles are so close that Van der Waals force between particles induces strong attractive interactions and particles inevitably adapt the morphologies of phase-separated or intercalated structures. Stage III is a dual state that exfoliated and intercalated structures coexist and stage II of intermediate concentration possibly has ordered exfoliated morphologies by dominating steric interactions. Lower concentration of clay particles at stage I eventually renders a disordered exfoliated morphology because the interactions between polymer chains and clay particles govern microstructures of this system.

It has been emphasized that relations between microstructures of PCN and their physical properties in nanocomposite field are different from conventional composites. In addition to state of dispersion and degree of aggregation, there is one crucial factor that has significant effects on PCN materials. This factor is the overall preferential orientation of clay platelets. The study of MAPE (PP)/CL20A [60] also considered the orientational behaviors of clay particles. 2D Small Angle X-Ray Scattering (SAXS) patterns reminiscent of strong anisotropic features on the equator direction were found for both MAPE/CL20A and MAPP/CL20A nanocomposite fibers,

which indicates that normal directions of clay platelets are perpendicular to the shear direction for fiber formation. A notable fact is that different anisotropic tendency and orientation parameter (S) in terms of concentration of clay particles was observed in MAPE/CL20A and MAPP/CL20A. While MAPE/CL20A showed monotonic increase of S as volume fraction of CL20A increased, S decreased when volume fraction was above 15 % in MAPP/CL20A nanocomposites. This was confirmed by two curves along with two series of SAXS photographs (Figure 2-13). Monotonic increase of S with increases in clay volume fraction in MAPE/CL20A was explained by the fact that increased possibility of collision between clay particles prevents particles from tumbling freely, hence facilitating intercalated structure of higher order ($S = 1$). Decrease in S above 15 vol% of clay in MAPP/CL20A was due to tactoids formed in the composite, which act as a domain. These tactoids were tumbled instead of completely separated into individual platelets, thus lowering S . These tactoids can be regarded as an exfoliated/intercalated structure of a global scale mentioned above. In conclusion, selection of appropriate volume fraction is a key factor in determining the desired microstructure under MAPP- or MAPE-based nanocomposite systems. General or intuitive response of clay platelet orientation in a polymer is ‘c-orientation’, which is a direction normal to the surface of a composite and ‘b-orientation’, which occurs during strong strain-induced hardening. Orientation of platelets shown in MAPE (PP)/CL20A nanocomposite is a typical b-orientation. Advent of a general ‘c-orientation’ was discovered in multilayered nanocomposite polymer films prepared by a layer-by-layer spreading exfoliated polymer-clay solution, which was confirmed by SANS patterns that have relatively more isotropic patterns in the y beam direction and relatively large anisotropy in the z-beam configuration (Figure 2-14) [39]. Laponite RD (LRD) particles with a lower aspect ratio and Cloisite Na⁺ (CNa) particles with a higher aspect ratio exfoliated in

polyethylene oxide (PEO) were oriented by spreading. Collapsed network structures during drying processes leads to an increase in concentration of particles in the system and subsequently reduces the rate of relaxation toward their original structure from the oriented structures by spreading. LRD showed small amount of anisotropy in film samples of higher concentrations as shown in (a – d) of Figure 2-14. It is generally expected that larger particles align more preferentially than the smaller ones at a similar concentration. However, the orientation of LRD was stronger than that for CNa in a spreading process. LRD contains more particles in a restricted space than CNa at the same volume fraction because of small aspect ratio and lower density of LRD. Closer distance between particles induced more attractive interactions resulting in a stronger network. Strong networks in solution assisted in good alignment of LRD particles, showing a higher degree of orientation during the film-spreading process. Dependence of orientation on volume fraction of LRD indicated that there is a critical concentration at which highly aligned networks occur as also shown in MAPP/CL20A. Similarly, a critical concentration for an intercalated microstructure was observed in poly (methyl methacrylate) (PMMA)/Cloisite composites prepared by in-situ solution polymerization using supercritical carbon dioxide (ScCO₂) as a solvent. Cloisite particles in PMMA formed highly ordered nematic architecture when concentrations reached 40 wt%, which is considered a critical limit. Above this critical transition concentration, d-spacing decreases and the polymer volume is homogeneously distributed, resulting in fully intercalated microstructure [57]. It can be concluded from three cases [39,57,60] that different preferential orientations can be rendered depending on the types of clay as well as the shearing methods. There also exists a critical concentration at which highly ordered microstructures and highly concentrated nanocomposites are formed.

For the purposes of maximizing functions for specific applications, the microstructure of PCN materials sometimes displayed unique structures that are completely different from those described so far. Epoxy/Na-MMT fabric film composite was successfully obtained by dip coating a heterostructured mixed-ion clay film with a mixture of diglycidyl ether of bisphenol-A (DGEBA) and Jeffamine. Upon curing, this system produced unprecedented oxygen barrier properties. Figure 2-15 represents the structure of heterostructured mixed-ion clay film. Heterostructured mixed-ion clay film was able to be prepared by a partial cation exchange reaction which is possible due to the diffusion-limited exchange process. Partial cation exchange in outer surface of a clay self-supporting film made it possible to insert polymer resin between particles by modifying the swellability of the particles in this region. A densely stratified unmodified layer and polymer filling of microvoids between organoclays are two key factors to attain superior barrier properties.

An orientationally ordered hierarchical nanocomposite for the purpose of mechanical and barrier enhancements was attained by inserting polystyrene (PS)-functionalized clay particles into the PS domain of styrene-butadiene-styrene (SBS) tri-block copolymer (BCP) through roll casting. Individually dissociated clay sheets were stabilized by tethering high molecular weight PS chains to clay layers and as relaxation time decreased, individual exfoliated clay layers likely formed a ‘discotic nematic’ because of large areal dimensions and curved shape of exfoliated clay platelets (Figure 2-16 (b)). As exfoliated clay sheets served as a template for the lamellar domains, more layer misorientation with more defects in microstructures of SBS C-BCP were significant when compared to neat SBS BCP [64].

In order to attain super barrier properties with moderate flexibility, new densely stratified clay structures were devised [65,66]. Unlike highly concentrated nanocomposites with the clay

content at about 50 wt% or general PCN materials with small loading usually less than 10 wt%, these structures use clay particles as a major component to maximize barrier function with addition of a few binder additives. Densely packed clay platelets with face-to-face parallel stacking was realized by ionic bonding between anionic pendent groups of polymer chain and the positively charged edges of platelets. The attached anionic polymer chains on one edge of a platelet further promoted parallel arrangement as shown in the left picture of Figure 2-17. As a result, the limitations of low flexibility and transparency were overcome.

Flexible clay films using carboxymethyl cellulose (CBMC) sodium salt or poly(acrylic acid) (PAA) sodium salt as binder additives were prepared by casting aqueous dispersion of saponite with these binder additives [65]. The microstructure of CBMC clay film was different from that of PAA clay film in that CBMC molecules entered both the interlayer space and the edge space as shown in Figure 2-18 (b) showing larger d-spacing value.

Sodium polyacrylate (SPA) was also adapted as a binder to fabricate a flexible saponite clay film [66]. WAXRD results showed that increases in polymer loading lowered stacking faults, and lower full width at half maximum (FWHM) values obtained from (001) rocking curves of samples of lower polymer loadings indicated high degrees of preferential c-axis orientation. Thus, as polymer loading decreased, degree of preferred orientation increased with increasing stacking faults. Figure 2-19 exhibits schematics of crystal structures and TEM micrographs at different planes [66].

Highly efficient load transfer required for higher strength and modulus was realized by layered polymer nanocomposites consisting of PVA and MMT. The microstructure shown in Figure 2-20 was built by layer-by-layer (LBL) process of clay platelets. By achieving a high degree of structural organization, number of interactions was maximized promising efficient load

transfer. Scanning electron microscopy (SEM) micrographs in Figure 2-20 show 200-300 bilayer films as well as dense coverage of nano platelets and strict planar orientation [5].

Interplay between clay orientation and segmental motion of polymer chains

When a PCN material forms, polymer chains and anisotropic nanoplatelets have mutual effects on their behavior. In fact, behaviors of polymer chains and orientational behaviors of clay particles would be varied on a case-by-case basis.

Specific types of processes determine crystallization behavior. Different orientations of clay platelets between the surface and bulk of the PCN (Figure 2-6) lead to a different crystalline phase. Bulk regions contained more perfect α -phase crystals for Nylon 66 because of relatively lower cooling rates in the bulk. Surface regions showed that the oriented crystallization of Nylon 66 was induced by the oriented clay platelets [58]. PE/modified clays (MC), CL15A and 20A and PP/MC PCNs were obtained by melt processing and orientation during drawing was analyzed using x-ray and Raman spectroscopy. Presence of clay particles in PE and PP matrix reduced the orientational ability of polymer chains in amorphous regions during drawing. In comparison with corresponding neat polymer drawn by the same drawing ratio, total orientational order as well as crystallites of polymer matrix was lower. However, clay platelets did not have any significant effects on the orientational ability of PE and PP crystallites [67].

Clay platelets in copolyamide/CL30B PCN obtained by melt processing acted as a nucleation agent, changing degree of crystallization and crystalline phases, α and γ -phases, that formed lamellar with different thicknesses at different cooling rates [68]. Exfoliated clay platelets in PE-g-MAN increased polymer crystallization rates by promoting heterogeneous nucleation and two-dimensional crystallite growth following the diffusion-controlled mechanism. Fast crystallization did not guarantee higher degree of crystallization because the exfoliated clay particles reduced mobility of crystallizable chain segments. Decreased intensity in a 110

reflection for PE-g-MAN peaks by insertion of 5 wt% of clay platelets was given to prove lowered degree of crystallinity (Figure 2-21 (right)). Chain confinement effects were confirmed by investigating T_c (Figure 2-21 (left)). Depressed T_c for PE-g-MAN relative to PE is caused by pendant MAN groups. Lower energy was required for the crystallization process because of more affinity obtained from hydrogen bonding from MAN groups. However, increased T_c , with increasing volume fraction of clay platelets is caused by chain confinement effects. Chains confined by clay platelets required more energy to be crystallized. While well dispersed particles can increase crystallization rate by donating more available nucleation sites, the degree of crystallization is controlled by chain confinement effects in composite systems [69].

The concentration factor of well-exfoliated clay has critical effects on orientation of polymer. According to the calculation of spherulites radius using Hv patterns of CL15A filled HDPE and HDPE-g-MAN PCNs prepared by a melt compounding and compression molding as shown in Figure 2-22 and Table 2-2, average spherulites radius decreases in the presence of clay platelets. Spherulites size decreased due to an increased nucleation rate, which was accelerated because clay platelets act as a nucleation agent for the polymer crystallization. Thus, orientation of PE was determined by nucleation mode and confined nature of spherulitic crystallization process among oriented clay platelets resulting in significantly anisotropic HDPE spherulites [70].

Thermoplastic polyurethane (TPU)-clay PCN (PUCN) has different confinement behaviors depending on the types of clay. Preferential confinement of CL20A with soft segment and that of unmodified Laponite (LP) with the hard segment as the more polar part were confirmed by TEM and atomic force microscopy (AFM) as shown in Figure 2-23. PUCN with Laponite clay is represented here as PULCN and that with Cloisite is represented as PUCCN in the figure.

Preferential association of LP with the hard segment was also reflected from the change in soft segment degradation temperature [71]. This work suggested that confinement effects can be varied depending on the characteristics of clay such as chemical composition, hydrophobicity, aggregation tendency, and degree of dispersion in copolymer matrix-based composites or polymers having two more different types of segments such as PU.

PS/Cetyltrimethylammonium bromide-exchanged (CT-) MMT composite exhibited a unique behavior during heating process. Initially, a preferential orientation that is parallel to shear flow direction was observed at room temperature. As temperature increased to 85 °C, intensities of peaks from shear-induced ordered structures decreased. After heating to 95 °C, phenyl rings obtained enough transition moment for face-to-face orientation and perpendicular orientation to the clay particles as suggested as in Figure 2-24 (b). This affected orientation of clay particles resulting in self-assembled structures as shown in Figure 2-24 (a)-c. Further increasing thermal energy damaged this self-assembled structure. Segmental motions of phenyl rings were evidenced by the dichroic ratio obtained from fourier transform infrared (FTIR) spectroscopy [72].

Effects of Microstructures on Physical Properties

Mechanical property

Modulus of PCN materials is usually a function of polymer crystallinity, which can be increased by filler reinforcement. Similar to the theory of reinforcement mechanisms for macrocomposite materials, the degree of stress transfer to the reinforcement phase governs overall mechanical properties of nanocomposite structures. And nano-dimensionally dispersed particles usually result in extremely large surface areas exposed to polymer chains, strong interactions between polymer and clay, leading to better mechanical properties. A dramatic increase in modulus with low volume fraction was achieved in PVA/CNa PCN and HMW

copolyamide/CL30B PCN [68,73]. Highly stabilized interface evidenced by strong interaction between clay and polymer was found in EVOH/MMT PCN. Dramatic increases of mechanical properties of EVOH/MMT PCN compared to poor mechanical properties of styrene acrylonitrile copolymer (SAN)/MMT PCN showed roles of interfacial interaction for mechanical enhancement [47]. Interfacial agents improving adhesion between polymer and clay played a significant role to enhance phase adhesion. As a result, improved stiffness and high elastic modulus were attained in HDPE/CNa PCN that is prepared using PE-g-MAN as an interfacial agent [69]. Three clay types were used to prepare EVOH with VA content of 28% based PCN, and effects of modifier on mechanical properties showed that better dispersion of platelets in polymer promised higher storage modulus. In addition, modulus increased with increasing clay content for EVOH/modified-clay PCN. No effect from clay layers on modulus was found when natural MMT was used as filler [43]. Aspect ratio and degree of orientation of clay platelets are two dominating factors for mechanical property improvement of Nylon6/MMT PCN materials, which can be both obtained by large-scaled, simple shear processing. When these two factors decreased, modulus and strength of resulting PCN also decreased, while fracture toughness and ductility increased [74]. Degree of orientation of clay platelets was also reported by Zerda. According to this work, PMMA/organically modified layered silicates PCN prepared by $scCO_2$ -MMA polymerization was post-treated using melt processing. Orientation induced from a post melt process increased tensile modulus up to 220% compared to untreated [57]. For cross-linked polymer based PCN, enhancement in mechanical properties from cross-linked chains dominates rather than interaction between clay and polymer. As a result, moduli decreased with increasing clay content monotonically. Exfoliation at a global scale also leads to this unique mechanical property which is opposite to normal PCN materials [63]. Recently, PVA/MMT transparent

flexible film was developed using LBL process. This structural composite exhibited four times higher strength and nearly one order of magnitude higher modulus when compared with pure PVA. Highly efficient load transfer process was given as a basis of breakthrough in mechanical properties. Highly efficient hydrogen bonding between clay and polymer referred to as the Velcro effect and six-membered ring structure between PVA and MMT were reported as two main driving forces for highly efficient load transfer. When glutaraldehyde (GA) was used as a crosslinking agent, much higher modulus, comparable to that of Kevlar, was observed with exceptional stability under humid condition [5].

Thermal property

Thermal stability has been known as one advantage of PCN because clay platelets in PCN act as a barrier that maximize heat insulation and minimize permeability of volatile degradation products [52,75-77,81]. It has been noted that thermal decomposition of PCN materials usually shifts toward higher temperature because clay platelets prevent diffusion of oxygen and assists in formation of char after thermal decomposition [43,58,73,78,79]. Thermal stability increases as the clay content in PCN increases [58,80]. Depending on the intrinsic thermal characteristics of polymer or clay, different observations with general functions of clay for thermal stability can be found [63,81].

In contrast with the normal phenomenon that onset of degradation is retarded (left thermal gravimetric analysis (TGA) plot of Figure 2-25), crosslinked PCN systems have shown a different trend. Onset of degradation was hastened as the clay content increased and degradation between 25 and 400 °C occurred at faster rate. There was a monotonic increase in degradation rate with increasing clay content because of the presence of hydroxyl group in the modifier of CL30B providing a supply of oxygen [63]. Thermal stability of PLA-based PCN has a unique characteristic in that clay platelets dispersed in PLA matrix hindered degradation of crystalline

structures of PLA hybrid at low temperature and accelerated deformation at high temperatures [81].

Optical property

Properties of a matrix such as the degree of crystallization and the size of spherulites, interfacial refractive index difference between matrix and filler particles, and size of dispersed particles are factors needed to determine optical transmittance of polymer composites [44]. Deng et al. reported that optical transmittance was dependent on size of dispersed particles over the basal spacing of clay in their proposed model for epoxy/clay nanocomposites, (Equation (2-1)) [82].

$$T = e^{\left[-C(d+1)f_w R_C^{m-1} \left(\frac{2\pi n_m}{\lambda} \right)^m \right]} \quad (2-1)$$

where T is the optical transmittance of nanocomposites, C is dependent on the ratio of the refractive index of clay and matrix, d is the d-spacing, f_w is the weight concentration of clay particle per unit volume, R_C is the average aspect ratio, m is the Rayleigh scattering factor, n_m is the refractive index of matrix polymer, and λ is the wavelength of incident light. Weight fraction of clay particles and their size determine optical transmittance of a composite based on this equation. Light scattering by uniformly dispersed particles in polymer that are much smaller than the wavelength of incident visible light will produce Rayleigh scattering. Therefore, it is generally acceptable that the size and dispersion of clay platelets are dominating factors to obtain better optical properties [32,73,78]. Lower optical clarity at higher clay loading was observed in PVA/MMT PCN because of the strong scattering of MMT [32]. Haze and gloss of Na^+ -saponite particles dispersed PVA hybrid films was not significantly different from those of pure PVA because of small aspect ratio of filler particles [78].

Barrier property

PCN materials with high gas barrier properties are attractive for packaging materials. The barrier property of PCN is affected by the arrangement of each inorganic platelet in polymer as well as aspect ratio of these platelets. The length of diffusion path of gas molecules strongly influences the barrier property of a material and this can be extended or shortened by arranging impermeable platelets in polymer matrix. Therefore, depending on the materials used as a matrix or filler, the type of processing, and various processing variables such as volume fraction, barrier properties of resulting PCN materials are varied.

Effects of Microstructure on Barrier Property

Extended Barrier Model for Polymer Clay Nanocomposite

Barrier properties of PCN can be affected by geometry and orientation of filler particles. Various barrier models have been proposed to predict the permeability of PCN. Based on the basic assumption that the direction of diffusion is normal to the surface, relative permeability (R_p) can be defined as permeability of PCN film relative to the unfilled film as following Equation (2-2).

$$R_p = \frac{P}{P_o} \quad (2-2)$$

Where, P and P_o are permeability of polymer clay nanocomposites and that of matrix polymer without nanoclay, respectively. As suggested by Takahashi et al. [83,84], each model has different particle geometries which then result in different barrier formulas. Figure 2-26 depicts three particles' geometries which have been used.

Nielsen and Cussler used ribbon-shaped filler for their models, suggesting the following barrier formulas.

$$R_p = \frac{(1-\phi)}{1 + \frac{\alpha\phi}{2}} \quad (2-3)$$

$$R_p = \frac{(1-\phi)}{1 + \left(\frac{\alpha\phi}{2}\right)^2} \quad (2-4)$$

$$R_p = \frac{(1-\phi)}{\left(1 + \frac{\alpha\phi}{3}\right)^2} \quad (2-5)$$

where α is the aspect ratio of a particle, which can be obtained by dividing the width by its thickness and, for the purpose of simplifying comparison between models, thickness, t , is set to 1 nm for all models. This assumption is quite reasonable when considering that the actual thickness of clay platelets typically used as filler particles, such as Cloisite and Laponite, is about 1 nm (the range of size is from 0.9 to 2 nm) [85-89]. And ϕ is the volume fraction of filler particles in the matrix. Cussler [90] divided the model into two patterns, regular (Equation (2-4)) and more general random pattern (Equation (2-5)). Even though random array has lower barrier permeability than regular array, both cases commonly show that the change in barrier properties will be dominated by the increase in distance traveled for a gas molecule crossing the platelets-filled film and the decrease in area available for diffusion as shown in Figure 2-27. Cussler also explored the efficient size of platelets to enhance the barrier properties and concluded that a small platelet could act as a shunt, allowing fast diffusion of gas molecules across that part of the film containing one layer of platelets. Therefore, this model has an advantage in that the design of material is possible to optimize the mechanical and optical properties of a barrier film by varying the size of platelets. Models devised by Nielsen [31] and Cussler did not contain any factor for confinement in polymer matrix.

Gusev [91] and Fredrickson [92] both developed barrier models based on disk-shaped particles as drawn in Figure 2-28 (b). The aspect ratio can be calculated by dividing the disk diameter, d , by the thickness, t , in these two models. Both models focused on the effect of the platelets geometries and concentrations on the reduction of permeability of PCN. Gusev established the role of the geometric factor alone with the barrier formula (Equation (2-6)) by assuming the platelets were randomly dispersed and non-overlapped. Rational reference point for the understanding of the contribution of molecular-level transformation such as crystallization and segmental motions was also provided in this model.

$$R_p = \frac{1 - \phi}{\exp[(\alpha\phi/3.47)^{0.71}]} \quad (2-6)$$

Fredrickson suggested a quantitative framework to estimate the degree of disorder and polydispersity of platelets with the assumption of randomly distributed disk centers-of-mass with no spatial correlations. Fredrickson also investigated how two levels of concentrations, dilute and semi-dilute, affect the barrier formulas and reported the following crossover barrier formula, Equation (2-7), which is quite versatile and can be easily extended to more realistic situations.

$$R_p = \frac{1 - \phi}{4((1 + x + 0.1245x^2)/(2 + x))^2} \quad (2-7)$$

Where $x = \pi\alpha\phi/2\ln(\alpha/2)$

As drawn in Figure 2-28, some differences were observed in effects of volume fraction on R_p as the aspect ratio increased. The changes in R_p were more sensitive to volume fraction of platelets with higher aspect ratio at loading level below 0.05 in Gusev model than Fredrickson model.

Xu [93] evaluated R_p by combining R_p theory of semi-crystalline polymers with the detour theory. Assuming clay platelets as impermeable crystalline domains in semicrystalline polymer matrix based on Klute's theory [94], Equation (2-2) can be also defined as Eq. (2-8), where

$$R_p = (1 - \phi)\xi(\phi) \quad (2-8)$$

and ϕ and ξ are volume fraction of clay particles in PCN and the reduction parameter of permeability as a function of ϕ due to the nanoclay particles, respectively. Reduction parameter usually varies when the geometry of clay particle and orientation of these particles in polymer matrix are changed. In general, permeability reduction in PCN arises from two factors, polymer chain-segment immobility factor, ζ_1 , and detour factor, ζ_2 . Total permeability reduction parameter in PCN is a function of these two factors as given in Equation (2-9) and this relation made it possible to combine R_p theory of semi-crystalline polymer with the detour theory.

$$\zeta(\phi) = \frac{\zeta_2(\phi)}{\zeta_1} \quad (2-9)$$

The factor of the detour ratio was obtained by calculating the traveling path length of gas molecules when the dimension of clay platelets and the distances between these platelets vary. Figure 2-29 is a unit consisting of three silicate platelets (the geometry of platelet is a cuboid) which represent the arrangement of platelets in whole system of idealized PCN structure. From the definitions of effective volume and volume fraction suggested by Saunders [95], H was expressed using L , b , t and volume fraction as shown in Equation (2-10).

$$H = \frac{L^2 t}{\phi(L+b)^2} - t \quad (2-10)$$

As a result, detour based barrier formulas were presented by Xu as the following Equation (2-11) and this formula can be converted into Equation (2-12) by means of Equation (2-10)

$$R_p = \frac{(1-\phi)/\zeta_1}{1 + \frac{L}{2t} \left(1 + \frac{b}{L}\right)^3 \phi} \quad (2-11)$$

$$R_p = \frac{(1-\phi)/\zeta_1}{1 + \frac{L}{2} \left(\frac{t}{\phi}\right)^{\frac{1}{2}} (t+H)^{-\frac{3}{2}}} \quad (2-12)$$

Comparing to other barrier formulas, Xu's formula showed more complexity due to the consideration of edge-to-edge lateral distance and the relation among all dimension and spacing in a fixed volumetric space. Additionally, the chain segment immobility factor added complexity to the equation. Chain segment immobility factor (ζ_1) implying the confinement effect of clay platelet on polymer matrix was contained in this model. When there is no confinement effect, or $\zeta_1=1$, no effects of crystallization on a diffusion constant of gas molecules would be found. Comparing R_p of the unconfined matrix with that of confined one, PCN with confined matrix has more enhanced barrier properties due to increased crystallinity as shown in Figure 2-30. As more clay is included in the system, more reduction in both ζ_1 and H are expected, resulting in entropic penalty of polymer confinement. This accelerates the confinement effect of platelets on polymer chains. As a result, a drastically decreased R_p was obtained and this is closer to the actual R_p value which is lowered diffusion due to increased crystallinity.

One remarkable feature of Xu's model is that the effect of lateral distance, b, on H and that R_p varies depending on the aspect ratio of clay platelets as plotted in Figure 2-31. Meanwhile, the smaller particles show somewhat similar tendency of decreasing in both H and R_p as b increases, the larger particles reveal a slight decrease in both H and R_p showing less dependence on b. This was explained using the concept of effective volume as described in Figure 2-32 that when there is the same amount of increase in b for both smaller and larger particles, smaller

particles form more layers and subsequently shorten H significantly within the same volumetric space and the same volume fraction.

The basic assumption of all models is that the direction of diffusion of a gas molecule is perpendicular to the surface of platelets. However, this assumption causes some significant deviation from the actual permeability of PCN material. To overcome this limitation, Bharadwaj [96] introduced the orientational order parameter, S , which usually is used to describe an orientational order of a nematic phase in his barrier model. S is defined as

$$S = \frac{1}{2} \langle 3 \cos^2 \theta - 1 \rangle \quad (2-13)$$

where Θ represents the angle between the direction of preferred orientation and the sheet normal unit vectors (refer to Figure 2-33). This descriptor reflected well the dependence of tortuosity on the orientational order of the platelets in a continuous manner. Figure 2-33 represents how S varies depending on the degree of orientation of platelets schematically. Planar orientation of platelets is a perfect orientation for nematic structure which is regarded as an ideal barrier model. In contrast, any benefit in barrier properties can be achieved by orthogonal orientation of platelets. Tortuosity factor based barrier formula containing orientation order parameters was given by

$$R_p = \frac{1 - \phi}{1 + 0.667 \alpha \phi (S + \frac{1}{2})} \quad (2-14)$$

where, S varies from $-1/2$ to 1 .

Figure 2-34 is a plot of R_p versus volume fraction drawn by Equation (2-14) when the orientation is completely random, or $S = 0$. When the assumption of fully exfoliated structure was made, there was no significant difference or remarkable feature observed in comparison to other barrier models. The effect of orientation of platelets on R_p as aspect ratio varies was

investigated. As a result, small aspect ratio was much more sensitive to S , showing that small rotation of platelets degraded barrier significantly. However, in the case of platelets with larger aspect ratio, enhancement in barrier with a random orientation of platelets is nearly as good as the case where the platelets were aligned perpendicular to the diffusing path (the right curve showing two red dot lines are positioned similarly). These tendencies were identified from two lower plots in Figure 2-34. As shown in the figure (completely overlapped two solid lines in the right curve), when orthogonal orientation was set for PCN structure, no barrier effects were found as expected, regardless of the aspect ratio.

It is noteworthy that all models predicted comparable improvement in barrier properties and these models agreed on the fact that the degree of enhancement in barrier properties was higher with higher aspect ratio than with lower aspect ratio. Two curves in Figure 2-35 represent the case where at higher loading above 0.2 vol% of clay platelets with high aspect ratio, there is no further enhancement, and the value converges to 0. Based on these models, the smaller particles can fill more space in the polymer matrix to enhance the barrier properties further in comparison to larger particles. This fact also can be explained by the limitations of models in terms of volume fraction and/or aspect ratio. As shown in curves for all models drawn at the same volume fraction in Figure 2-36, every model has a certain limited aspect ratio above which it is no longer applicable to estimate barrier properties precisely. In other words, the estimation of barrier properties of PCN using high aspect ratio above 1000 can be achieved using Fredrickson, Bharadwaj and Xu's barrier models. Therefore, models that can precisely predict the barrier properties of PCN have to be developed and more variables might be included. However, present models have suggested a good guidance for the design of PCN for barrier application with good consistency validated by reported experimental results.

Practical Polymer Clay Nanocomposite for Barrier Applications

In general, the degree of enhancement in barrier performance of the nanocomposites relative to the neat films is dependent on the microstructures of platelets in the polymer matrix with the intrinsic nature of impermeable particles such as large aspect ratio and surface area. The general barrier properties of PCN are based on the fundamental theory of physical tortuous paths which are maintained similarly in actual system with some exceptions. As shown previously, barrier models have shown that the degree of tortuosity is determined by geometric influences such as the extent of exfoliation/intercalation of the platelets and their mean orientation in the polymer matrix. Tortuosity was given as two permeability reduction parameters, polymer chain-segment immobility factor, ζ_1 , and detour factor, ζ_2 , in barrier models [97,98]. In the real barrier system, these two factors are also meaningful in determining a permeability of a PCN material.

The effects of microstructure of clay platelets on barrier properties

Microstructure of platelets is a dominating factor when designing a high barrier material. The microstructure of practical PCN materials is a broad mixture of stacked particles, intercalated region, global-scaled exfoliation, and fully exfoliated region. A dominating microstructure in a PCN that can represent the whole structure usually determines the physical parameters such as the barrier properties. Bharadwaj [63,96] suggested that the effective width of silicate layers in his barrier model to describe the effect of exfoliation on barrier properties as drawn in Figure 2-37. Aggregation increases the effective width and disperses the same total number of sheet as this aggregated two-sheet results in a dramatic decrease in tortuosity. Thus, exfoliation is a crucial factor for obtaining the maximal performance of practical PCN materials for barrier application.

A significant improvement in oxygen barrier properties was attained in HMW copolyamide/CL30B nanocomposite films obtained by a melt processing. Uniform dispersion

and high degree of exfoliation with a preferential orientation of clay platelets were proved by pronounced shear thinning rheological behavior [68]. Low molecular weight polymer chains were able to be crystallized readily in solution casting process such as PVA/MMT, leading to lower permeability [44]. However, for the melt process, high molecular weight has an advantage on permeability since it promotes higher shear stresses, hence favoring the delamination of clay platelets into individual platelets and maximizing tortuosity. Confinement of amorphous polymer chains in intergallery region also contributed to lowering permeability because hindered molecular motions restricted the channel formation for gas diffusion [68].

Intergallery modifiers have played crucial roles in obtaining a desired microstructure by enlarging the intergallery region and accelerating the diffusion of polymer chains into this enlarged gallery space. Thus, the use of intergallery modifier is an efficient way to enhance barrier property of PCN materials [7,42,99-101]. It was reported that 1wt% of N-methyl diethanol amine (MDEA) based organoclay dispersed in PET specimen (obtained by in-situ polymerization) lowered the permeability by two-fold, compared to pure PET. As illustrated in Figure 2-38, MMT-PCN had higher permeability than MDEA-PCN. This was explained by the effect of modifier, MDEA, in this specific system since the hydroxyl and carboxylic end groups in MDEA reacted with ethylene glycol (EG) in PET, resulting in higher affinity of polymer chains to the intergallery region. As a result, while there observed large nanoclay bundles in MMT-PCN (a) which are phase-separated and intercalated regions, more exfoliated and well-delaminated clay platelets were found in MDEA-PCN (b), promising much longer retention time of oxygen gas molecules in this PCN material. A similar barrier tendency depending on the use of organic modifier was also found in melt-blended acrylonitrile-butadiene copolymer (NBR) nanocomposites. In contrast with an unmodified MMT PCN, modified MMT by dimethyl

distearyl ammonium bromide (DDAB) was separated and dispersed well in NBR matrix. A few tens of layers were found in TEM micrographs and such separated layers extended the routes of diffusion significantly as suggested in the TEM micrographs of Figure 2-39. Increased volume of platelets further decreased the permeability and some deviation from Neilson's theory was caused by the assumption of ideal perpendicular alignment of platelets to the direction of gas diffusion [100].

The effects of processing and selection of matrix on barrier properties

Effects of shear stress and shear direction on microstructure of clay platelets in the polymer matrix have been reported so far [45,50,58,60,68,95]. Finding appropriate shear stress to exfoliate stacked particles and shear direction to obtain a preferred orientation is the main factor to achieve the ideal microstructure for barrier application with the use of intergallery modifier. Once a proper process is adapted from one of the three typical processes, melt process, solution casting or coating, and in-situ polymerization, the next step is to find the optimum processing parameters, which largely depend on the characteristics of materials. For instance, modified clay platelets that have larger d-spacing value require relatively lower shear stress for exfoliation than natural MMT. Subsequently, exfoliated platelets would promise much lower permeability. Therefore, for enhancement of barrier properties of PCN, processing parameters should be considered in the design of practical PCN materials.

The PU/clay nanocomposites were prepared by in-situ polymerization [102]. To form an intercalated structure, PEG-MDEA-PEG (UE400) was used as a modifier and sonication process aided better dispersion of the modified clay platelets. As a result, an intercalated structure with some disorder was attained and their d-spacing was about 2.6–2.7 nm. In this study, varying clay contents and sonication time resulted in different degree of dispersion and dissociation of platelets. Fitting the results of gas permeability to a general physical detour theory suggests that

the incorporation of clay into polymer matrix decreases gas permeability by extending the tortuous path, as shown in Figure 2-40. PU/CLUE400S60 had lower gas permeability than PU/CLUE400S00, which means that the degree of dissociation could be increased by the sonication process. (S60 denotes that sonication process was conducted for 60 minutes) PU/CLUE400S60 5 wt% had the lowest gas permeability and its oxygen permeability was 41% lower than that of pure PU. Red dotted lines in the TEM micrographs illustrated the intuitive diffusion path of gas, showing that most lines are blocked by uniformly dispersed platelets in PU/CLUE400S60 5 wt%. As shown in this work, adapting optimum processing parameters depends on the specific materials and is a fundamental consideration to attain a high barrier property.

Polyesteramide/nanomer composite films were obtained by melt mixing and subsequent compression molding [99]. Figure 2-41 is a TEM micrograph of a compression molded specimen containing 5 wt% of clay filler. The white arrow represents a void which still exists after compression molding. These microvoids usually deteriorate barrier properties of a composite film. Transmission rate of oxygen and water vapor decreased as the filler content increased, as generally expected. Compression molding could contribute to the reduction in permeability modestly by decreasing the void contents in films and increasing crystallinity.

Ultrasonic treatment enhanced the intercalation of HDPE/organoclays nanocomposite system [103]. HDPE/organoclay nanocomposites were obtained using a single screw compounding extruder with the attached ultrasound die operating at various amplitudes. The die pressure and power consumption due to ultrasound were measured at different feed rates of nanocomposites with various clay concentrations (Table 2-3). The microstructures induced by the ultrasound treatment showed an increasing d-spacing up to 50% and these structures exhibited enhanced barrier properties such that a reduction in oxygen permeability of

nanocomposites was found after ultrasonic treatment at amplitude of 10 μm with the highest reduction by 20% at 2.5% clay concentration and a residence time of 21 s. According to this research, the reduction in permeability was achieved regardless of the reduced crystallinity induced by ultrasonic treatment indicating that the effects of extended detour path by incursion of homogeneously dispersed filler dominated the permeability coefficient rather than crystallinity of a polymer matrix in this specific condition.

There is also a case that there is no significant effect of processing parameters on barrier properties. The role of processing parameter, specifically the screw speed for melt compounding process of poly(L-lactide) (PLA) and PLA/MMT, on barrier properties of nanocomposites was explored by Thellen [104]. Plasticized PLA/organically modified MMT nanocomposites were compounded and blown-film processed using a co-rotating twin screw extruder at various conditions (Table 2-4). Figure 2-42 represents effects of screw speed on oxygen permeability of resulting blown film samples. According to results (Figure 2-42), oxygen permeability of nanocomposite films was lower than the pure PLA films in all cases. Reduction in oxygen permeability ranged from 15 to 48%. It is generally true that the microstructure of platelets is controlled significantly by processing parameters and the optimum microstructure of these such as an exfoliation in polymer is one of the crucial factors to obtain high barrier properties. In this work, however, as screw speed varies at the same feed rate, no significant relationship between screw speed and oxygen permeability was observed. In contrast, oxygen permeability of PLA homopolymer was sensitive to processing conditions. Optimizing processing parameters was more critical when working with the PLA homopolymer than when working with the PLA/MMT nanocomposite. Apparently, variations in screw speed did not affect dispersion of platelets in PLA, nor did it influence final properties of blown-film nanocomposites.

Selection of polymer is another consideration for compatibility with clay platelets and dispersion of clay platelets. Because packing densities of polymer chains is an intrinsic characteristic that cannot be modified, selection of polymer should be considered carefully for high barrier applications. Permeability of styrene butadiene rubber (SBR) nanocomposite is mainly influenced by fractional free volume and tortuous diffusion path effects attributed to the clay platelet morphology [105-107]. Positron annihilation lifetime spectroscopy (PALS) suggests a useful method to probe the free volume between polymer chains which contributes to its barrier properties. The study on effects of free volume on barrier properties of SBR nanocomposites by Stephen et al. [107] reported that the gas barrier properties of nanoplatelets-filled latex membranes were enhanced due to platelet-like morphology and high aspect ratio of layered silicates. The free volume in the latex membranes decreased when layered silicates were embedded and this phenomenon was explained using the confinement of the chain segments. From the perspective of free volume, PVA is a potentially useful material for preparation of PCN. Because the large inter- and intramolecular cohesive energy resulting from the highly polar hydrogen bonding makes PVA a material with excellent barrier to oxygen, modified PVA or EVOH have been used as a promising matrix material to achieve high barrier properties. Strong hydrogen bonding and high degree of crystallinity of PVA significantly reduces excess free volume, which is used as a source to form channels for jumping of permeant gas. However, a significant drawback that oxygen permeability is increased in elevated humidity has been an obstacle for the use of PVA as a barrier application. The moisture in atmosphere is absorbed at high porosity sites weakening the cohesive energy of polymer by breaking secondary bonding. As a result, oxygen molecules diffuse into the structure and easily increase permeability. Thus, adding clay platelets to the polymer may be an efficient way to maintain and increase barrier

properties of water-soluble polymer in humid conditions. Yeun et al [78] enhanced barrier properties by casting PVA/saponite hybrid films onto BOPP and PET. The more clay added in hybrid film, the better barrier properties were attained. Higher amount of clay increased the degree of crystallization due to the role of clay platelets as a nucleation site and increased crystallinity led to decreased permeability. Coexistence of intercalated and exfoliated structure in all PVA/CNa hybrid films obtained by a solution casting method, over the full range of clay loading, was observed even though there were some differences found in the relative amount of intercalated region. The mixed structure in these practical composite films also gives rise to enhanced barrier properties [73]. Low compatibility with polymer of kaolinite caused by the large cohesive energy density resulting from the intrinsic formation of hydrogen bonding between consecutive layers was modified by intercalation of dimethyl-sulfoxide, methanol and octadecylamine. As a result, EVOH/kaolinite nanocomposite with well-intercalated/exfoliated structures was obtained by a simple melt blending. Because of the extremely low permachor value of EVOH, oxygen transmission rate of EVOH films is very low. As a result, the permeability of all prepared nanocomposite was below the detection limit of the instrument (i.e. below 10^{-5} (cm³ m)/(m² day atm)) even at high temperature [108]. Barrier properties of PVA/CNa hybrid films coated on PET substrates using PVA with 87-89% of degree of saponification (DS), PVA with 99% of DS, and modified PVA, respectively, were investigated under various relative humidity (RH) conditions [44]. Modified PVA, a terpolymer used in the work consists of 97 wt% of VA, 2wt% of VAc and 1wt% of itaconic acid, as illustrated in Figure 2-43. Permeability of terpolymer at 0 %RH showed the lowest value and the higher VAc content contained, the higher permeability observed, as shown in the results of permeability of Figure 2-44. The author explained this in terms of the hydrogen bonding effect. While stronger hydrogen

bonding by –COOH on itaconic acid unit of terpolymer than –OH on vinyl alcohol unit induced larger cohesive energy, lower VA contents reduced the number of hydrogen bonding resulting in lower cohesive energy. 10 wt% of CNa in terpolymer decreased the oxygen permeability below 0.001 cc.mil/m².day at 55 %RH due to two effects, enhanced cohesive energy caused by stronger hydrogen bonding and extended diffusion path induced by highly exfoliated clay platelets.

Three different clay platelets, Hexadecylamine-MMT (C16-MMT), dodecyltrimethyl ammonium MMT (DTA-MMT), CL25A were dispersed in two different polymer matrices, PU and PLA, respectively, by solution intercalation method [80,81]. For both cases, permeability reduced linearly with increases in clay content regardless of clay types. However, while C16-MMT reduced the permeability significantly, when comparing to other two clay types, DTA-MMT and CL25A in PU matrix, there was no significant differences in the degree of reduction of permeability among the three types of clay in PLA matrix. This might be explained by the better compatibility of C16-MMT with PU polymer chains. In other words, C16-MMT that has good compatibility with PU reduced the permeability by the reduction of the transport cross section and the increase in tortuous path for gas molecules through the completely dispersed platelets.

The barrier properties based on geometry of clay platelets

According to the theoretical barrier model, permeability of a PCN material is a function of the volume fraction and the aspect ratio of clay platelet under a general assumption that the flow direction of diffused molecules is perpendicular to the platelets. To understand the actual permeability values, orientational order parameter [96], the concept of lateral spacing and effective volume [93], random or regular array model [90], and other factors [91,92] have been developed. To relate the aspect ratio of platelet to barrier properties of PCN, Kadanoff cell was used under the same general assumption as made previously [109]. To construct a barrier cell, at

least one vertex should be occupied with a platelet to the direction of permeation path as shown in Figure 2-45. The critical value of clay content for minimum permeability was obtained from the summation of probabilities that the cell is a barrier by iterative relation. And also, in this work, three main factors affecting barrier properties, aspect ratio (or degree of exfoliation, length/thickness (L/w)), orientational order parameter (S), and dispersion distance were included in barrier probability as shown in Equation (2-15). This equation also suggests that the theoretical prediction of barrier properties conformed well to the experimental critical thresholds as illustrated in the plot of various kinds of platelets of Figure 2-45.

$$\phi_c = \frac{3}{2S+1} \frac{w}{L} p_c \quad (2-15)$$

where P_c represents the critical value of clay platelets for minimum permeability. This suggests a good indicator for aspect ratio controlled volume fraction in order to estimate the permeability of PCN materials.

Four different types of clay, hactrite (Raponite RD, Kakuhachi Ind. Co.), saponite (Smecton SA, Topy Ind. Co.), MMT (Kunipia F, Kunimine Ind. Co.) and synthetic mica (DM clean A, Topy Ind. Co.) were used to prepare polyimide (PI)/clay hybrid films [110]. As a result, synthetic mica with the largest aspect ratio of 1230 nm showed the lowest permeability. This result conforms to the theoretical expectation from Nielsen models [90-93,96] that relative permeability should be smaller as aspect ratio becomes larger.

Good agreement was also seen with the result of barrier probability [109] as shown in Figure 2-45. From the comparison between theoretical and experimental results, it was concluded that the critical threshold of clay platelets with larger aspect ratio was smaller than platelets with other aspect ratios in reducing the oxygen permeability. The state of dispersion of clay types in PI/clay PCN specimens is another challenge to be considered for high barrier

solutions. While MMT and synthetic mica hybrid has no peak, hectrite and saponite hybrid showed small peak, representing the possibility of aggregated stacks of particles because weak ionic bonding between a protonated amine in the modifier and clay surface resulted in the detachment of organic modifier molecules from the surface during heating process. The state of dispersion and relative length of clay mainly determined a range of relative permeability in an order from the largest to the smallest: hectrite, saponite, MMT and synthetic mica [110]. Figure 2-46 illustrated TEM micrographs for various PI/Clay hybrid films. Cussler insisted that based on his theoretical model and brief experiments, platelets with small aspect ratio could act as a shunt, which allows fast transport across that part of a film containing one layer of platelet [111]. This fact also supports the importance of aspect ratio for the design of barrier materials.

Different types of barrier structure

It is well known that a preferred orientation in the microstructure of PCN along the shear direction can be induced during processing and there exists a critical concentration to obtain highly ordered microstructures for highly concentrated nanocomposites [39,57,60,61]. Oxygen permeability of PCN is at its lowest value when the orientation of platelets is perpendicular to the direction of diffusion of gas molecules because perpendicularly orientated platelets spontaneously maximize their function to block the diffusion of gas molecules during shear process. And it is true that the OTR value of a film decreases to 1/5 and 1/2400 of the pure film, for a 5 wt% and 95 wt% content of inorganic clay platelet according to Nielsen's tortuous-path model. Based on these two ideal concepts, several researchers have started to study the ideal stratified nematic microstructure of clay platelets for super barrier property [9,65,66]. Ebina [65] prepared a flexible transparent clay film by casting aqueous dispersion of synthetic saponite as a clay platelet and carboxymethyl cellulose sodium salt and PAA sodium salt as the binder additives. Oxygen transmission rate (OTR) of resulting clay film is 0.1 cc (20 μm)/ $\text{m}^2 \cdot \text{day} \cdot \text{atm}$

and there have been no polymer films that have comparable gas barrier properties. Similarly high clay volume nanocomposite films were obtained with Na⁺-saponite and SPA as a binder additive. Resulting specimens obtained by the same experimental procedure have similar barrier properties [66]. However, gas barrier performance of these clay films was deteriorated under humid condition because hydrophilic clay platelets were swollen and subsequently densely stratified nematic morphology was collapsed. Like PVA-based PCN films, barrier properties can be damaged under humid conditions. A variety of techniques used to reduce oxygen permeability under high relative humidity have been developed by several research groups and one of the most common method used for commercial packaging film is to sandwich the material having high barrier property between two exterior materials which help maintain the barrier property and good looking exterior aesthetics. Figure 2-47 shows the laminated structure of commercial packaging products. For instance, the commercial food packaging film 'Kurarister™ C' developed as a laminated structural composite by Kuraray Inc. Japan focused on its properties of easy printing and additional coating. The structure of Meal-Ready-to Eat (MRE) also consists of several layers to sustain its good barrier properties under various conditions such as radio frequency sterilization, microwave processing, and high pressure pasteurization.

The limitation of clay film can be overcome with epoxy-clay fabric film composite developed by Triantafyllidis [9], which is a similar laminating structural composite. The resulting films consist of interior non-swellable inorganic clay barrier phase and modified organoclay phase. Cured epoxy exterior layers on both sides protect clay barrier phase inside. Oxygen permeability of these specimens was lowered by 2-3 orders of magnitude from the polymer films and lowered by 3-4 orders of magnitude from the clay films. The dramatic enhancement in barrier properties of clay composite films was independent of both aspect ratio

of the clay and the nature of the exchanging cations at the external surfaces of the film. Rather, barrier properties of resulting films were enhanced by the filling of voids between platelet edges. This contribution factor for high barrier property different from normal PCN material caused some deviation from the extended barrier model based on Nielsen's detour theory. The more appropriate barrier model for this material was suggested by Beall [112]. According to Beall's barrier model, the polymer at the interface of the particle filler determines the overall barrier properties of the composite. However, the flexibility became a trade off for such unprecedented oxygen barrier property.

Table 2-1. Four different formulations to prepare polymer-clay composites [45]

	Polymer matrix	Clay	Process
F1	HMW PDMS	I.44P (4 wt%)	1. Intensive batch mixing, 2. Twin screw extruder
F2*	LMW PDMS (Silanol terminated)	I.44P	1. immediate curing with continuous sonication 2. Twin screw extruder
F3	PP	I.30E	Intensive batch mixing
F4	PPMA	I.30E	1. Intensive batch mixing, 2. Twin screw extruder

*Low viscosity newtonian polymer to minimize

Table 2-2. Average spherulites radius (R_{sph}) and T_c crystallized from the melt as a cooling rate of $1^\circ\text{C}/\text{min}$ [70]

Sample	R_{sph} * (μm)	T_c ($^\circ\text{C}$)
HDPE	7.6	122.7
HDPE/CL15A (5 wt%)	4.5	123.3
HDPE-g-MA	7.1	119.0
HDPE-g-MA/CL15A (5 wt%)	4.4	123.0
HDPE-g-MA/CL15A (10 wt%)	4.3	121.0

* The average dimensions of the spherulites were determined from the Hv patterns by means of the equation, $R_{sph} = c\lambda / (n\pi \sin\Theta_m)$, where c a constant ($c = 2.05$ for spheres and 1.95 for discs), λ/n the wavelength of the light in a medium of refractive index n , Θ_m the angle between the incident and the scattered beams corresponding to the maximum intensity.

Table 2-3. Oxygen permeability of HDPE/clay nanocomposites at different clay concentrations and ultrasonic amplitudes [103]

sample	Clay (%)	Amplitude (μm)	Feeding rate (g/s)	Oxygen Permeability ($\text{cm}^3\text{day m}^{-2}$)
1	0	0	0.75	75.9
2	2.5	0	0.75	76.2
3	5	0	0.75	76.4
4	10	0	0.75	79.7
5	2.5	5	0.75	76.8
6	2.5	7.5	0.75	80.6
7	2.5	10	0.75	69.7
8	5	10	0.75	71.2
9	10	10	0.75	73.3
10	2.5	10	0.5	65.9
11	2.5	10	0.25	61.8

Table 2-4. Processing conditions for blown film [104]

Sample name	Screw speed (rpm)	Feed rate (g/min)	Die temp. ($^{\circ}\text{C}$)
Neat no.1	80	40.5	175
Neat no.2	110	40.5	175
Neat no.3	130	40.5	175
Neat no.4	80	40.5	175
Nano no.1	80	40.5	165
Nano no.2	110	40.5	165
Nano no.3	95	40.5	165
Nano no.4	80	40.5	165

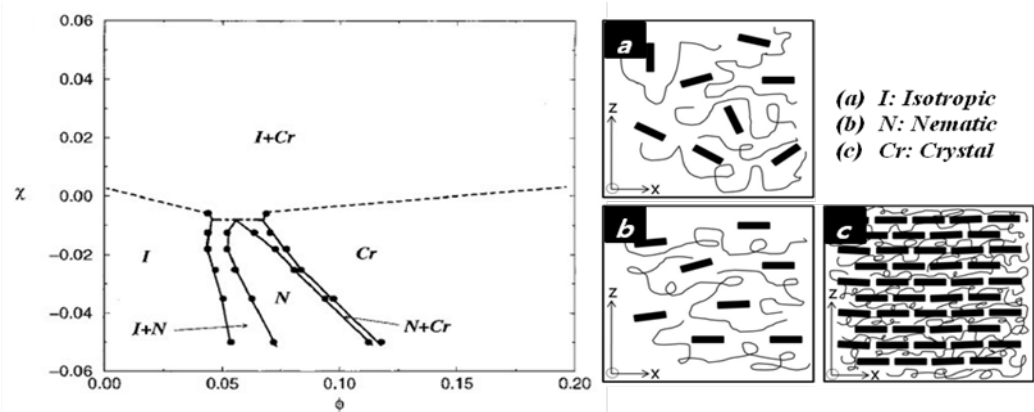


Figure 2-1. Phase diagrams of polymer-clay mixtures at $\rho_{gr}=0.2$, $N_{gr}=5$ (the lowest value of N_{gr} suggested in Ref.), Points represent calculated coexistence densities; lines serve as guide to the eye. Dashed lines represent approximate locations of phase transition boundaries (exact calculation is impossible because one or both coexistence points lie in the region $\frac{1}{4} > 0.6$). ϕ is the clay volume fraction, and χ is the Flory-Huggins χ -parameter between the surfactant and the polymer [33].

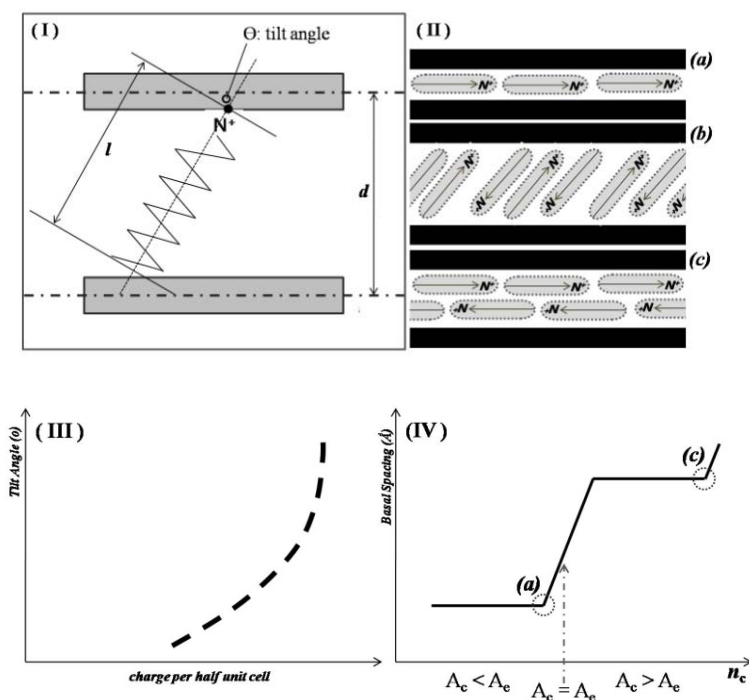


Figure 2-2. Expectation of arrangements of modifiers in the intergallery regions: Schematic diagram for tilt angle measurement of organic modifier, (I) [41]; typical arrangements of organic modifier in the intergallery space, (II); dependence of tilt angle of modifier molecules on layer-charge density of high-charge 2:1 phyllosilicates., (III) [40]; the formation of monolayers and bilayers in low charge 2:1 clay minerals depending on A_c and A_e in terms of d -spacing, (IV) [40].

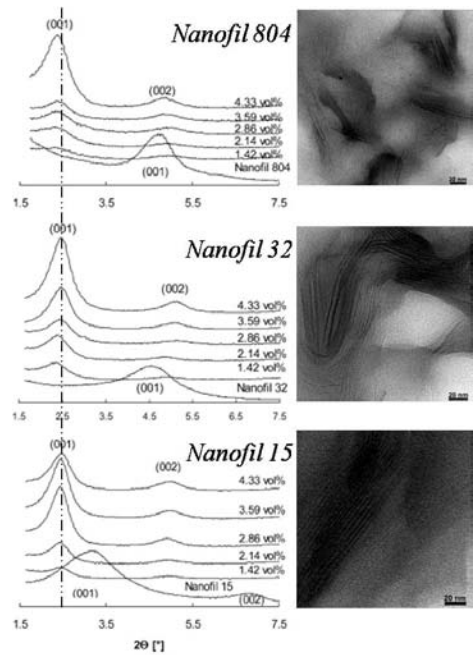


Figure 2-3. WAXRD patterns of the organically modified nanoclays and their nanocomposites and corresponding TEM micrographs [7]

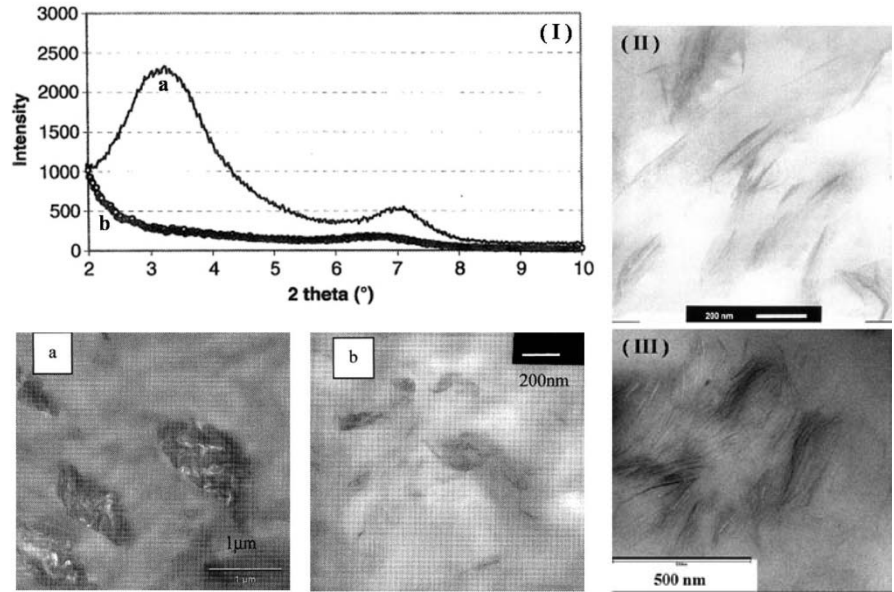


Figure 2-4. WAXRD Pattern of (a) HDPE/MMT–Nanofil 15 and (b) HDPE/HDPE–g-MA/MMT–Nanofil 15 nanocomposites and corresponding TEM micrographs [42], (I); a TEM micrograph of PP/MAPP/I-30.E prepared by twin screw extruder [46], (II); a TEM micrograph of the same nanocomposite with (II) prepared by intensive batch mixing and twin screw extruder [45], (III)

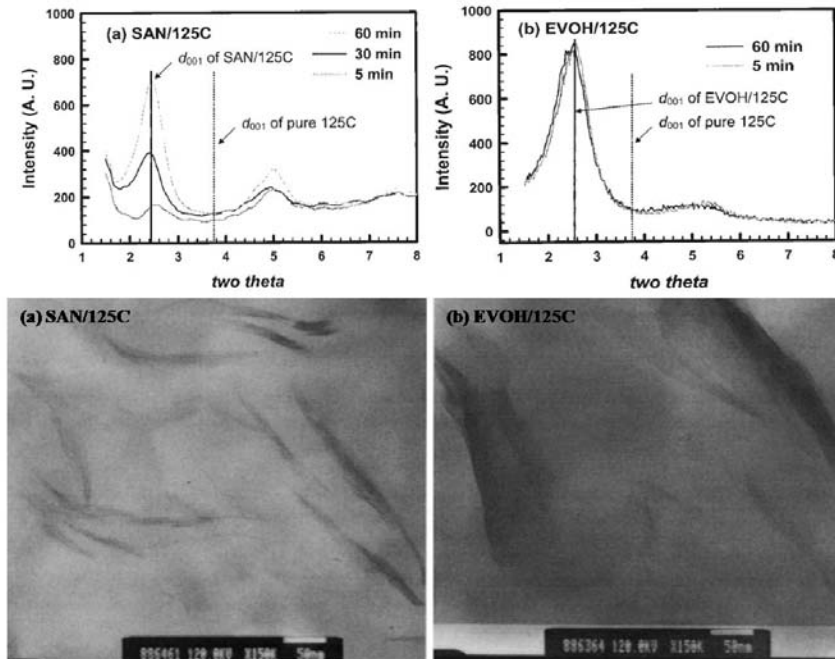


Figure 2-5. WAXRD Patterns of (a) SAN/MMT and (b) EVOH/MMT at each reaction time and TEM micrograph of the final morphology of corresponding composites [47]

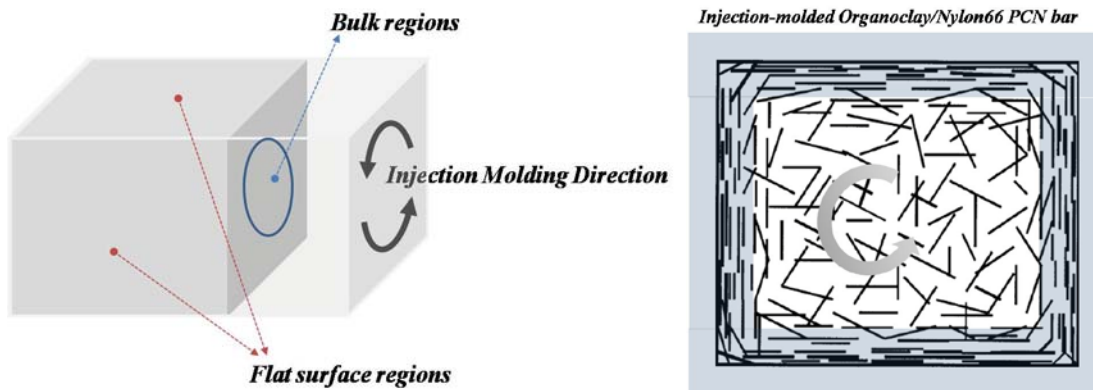


Figure 2-6. Illustration showing distribution of organic MMT layers in a cross section of nylon-66/organic MMT nanocomposites. The black lines represent the intersections of MMT layers, and the background is the polymer matrix [58]

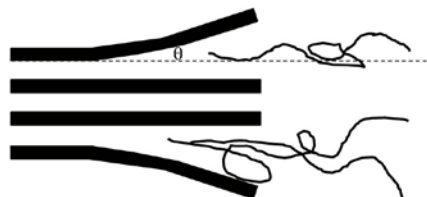


Figure 2-7. Illustration of peeling mechanism for the exfoliation process [50]

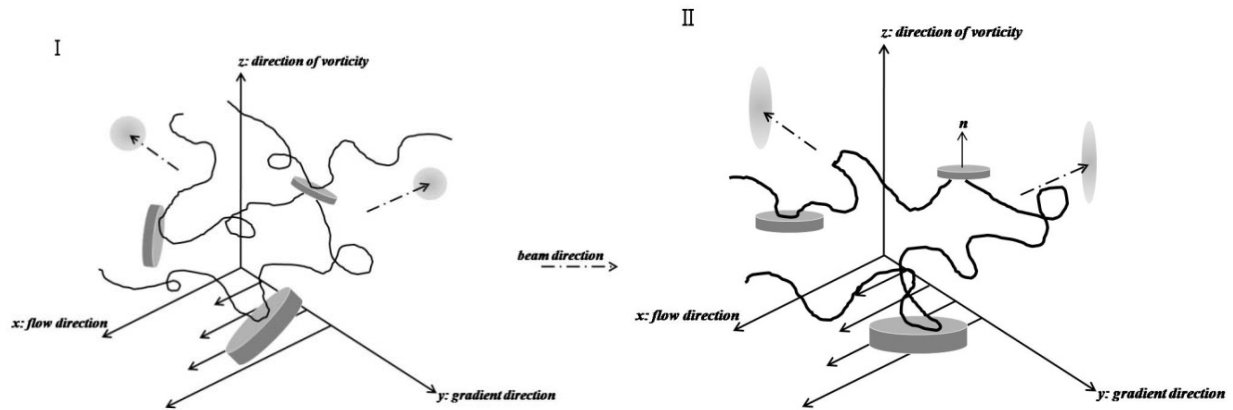


Figure 2-8. Shear-induced orientation of platelets with the flow (x), gradient (y) and vorticity (z) directions, as indicated is illustrated. A beam direction and general SANS patterns to show the effect of shear on the orientation are added to the figures [61]

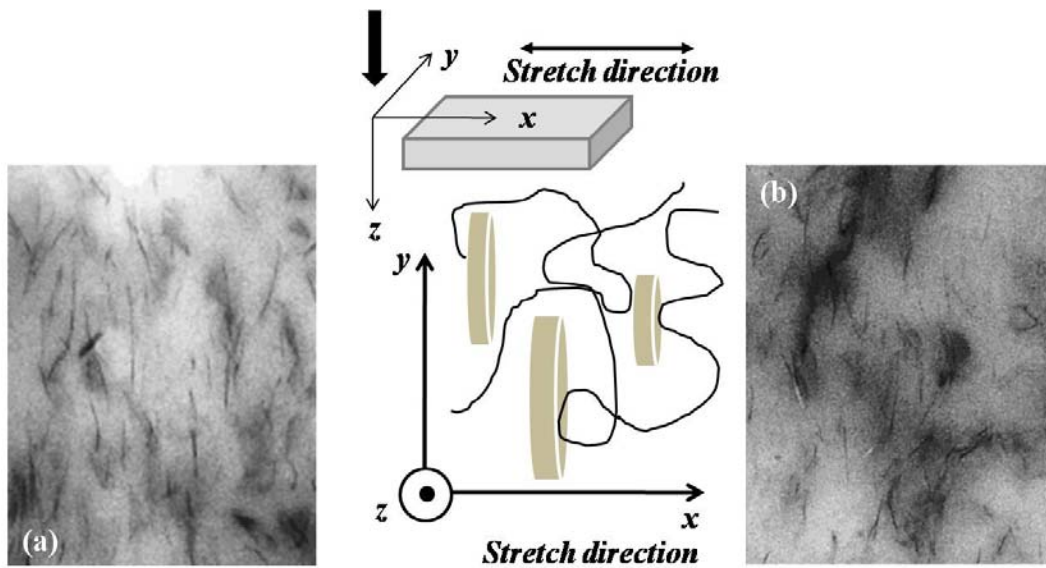


Figure 2-9. TEM micrographs showing PP/clay elongated at 150 °C with (a) elongation flow rate from 1.0 s⁻¹ up to 1.3 ($\lambda= 3.7$) and (b) from 0.001 s⁻¹ up to 0.5 ($\lambda= 1.7$), respectively. Illustration shows the stretching direction and the orientation of clay platelets which is perpendicular to the stretching direction [62]

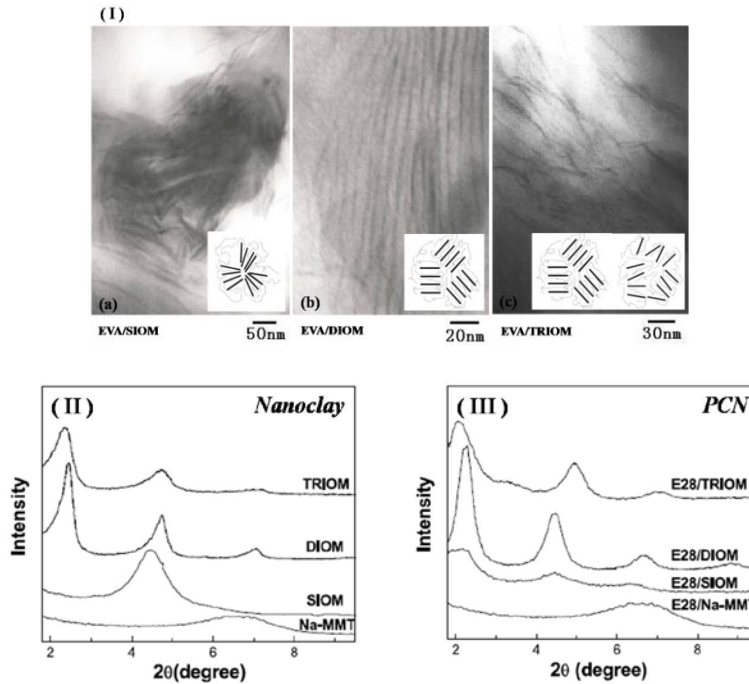


Figure 2-10. TEM micrographs for EVA/SIOM, EVA/DIOM, EVA/TRIOM, (I); WAXRD patterns for organoclays (II) and corresponding PCN (III) [43] (inset figures in each TEM micrograph represent schematic diagrams for each structure)

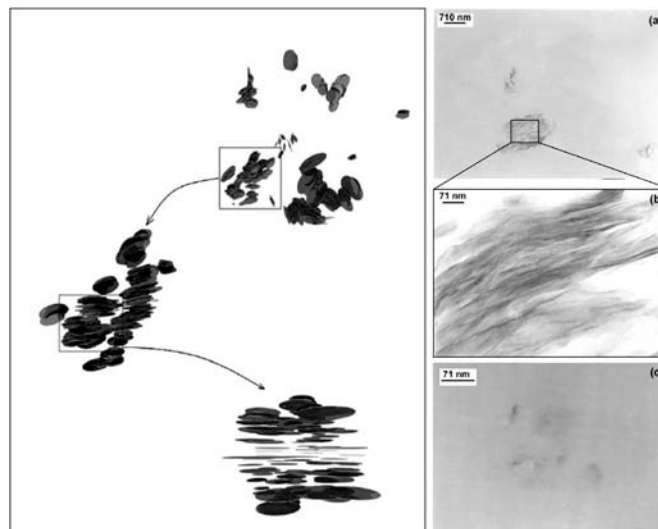


Figure 2-11. Illustration of the morphological hierarchy at different length scales extant in the PET/CL30B showing the dispersion of intercalated/exfoliated aggregates throughout the matrix and the local orientation ordering of the sheets within the aggregates and TEM micrographs of (a) a global scale exfoliation, (b) intercalated/exfoliated sheets at high magnification in exfoliated aggregates and (c) fully exfoliated structure in cross-linked PET/CL30B nanocomposites [63]

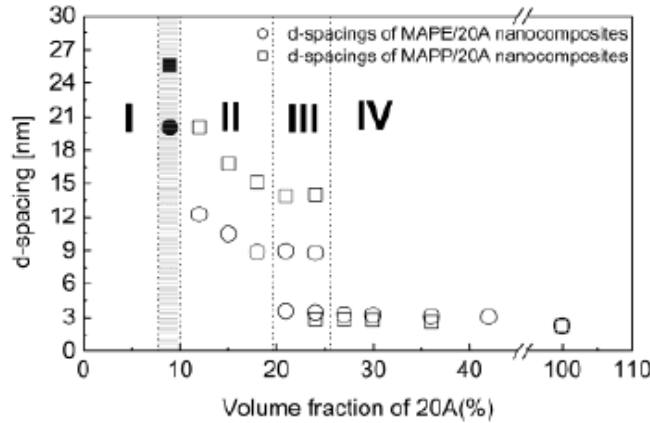


Figure 2-12. Variation of d-spacings of the MAPE/CL20A and MAPP/CL20A nanocomposite fibers depending on volume fraction of clay; Open circle symbol and open rectangular symbol indicate d-spacings of MAPE/20A and MAPP/20A calculated from SAXS data, respectively. Solid symbols mean d spacing created by shear-induced orientation [60]

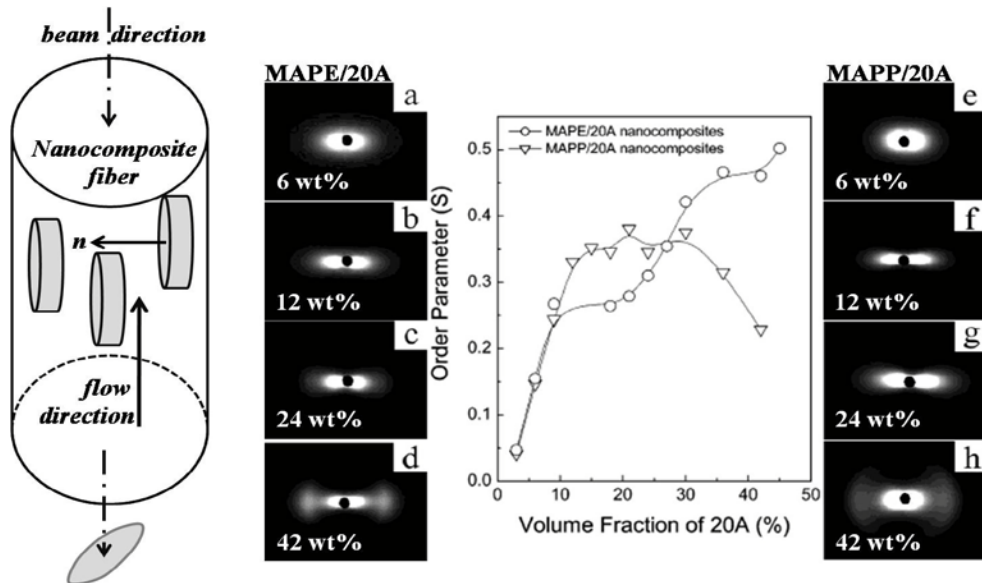


Figure 2-13. A beam configuration of SAXS measurement and resulting SAXS photographs of MAPE/CL20A nanocomposite fibers with clay concentration of (a) 6, (b) 12, (c) 24, and (d) 42 vol % and MAPP/20A nanocomposite fibers with clay concentration of (e) 6, (f) 12, (g) 24, and (h) 42 vol %, extruded at shear rate of 1000 s⁻¹. Order parameter (S) of MAPE/CL20A and MAPP/CL20A fibers with the concentration of silicates was shown between two series of SAXS photographs [60]

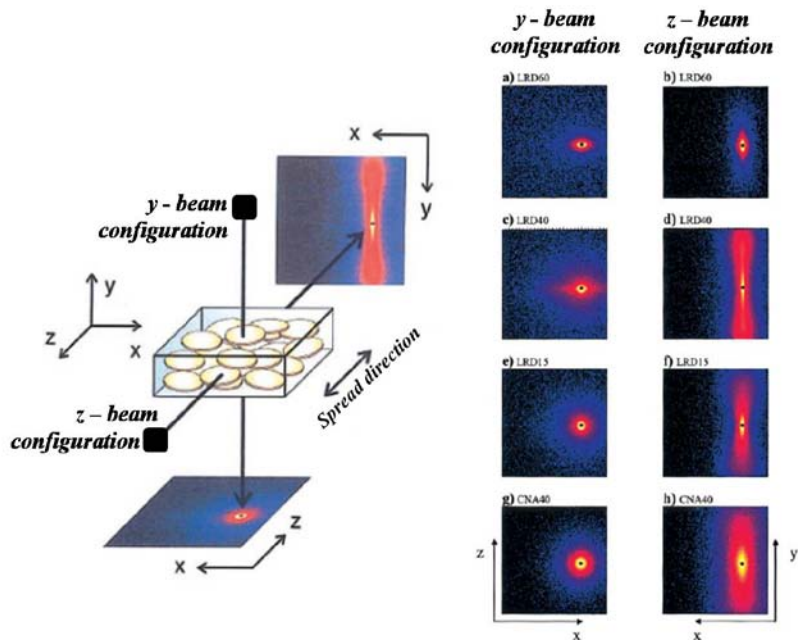


Figure 2-14. Y- and Z- beam configuration of SANS measurement and resulting SANS patterns of both configurations of films consisting of PEO/LRD with lower aspect ratio or PEO/CNA with higher aspect ratio [39]

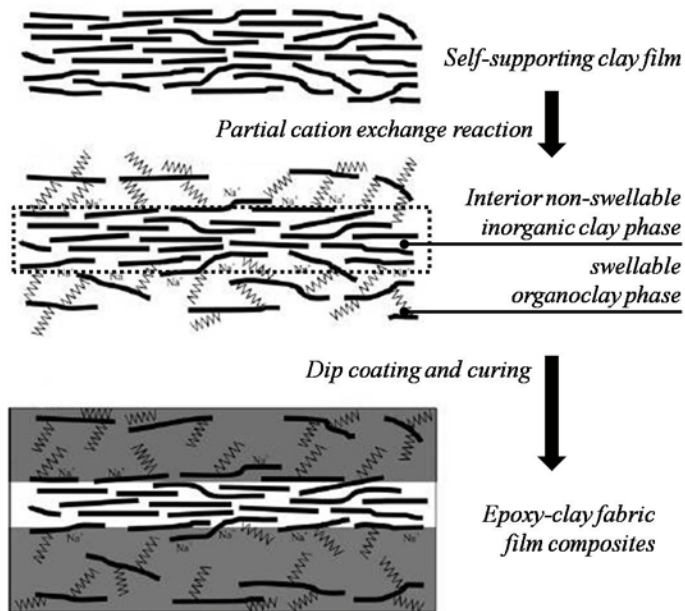


Figure 2-15. Schematic diagram to represent the procedure for the preparation of a cured epoxy-clay fabric film composite with with exfoliated clay nanolayers at the outer surfaces of the clay film [9]

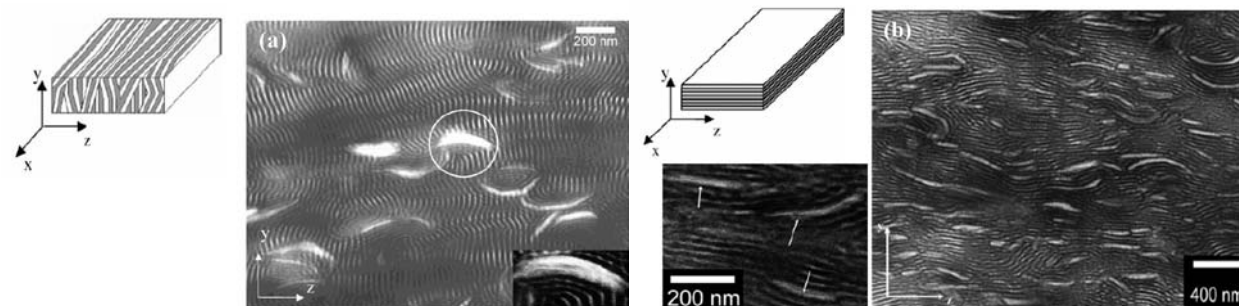


Figure 2-16. (a) TEM of the nanocomposite viewed along x^{\wedge} showing layered-silicates oriented orthogonally to the BCP lamellae. PS layers appear light due to OsO₄ staining of the PB layers. The high-magnification inset shows finely spaced black and white fringes indicative of the intercalated nature of the layered-silicates embedded in the PS domains, (b) parallel-oriented BCP lamellae and TEM image viewed along x^{\wedge} of the nanocomposite showing layered-silicates oriented parallel to the BCP lamellae. The small TEM micrograph is a high-magnification image showing the exfoliated nature of the layered-silicates, shown as single dark lines, surrounded by the thicker PS domains [64]

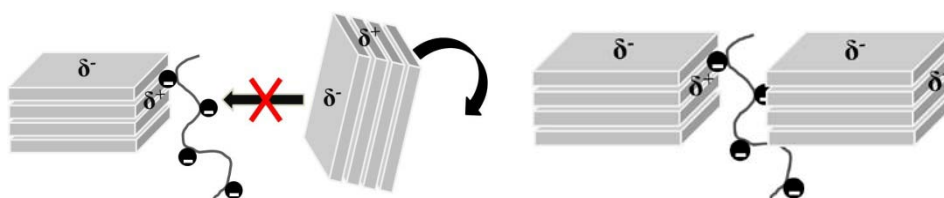


Figure 2-17. Schematic picture to represent the fundamental concept for the use of anionic polymer as a binder additive to achieve a clay film of densely packed structures

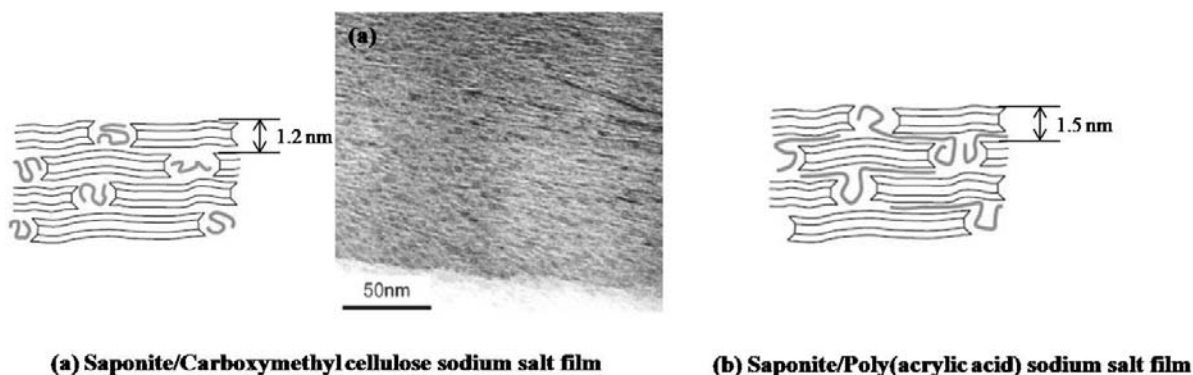


Figure 2-18. (a) TEM image of a cross section of the saponite film with 20 wt% of carboxymethyl cellulose sodium salt and corresponding schematic microstructure, (b) Schematic microstructures of the clay films of saponite/polyacrylic acid sodium salt film [65]

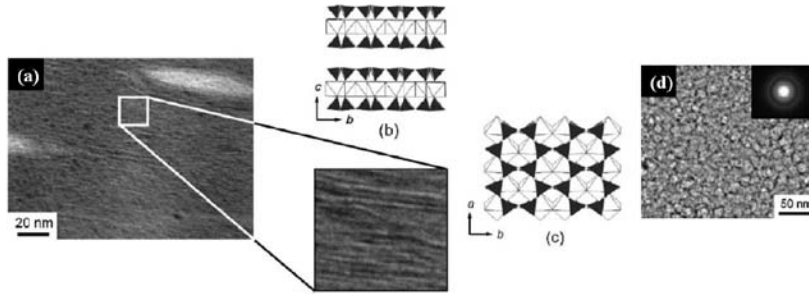


Figure 2-19. (a) TEM image of the film with a polymer loading of 20 wt%, showing the c-axis direction (crosssection), (b) Schematic crystal structure of saponite with [110] face in cb-plane, (c) Schematic crystal structure of saponite with [110] face in ab-plane, (d) TEM image of the film with a polymer loading of 20 wt%, showing the ab-plane (surface) and the corresponding SAED pattern (inset) [66]

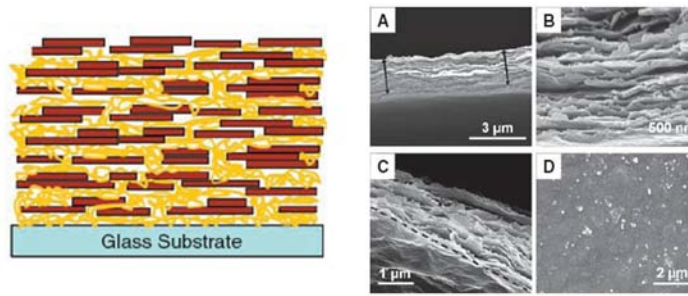


Figure 2-20. Schematic representation of the internal architecture of the PVA/MTM nanocomposite (left side) and (A) Cross section of the film, (B) Close-up of the cross section showing the separation of layers, (C) Top-down view of a fracture edge of the composite after tensile testing, (D) Top-down view of the composite's surface [5]

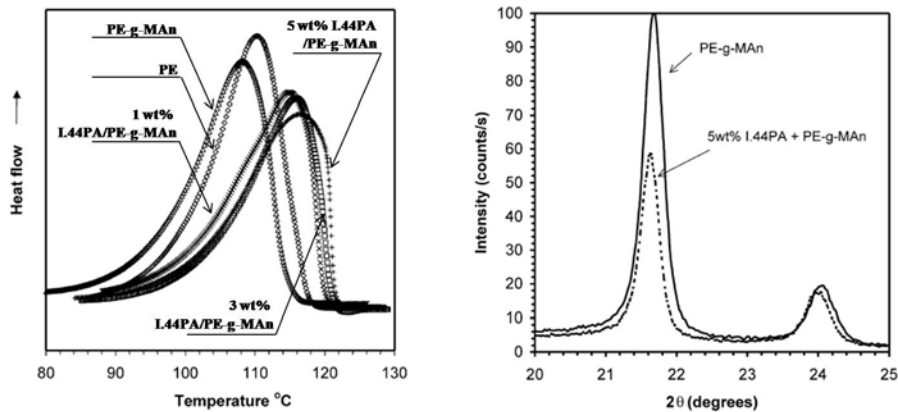


Figure 2-21. DSC crystallization exotherms plots of PE-g-MAN and I.44PA/PE-g-Man nanocomposites recorded at 20 °C/min (left) and XRD patterns for PE-g-MAN and I.44PA/PE-g-MAN systems depicting 110 and 200 reflections of polyethylene (right) [69]

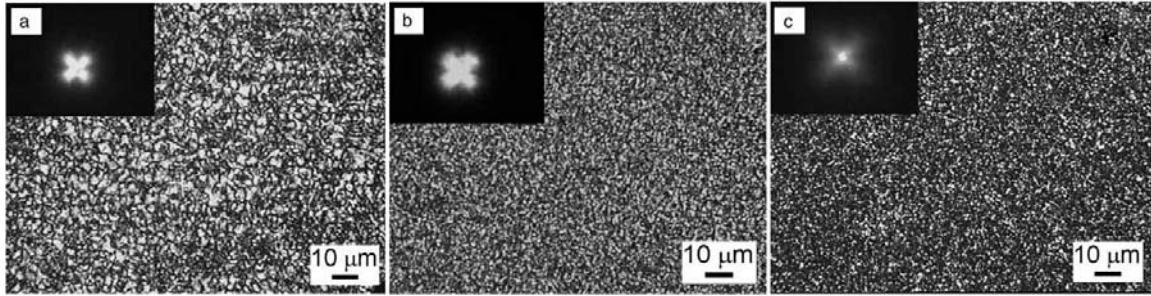


Figure 2-22. Optical micrographs and Hv patterns of: (a) HDPE-g-MA, (b) HDPE-g-MA/CL15A (10 wt.%), and (c) HDPE/CL15A (5 wt.%) [70]

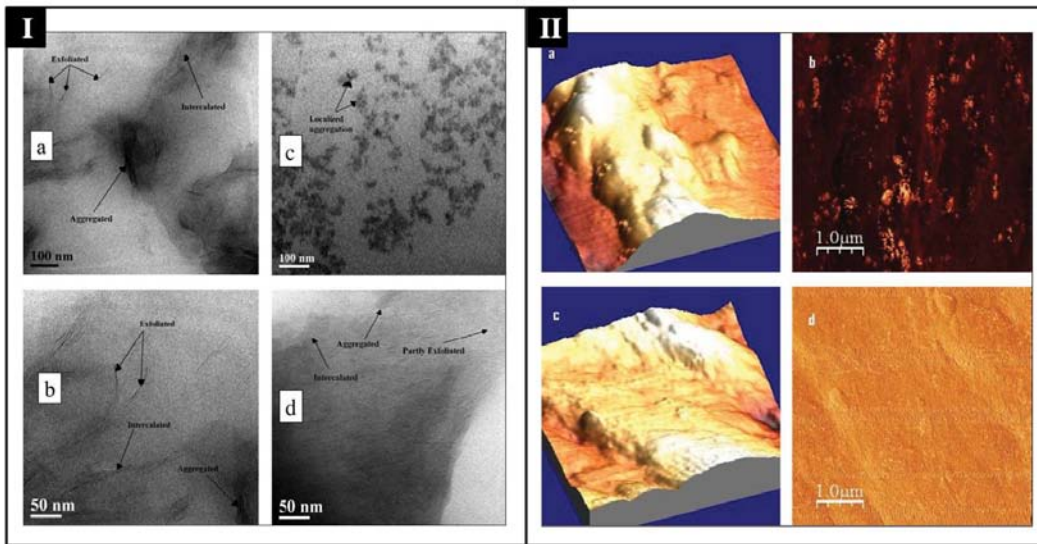


Figure 2-23. TEM images of PUCCN with 5% C (a and b) and PULCN with 3% L (c and d), (I); AFM images of PUCCN (a and b represent height and phase image with 5% C) and PULCN (c and d represent height and phase image with 3% L), (II) [71]

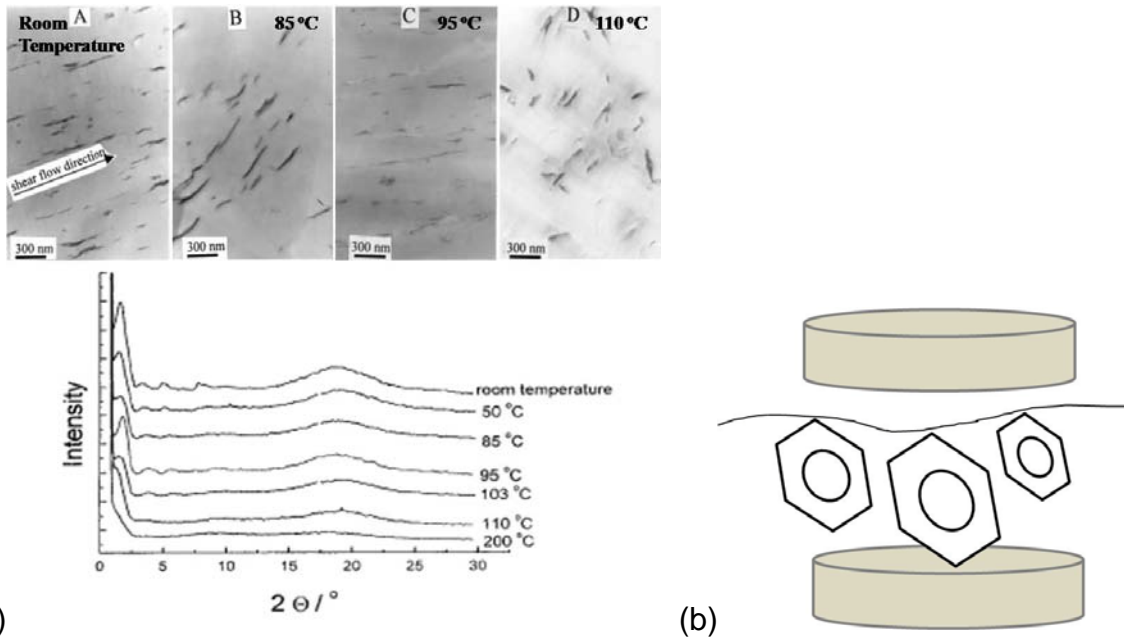


Figure 2-24. (a) Bright field TEM images of the extruded polystyrene/montmorillonite pellet A: room temperature, B: after heating at 85°C, C: 95°C, D: 110°C and corresponding in situ WAXD patterns between room temperature and 200°C [72], (b) expected orientation of phenyl ring with respect to clay particle after heating at 95 °C.

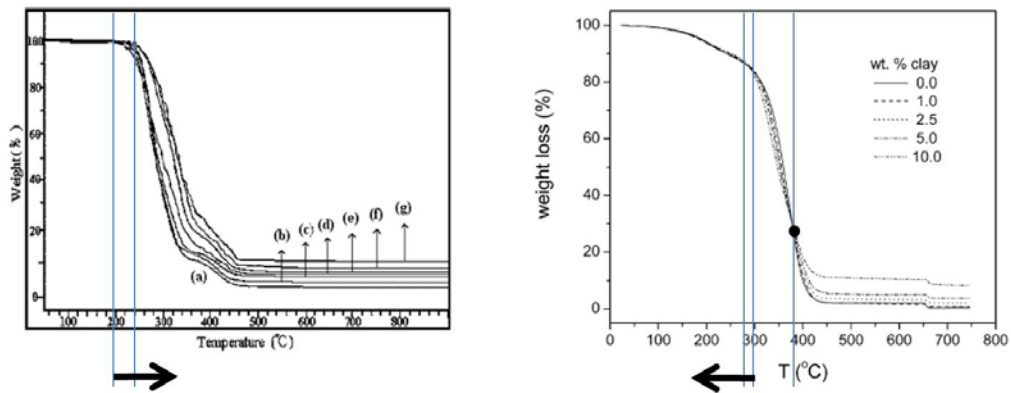


Figure 2-25. TGA result for normal PVA/organoclay PCN (left, [32]) and crosslinked PET/CL30B PCN (right, [63])

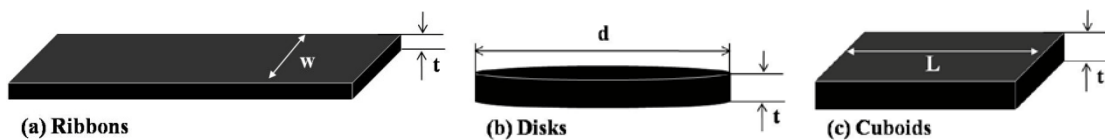


Figure 2-26. Three common particles' geometries used in models

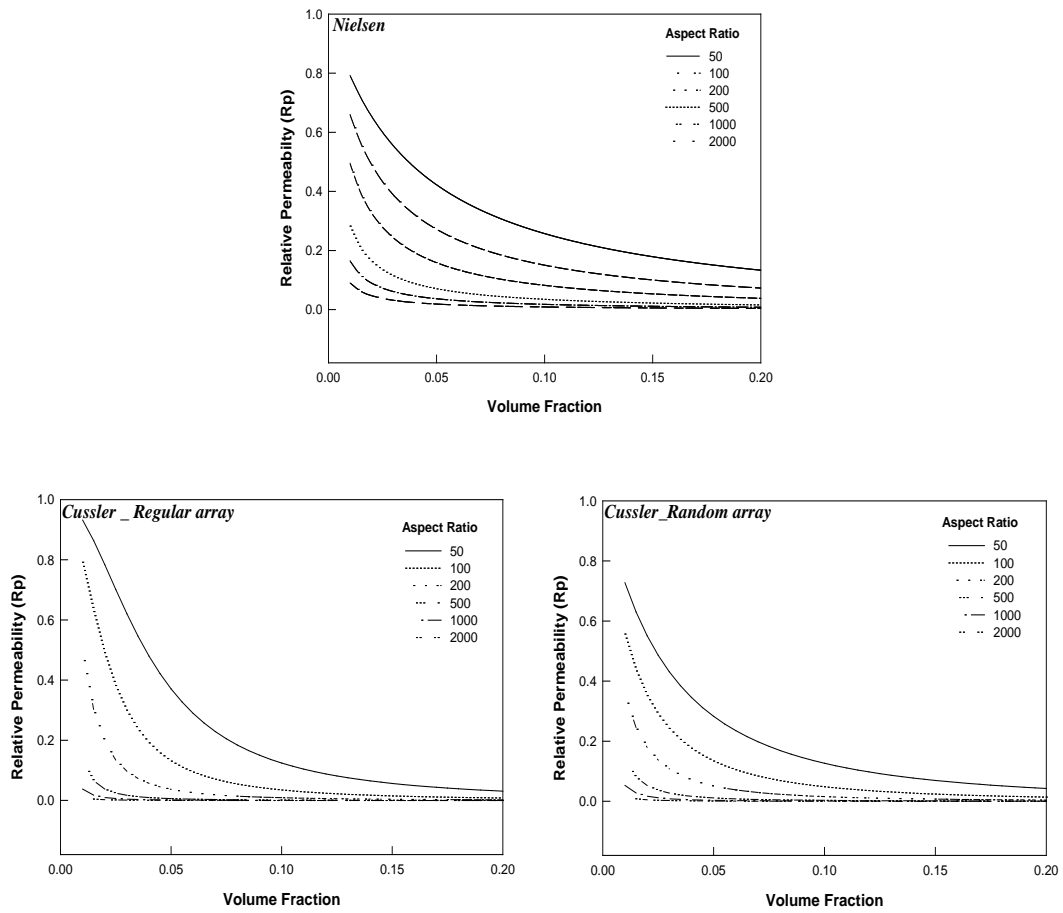


Figure 2-27. Theoretical effects of volume fraction on relative permeabilities, Upper curve calculated from Equation (2-3) and lower two curves of the Cussler model were drawn from Equation (2-4) and (2-5). (Redrawn from [90])

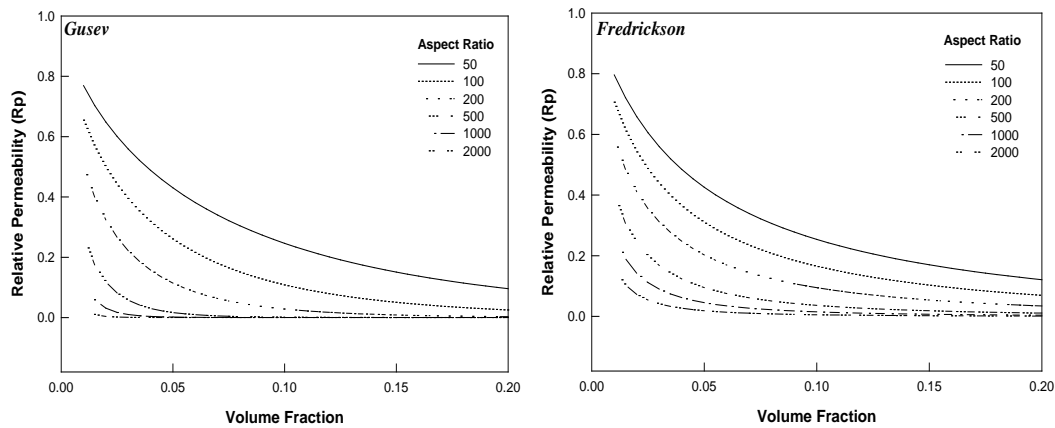


Figure 2-28. Theoretical effects of volume fraction on relative permeabilities, Left curve calculated from Equation (2-6) of Gusev model and right plot of the Fredrickson model were drawn from Equation (2-7). (Redrawn from [91,92])

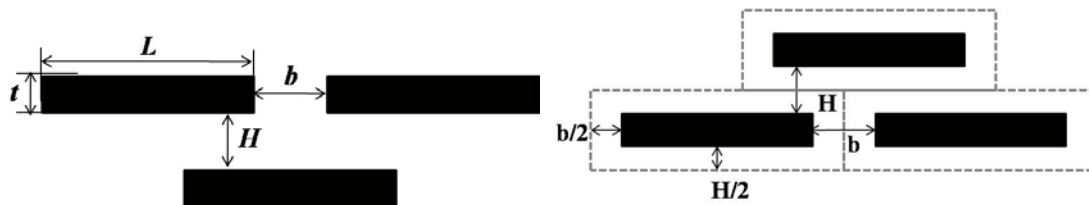


Figure 2-29. A unit of three silicate platelets representing the arrangement of platelets in whole system of idealized PCN structure (left); effective volume of a clay platelet was represented as dot line (right)

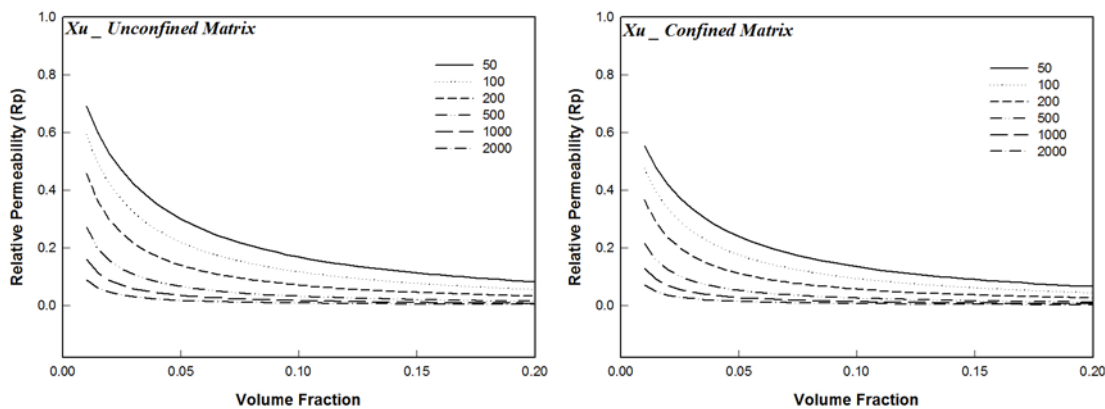


Figure 2-30. Effect of confinement of clay platelets on polymer chain-segment immobility and resulting relative permeability depending on volume fraction of clay, two figures are drawn and calculated based on Equation (2-12). Where, $\zeta_1=1$ for left unconfined matrix and $\zeta_1=1.25$ (empirical value suggested in [93]) for right confined matrix were used. (Redrawn from [93])

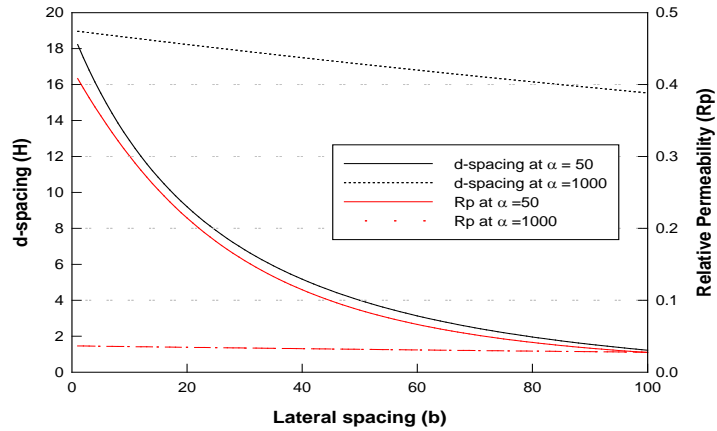


Figure 2-31. Effects of lateral spacing on d-spacing and relative permeability at different aspect ratio of platelets; this plot is based on Equation (2-12) ($\phi= 0.05$) (Redrawn from [93])



Figure 2-32. Comparison of the changes in H spacing as b varies between larger and smaller platelets was presented (drawn from the concept of [93] and [95]); upper figure represent occupancy of larger particles with effective volume of small spacing of b and when b increases, H has to be decreased to fill up the same volumetric space as shown in middle figure. In the case of smaller particle, H decreases drastically for the same amount of increases in b as represented in the bottom figure.

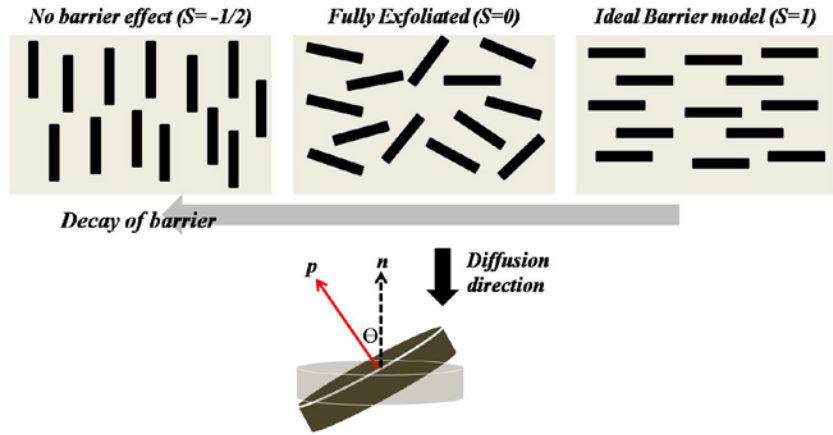


Figure 2-33. Schematic figure to depict the variance of S values depending on platelets' orientations. (Redrawn from [96])

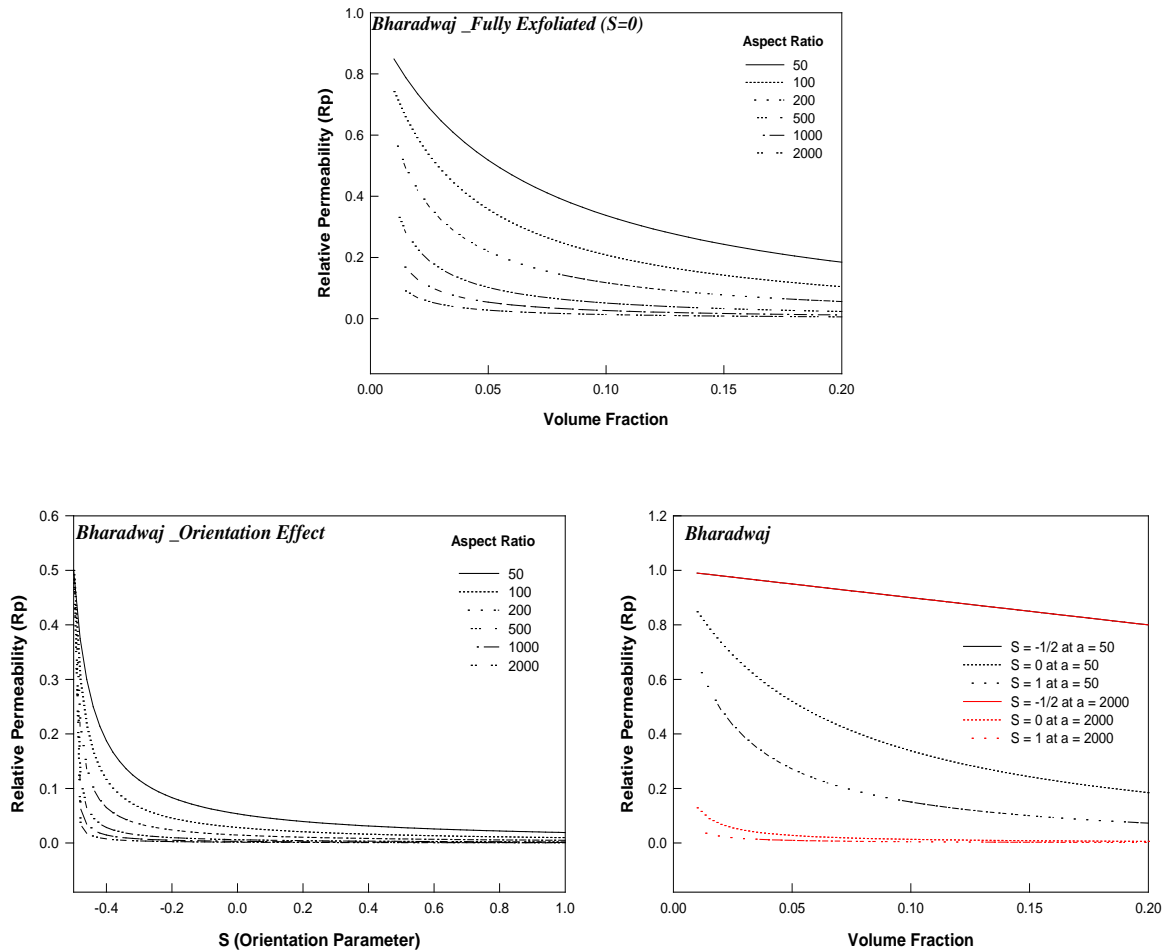


Figure 2-34. Effects of volume fraction on R_p when fully exfoliated structure (upper), two curves to depict the effect of S on R_p calculated at volume fraction = 0.05 using Equation (2-14) (Redrawn from [96])

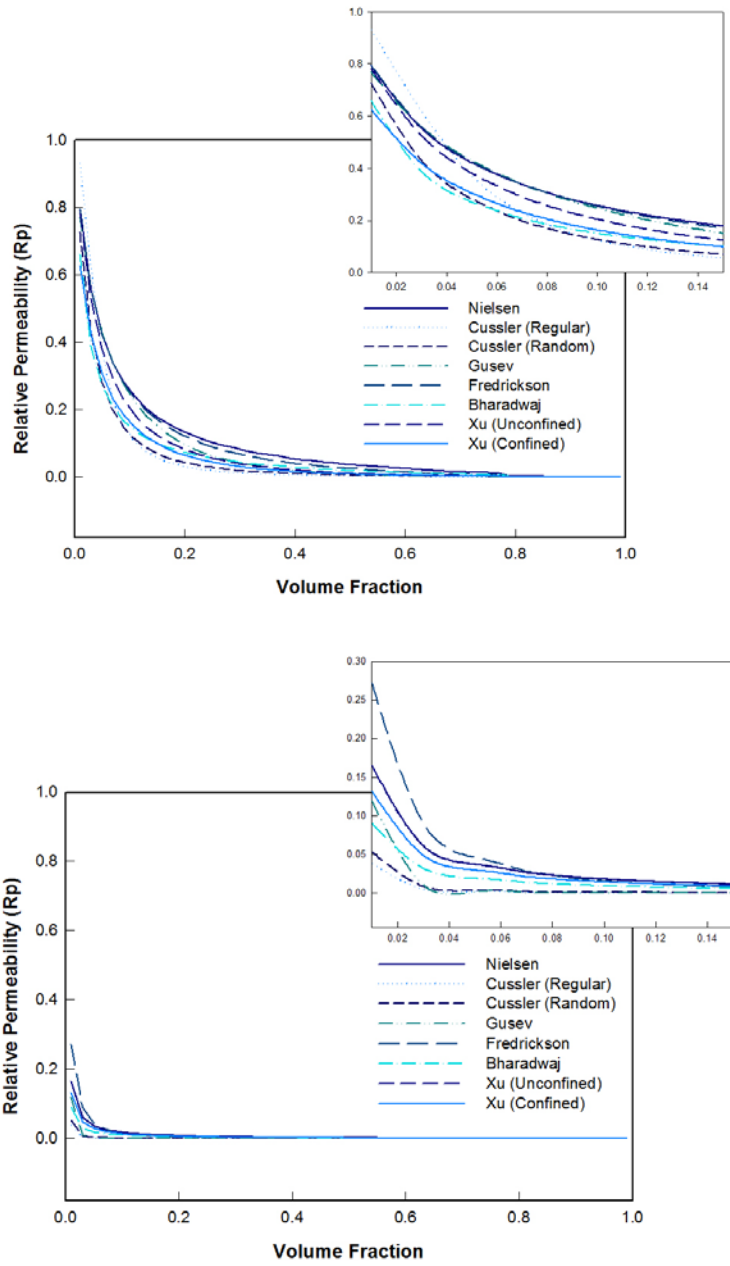


Figure 2-35. Effects of volume fraction on R_p for present barrier models calculated at aspect ratio of 50 (upper) and 1000 (lower)

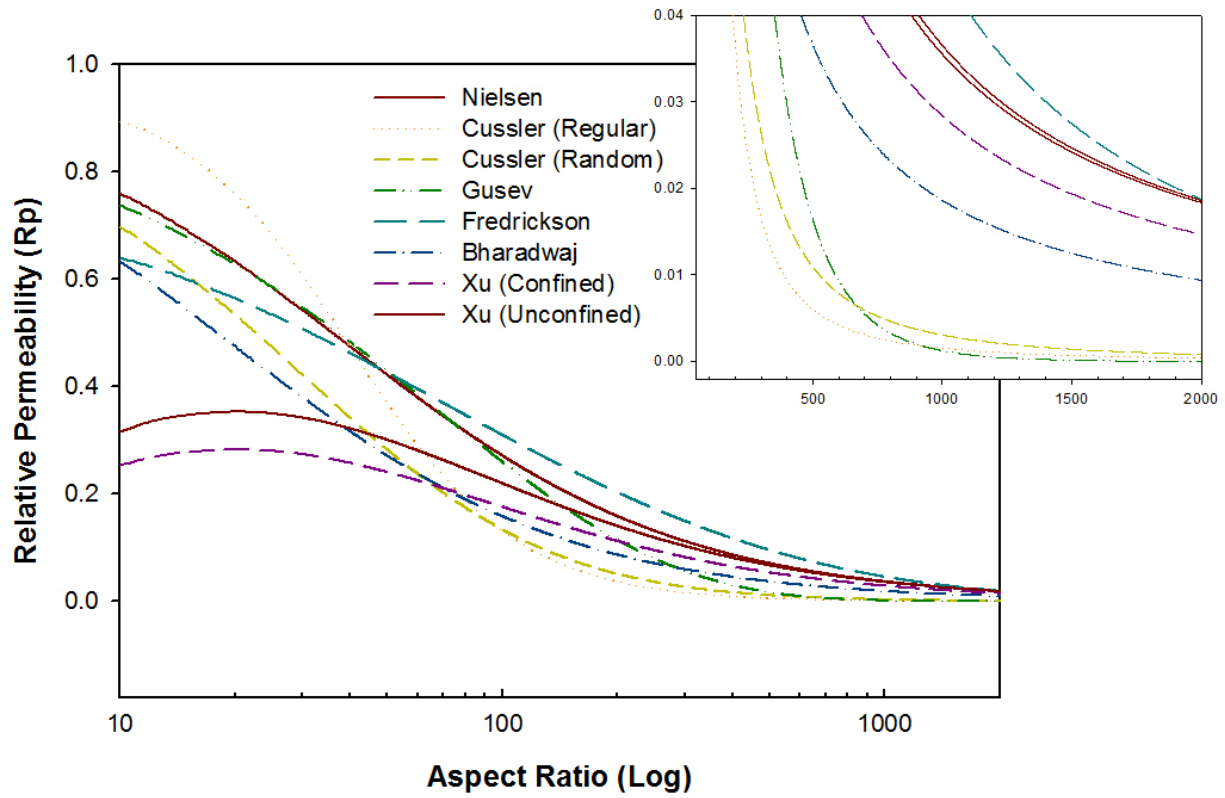


Figure 2-36. Comparison of prediction for R_p as a function of aspect ratio; all curves were plotted based on the Equation 2-2, 2-3, 2-4, 2-5, 2-6, 2-11, and 2-13 at $\phi = 0.05$

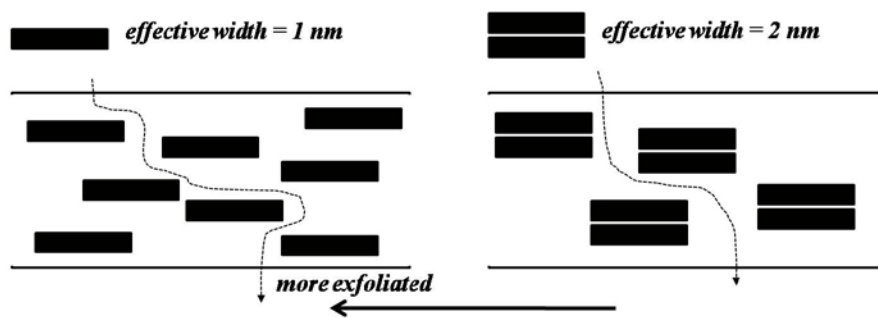


Figure 2-37. Illustration of effective width and its effect on barrier property of PCN (redrawn from [63,96])

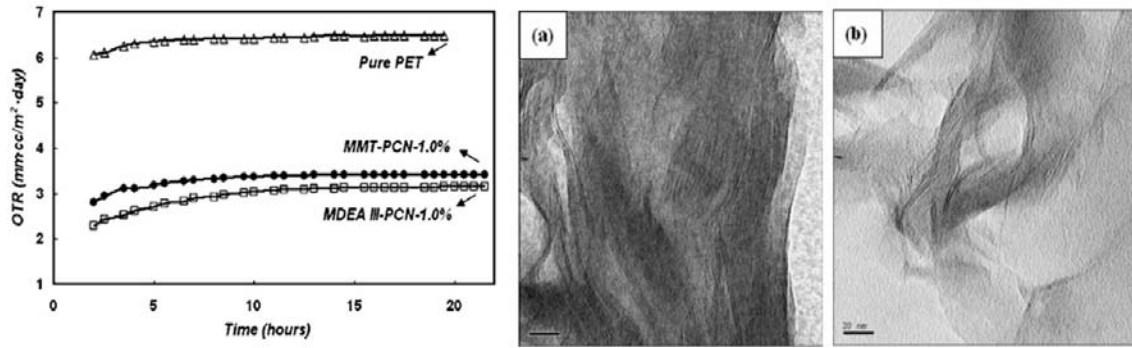


Figure 2-38. OTR chart of a pure PET sheet and PCN sheets (left) and corresponding TEM micrographs of MMT-PCN (a) and MDEA III-PCN (b) [101]

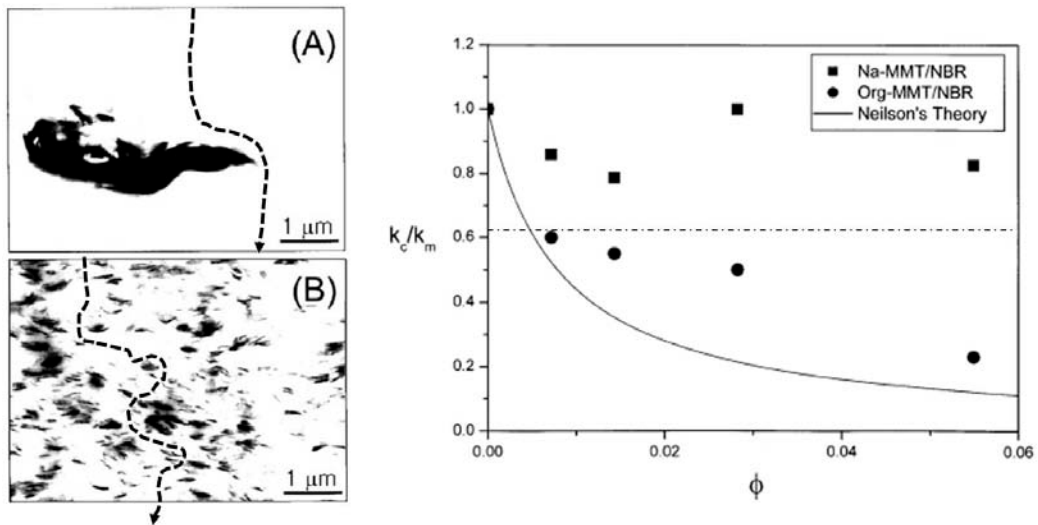
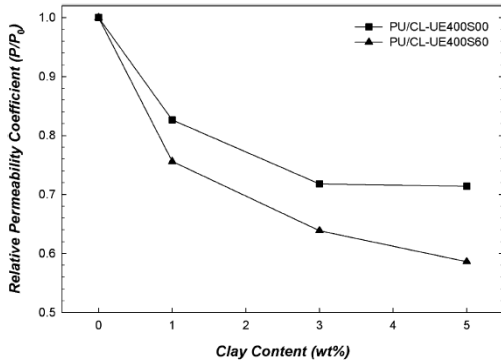


Figure 2-39. TEM micrographs to represent the difference in tortuosity (refer to dot lines) between phase-separated microstructure of unmodified MMT-PCN and exfoliated one of modified MMT-PCN (left) and relative permeability of two PCNs and Neilson's theoretical values (right) [100]



Sample	Clay Content (wt%)	R_p
PU/CL-UE400S00	1	0.827
	3	0.718
	5	0.714
PU/CL-UE400S60	1	0.756
	3	0.639
	5	0.586

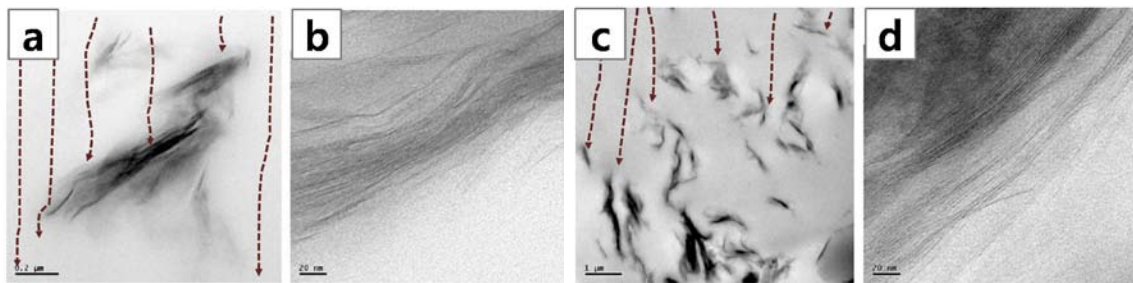


Figure 2-40. Oxygen relative permeability of composite depending on clay content (wt%) and TEM micrographs of PU/CL-UE400S00; (a) low and (b) high magnification of 1wt% clay and those of PU/CL-UE400S60; (c) low and (d) high magnification of 5wt% clay. (Red dot lines represent the diffusion path through the structure of composites) [102]



Figure 2-41. TEM micrograph of a compression molded specimen containing 5 wt% of clay filler dispersed in polyesteramide matrix [99]

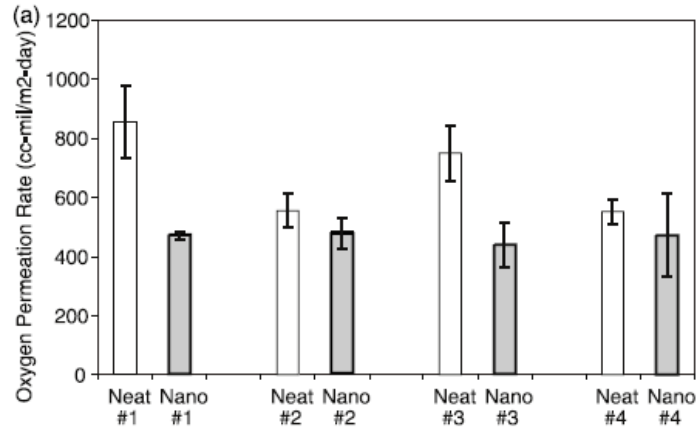


Figure 2-42. Oxygen permeability rate of various blown composite/neat film samples [104]

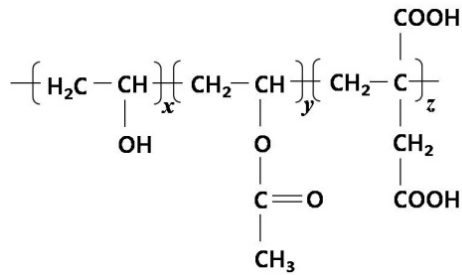


Figure 2-43. Chemical structure of poly (vinyl alcohol-co-vinyl acetate-co-itaconic acid) where, x, y and z is 97, 2 and 1, respectively [44]

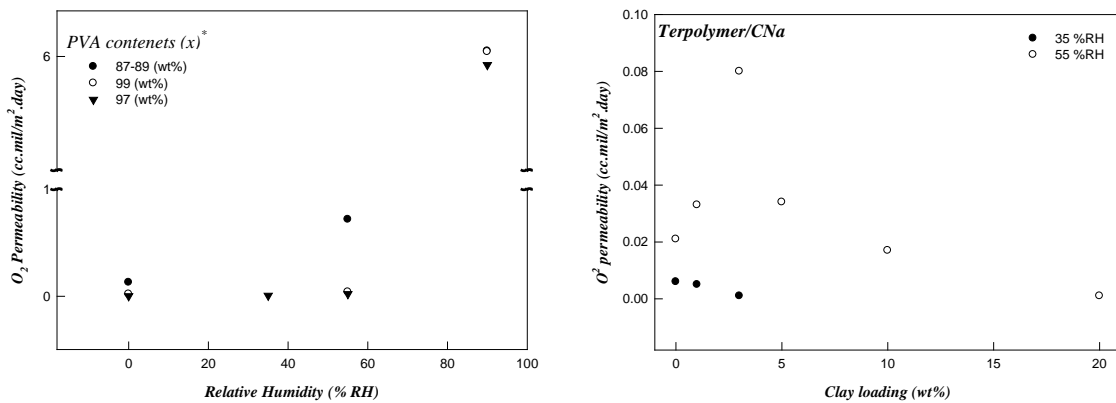


Figure 2-44. Effects of PVA contents on oxygen permeability of neat polymer containing no fillers (left) and effect of clay loadings on oxygen permeability of terpolymer/CNa composites; x represents the weight percent of vinyl alcohol group as shown in chemical structure in Figure 2-43. Thickness of all samples is 6 μm and permeability is the product of film thickness and oxygen transmission rate (OTR) measured at 23°C (plotted based on results from [44])

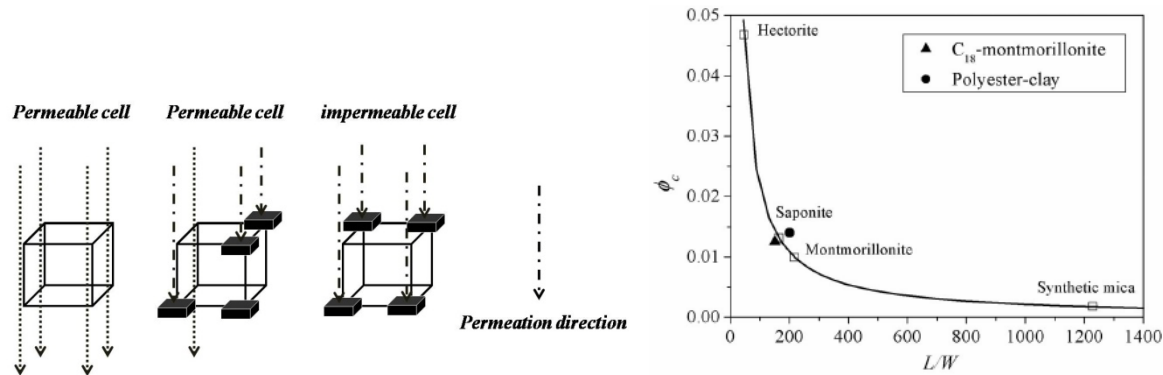


Figure 2-45. Concept of probability of a barrier cell using Kadanoff cell (left) and Critical volume fraction versus aspect ratio of platelets with $S= 0$. Thresholds for several typical clay fillers are obtained directly from Equation (2-15) based on their aspect ratios [110] (open symbols). Two solid symbols indicate the test data of O_2 gas permeability in C_{18} -montmorillonite ($L/W= 150$ and $\phi_c=1.25$ (Ray et al., 2003)) and polyester-clay ($L/W =200$, and $\phi_c=1.4$ [63]) nanocomposites (right) [109]

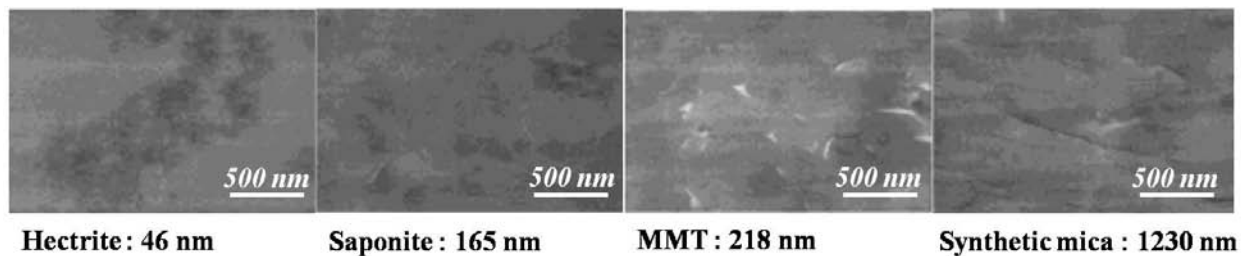


Figure 2-46. TEM micrographs of various PI/clay hybrid films [110]

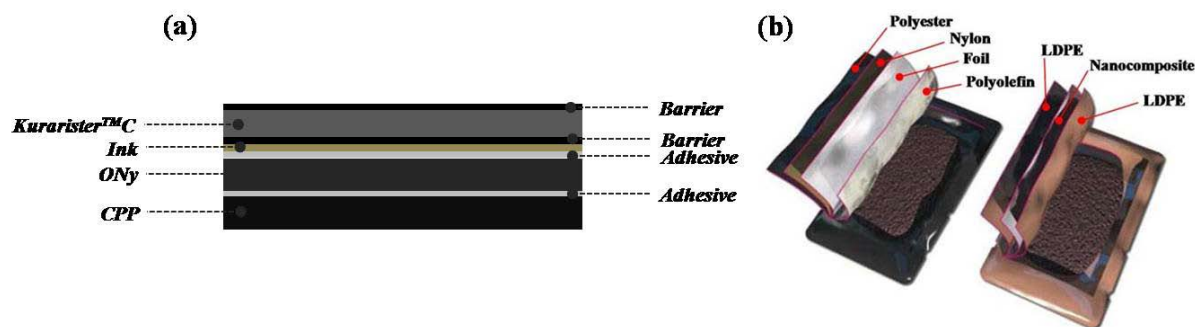


Figure 2-47. Commercialized structural composite to enhance oxygen barrier property (a) Kurarister™ C developed by Kuraray Inc. Japan; and (b) Composite structure developed for US army MRE case

CHAPTER 3
POLYMER CLAY NANOCOMPOSITE COATINGS ON NON-POLAR POLYOLEFIN
SUBSTRATE TO ENHANCE BARRIER PROPERTY

Introduction

Polymer clay nanocomposite (PCN) have been widely studied as property enhancers for polymers for mechanical strength [1,114], thermal stability [115] and barrier properties [116,117]. PCNs are sometimes referred to as “hybrids of inorganic functional fillers” and are an area of intense research activity. Dispersion of nanoparticles in polymers results in three typical structures that are classified as non-intercalated, intercalated and exfoliated as explained in Chapter 1. Exfoliated structures involve complete separation of particles into random arrangements [118,119]. Exfoliated structures are necessary to obtain maximum benefits from nano-particles. Exfoliation requires relatively high shear forces to separate particles in solution and complicates processing and production of PCNs [112,120]. Once the fully-exfoliated structure is obtained, maintaining the exfoliated structure without particle aggregation is another challenge in PCNs. Additionally, obtaining fully-exfoliated PCN in non-polar polyolefin polymers has been difficulties because silicate layers of clay are polar and therefore, incompatible with polyolefin. Significant efforts are underway to overcome this limitation [7,121,122].

In this study, Laponite JS (Southern Clay Products, Louisville, KY) and polyvinyl alcohol were used to produce polymer nano-composite coatings as inorganic filler and a hydrophilic polymer matrix, respectively. Laponite JS is a synthetic layered fluorosilicate modified with an inorganic polyphosphate dispersing agent. Figure 3-1 shows SEM micrographs of Laponite JS powder and a schematic structure of Laponite JS. This clay is hectorite, prepared in a reaction between Mg, Li, and Na-silicate salts, which results in partially crystalline, monodispersed in size discs, 0.92 nm thick and ca. 25 nm long (aspect ratio of 25-55), with a bulk density of 950

kg/m³ and specific surface area of ca. 300 cm²/g [118]. As shown in scanning electron microscopy (SEM) micrographs in Figure 3-1, Laponite powder exhibited typical agglomerated and grained features of layered silicate particles. It hydrates and disperses in water to give virtually clear and colorless colloidal sols of low viscosity. Therefore, Laponite colloidal solutions of up to 18 wt% are stable for one month.

Poly(vinyl alcohol) (PVA) is a water-soluble polymer with linear chains. Figure 3-2 shows the representative chemical structure of general PVA grades. Depending on the degree of saponification (DS) of PVA, which is the degree of conversion to PVA through the saponification process, the physical properties of PVA varies significantly. PVA is known to be non-toxic and is recognized to be “generally recognized as safe” (GRAS) by the United States Food and Drug Administration (FDA). PVA is recognized to be a biodegradable polymer and has found uses as a coating material, stabilizer, polarizing film, sizing agent, adhesive, drug delivery system, contact lens material, basic bio-material with expanding applications in nanotechnology [123,124]. PVA alone offers excellent oxygen barrier properties; however, ethylene vinyl alcohol (EVOH) is often the preferred polymer used in multilayer packaging film structures.

Polymers with excellent oxygen barrier properties inherently have high crystallinity and large cohesive energy caused by highly polar hydrogen bonding. Nano-composites involving clay nano-particles in PVA have been studied in many laboratories [29,78,125-128]. While wet, PVA nano-composites demonstrate excellent particle dispersion in PVA gels. This state represents a true nano-scale organic-inorganic hybrid material. However, drying causes portions of clay layers to reaggregate. Steric constraints of PVA impede complete reaggregation of clay, allowing some to remain in the dispersed state [128].

Nano-composite preparation techniques are designed to create amorphous domains with uniformly distributed mineral layers, but this approach is limited as the preparation of PVA/clay nanocomposites from solutions is difficult because of reaggregation of clay [129]. To prevent reaggregation, Yeun, et. Al [78] prepared PVA/Saponite nano-composites with various clay concentrations successfully. They reported that oxygen permeability values decreased with increasing clay loading within a 0-10 wt% range, while optical properties remained nearly constant.

Another major limitation of PVA as a nano-composite matrix polymer can be caused by the polar nature of the hydroxyl (-OH) groups that make PVA hydrophilic and soluble in water. Small amounts of water, particularly relative humidity above about 35%, plasticize PVA resulting in dramatic loss of oxygen barrier properties [130,131]. A variety of techniques used to reduce oxygen permeability under high relative humidity have been developed by several research groups. One of the most common is sandwiching the water-sensitive polymer between hydrophobic layers such as polypropylene (PP) and/or polyethylene (PE) [24,132]. However, laminated structures are expensive and may suffer from poor flexibility.

PP is an attractive packaging material because it is readily available, low cost and offers good overall mechanical properties. However, PP suffers from low oxygen barrier properties. Improvement of barrier properties of PP without creating expensive laminate structures would greatly enhance the usefulness of the polymer. Therefore, this work focused on development of techniques to produce and apply nano-based barrier coatings to PP, the substrate. Critical to this work was enhancement of bonding between the hydrophobic substrate and the hydrophilic, PVA/Laponite coating. In this work, atmospheric pressure plasma (APP) treatments were used to enhance bonding of coatings.

Experiments

Materials

A PCN solution was made with synthetic layered silicate known as Laponite JS (Southern Clay Products, Louisville, KY). To evaluate effects of molecular weight (MW) and degree of saponification on coating adhesion and oxygen barrier, PVA provided by Celanese Company (Dallas, TX) and Scientific Polymer Product Co. (Ontario, NY) with MW and DS shown in Table 3-1 were used. Organic ammonia chloride (OAC); [2-(Acryloyloxy)ethyl]-trimethyl ammonium chloride was used for intergallery modification which can increase the intergallery distance by replacing swollen sodium ion with organic molecules to make it easier for polymer chains to be diffused into this space as shown in Figure 3-3. (For more explanation, refer to Chapter 1, Introduction) Preparation of PCN solutions was conducted through the four steps as presented schematically in Figure 3-4.

Step 1: Preparation of Polymer Clay Nanocomposite Solutions

OAC buffer solution of 1 wt% of clay was added into a corresponding amount of deionized water at 40 °C and pH 10 were premixed for 2-3 minutes with a magnetic stirrer. Laponite JS was added gradually to prevent aggregation. Prepared clay solutions were placed at room temperature for less than a day to obtain good ion-exchange reaction in the intergallery of clay platelets. Polymer stock solutions were prepared by dissolving PVA in deionized water at elevated temperature and stirring with magnetic stirrer for at least 6 hours. Prepared PVA stock solution was added to clay solutions and mixed for 1 hour with a magnetic stirrer and then mixed with a high shear mixer (KadyMill-L, Kady® International, Scarborough, ME). Prepared PCN solutions were placed in a hood at ambient temperature for 3–10 hours depending on viscosity in order to allow entrained air bubbles to dissipate. Table 3-2 outlines the compositions of all prepared PCN solutions for coating in this study.

Step 2: Atmospheric Pressure Plasma Treatment

APP treatments were performed using a Dyne-A-Myte VCP (Enercon Industries Co., Menomonee Falls, WI). Air and nitrogen gas (about 50/50) were used to create plasma. Figure 3-5 illustrates the four controllable variables when treating the surfaces. These variables are flow rate of nitrogen gas, working distance between the tip and the surface of target specimen, treatment times and belt speed. Table 3-3 lists specific conditions used in this study.

Step 3: Coating Samples after APP Treatment

Surfaces of rigid PP were spin coated with 20g PCN solution at fixed spin-coating parameters involving a two-step process to obtain uniform thickness of coated layer. First step was 500 rpm for 1.5 min. Second step was 700 rpm for 30s. The spin coater used was a Model Laurell WS-400B-6NPP/LITE (Laurell Technologies Co., North Wales, PA).

Step 4: Drying PCN-Coated PP specimens

PCN-coated PP specimens were dried at ambient temperature in vacuum desiccators to remove possible air bubbles for 10 – 12 hours.

Characterizations

Morphological effects of APP surface treatments were analyzed using Model JSM-6400 SEM (JSM-6400, Jeol Ltd., Tokyo, Japan). Samples were washed with acetone and then surfaces were sputter coated with gold-palladium alloy (Au-Pd). Micrographs of submicron-detailed surfaces were obtained under ambient conditions using atomic force microscopy (AFM) (Digital Instruments Dimension 3100, Veeco Instruments., Plainview, NY) by contact mode. Oxygen transmission rates of PCN-coated samples were measured in accordance with the procedure described in ASTM D-3985 using a Model OX-TRAN 2/20MH (Mocon Corporation, Minneapolis, MN). Permeation cell area was 50 cm². Degree of exfoliation was measured by analyzing changes in intergallery spacing of clay platelets. The change in spacing was measured

using an Wide Angle X-Ray Diffractometer (WAXRD) (Philips XRD APD 3720 powder diffractometer, Philips Electronics, Mahwah, NJ) with a Cu anode (CuK α radiation ($\lambda = 1.54056$ Å; scanning range from 5° to 69.99°). Clay powder was mounted on a sample holder with a large cavity and a smooth surface was obtained by pressing the particles with a glass plate. Samples for PCN solution were prepared by spin-coating using a silicon wafer as a substrate. The changes in the basal spacing at the small angle range from 2° to 10° of clay platelets for LP20PVA, LP40PVA, LP50PVA and LP70PVA were investigated by using XRD (Philips MRD X'Pert System, Philips Electronics, Mahwah, NJ) with a CuK α radiation. PCN-coated PP specimens were able to be used directly without a sample holder.

Results and Discussion

Surface Modification by Atmospheric Pressure Plasma Treatment

Degree of surface modification caused by APP is determined by several important factors such as plasma energy source, which can be classified regarding the excitation mode, exposed area energy density, and the collision time and intensity of the electron energy source [133]. In this research, air and nitrogen gas were used as a plasma source and the flow rate of nitrogen gas and the distance between tip and surface of specimen were controlled to investigate effects of APP treatment on surface modification as well as resulting oxygen barrier property. Resulting SEM micrographs of APP treated and untreated PP at 6k magnification are shown in Figure 3-6 (a-d). Enhanced roughness was observed microscopically depending on the APP treatment parameters. Generally, the harsher condition such as short working distance (WD) or higher N₂ flow rate resulted in more rough surfaces. As shown in Figure 3-6 (b), some pattern on the surface was observed along the treatment direction and this pattern was disappeared as WD was

getting closer to the surface. However, no significant effects of APP were observed for WD of 3cm or greater. This can be checked by comparing Figure 3-6 (c) and (d).

Surface topography of nitrogen plasma PP substrate measured by AFM on a 20 x 20 μm^2 area is shown in Figure 3-7. Non-treated surfaces in Figure 3-7 (a) appeared to be flat and smooth while APP treated surfaces appear to have surface contours (Figure 3-7 (b)). Figure 3-8 and 3-9 shows the effects of APP parameters on the surface roughness. These figures are the 3-dimensional height images taken by AFM on a 50 x 50 μm^2 area of (a) untreated surface and from (b) APP treated by App-Cond01 to (k) App treated by App-Cond10 as listed in Table 3-3. Apparently more surface contours were observed in (c) - (e) and (h) - (j) when comparing others. This could be caused by the fact that the harsher APP conditions make plasma jet to be excited more by obtaining more energy subsequently resulting in better etching effect on the surface.

For quantitative analysis of surface roughness of the AFM images, R_a , R_{max} and Root Mean Square (RMS or R_q) values were measured. R_a and RMS are both representations of surface roughness, but each is calculated differently. R_a is calculated as average roughness (Equation 3-1) of measured microscopic peaks and valleys. RMS is calculated as the root mean square of measured microscopic peaks and valleys (Equation 3-2). Each value uses the same peak and valley dimension measurements. A single large peak or flaw within the microscopic surface texture will affect the RMS value more than the R_a value. R_{max} is defined as a maximum height representative of a difference between a highest point and a lowest point [133-135].

$$R_a = \left(\frac{1}{L} \right) \int_0^L |z(x)| dx \quad (3-1)$$

$$R_q = \left[\left(\frac{1}{L} \right) \int_0^L z(x)^2 dx \right]^{\frac{1}{2}} \quad (3-2)$$

Where, L = evaluation length, Z(x) = the profile height function

The largest RMS value of 132 nm was obtained at 18 l/min nitrogen (Figure 3-10). No additional roughness was measured at greater nitrogen flow rates. Therefore, 18 l/min nitrogen was used for APP treatments for this study. The increase in surface roughness by APP treatment is caused by the surface activation involving grafts of active chemical functions onto the surface [133]. Working distance was the distance between the plasma jet tip and the sample. WD was determined to be critical for effectiveness. Figure 3-11 shows increased surface roughness at WD of 20 mm.

Clay Exfoliation

Degree of exfoliation depends on how platelets are modified and how well the intergallery is opened. Because of the small intergallery distance, high shear processes are needed to achieve exfoliation of nano-particles. Each platelet peels away from a stacked clay layer. WAXRD patterns of pure Laponite JS and PCNs are shown in Figure 3-12. As a silicate material, Laponite exhibits low angle peaks, much like natural MMT clay. Two high angle peaks were also observed for Laponites JS at about 48 degrees and 62 degrees. Therefore, according to Bragg's law ($d=n\lambda/2\sin\theta$), $d = 1 \times 1.54 / 2 \sin (48/2) = 1.89 \text{ \AA}$ and d-spacing for 62 degree = $1 \times 1.54 / 2 \sin (62/2) = 1.50 \text{ \AA}$. These d-spacings should correspond to the lattice spacings of the crystalline unit cells. The two typical peaks of Laponite JS at 48 and 62 degrees disappeared on curves in Figure 3-12 for exfoliated LP10PVA, LP30PVA and LP50PVA because of the exfoliation of the silicate or high disorder of the clay platelets [136]. However, as shown in Figure 3-13, a sharp strong peak at 48 degrees was shown at the unexfoliated LP20PVA, abbreviated as 'LP20PVA-UE', which means that silicate layers were not delaminated nor dispersed. XRD patterns of PCN showed no peak between 40 and 70 degrees and signal intensities showed a broad hump between 60 and 63 degree for LP30PVA and LP50PVA in Figure 3-12. This can be explained by

exfoliated silicate layers of the clay mineral showing characteristic XRD pattern of amorphous material when platelets are randomly dispersed. This pattern is a characteristic XRD pattern of a clay-exfoliated type of polymer-clay nanocomposite [122]. The more clay added in PCN, the more distinctive the hump observed by XRD. However, if the clay platelets are fully exfoliated, d-spacing cannot be detected by the XRD method because the d-spacing would become too large. X-ray diffraction patterns of coated samples were also obtained at low angle range from 2 to 10 degree as shown in Figure 3-14. As shown in this figure, the peaks for (001) plane around 5 to 6 degree were disappeared for LP20PVA, LP40PVA and LP50PVA indicating that exfoliation of clay was achieved for these three samples. However, a broad peak which is shifted to lower degree from the (001) peak position was observed for the sample containing higher amount of clay. Partial exfoliation which is a mixture of partially exfoliated and intercalated structures was occurred for LP70PVA because the amount of polymer is not enough to approach the complete exfoliation of all clay resulting in some aggregated particles.

Barrier Properties

PVA as a coating material for food packaging materials to reduce oxygen permeability has several advantages in terms of its structural properties as described in Chapter 2. The large inter- and intramolecular cohesive energy resulting from the highly polar hydrogen bonding provided PVA with excellent oxygen barrier properties at low relative humidities. Due to the combination of strong hydrogen bonding and high degree of crystallinity, PVA has lower oxygen transmission rate (OTR) values when comparing to PET by three orders of magnitude.

Clay platelets with large surface area and high aspect ratio were expected to show increased oxygen barrier properties in much the same way as increasing crystallinity of the polymer. Figure 3-15 indicates OTR was a function of clay concentration. Greatest barrier properties as indicated by lowest OTR values were obtained at 50 wt% of clay concentration in

the final dried film. Between 20 to 40 wt% of clay concentration, no significant difference in OTR values was observed. Additionally, dramatic increases in OTR values were observed for loadings in excess of 50 wt%. This is due to high degrees of reaggregation of clay resulting in reduced effective surface area per unit concentration as well as lower degrees of exfoliation caused by steric interference [7,44,63].

Once high degrees of exfoliation are obtained, oxygen barrier properties are dominated by adhesion strength between PCN-coated layer and the surface of substrate. Therefore, it was found that quality of surface treatment plays a significant role in determining extent of barrier achieved with PCN barrier coatings.

Figures 3-16 and 3-17 illustrate effects of parameters of APP treatment on OTR values. Similar tendencies were observed as a result of surface roughness. Figure 3-16 illustrates effects of nitrogen gas flow rate on the OTR values. Figure 3-16 shows that flow rate of nitrogen gas did not affect OTR, which was consistently in the range of about 10 cc/m²/day. Figure 3-17 shows effects of working distance on surface roughness. Working distance was shown to be critical. Poor results were seen when the plasma head was too close or too far away from test specimen.

DS of PVA used for making PCN solutions was important. Low DS PVA obtained from (Scientific Polymer Product co.) resulted in relatively poor control barrier coatings (0 wt% clay). High DS PVA obtained from Celanese resulted in good barrier properties with OTR values on the order of 10 cc/m²/day. Decreasing DS leads to relatively fewer number of OH groups comparing to that of high DS as well as larger number of bulky side group which remained from precursor. Therefore, the combination of strong hydrogen bonding and high degree of crystallinity might be lower resulting in poor barrier property. MW of PVA did not appear to be significant. OTR values of PVA-coated PP specimen were given in Table 3-4.

Table 3-1. Specific data of PVA samples

Grade	DS	MW	Company
Celvol107	99.3% +	31,000-50,000	Celanese Company
Celvol425	95.5 – 96.5%	120,000-150,000	Celanene Company
PVA-PH	88%	120,000-150,000	Scientific Polymer Product Co.

1) High DS: 99.3 +, 2) Fully saponified: 93 - 98, 3) Intermediate saponified: 91-93, 4) Partially saponified: 88

Table 3-2. Compositions of PCN solutions used for coating

Sample name	PVA grade (MW/DS)	Clay (wt%)	High shear process
LP0PVA	31,000-50,000/99.3%+	0	O
LP10PVA	31,000-50,000/99.3%+	10	O
LP20PVA-EX	31,000-50,000/99.3%+	20	O
LP20PVA-UE	31,000-50,000/99.3%+	20	X
LP30PVA	31,000-50,000/99.3%+	30	O
LP40PVA	31,000-50,000/99.3%+	40	O
LP50PVA	31,000-50,000/99.3%+	50	O
LP60PVA	31,000-50,000/99.3%+	60	O
LP70PVA	31,000-50,000/99.3%+	70	O

Table 3-3. Specific conditions of APP treatment

Condition no.	N ₂ flow rate (l/min)	WD (mm)	Treatment times	Belt speed
APP-Cond01	25	20	4	20
APP-Cond02	20	20	4	20
APP-Cond03	18	20	4	20
APP-Cond04	15	20	4	20
APP-Cond05	12	20	4	20
APP-Cond06	20	30	4	20
APP-Cond07	20	25	4	20
APP-Cond08	20	20	4	20
APP-Cond09	20	10	4	20
APP-Cond10	20	5	4	20

Table 3-4. OTR results of PVA coated PP specimens

PVA			APP condition	OTR value
MW	DS	(wt%)	(refer to Table 3-3)	(cc/m ² /day)
150,000	88	8	APP-Cond09	119.34
150,000	95	8	APP-Cond09	8.05
50,000	99	8	APP-Cond09	8.12

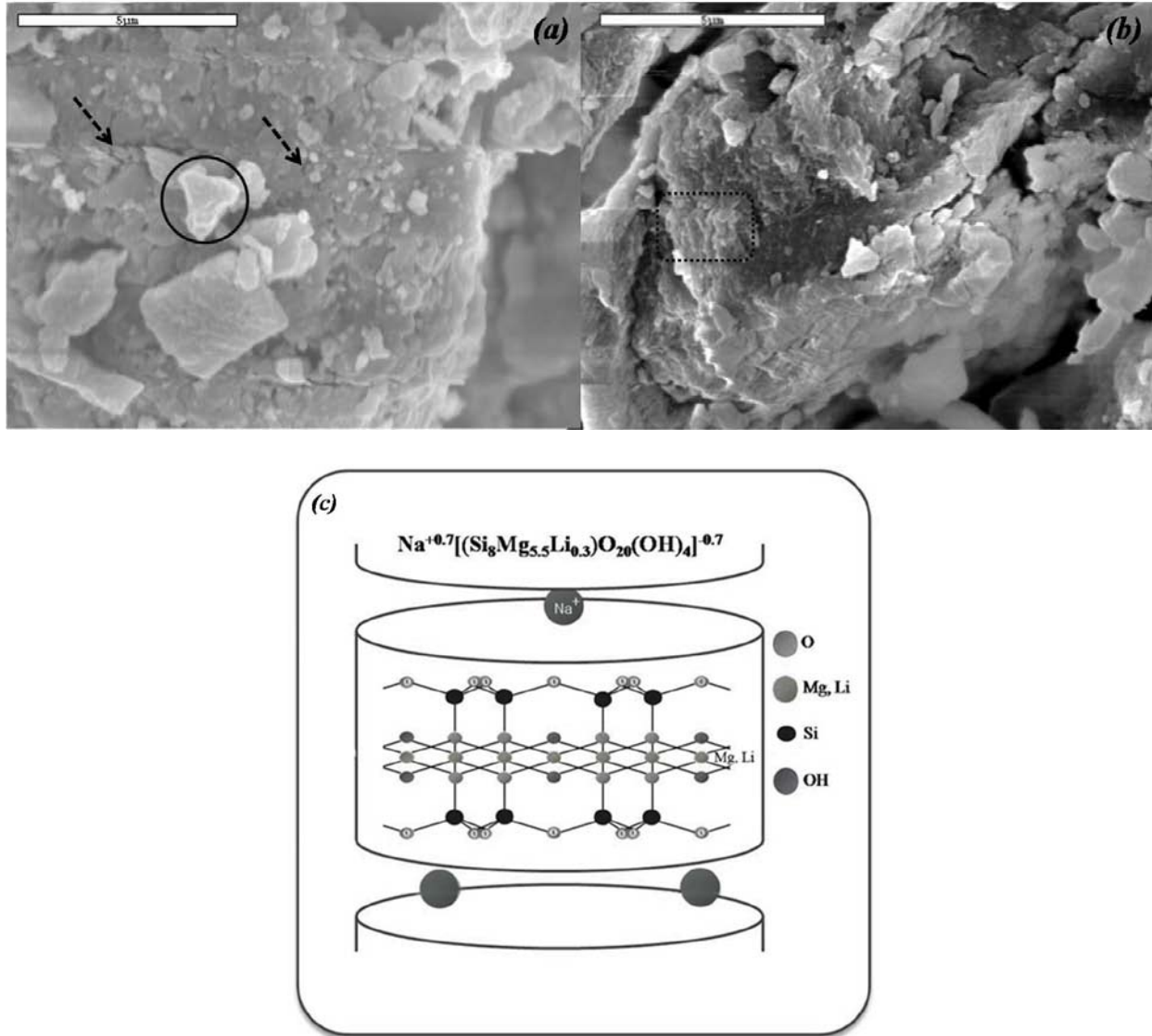


Figure 3-1. SEM micrographs of Laponite JS powder (a) showing agglomerated feature as indicated as dotted arrows and grained region in a circled region and (b) layered features as shown in a dotted rectangle. (c) schematic structure of Laponite JS. Laponite JS consists of platelets containing Mg, Li, Si, O and Na cations in intergallery regions. Average aspect ratio of Laponite JS is between 25 and 55 and its bulk density and specific surface area is 950 kg/m^3 and ca. $300 \text{ cm}^2/\text{g}$, respectively

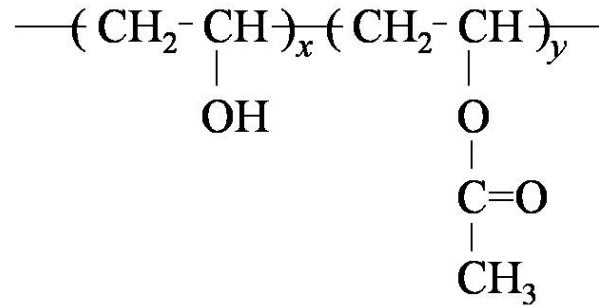


Figure 3-2. A chemical structure of PVA. Depending on x and y, DS of PVA is determined

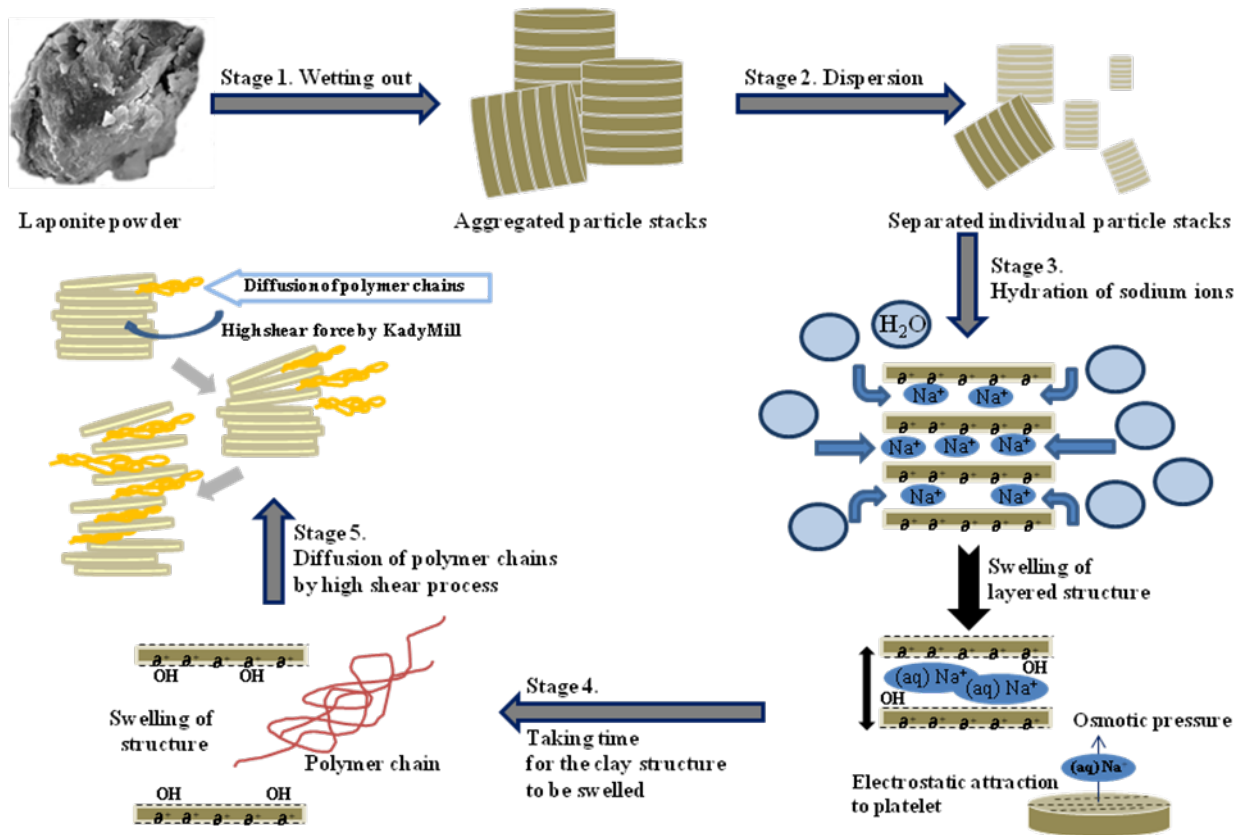


Figure 3-3. Schematic mechanism showing the formation of ideally exfoliated PVA/Laponite JS nanocomposite solution through the ordered experimental procedures

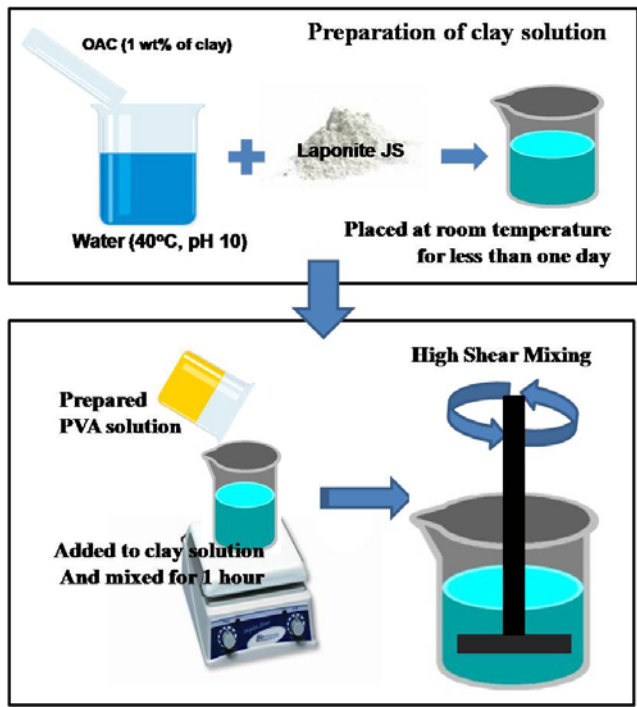


Figure 3-4. Schamtilly illustrated experiment procedures

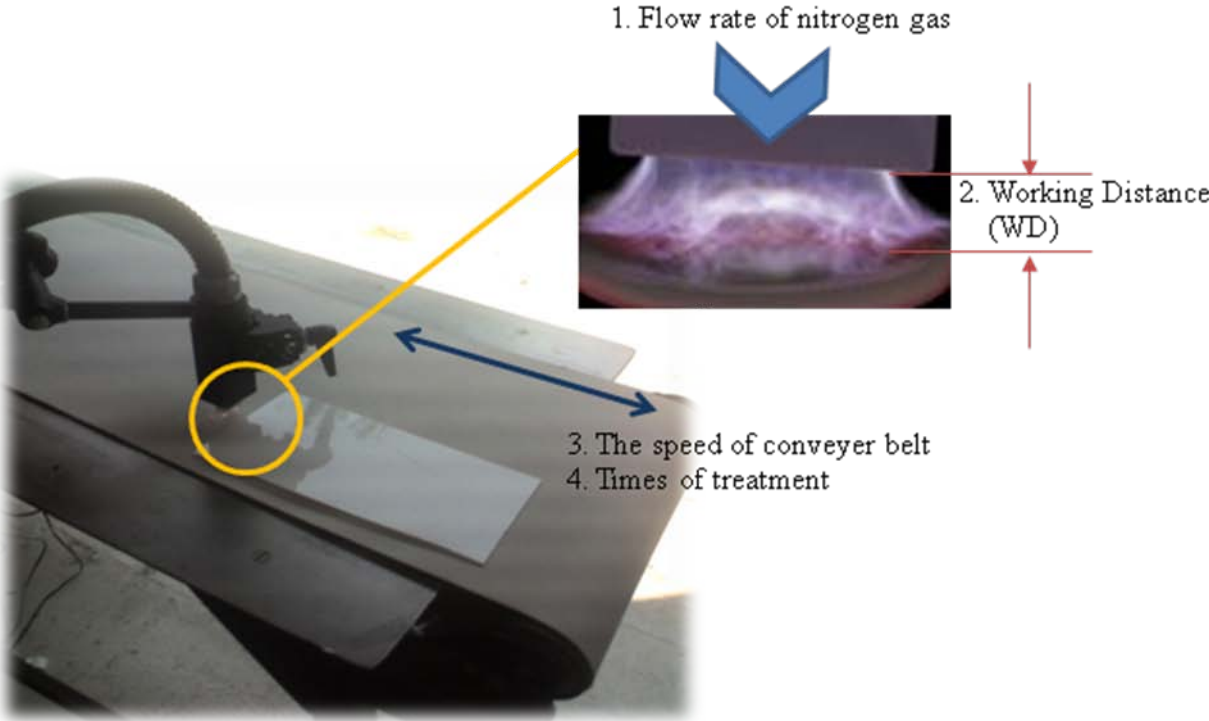


Figure 3-5. Controllable variables when APP-treating the surface of i-PP

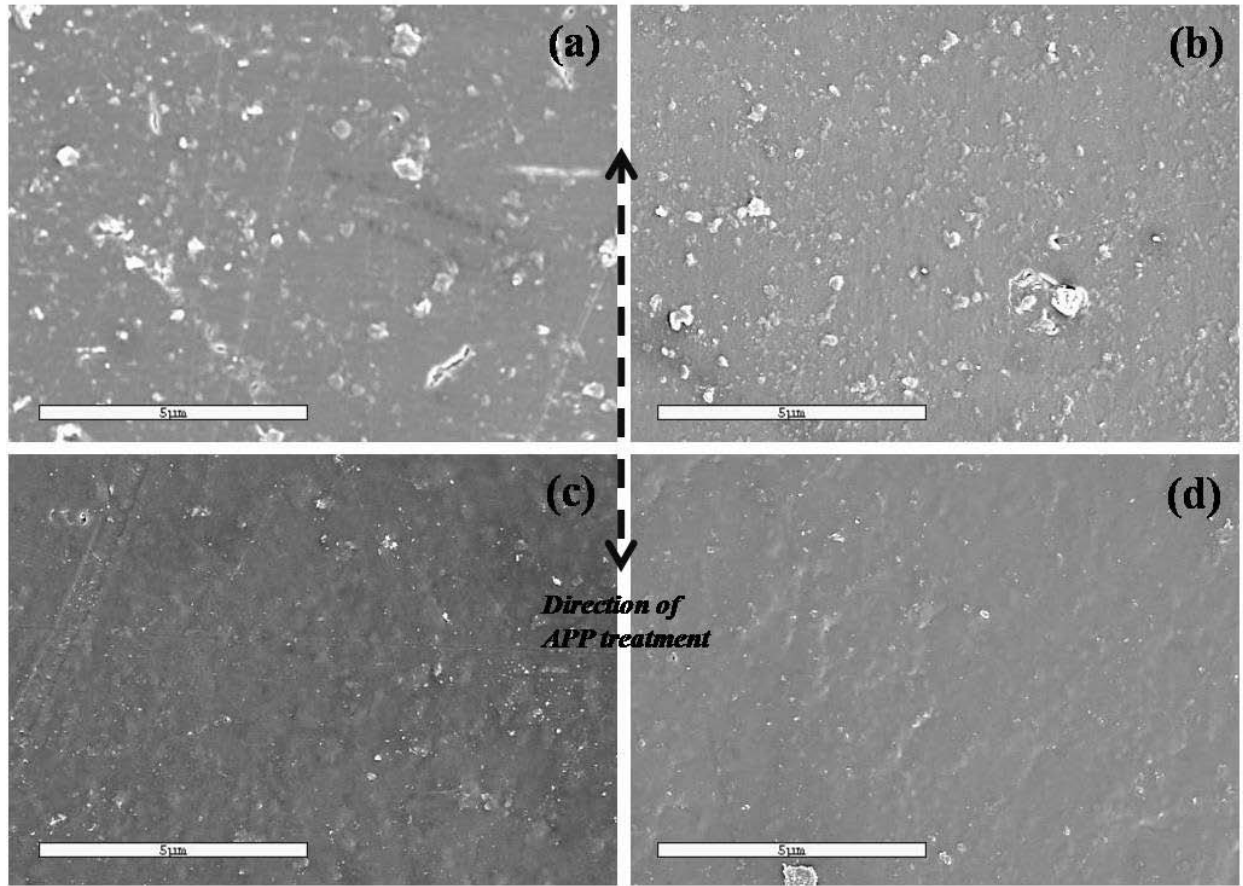


Figure 3-6. SEM micrographs taken at 6000X of (a) untreated surface, (b) APP-treated surfaces by APP-Cond06, (c) APP-Cond01 and (d) APP-Cond09

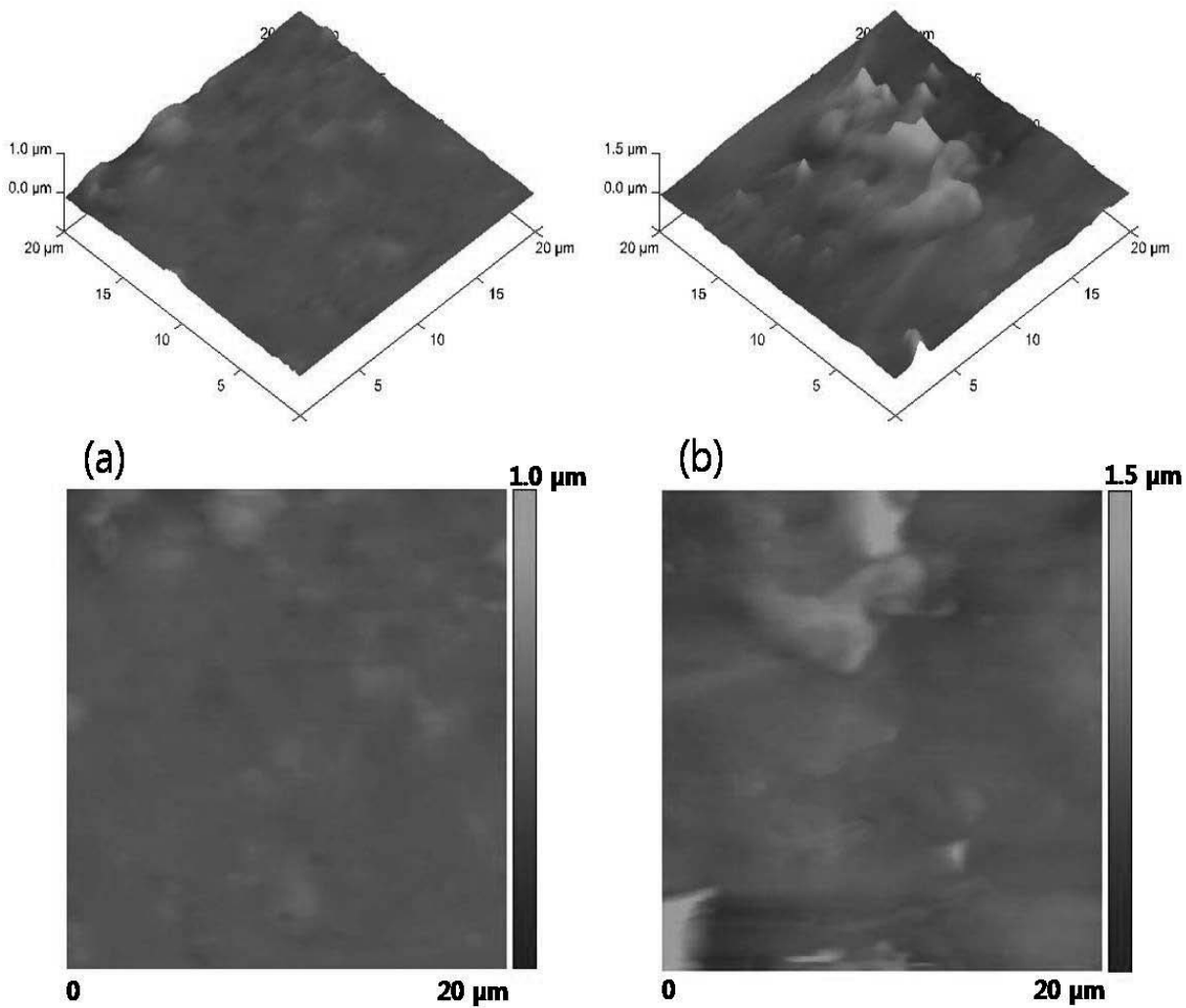


Figure 3-7. 3D surface and height images taken by AFM (contact mode) on a 20 x 20 μm^2 of untreated surface (a) and APP-treated surface by APP-Cond09 (b)

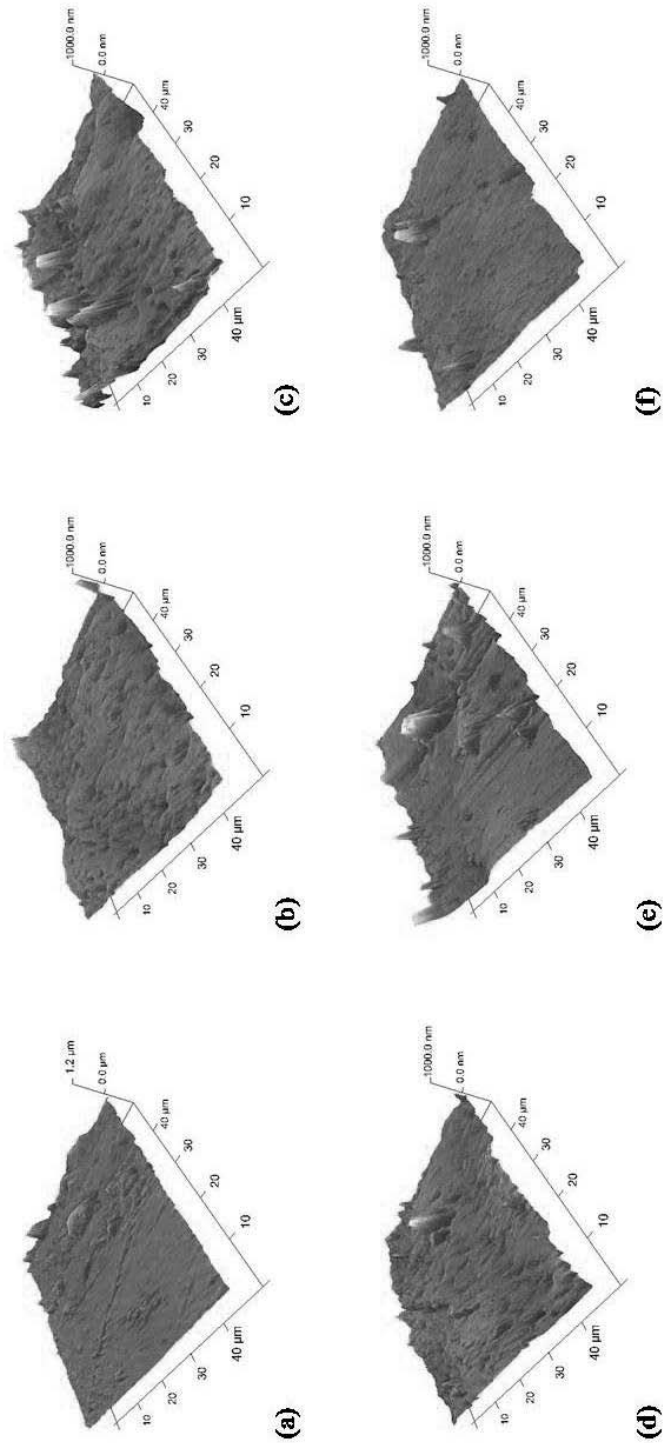


Figure 3-8. Influence of the flow rate of nitrogen gas which is one of the APP parameters; 3D surface images taken by AFM (contact mode) on a $50 \times 50 \mu\text{m}^2$ of untreated surface (a) and APP-treated surface by APP-Cond01 (b), 02 (c), 03 (d), 04 (e) and 05 (f)

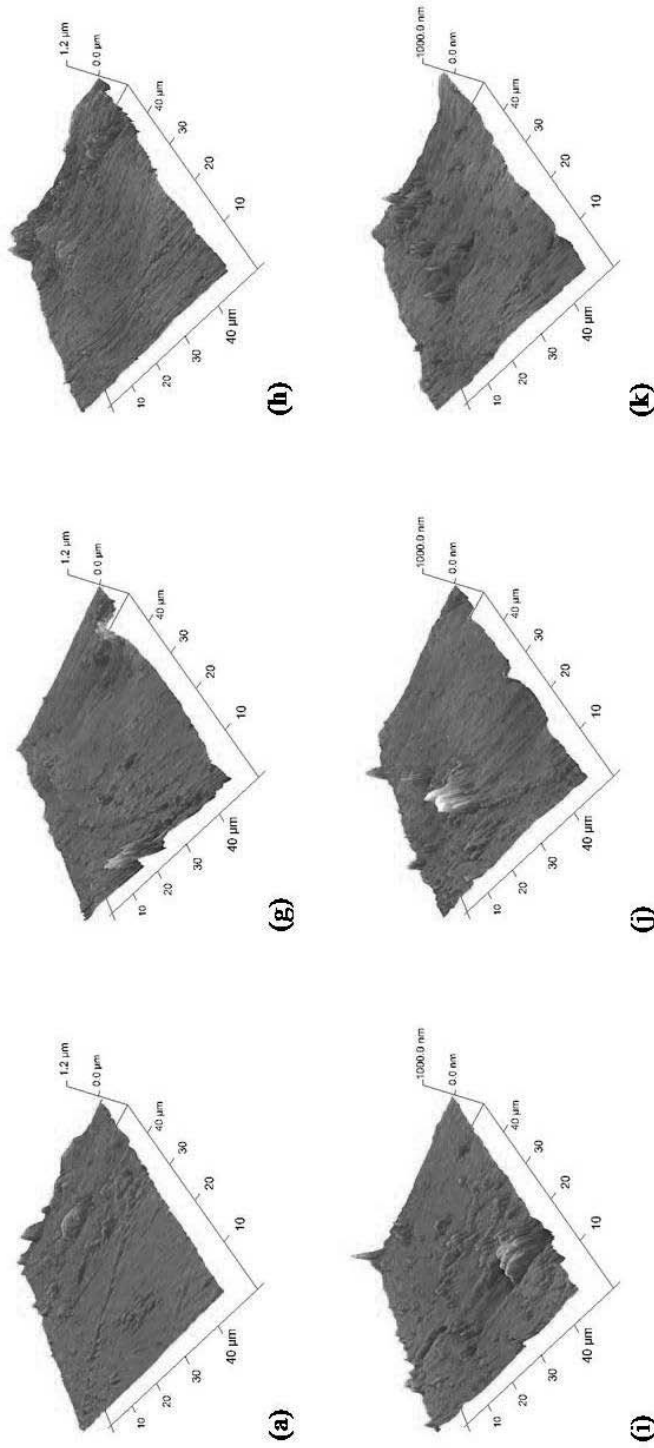


Figure 3-9. Influence of the WD which is one of the APP parameters 3D surface images taken by AFM (contact mode) on a $50 \times 50 \mu\text{m}^2$ of untreated surface (a) and APP-treated surface by APP-Cond06 (g), 07 (h), 08 (i), 09 (j) and 10 (k)

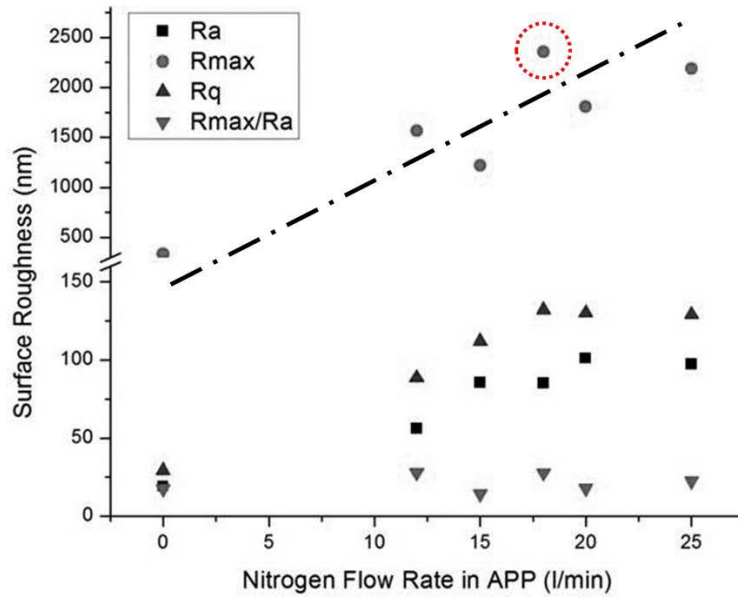


Figure 3-10. Influence of the flow rate of nitrogen gas which is one of the APP parameters on surface roughness

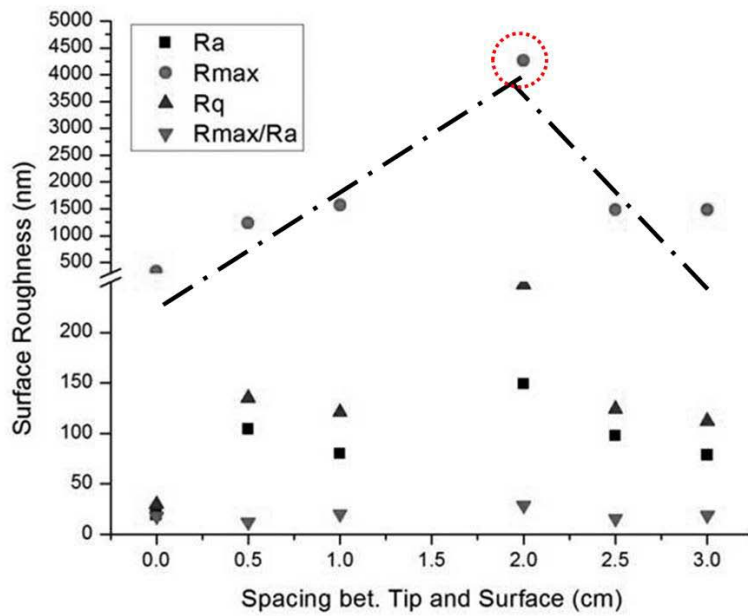


Figure 3-11. Influence of WD which is one of the APP parameters on surface roughness

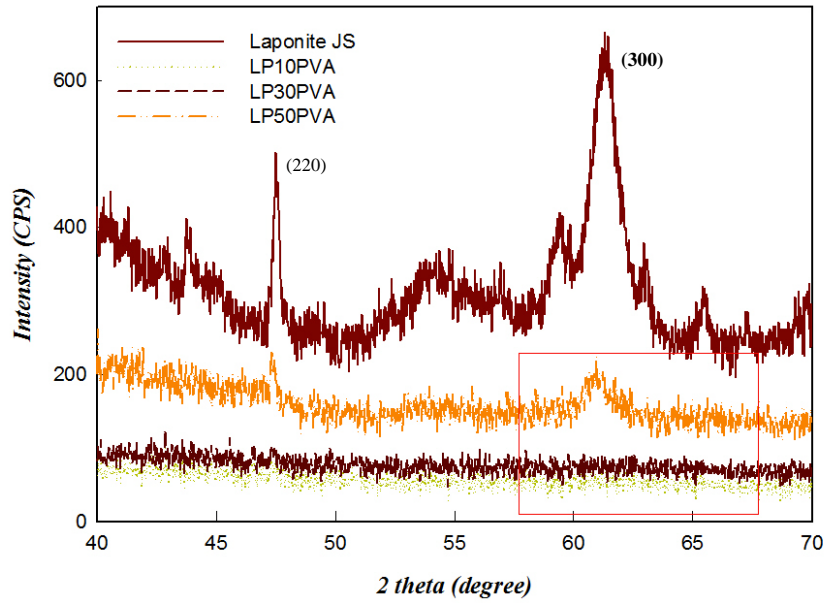


Figure 3-12. WAXRD patterns of the pure Laponite JS powder and several PCNs having exfoliated silicate layers in PVA matrix

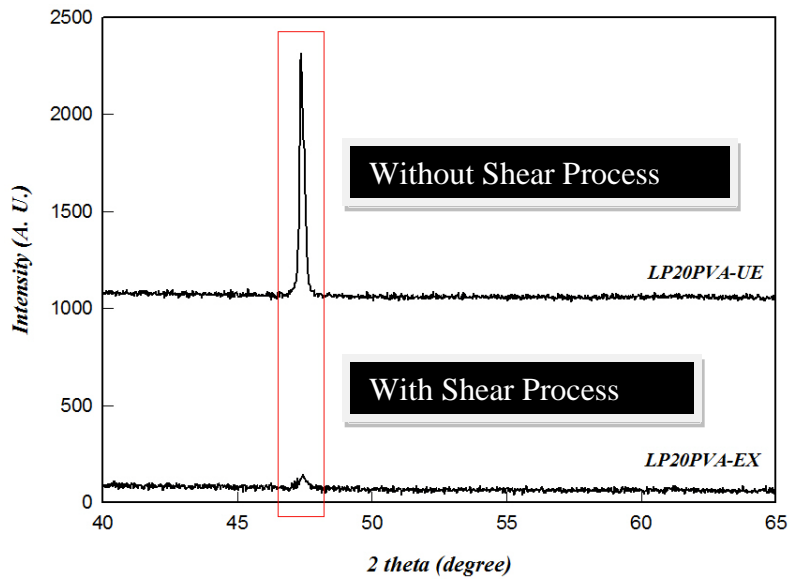


Figure 3-13. Difference in WAXRD patterns between LP20PVA PCN samples prepared with and without high shear process

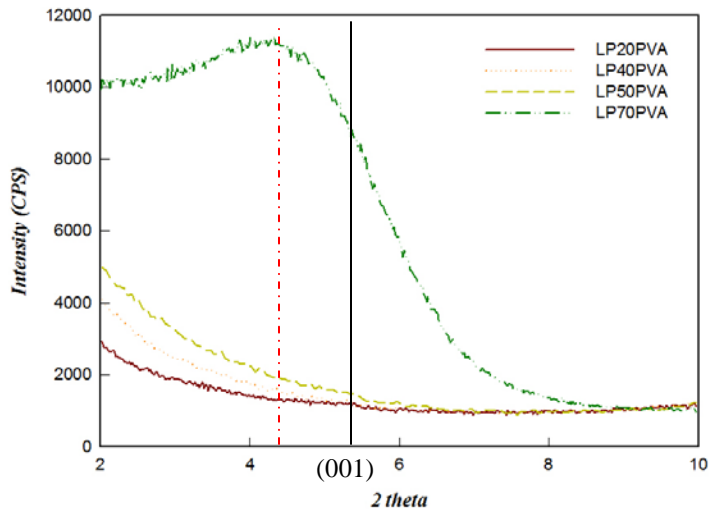


Figure 3-14. WAXRD patterns of several PCN-coated surface containing various amount of silicate particles obtained at low angle range from 2 to 10 degree

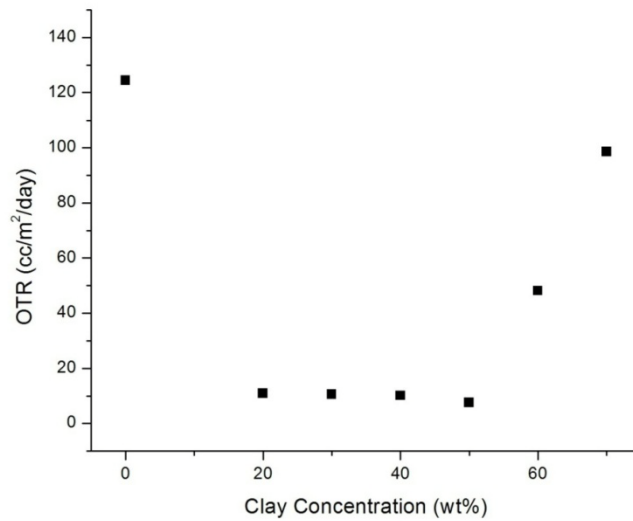


Figure 3-15. Dependence of the content of clay loaded in PCN on OTR values

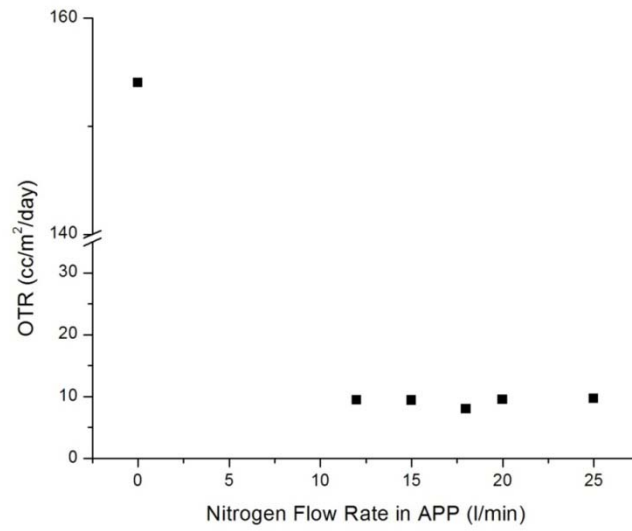


Figure 3-16. Effect of the flow rate of nitrogen gas on OTR values

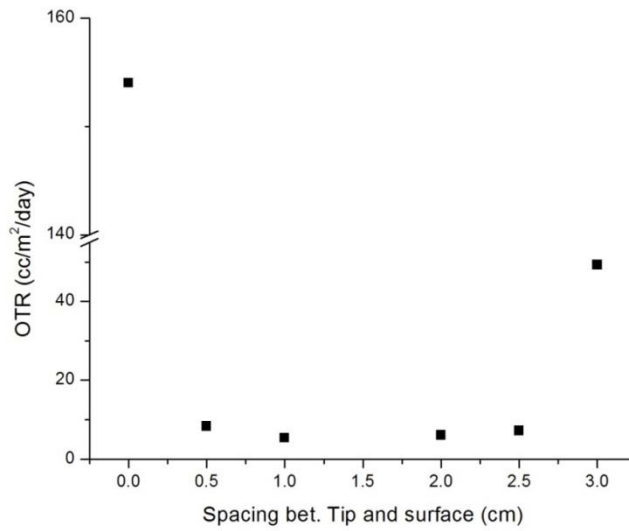


Figure 3-17. Effect of the working distance on OTR values

CHAPTER 4
EFFECT OF PH ON MICROSTRUCTURE OF LAYERED SILICATE AND BARRIER
PROPERTIES IN NANOCOMPOSITE COATING SYSTEMS

Introduction

Properties of polymer clay nanocomposite (PCN) materials can be enhanced by altering the characteristics of filler particles due to competitive interactions between attractive forces of polymer chains and silicate layers, and electrostatic forces between silicate layers. One of three microstructures of silicate platelets in a polymer matrix (phase-separated, intercalated, and exfoliated) usually dominates when a composite is formed. Each microstructure can be tailored by adjusting a variety of factors such as silicate particle types [7,42,45], volume fraction of particles [57,60,69], and the processing techniques used [45,46,56].

The aim of this study was to optimize barrier properties of PCN films by designing and engineering the microstructure of silicate particles. According to the detour models of permeability [31], parallel platelets are required to be perpendicular to the permeation direction to achieve superior barrier materials. However, in real nanocomposite systems, crystallization characteristics of the polymer [137,138], degree of dispersion / exfoliation [63,69,96] and orientation of clay particles [63,96,139] will hinder ideal barrier routes. To minimize these possible hindrance factors and extend attainable detour length in composite materials, a dense stratification of silicate platelets using a polymer as a binder material to be attached to the edges of platelets was devised.

The silicate particles used in this study was Laponite JS. The concentration of sodium ions over the whole surface range of the Laponite JS platelets in the intergallery regions was constant prior to addition of platelets into water. Initially, when clay platelets were added to the water, the clay powder formed the aggregated particle stacks. These stacks were separated and swollen by the hydration of sodium ions (Figure 4-1).

Hydrated sodium ions distributed in the intergallery are affected by two forces; electrostatic attraction with a negatively charged platelet surface and osmotic pressure caused by differences in chemical potential between intergallery phase and aqueous phase. The osmotic pressure applied to sodium ions at the edge of the crystal will be stronger than that at the center region. Furthermore, when two crystals approach, their mutual positive charges repel each other. Therefore, hydration of sodium ions and mutual repulsive forces open intergallery regions, lowering the osmotic pressure. As a result, sodium ions at platelet center are attracted more to the surface. Therefore this interaction resulted in concentration gradient of sodium ions over the surface of platelets proving that attractive forces of the platelet edge have been weakened and therefore displayed a relatively weaker positive characteristic due to lack of sodium ions (Figure 4-2 (a)).

To halt further diffusion of sodium ions and reach a stable equilibrium, addition of polar compounds is required. Addition of polar compounds results in a relatively weaker positive ions being attracted to the negative surfaces of adjacent particles forming a unique structure (Figure 4-2 (b) and (c)). As a result of a series of these successive interactions in the system, 'a house of cards' structure consisting of weak ionic bonds is formed. The microstructure of clay platelets formed by obtaining 'a house of cards' structure of dispersed clay platelets in a water-clay-polar compound system will collapse when water molecules evaporates with an orientation of clay platelets in [001] direction. Dense stratified arrangement of clay platelets maintaining this orientation and stronger ionic bonding among platelets may be required. To maintain this unique collapsed structure and fill microvoids, a polymer that attaches at specific locations as a filler and linker is required. Ogoshi and Chujo [140] proposed that optically transparent organic-inorganic polymer hybrids with anionic polymers could be prepared by controlling pH in an

aqueous solution. They also reported that the structure of the anionic polymer, poly(acrylic acid) (PAA), could be controlled by varying the pH due to the electric repulsion between polymer chains. Gudeman and Peppas [141] also found that the swelling ratio of poly(vinyl alcohol) (PVA)/PAA interpenetrating network can be adjusted by varying pH value in an aqueous solution.

In this study, PAA was used as a filler polymer. Anionic PAA can be prepared by placing PAA chains in a basic solution. As a result, PAA chains are extended by mutual electric repulsive forces between chains as the side chains are negatively charged (COO⁻). These PAA chains should be short enough to fill the microvoids. The driving force of PAA chains into microvoids is electric attraction (Figure 4-3(a)).

PAA chains are attracted to the center of the platelets as the positive ions at the edge are relatively weak and already bonded with adjacent crystals forming 'a house of cards' structure. Weak shear forces helped the short PAA chains diffuse into the structure and, with time, reorientation of clay platelets removes shear forces. The drying process and appropriate degree of external pressure leads to dense stratified clay structure filled with small amounts of PAA chains. Therefore, anionic PAA attaches two crystals by electrostatic force and the ideal barrier structure may be obtained by forming densely stratified structure (Figure 4-3 (b)). In this study, the microstructure of clay platelets for better barrier properties was devised based on the concept suggested by Ebina [65] and Tetsuka [66]. The effect of pH on the microstructure of clay particles and barrier properties of resulting composite-coated films as well as visual evidence revealed during experimental procedures have been explored using MOCON, scanning electron microscopy (SEM), transmission electron microscopy (TEM), fourier transform infrared (FTIR) spectroscopy, and x-ray diffractometer (XRD).

Experiments

Preparation of Polymer Clay Nanocomposite Solutions at Various pHs

'A house of cards' structure was identified by investigating the microstructure of clay aerogel. At first, a clay hydrogel was prepared from 15 wt% clay aqueous solution with ammonium chloride and sodium tetraborate as additives after aging for 24 hours. A clay hydrogel was frozen in 2L glass lyophilization shells at 173K (-100 °C) and a frozen clay hydrogel was sublimed using a labconco Freeze Dryer 8. Half-filled shells were rotated at 30rpm at a temperature of -80 °C until frozen and the ice from frozen shells was then evacuated for 36 hrs.

To prepare composite coating solution, first of all, low molecular weight PAA (Degree of Polymerization (DP) of 25) was dissolved in distilled water and the pH of the mixture was controlled using aqueous HCl (1 M) or NaOH (1 M) solution. PAA chains under three different conditions (acidic, basic and intermediate condition) were prepared to compare effects of pH on the filling void and stratifying clay platelets. An amount of Laponite JS based on weight ratio of clay to PAA in the final dried film was added into deionized water gradually to prevent aggregation. Samples were premixed for 1-2 minutes with a magnetic stirrer. Polar compound, ammonium chloride (NH₄Cl) buffer solution, at 1 wt% (according to the amount of clay used) was added to solution to maintain 'a house of card' structure by lowering osmotic pressure in the intergallery. Prepared PAA stock solution was added into the clay mixture and mixed gently for 1 hour with a magnetic stirrer. A prepared mixture of water, clay, polar compound, and PAA was degassed in vacuum to minimize structural defects by removing remaining flocculated or aggregated clay impurities. Specific conditions for preparation of nanocomposite solutions are listed in Table 4-1. A schematic of experimental steps is represented in Figure 4-4.

Coating Samples After Atmospheric Pressure Plasma Treatment

The optimum conditions for atmospheric pressure plasma (APP) treatment were chosen based on the previous results [55]. These conditions were 18 *l/min* of nitrogen gas flow rate, 20 mm of working distance, and 4 treatment times. Composite solutions were coated on isotactic (i-) polypropylene (PP) film after APP treatment to enhance adhesion. Surfaces of rigid PP were spin coated with 20g coating solution at fixed spin-coating parameters involving a two-step process. First step was 500 rpm for 1.5 min. Second step was 700 rpm for 30s. The spin coater was a Model Laurell WS-400B-6NPP/LITE (Laurell Technologies Co., North Wales, PA). Samples were dried at ambient temperature in a vacuum desiccator.

Characterizations and Analysis

Chain conformations of anionic PAA in composite material were identified by Diffuse Reflectance Infrared Fourier Transform (DRIFT) Spectroscopy (Thermo Electron Magna 760, Thermo Scientific Inc., MA). The structure of the clay film was characterized by WAXRD (Philips XRD APD 3720 powder diffractometer, Philips Electronics, Mahwah, NJ). The change in spacing was measured using an X-ray diffractometer with a Cu anode (CuK α radiation $\lambda = 1.54056 \text{ \AA}$) with a wide range scanning angle. Clay and clay composite powder were mounted on a sample holder with a large cavity; a smooth surface was obtained by pressing particles with a glass plate. A clay composite sample prepared by rod coating on a silicon wafer was compared with the composite powder to investigate effects of coating shear direction on orientation of clay platelets. X-ray diffraction patterns were obtained at the small angle range from 2° to 10° to investigate effects of polymer loadings on microstructures of clay platelets using WAXRD (Philips MRD X'Pert System, Philips Electronics, Mahwah, NJ) with a rotation anode and CuK α radiation. PCN-coated PP specimens were able to be used directly without a sample holder.

In order to analyze the morphological characteristics of clay aerogel and surfaces of composite films, those samples were sputter coated with gold-palladium alloy (Au-Pd) and observed using SEM (JSM-6400, Jeol Ltd., Tokyo, Japan). TEM (TEM-200CX, Jeol Ltd., Tokyo, Japan) micrographs of clay film showed microstructure of clay platelets. TEM was operated at an accelerating voltage of 200 kV. The dispersion liquid was dropped directly on a copper grid supported with a collodion membrane. Oxygen transmission rate (OTR) values of coated specimens were measured in accordance with the procedure described in ASTM D-3985 using a Model OX-TRAN 2/20MH (Mocon Corporation, Minneapolis, MN) to investigate barrier properties.

Results and Discussion

A House of Cards Structure

'A house of cards' structure of Laponite JS clay powder in the aqueous solution was identified by investigation of the microstructure of clay aerogel. Figure 4-5 shows the changes in morphology from the clay powder to clay aerogel. As shown in SEM micrographs (Figure 4-5 (a) and (b)), the structure of nanoclay powder as received was a randomly stacked aggregate while the clay aerogel (Figure 4-5 (c) and (d)) showed regular microchannels in the range of 5 – 20 μm in the bulk. This structure is representation of a house of cards formation mechanism (Figure 4-2 and 4-3). Morphological features and formation of house of cards structure have been reported by several researchers [62,89,95,142]. Corresponding TEM micrographs are shown in Figure 4-6. Aggregated platelets are clumping together because of the van der Waals attraction in dry condition showing a large dark spot containing several dark lines which represent edge-standing platelets. However, clay platelets were arranged with three features tilted, edge-standing, and paralleled platelets to the surface through the formation of house of cards structure as illustrated schematically in Figure 4-6 (c). These three orientations result in confined

spaces for short PAA chains that are negatively charged to be diffused into microvoids by ionic attraction toward the center of the surface of platelets rather than platelet edges.

Effects of pH on the Clay Platelet Microstructure

It has already been reported that PAA changes depending on pH in an aqueous solution [141]. PAA chains under basic condition can be expanded by electric repulsive force according to the dissociation of ionic groups. Therefore, it was necessary to estimate the range of molecular weights of PAA to obtain a best fit on microvoids, which clay microstructure produces. It was assumed that PAA chains are fully extended under basic condition due to electric repulsion among adjacent carboxylate anions, end-to-end distance $\langle R \rangle$ ($\langle R \rangle = nl$, where n is the number of repeat unit and l is the bond length) can be used to estimate an approximate molecular weight of PAA that can diffuse into the space of the densely stratified structure of clay platelets resulting from the collapse of the house of cards structure. Average surface diameter of Laponite JS is 55 nm and bond length of C-C is 0.15 nm and therefore 'n' should be in the range of 1 and 336, which means that low molecular weight or oligomer of PAA is required.

The chain conformations of anionic PAA in composite material were identified by DRIFT Spectroscopy as shown in Figure 4-7. The peaks at 1550 cm^{-1} and 1710 cm^{-1} are for C=O stretching vibration of the carboxylate anion ($-\text{COO}^-$) and carboxylic acid group ($-\text{COOH}$), respectively. In the case of PAA under basic condition, relatively higher peak at 1550 cm^{-1} were detected, while the much higher peak at 1710 cm^{-1} for PAA under acidic condition were observed. Under acidic condition, short PAA chains will be entangled together rather than extended showing a critical concentration which will not allow PAA chains to diffuse into the clay platelets and this was confirmed by experimental evidence. Aggregated white small particles were dispersed in a composite gel as shown in Figure 4-8 in the case of the samples prepared under acidic and isoelectric point (IEP) conditions of PAA after 3 weeks storage.

These particles can be formed by two possible reactions. The first potential reaction is salt extraction caused by the sodium cations that diffuse from the intergallery region and dissociated chlorine anions from added ammonium chloride added. Second reaction can be a phase separation of entangled PAA chains due to the higher intra- and intermolecular hydrogen bonding in acidic conditions. To examine which reaction occurred in the system at various pH levels, SEM samples were prepared by drying the gel-like sample on a glass slide at 70 °C for 1 day. The white particles were mounted on the SEM sample holder using a sharp tweezers. Some small residual dried clay particles were shown adjacent to these larger particles and there are some coated layers along the surface of these particles (Figure 4-9). Particles sizes in acidic condition were larger than ones in Isoelectric Point (IEP) condition because there were more favorable interactions between PAA chains at lower pH resulting in larger sizes of particles of 400 – 600 μm . Energy dispersive X-ray spectroscopy (EDS) result (Table 4-2 and Figure 4-9) showed that the white particle portion had greater amounts of C and O and relatively small amounts of Si atoms. Other spots on broken dried clay gel particles and coating layer showed higher intensity of Si and relatively weaker peaks of C and O. Therefore, phase-separated PAA particles are aggregated and dispersed in a clay gel. There were no particles in basic conditions of PAA after 6 weeks storage, which proves that diffusion of short PAA chains to the surface of clay platelets had occurred. Therefore, particles formed as a result of the phase separation of entangled PAA chains caused by effects of pH.

To investigate the specific differences in interspacing of particles among samples depending on pH and the relative amount of PAA in the composite system, three plots were obtained from WAXRD results as presented in Figure 4-10. These results confirmed the possibility of aggregated PAA particles observed during experiments. All samples showed a

similar increase in d-spacing regardless of the amount of PAA used. Red lines represent positions of peaks for pure Laponite JS powder [143]. As shown in Figure 4-10 (a), the interplanar distances for (110) and (300) planes, corresponding to peak positions of 36.5 and 62 degrees, respectively, showed some increases for all pH conditions, while the characteristic peak for Laponite JS at 47.6 degree showed much larger increase under basic conditions. Under acidic conditions, no peak for (005) plane at 27.5 degree was found. Among these three samples, having the lowest PAA contents, the largest overall increase in interplanar distances at pH 6 for all planes was observed.

The peaks for (005) plane decreased as the amount of PAA increased as presented in Figure 4-10 (b) and (c). More PAA content resulted in disappearance of regularity of particle orientation by the insertion of PAA into the intergallery region. In the case of acidic conditions of (b), there was a significant increase for (100) plane from 20.4 to 16.3 degrees, which means the distance increased from 4.35 Å to 5.44 Å according to the Bragg's law. This may be explained by the fact that entangled short PAA chains inserted into platelets and enlarged the spacing. pH 4 and 7 showed similar increases in interplanar distance of most planes. Less than critical amount of PAA has no effect on interplanar distances and subsequent microstructure of clay platelets. There was no change for (100) under acidic and IEP conditions when more PAA content were used (Figure 4-10 (c)) because more PAA increases possibility of forming phase-separated PAA chains resulting in aggregates that are too large to be inserted between platelets. Under basic condition, the similar tendency for increase of each interplanar spacing is shown for all PAA content except for (005) and (110) planes. To investigate changes in position of (001) peaks depending on the amount of PAA at basic condition, X-ray diffraction was obtained at lower angle ranges from 2 to 10 degrees (Figure 4-11). As shown in this figure, the peak

observed in C5PA91BS disappeared at C5PA73BS and reappeared at C5PA55BS. This might be explained by a larger amount of oriented clay platelets in [001] direction resulting in a peak for C5PA91BS that contains more clay. However, this peak disappeared as the amount of polymer increased showing similar characteristic peaks with exfoliated samples (C5PA73BS curve of Figure 4-11). Finally this peak was shifted to a lower degree due to some diffusion of PAA chains into intergallery. Because of the relatively small aspect ratio compared to natural montmorillonite (MMT) or other clay types, it would be easier for the structure of Laponite JS to collapse by diffusion of polymer. Therefore, randomly collapsed structure of C5PA55BS could result in microvoids and subsequently showing poor barrier properties.

Figure 4-12 shows TEM micrographs of samples prepared under basic condition (a) and acidic conditions (b) of PAA. Figure 4-9 (a) shows that there was no apparent feature of edge-standing clay platelets or tactoids under basic conditions of PAA, while several black lines in (b) represent edge-standing clay tactoids were separated from entangled PAA chains. Effects of shear direction on orientation of clay platelets for coating processes were shown in Figure 4-13. Overall intensities of C5PA91BS_c (coated layer by a coating rod) were much lower than those of C5PA91BS_p (clay composite powder) and all peaks except for (005) plane disappeared. This suggests that clay platelets were oriented in the direction that was parallel to the shear direction as illustrated in Figure 4-13, which conforms to the relation of shear direction with relative orientation of clay platelets reported [39,60,95]. This shows that the coating processes with inherent shear direction such as rod coating, doctor blade, or calendaring promise orientation of filler particles in the composite system resulting in better barrier properties.

Barrier Properties

Barrier properties of prepared composite solutions with PAAs of different pH values were investigated by measuring OTR of prepared films from each solution. From our previous work

[55], it was reported that significant increases in OTR were observed for loadings in excess of 50 wt%. This is due to high degrees of reaggregation of clay as well as lower degrees of exfoliation caused by steric interference. The amount of clay in this composite system is over 50 wt% and, according to our previous results, significant decrease in barrier properties should be observed regardless of pH of polymer used. However, C5PA91BS, which contains 90 wt% of clay in the system showed good barrier properties of 9 - 10 cc/m²/day, which is similar with OTR of composite solution coated specimens having lower clay content with good exfoliation. This lower OTR value could be approached by densely stratified structures as shown in Figure 4-14. The difference in microstructure of clay platelet resulted in different barrier properties at the same amount of clay.

Figure 4-15 shows SEM micrographs of composite-coated i-PP surfaces. Figure 4-15 (a) and (b) shows small cracks in the coating surface and this lowered barrier properties of specimen dramatically by allowing gas molecules to contact to the substrate directly. The more PAA in the composite solution such as C5PA73 and C5PA55 added, the more cracks on the surface were observed, with associated high OTR values over 100 cc/m²/day. Lower pH also has significant effects on barrier properties. The poor interactions between negatively charged PAA under lower pH and clay platelets squeezed polymer out from the microvoids and microchannel and resulted in many cracks on the coated surface (Figure 4-15 (c) and (d)). Figure 4-16 illustrates OTR results depending on pH, which confirm morphological features of the surfaces of coated layers.

Table 4-1. Specific conditions for the preparation of each specimen

#.	Sample name	Clay (wt%)	PAA	
			pH	Ratio (by weight)
1	C5PA91AS	5	2	9:1
2	C5PA91IS	5	4	9:1
3	C5PA91BS	5	6	9:1
4	C5PA73AS	5	2	7:3
5	C5PA73IS	5	4	7:3
6	C5PA73BS	5	6	7:3
7	C5PA55AS	5	2	5:5
8	C5PA55IS	5	4	5:5
9	C5PA55BS	5	6	5:5

Table 4-2. EDS results for white unknown particles dispersed in clay composite solutions

Element	Spot 1		Spot 1-2		Spot 2		Spot 3	
	Elmt %	Atom %	Elmt %	Atom %	Elmt %	Atom %	Elmt %	Atom %
C K	15.08	21.97	25.06	35.64	26.24	41.95	4.46*	8.38*
O K	47.75	52.23	36.26	38.71	11.00	13.20	12.64	17.83
Na K	2.64	2.01	1.50*	1.11*	3.57	2.98	29.81	29.25
Mg K	23.61	16.99	20.55	14.43	13.22	10.44	15.19	14.10
Si K	10.92	6.80	16.62	10.11	45.97	31.42	37.90	30.44
Total	100.00	100.00	100.00	100.00	100.00	100.00	100.00	100.00

* = <2 Sigma

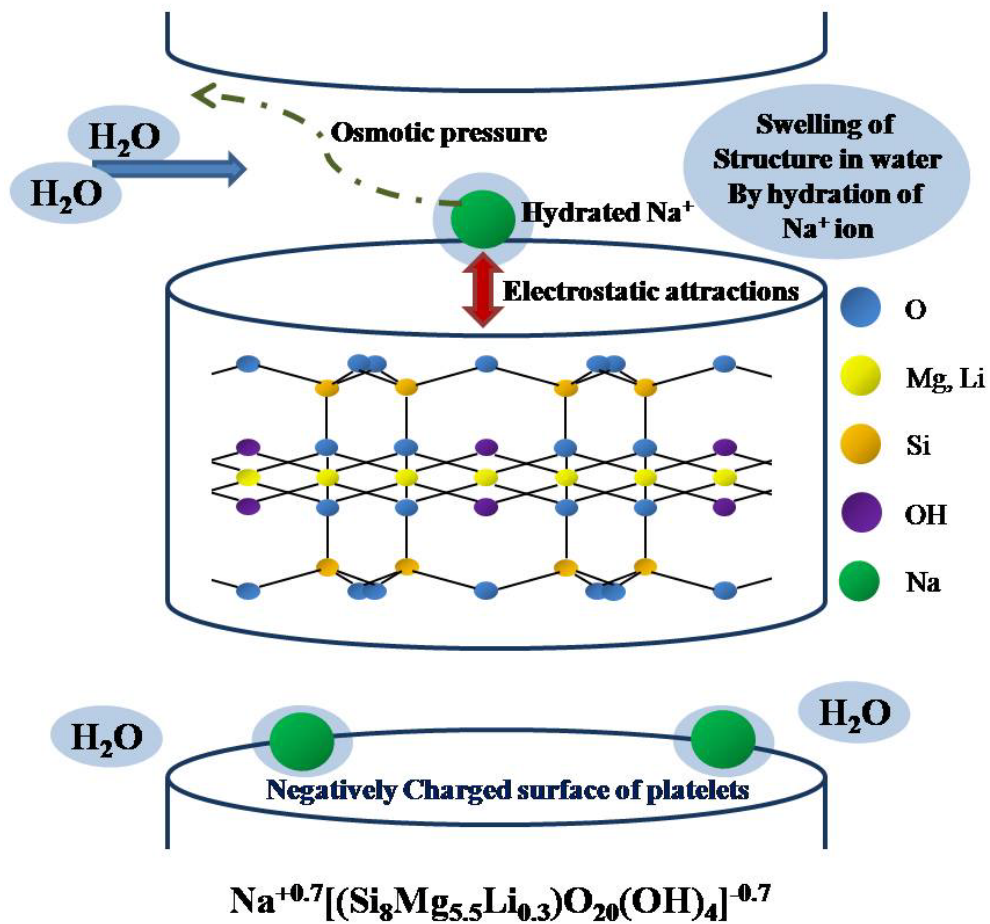
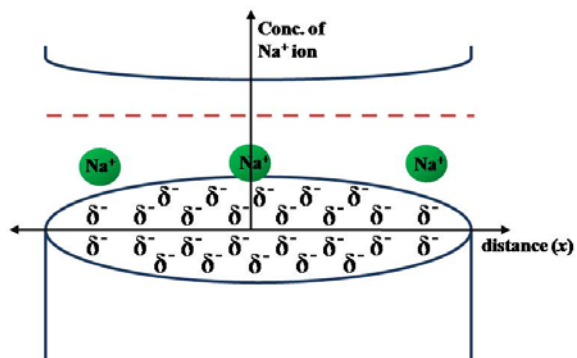
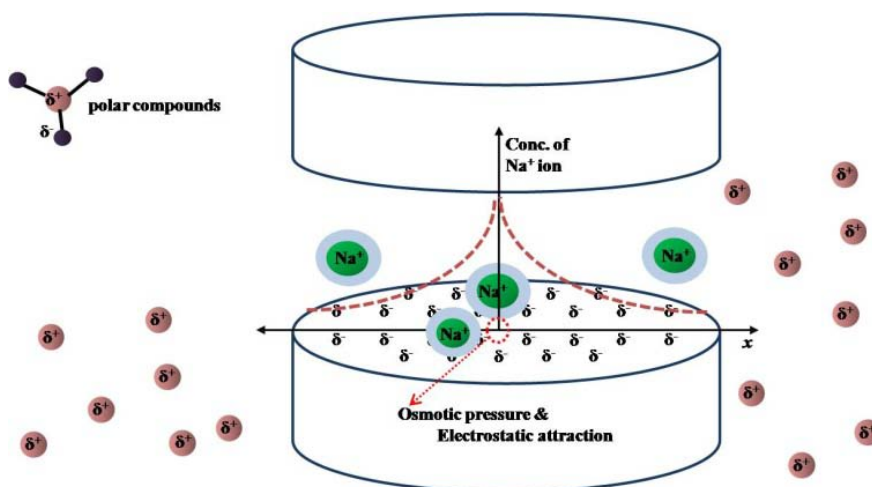


Figure 4-1. Structure of silicate layers, Laponite JS when dispersed in water phase

(a)



(b)



(c)

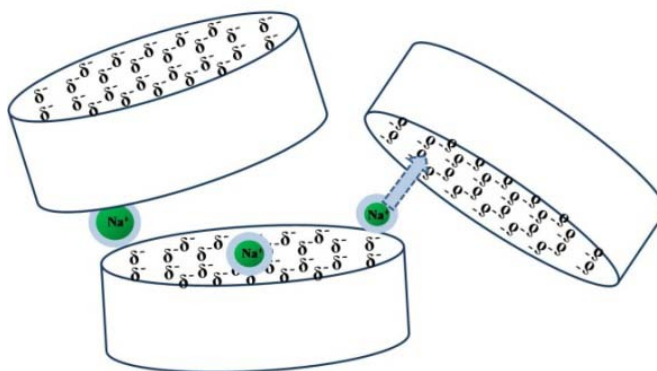


Figure 4-2. Schematic mechanism of ‘a house of cards’ structure (a) initial stage as a powder state, (b) the formation of concentration gradient of sodium ions in the intergallery regions and the addition of polar compounds and (c) the formation of ‘a house of cards’ structure

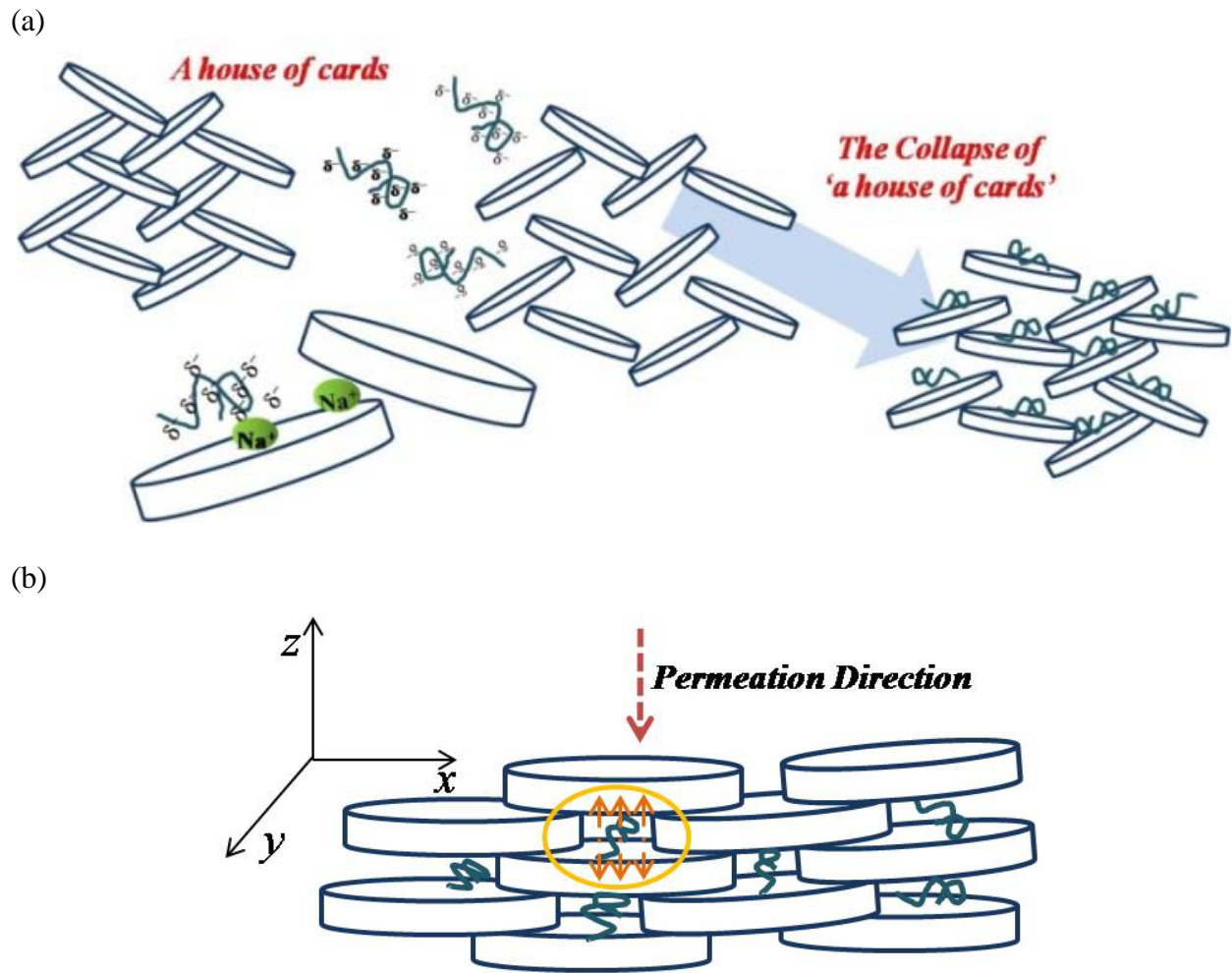


Figure 4-3. (a) Schematic mechanism of ‘a house of cards’ structure through the diffusion of LMW anionic PAA chains into a clay structure and (b) expected ideal barrier structure

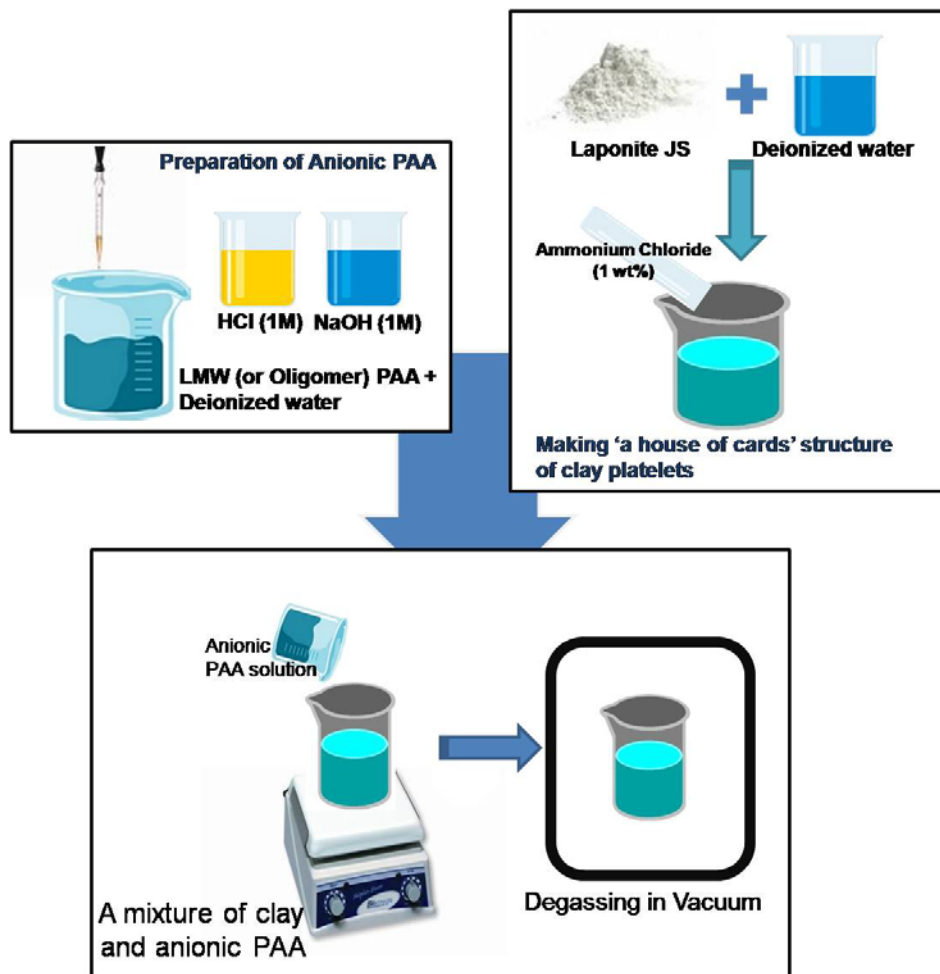


Figure 4-4. Schematically illustrated experiment procedures

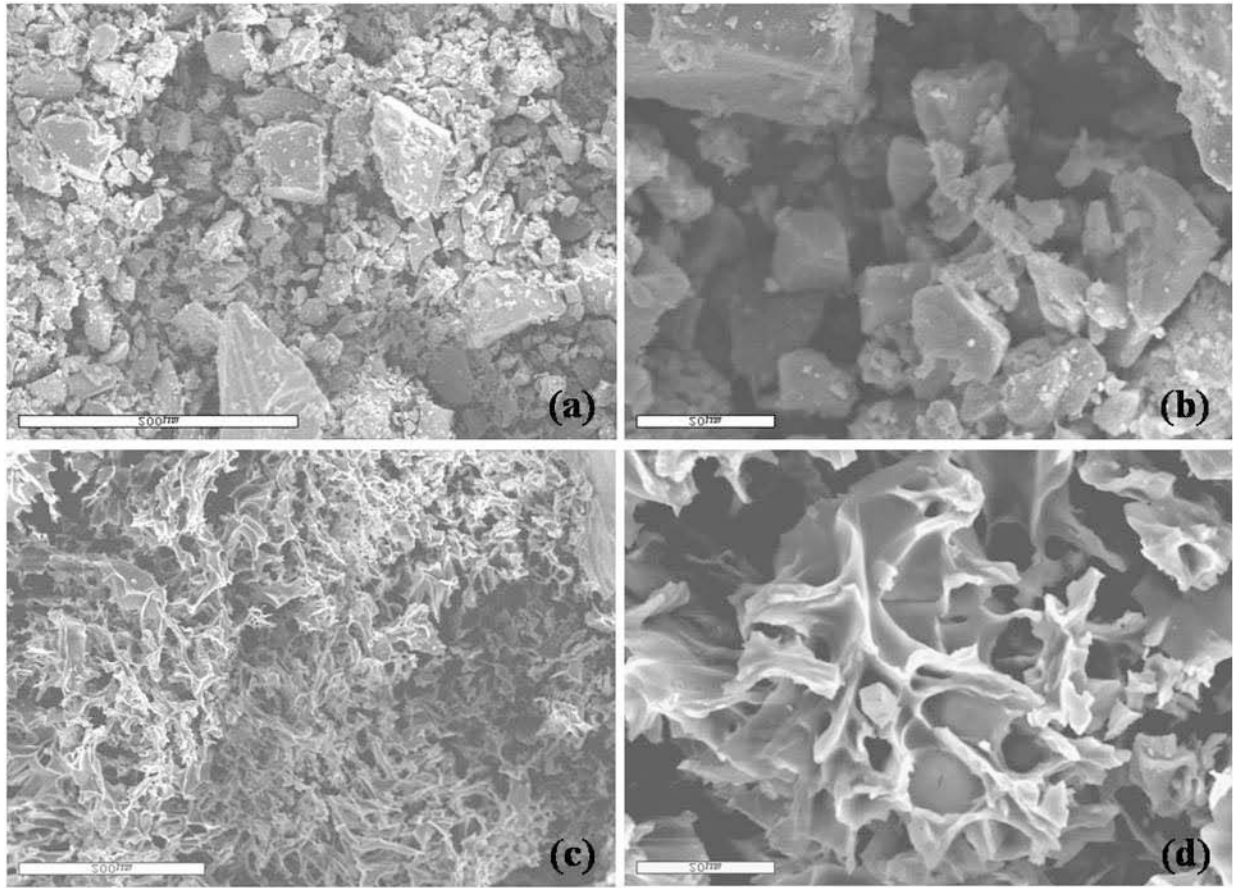


Figure 4-5. SEM micrographs of (a, b) Laponite JS clay powder and (c, d) corresponding clay aerogel

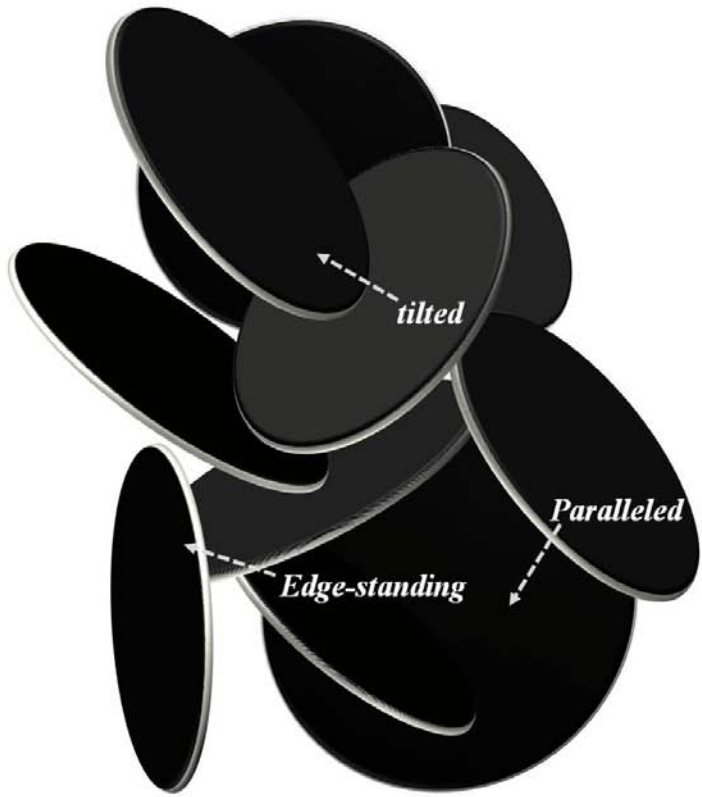
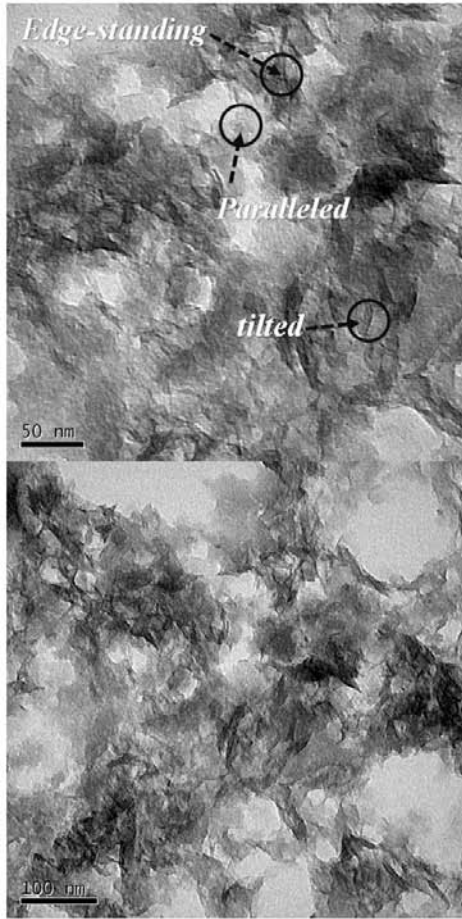


Figure 4-6. TEM micrographs of clay aerogel consisting of three structural features, edge-standing, tilted and paralleled as indicated as arrows

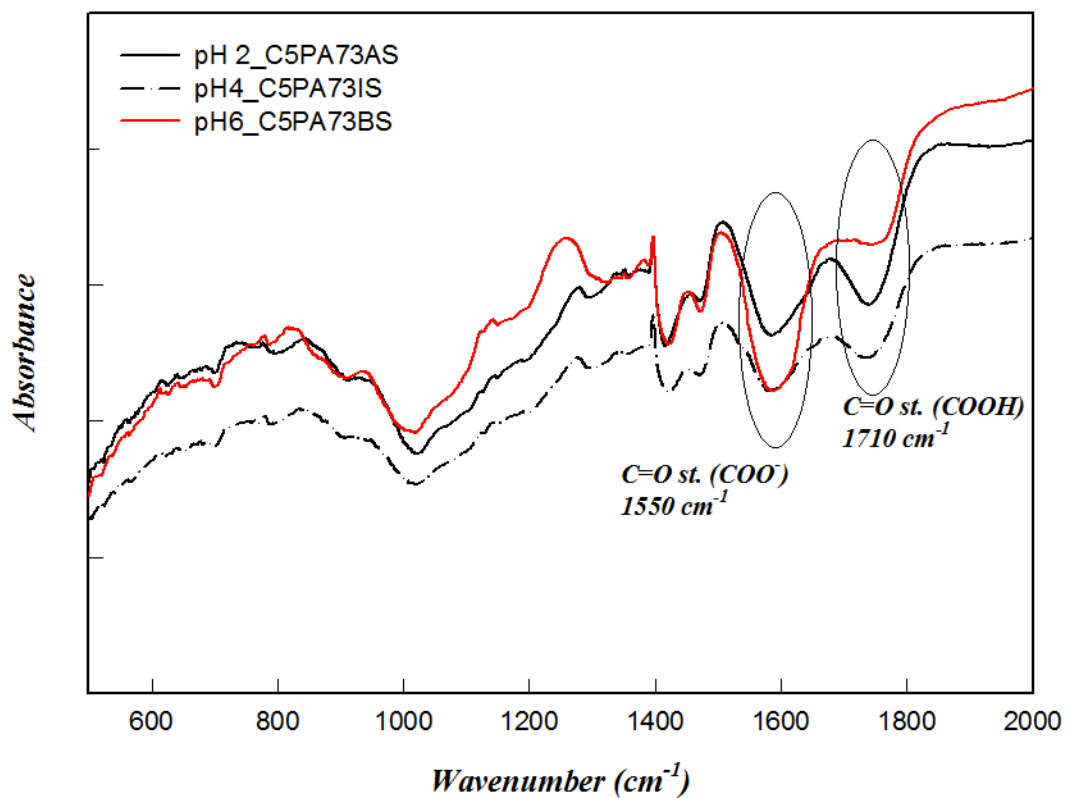


Figure 4-7. DRIFT results of composite samples of C5PA73 prepared at pH 2, 4, and 6

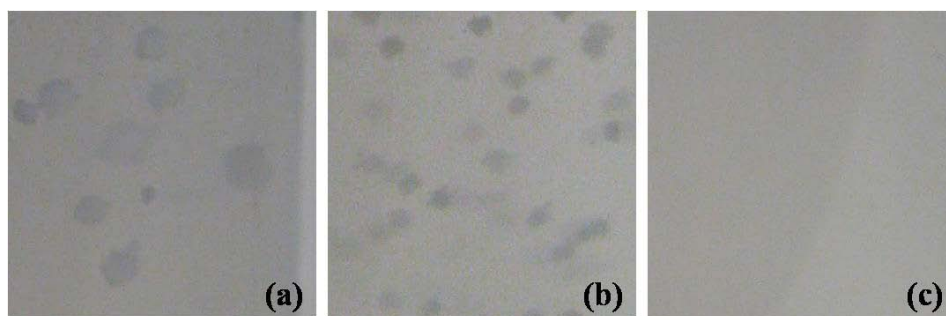


Figure 4-8. Photographs of the states of composite solutions prepared under different pH conditions; (a) pH 2 (b) pH 4, and (c) pH 6 after 3 weeks storage

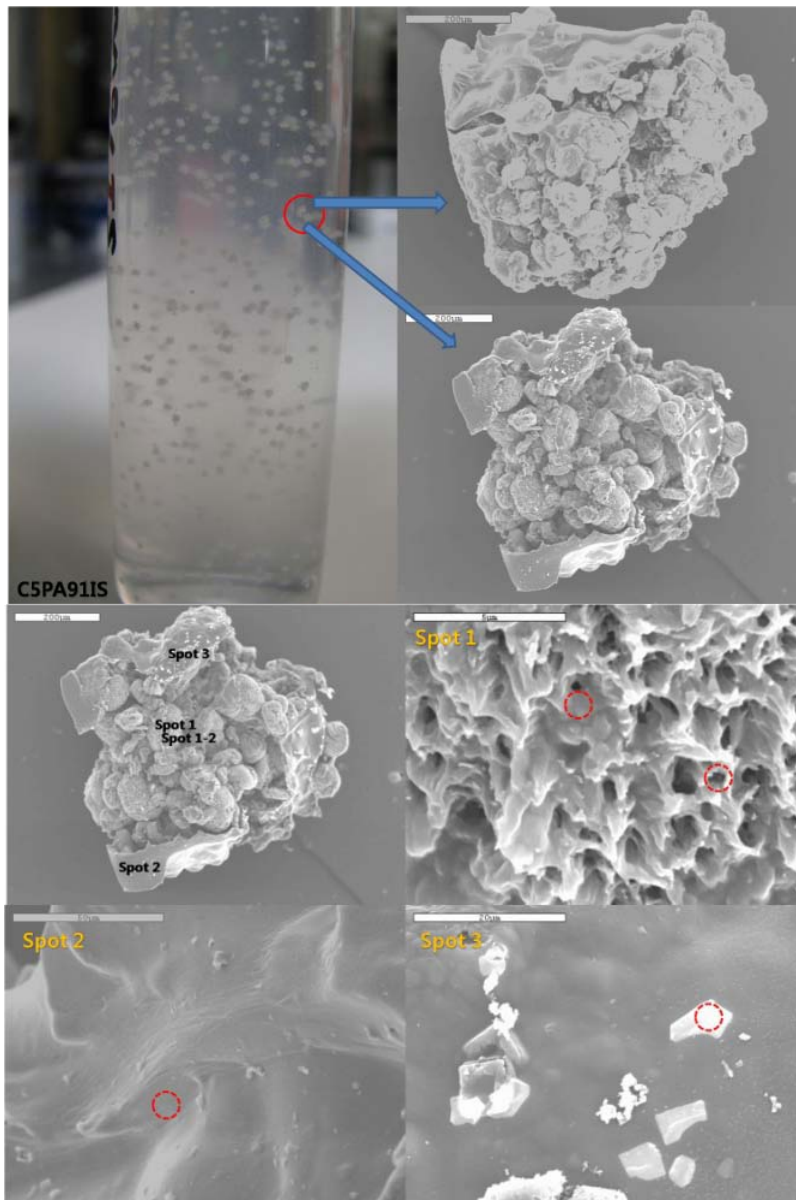


Figure 4-9. Picture of C5PA91IS solution after 2 weeks storage and SEM micrographs of its by-product, white particles dispersed in the solution

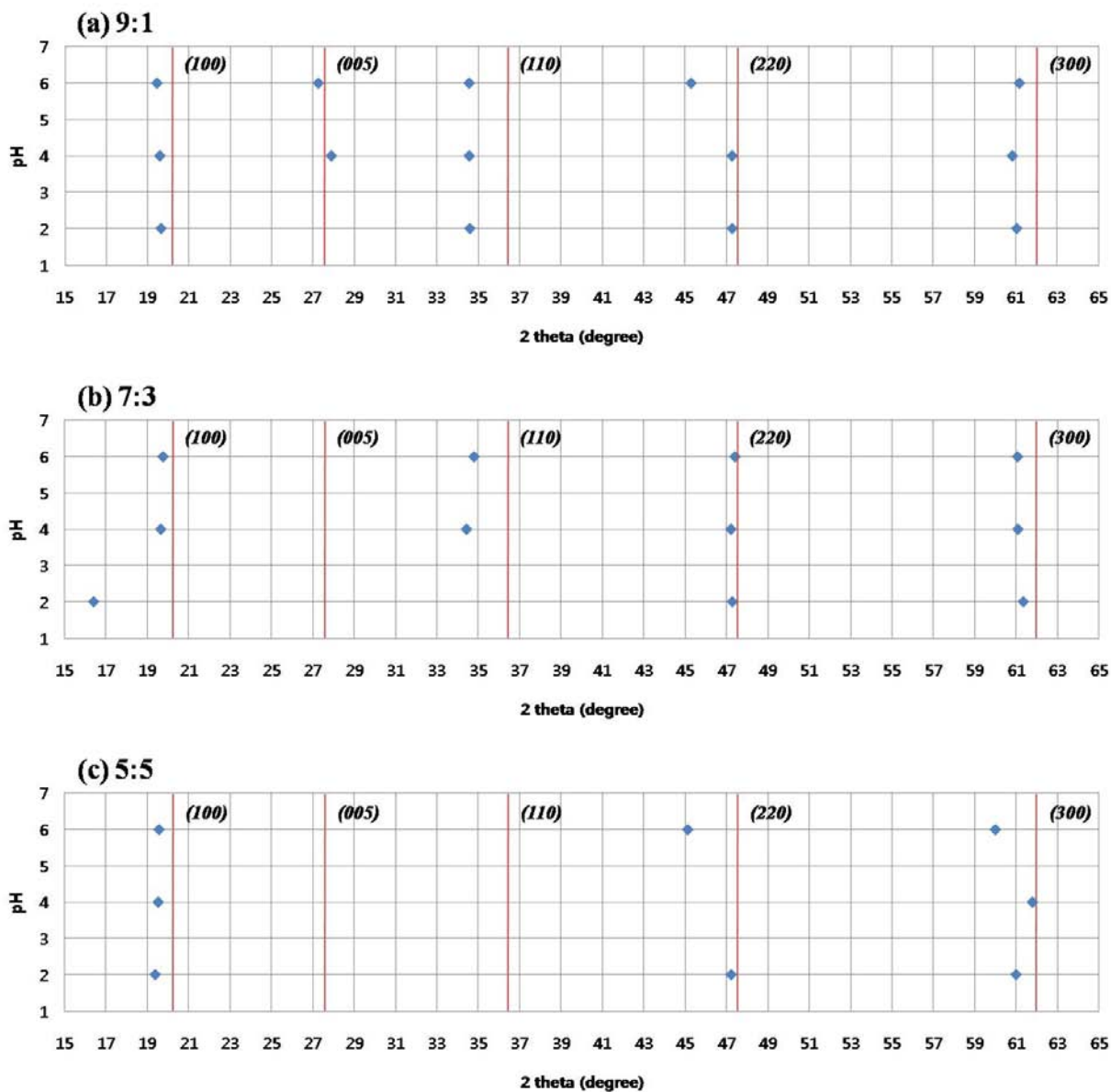


Figure 4-10. Effects of the pH on the peak positions of XRD results depending on PAA contents. The positions of peaks for pure Laponite JS powder were indicated

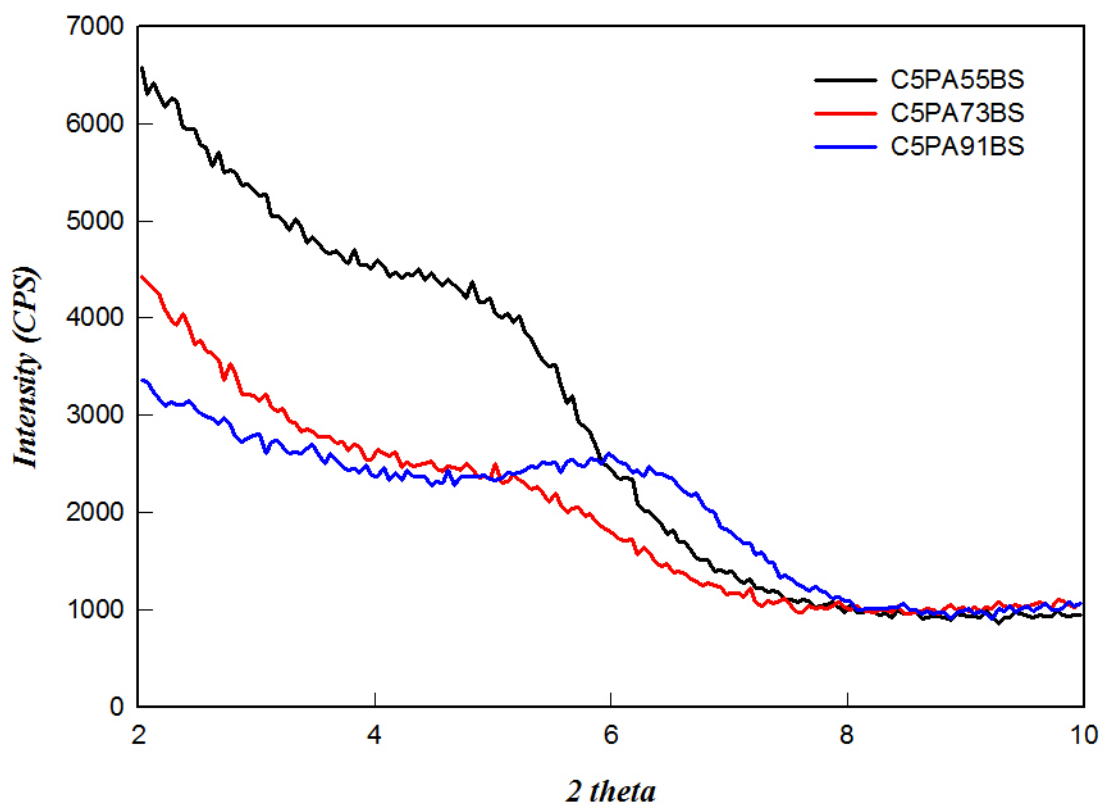


Figure 4-11. Effects of the amount of PAA on the changes in basal spacing ((001) peak position) of PCN samples prepared at basic condition

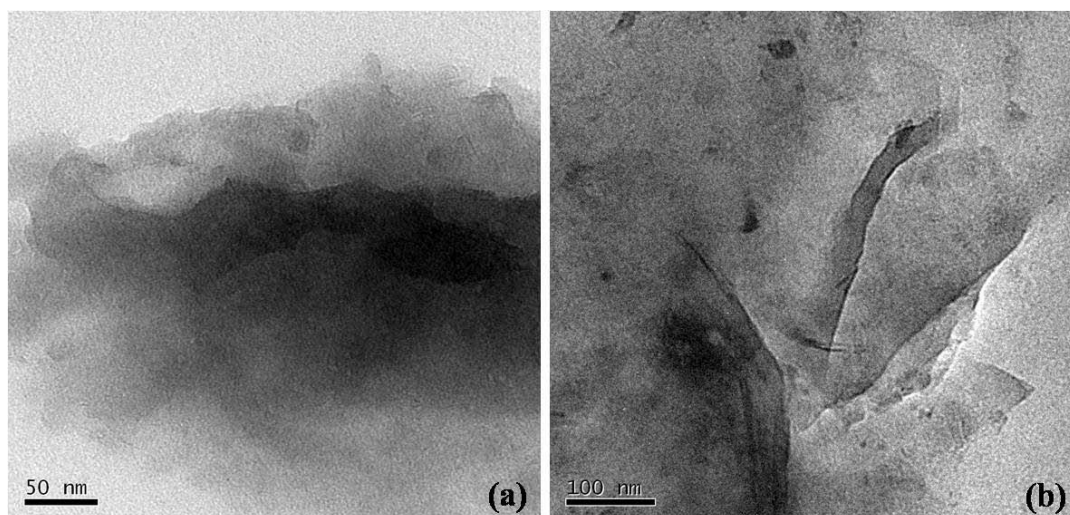


Figure 4-12. TEM micrographs of C5PA73BS (a) and C5PA73AS (b)

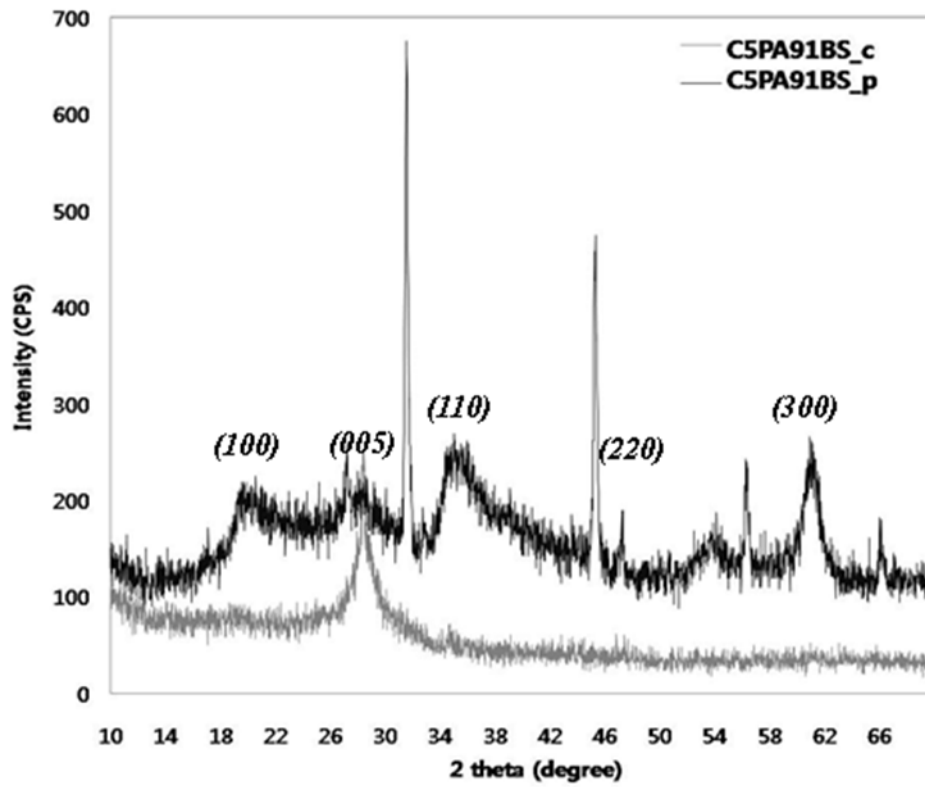


Figure 4-13. XRD results of clay composite powder (C5PA91BS_p) and corresponding coated layer by a coating rod (C5PA91BS_c)

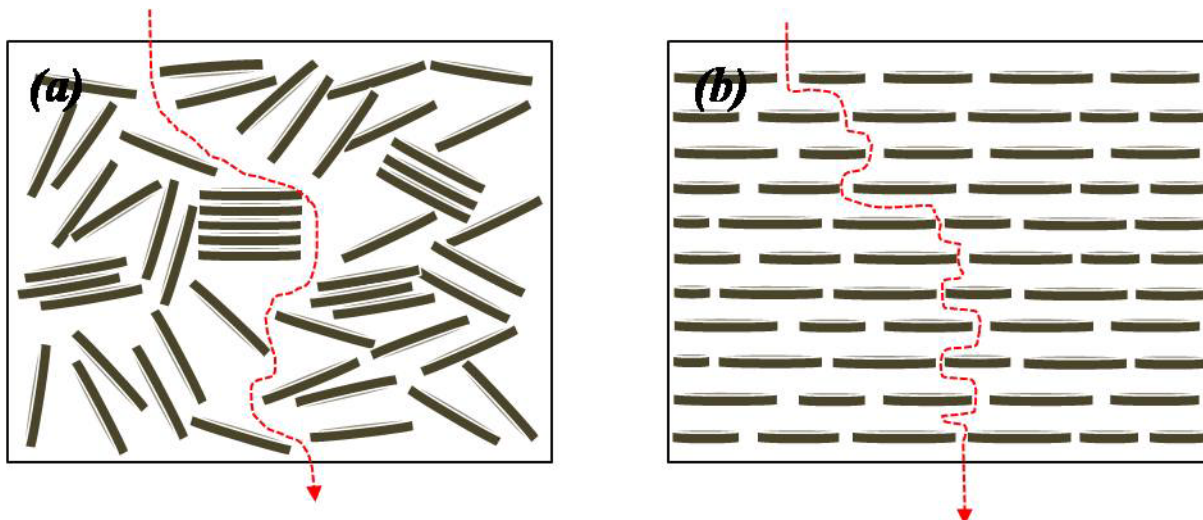


Figure 4-14. Effect of clay platelet microstructure on barrier properties when the same amount of clay was arranged (a) as a randomly dispersed state and (b) as a stratified state. Red dot lines show the diffusion path of oxygen gas molecules through the PCN material

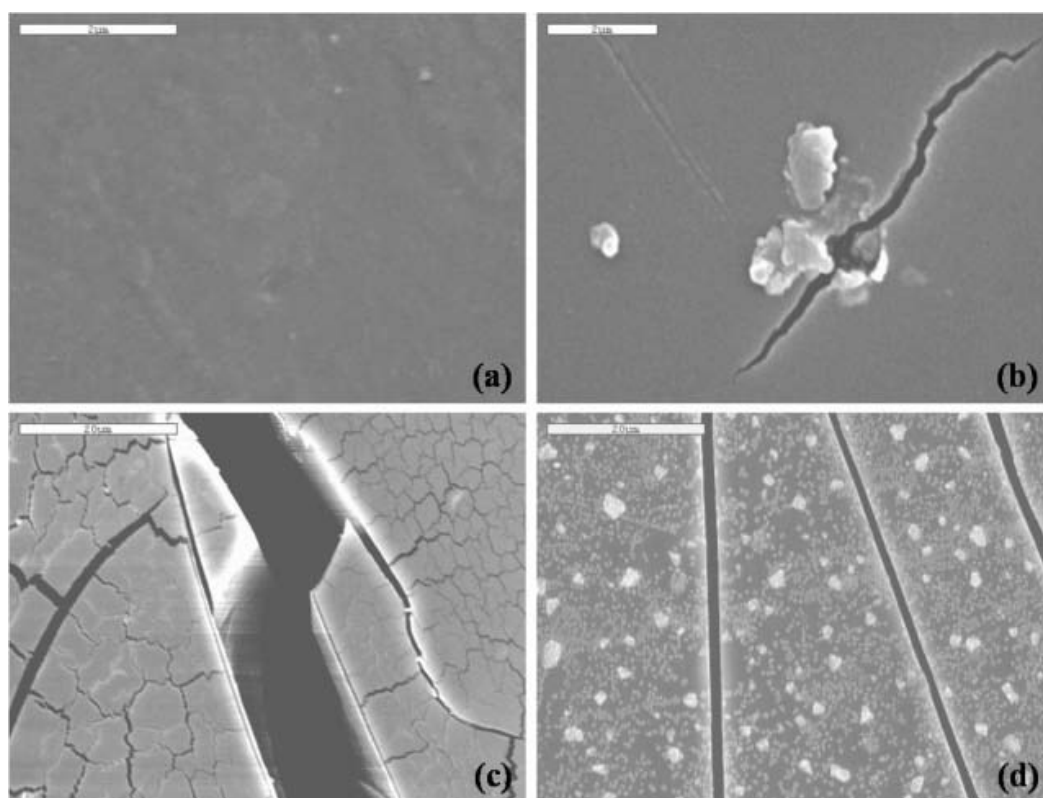


Figure 4-15. SEM micrographs of nanocomposite-coated surfaces (a), (b) C5PA91BS (c) C5PA91IS (d) C5PA91AS

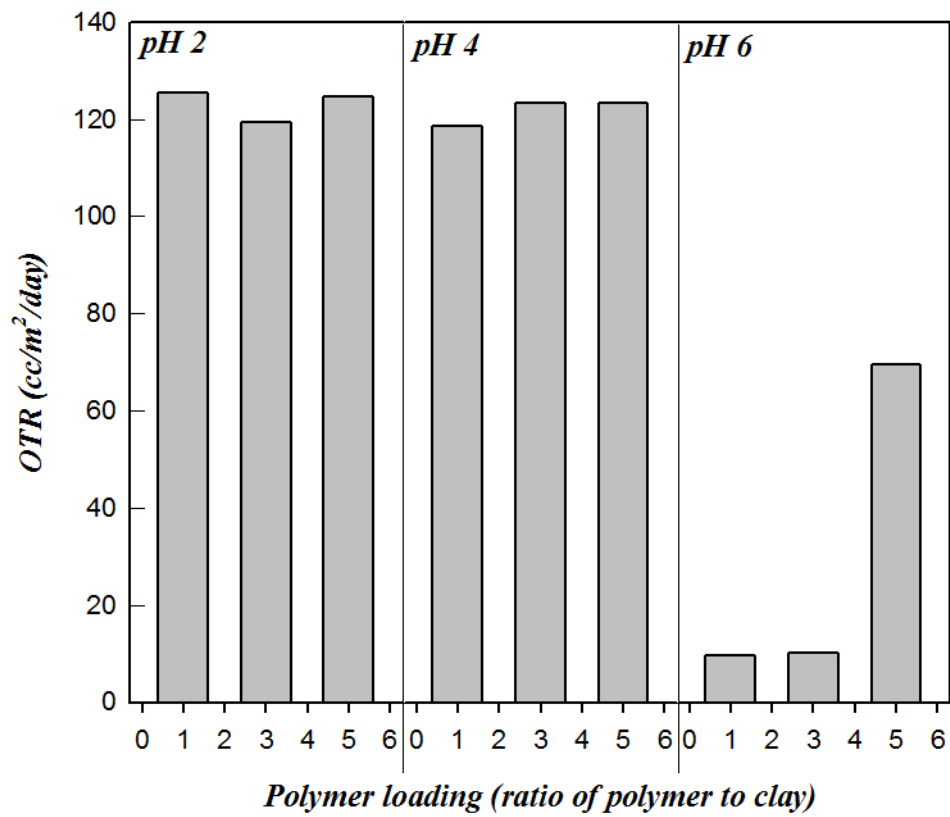


Figure 4-16. Dependence of permeability on pH and the amount of PAA for highly filled PCN coating system

CHAPTER 5
THEORETICAL ESTIMATION OF BARRIER PROPERTIES OF POLYMER CLAY
NANOCOMPOSITE CONTAINING TWO CLAY TYPES "PC2N"

Introduction

Polymer clay nanocomposite (PCN) are attractive for packaging materials because of superior barrier properties such as gas permeability and water vapor transmittance when compared to conventional polymer materials. As explained in previous chapters, barrier properties of PCN are affected significantly by the arrangement and orientation of platelets in the polymer matrix. Gas permeability in PCN is a function of the aspect ratio, volume fraction, and relative orientation of anisotropic nanoclay filler in the polymer matrix. Impermeable platelet arrangement and/or aspect ratio will result in the extension or reduction of the diffusion path as suggested by Nielsen [31].

Recently, improvements in the gas barrier properties of PCN especially at low concentrations of clay platelets (below 5 wt%) have been widely reported and it is important to use model to predict the optimized barrier properties. Several models [31,91-93,96] which are based on a tortuous path of diffusants have been proposed to relate permeability of PCN to volume fraction, particle dimension and arrangement of filler particles. To date all models predicting the barrier properties of PCN are based on using one nanoclay type. In order to obtain super barrier properties which cannot be prepared by using one nanoclay in PCN, new types of microstructure are required. The author anticipated that by inserting small-sized clay particles in the intergallery region of large platelets, the tortuous path, which diffusants need to travel around, is expected to be maximized. Recently, the same type of microstructure consisting of two different clay types was suggested by Stefanescu et al [144,145]. This work proved that the mechanical behavior of PCN could be controlled by adjusting the ratio of Laponite (small aspect ratio) to montmorillonite (MMT) (large aspect ratio) in PEO matrix. Stefanescu et al. also

proposed an idealized orientation for two clay types. However, no model has been proposed to predict the idealized microstructure and subsequent optimized barrier properties for PCN of two clay types. In this study, estimation of relative permeability (R_p) of PCN consisting of two clay particles having different aspect ratios (PC2N) is modeled by modifying existing tortuosity-based models in order to explore the benefit of using two different particle types and compared with experimental R_p results of several PC2N specimens

Experiments

Preparation of PC2N Films

In order to compare with the barrier model and equation, brief experiments were conducted. Cloisite Na⁺ (CNa), Cloisite 30B (CL30B) and synthetic layered silicate, Laponite JS (Southern Clay Products, Louisville, KY) were used to prepare a PC2N solution. Table 5-1 lists the specific information on the clays used. A 7 wt% poly(vinyl alcohol) (PVA) (Sigma-Aldrich co, St. Louis, MO; Mn = 132,000 and degree of saponification = 99%) aqueous solution was prepared as the polymer matrix. Organic ammonium chloride (OAC), [2-(Acryloyloxy)ethyl]-trimethyl ammonium chloride was used for an intergallery modification reaction of the natural clay. Two PCN solutions were prepared following the procedures reported in 16-22. To prepare a PC2N solution, polymer stock solution was prepared by dissolving high molecular weight (HMW) PVA in deionized water at elevated temperature and stirring with magnetic stirrer. Laponite powder was added in predetermined amounts of deionized water with vigorous agitation with a mechanical stirrer at room temperature until all powder was well hydrated. Aging was required to complete hydration. Laponite solution was added to polymer stock solution with agitation. Vigorous agitation with a mechanical stirrer for 10 minutes was conducted to prepare a completely exfoliated Laponite in a PVA matrix. The intergallery of Cloisite platelets was modified with OAC and prepared as an aqueous solution and then added to a PCN solution

consisting of PVA and Laponite. Further shearing with a mechanical stirrer was required for the final insertion process. This process was carried out by inserting PVA mixed with the smaller Laponite particles into the intergallery region of Cloisite. All prepared solutions were arranged as films with the size of 4 inch diameter by a casting method using a Teflon petridish.

Characterizations

Oxygen transmission rates (OTR) of prepared film specimens were measured in accordance with the procedure described in ASTM D-3985 using a Model OX-TRAN 2/20MH (Mocon Corporation, Minneapolis, MN). Permeation cell area was 50 cm². Table 5-2 lists the specific experimental conditions followed to prepare each composite sample and the associated OTR results. R_p values for samples were calculated by Equation (5-1) with obtained OTR values. Optical transmittance values were measured using an UV-visible photometer with wavelength range of 350 – 800 nm.

Discussion of Model and Results

PC2N consists of two clay types such as clay 1 a natural MMT with a large aspect ratio and clay 2 a synthetic layered silicate particle with a relatively smaller aspect ratio. Figure 5-1 shows relative dimensions of clays used. Synthetic layered silicates are aligned readily as a ‘house-of-cards’ structure due to the smaller aspect ratio and their charge interaction along the electrical double layers resulting in good exfoliation with relatively weak shear forces [89,118,142]. A natural MMT can also be exfoliated or intercalated by the surface-modification of nanoclay and subsequent shear processing as reported in many papers [39,43,74,118,146].

High barrier properties may be achieved by designing the maximum detour length in the microstructure of PC2N composite materials. Based on detour theory, R_p of PC2N system is given as Equation (5-1)

$$R_p = \frac{2H_1(1-\phi_T)}{\left(L_1 + L_2 \left(\frac{\phi_2}{v_{eff2}} \right) \right) + 2H_1} \quad (5-1)$$

Where, L_1 , L_2 and H_1 can be defined as lateral length including edge-to-edge distance, (l_1+b_1) and (l_2+b_2) of clay 1 and 2 and vertical length (h_1+w_1) occupied by clay 1 per unit volume, respectively.

Figure 5-2 represents how the ratio of volume fraction of clay 2 to clay 1 affects R_p of PC2N system, which is calculated from Equation (5-1). R_p decreases linearly as total volume fraction of filler increases, but there is no apparent difference among the five ratios showing a completely overlapped line. The effect of increased d_a caused by an increase in the quantity of clay 2 on R_p might be diminished by the lower quantity of clay 1 platelet in the system. There was no difference in R_p values when one clay type systems and two clay types systems were compared. Therefore the fact that R_p of PC2N can be determined by total volume fraction of two fillers can be confirmed theoretically, the model and the equation established in this paper is important for predicting the relationship between permeability and microstructure of particles in the matrix.

Figure 5-3 shows R_p for various composite systems with the ones as shown in Table 5-2. OTR value of HMW PVA film was $34.5 \text{ cc/m}^2/\text{day}$ and R_p values of all composites were calculated using Equation (5-2).

$$R_p = \frac{P}{P_o} \quad (5-2)$$

Where, P and P_o are permeability of polymer clay nanocomposites and that of matrix polymer without nanoclay, respectively. P, L, and 30B represent HMW PVA, Laponite JS and Cloisite 30B, respectively. Therefore, PC2N Sample 'PLCNa' consists of HMW PVA, Laponite

JS and CNa. There is no significant change in OTR values when varying the size of particles at the same total fraction of particles for the composite films prepared as expected from theoretical values as shown in Figure 5-2. Contrary to our expectation, in fact, there was no significant effect of inserting smaller nanoclay into the interspacing between larger clay platelets on R_p of PCN. However OTR values of composite films containing 30B were lower apparently than those of others composites in Figure 5-3. That is because that larger size particle exhibited better barrier properties as expected in Bharadwaj's model [96]. The reason that both two values for 1:0 and 0:1 of $\phi_1 : \phi_2$ are similar in Figure 5-2 may be explained the fact that orientation was not incorporated into this model. Also deviations caused by lateral distances, b_1 and b_2 at lower volume fractions may have affected permeability. Considerations such as the orientation of particles, the possibility of existing aggregated particles in the matrix, and actual lateral distances were not considered here. Even though there have been limiting factors for accuracy of the model, some consistency between theoretical expectation and real permeability that volume fraction of clay particles in PC2N system is significantly affects permeability rather than the relative size of two particles was observed.

Although extended experiments need to be done with this concern, our preliminary results clearly shows that, though higher volume fraction of clay particles led to lower permeability, the ratio of three components in the PC2N system should be optimized to take advantage of the properties of each clay platelet. For example, while Cloisite gives poor transmittance and relatively heavier weight, it exhibits better barrier properties. Therefore when mixed with Laponite much improved transmittance and reduced weight can be obtained while maintaining similar barrier properties. This fact could be confirmed by the results in Figure 5-4 and 5-5. Generally, properties of a matrix such as the degree of crystallization and the size of spherulites,

the interfacial refractive index difference between matrix and filler particles, and the size of dispersed particles determine the optical transmittance of polymer composites [82,147].

The scattering of light by well dispersed particles in matrix which are much smaller than the wavelength of incident visible light will lead to Rayleigh scattering. Therefore Laponite JS with the average aspect ratio of 25 nm was able to produce a near transparent film. However CL30B with higher aspect ratio can be utilized only for a better barrier material because of its high density and poor optical transmittance. PLCNa which is a PC2N composite shows median transmittance value between those of PL and PNa.

Derivation of Barrier Equation for PC2N

In order to develop a model to estimate R_p of PC2N, several assumptions were made. First it was assumed that clay platelets have no effect on crystallization of the polymer matrix as assumed in other detour-based models. The second assumption was that lateral separations (edge-to-edge distance) ' b_1 ' and ' b_2 ' were much smaller than the lengths of particles ' l_1 ' and ' l_2 ' respectively as shown in Figure 5-1.

In order to reduce the complexity of PC2N model, the author also assumed that both clay types maintained a parallel arrangement to the surface of specimen as shown in Figure 5-1. The direction of diffusion is normal to the surface. R_p can be defined as permeability of PCN film relative to unfilled film.

$$R_p = \frac{P}{P_o} \tag{5-2}$$

Where, P and P_o are permeability of polymer clay nanocomposites and that of matrix polymer without nanoclay, respectively. Assuming clay platelets as impermeable crystalline domains in semicrystalline polymer matrix based on Klute's theory [94], Equation (5-2) can be also defined as Equation (5-3)

$$R_p = (1 - \phi_T) \xi(\phi_T) \quad (5-3)$$

Where, ϕ_T and ξ are total volume fraction of clay particles in PCN and a function for the reduction of permeability due to the nanoclay particles, respectively. As with other researches the authors have made the assumption that the polymer matrix is unconfined. Therefore the permeability is only a function of the volume fraction of filler, i.e. nanoclay, when all the variables are fixed. The total volume of nanoclays, v_T , in the polymer matrix is defined as Equation (5-4),

$$v_T = v_1 + v_2 \quad (5-4)$$

Where v_1 is volume of nanoclay type 1 and v_2 is that of nanoclay type 2. The authors have assumed as with Bo Xu et al [93] and Saunder et al [95] that the shape of a nanoclay platelet is a hexahedron which its length and depth are equal. Therefore total volume of nanoclays is

$$v_T = l_1^2 w_1 + l_2^2 w_2 \quad (5-5)$$

And, based on the effective volume model suggested by Saunders et al [95], the effective volume model for this system is modified as illustrated in Figure 5-6. As shown in Figure 5-6, the left top quadrant is an effective volume which is dispersed uniformly in the whole system. This unit space represents the whole composite system, which contains both nanoclay types arranged in layers. Each unit cell is defined by the length of the larger nanoclay platelet. The unit cell cannot be smaller than this dimension. A number of the smaller nanoclay platelets can occupy a layer in the unit cell and the total number of the smaller platelets, n , is dependent of the size of this platelet.

Total volume fraction of nanoclays can be defined as Equation (5-6).

$$\phi_T = \phi_1 + \phi_2 = N_1 v_1 + N_2 v_{eff2} \quad (5-6)$$

Where ϕ_1 , ϕ_2 are the volume fraction of particles 1 and 2, respectively, and N_1 and N_2 represent the number of nanoclay 1 and 2 per unit volume within the effective volume of clay 1, respectively. Note that total volume fraction in the composite system can be regarded as $\phi_T + \phi_{Polymer} = \phi_1 + \phi_2 + \phi_{polymer} = 1$. Once the fully occupied nanoclay 2 platelets between two larger platelets is regarded as a tactoid which moves together, the volume fraction of clay 2 can be estimated using effective volume of clay 2 instead of the volume of clay 2.

The number of clay platelets of type 2 (N_2) should be described in a different manner than N_1 because effective volume of clay 2 falls within the effective volume of clay 1 (V_{eff1}) by the assumption. Since the effective volumes for clay 1 and clay 2 are calculated from

$$v_{eff1} = (l_1 + b_1)^2 (h_1 + w_1) \quad (5-7)$$

$$v_{eff2} = (l_2 + b_2)^2 (h_2 + w_2) \quad (5-8)$$

Total number of nanoclay per unit volume in the system, N_T can be written as following

$$N_T (= N_1 + N_2) = \frac{\phi_1}{v_1} + \frac{\phi_2}{v_{eff2}} \quad (5-9)$$

Equation (5-10) and (5-11) are obtained from V_{eff} and the definition of N_1 and N_2 ,

$$N_1 = \frac{1}{v_{eff1}} = \frac{1}{(l_1 + b_1)^2 (h_1 + w_1)} = \frac{\phi_1}{v_1} \quad (5-10)$$

$$N_2 = \frac{nl}{v_{eff1}} = \frac{nl}{(l_1 + b_1)^2 (h_1 + w_1)} = \frac{\phi_2}{v_{eff2}} \quad (5-11)$$

The tortuous path (d') per unit volume of diffusant may be estimated by summing lateral distances that a diffusant must travel due to particles (d_a) per unit volume relative to the shortest path through unfilled polymer (d) per unit volume. The distance of diffusant through the matrix without filler can be calculated from Equation (5-12). The additional lateral distance created

when clay 2 particles are embedded into the gap between the layers of clay 1 particles (d_{a2}) per unit volume is described in Equation (5-13) and total detour distance (d_a) per unit volume caused by all fillers in the system may be estimated from the extended term as given in Equation (5-14). Note that the dimension of all tortuous path described here is length/volume and the 'N' is also the number per unit volume.

$$d = N_1(w_1 + h_1) = \frac{\phi_1}{v_1}(w_1 + h_1) \quad (5-12)$$

$$d_{a2} = N_2 \left(\frac{l_2 + b_2}{2} \right) \quad (5-13)$$

$$d_a = N_1 \left(\frac{l_1 + b_1}{2} \right) + N_1 d_{a2} = N_1 \left(\left(\frac{l_1 + b_1}{2} \right) + N_2 \left(\frac{l_2 + b_2}{2} \right) \right) \quad (5-14)$$

From Equation (5-11), nl may be expressed as Equation (5-15)

$$nl = \frac{(l_1 + b_1)^2 (h_1 + w_1)}{(l_2 + b_2)^2 (h_2 + w_2)} \phi_2 \quad (5-15)$$

According to the definition of d_a , maximum values of d_a promise the longest path distance corresponding lower R_p values. By the definition of $\xi(\phi_T)$,

$$\xi(\phi_T) = \frac{d}{d'} = \frac{N_1(w_1 + h_1)}{N_1 \left(\left(\frac{l_1 + b_1}{2} \right) + N_2 \left(\frac{l_2 + b_2}{2} \right) + (w_1 + h_1) \right)} \quad (5-16)$$

Therefore R_p of PC2N system is given as Equation (5-17) after combining Equation (5-3) and (5-16)

$$R_p = \frac{2H_1(1 - \phi_T)}{\left(L_1 + L_2 \left(\frac{\phi_2}{v_{eff2}} \right) \right) + 2H_1} \quad (5-1)$$

Where, L_1 , L_2 and H_1 can be defined as lateral length including edge-to-edge distance, (l_1+b_1) and (l_2+b_2) of clay 1 and 2 and vertical length (h_1+w_1) occupied by clay 1 per unit volume, respectively.

Table 5-1. Specific information of all clays used for the preparation of PC2N

		Cloisite 30B	Cloisite Na ⁺	Laponite JS
d-spacing	h (nm)	1.85	1.17	0.001
aspect ratio	l (nm)	200-1000	75-150	25
avg. aspect ratio*	l (nm)	600	112.5	25
	w (nm)	1	1	0.92
lateral spacing**	b = l/10 (nm)	60	11.25	2.5
Density	((g/cm ³))	1.98	2.86	0.95

*, ** these two values are based on the assumptions of the R_p equation of PC2N

Table 5-2. Specific experimental conditions for the preparation of composite films

samples	Conc. of PVA (wt%)	Φ ₁ **	Φ ₂ **	Φ _t	OTR (cc/m ² /day)
P	7	0	0	0	34.500
PL	7	0	0.050	0.050	0.734
PCNa	7	0.050	0	0.050	0.650
P30B	7	0.050	0	0.050	0.488
PLCNa*	7	0.025	0.025	0.050	0.657
PL30B*	7	0.025	0.025	0.050	0.504

*PC2N, **1; Cloisite Na⁺ or 30B, 2 ; Laponite JS

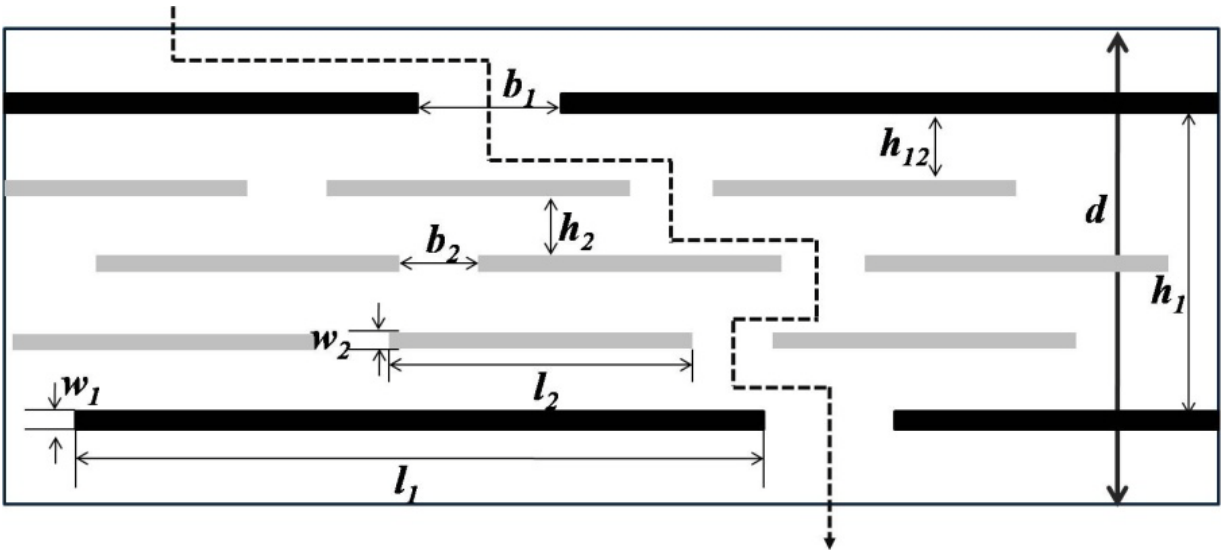


Figure 5-1. Schematic diagram showing a filled polymer with (a) one clay type and (b) two different clay types (dark rectangle represents clay 1 with the dimension of width of w_1 and length of l_1 and grey scaled rectangle is clay 2 with the dimension of width of w_2 and length of l_2 . The separations of each particle are denoted as b_1 and b_2 for lateral edge-to-edge distance and h_1 and h_2 for face-to-face distance between the same clay type platelets. The face-to-face distance between two different type platelets is denoted as h_{12} . Note that the dot line is the tortuous path for a gas molecule in PCN (P) and thick solid arrow line can be described as the shortest path (d) through unfilled polymer (P_0))

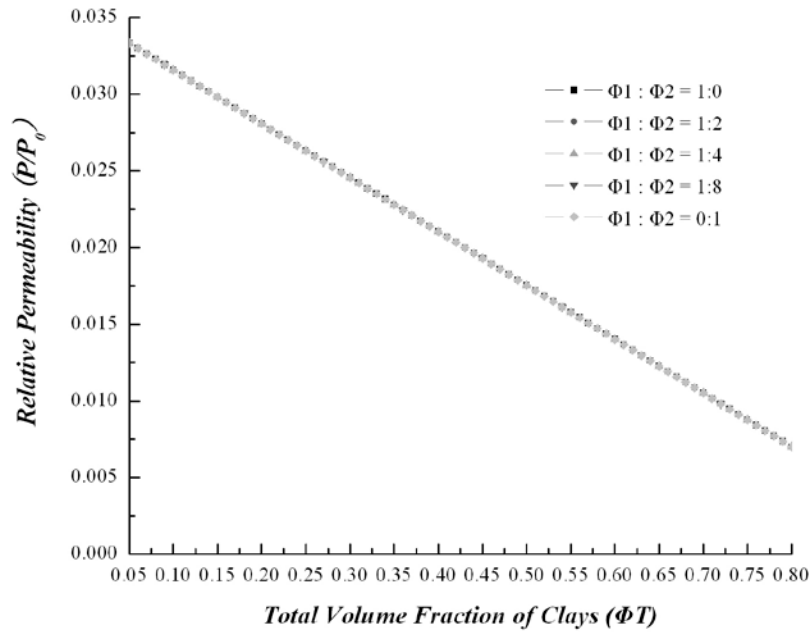


Figure 5-2. Effect of the total volume fraction of clay2 on the relative permeability of PC2N: obtained by Equation (5-1) from $l_1=100$ nm, $l_2=5$ nm, $w_1 = w_2 = 1$ nm, $b_1=l_1/10$, $b_2=l_2/10$, $h_1=1$ nm, $h_2=0.001$ nm

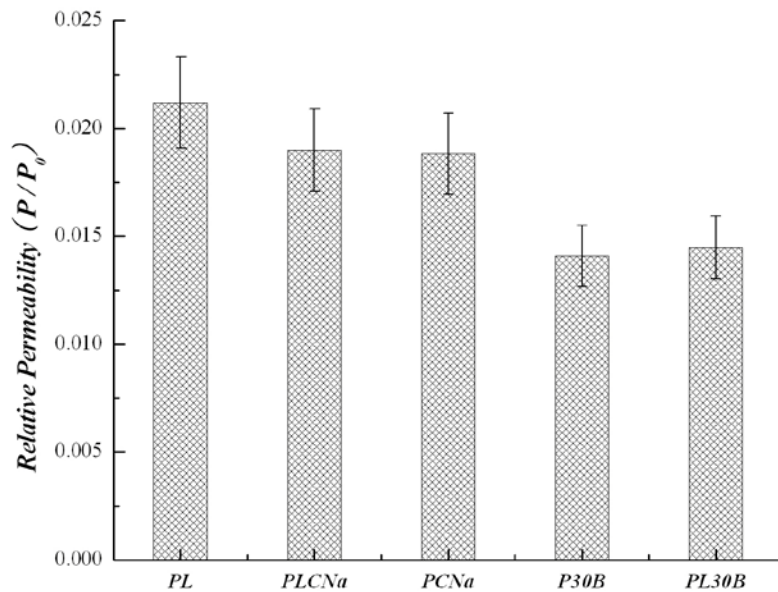


Figure 5-3. Actual relative permeability of various composite films calculated from OTR values measured by MOCON

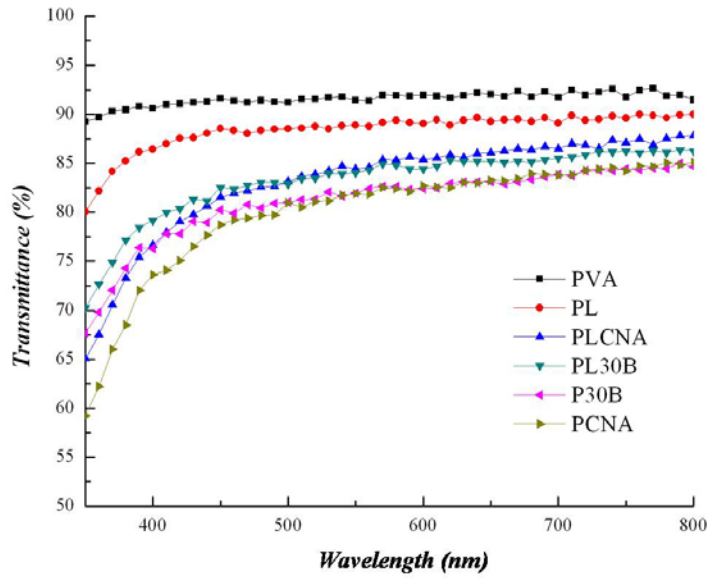


Figure 5-4. Optical transmittance of composite films at the visible wavelength range (350 – 800 nm)

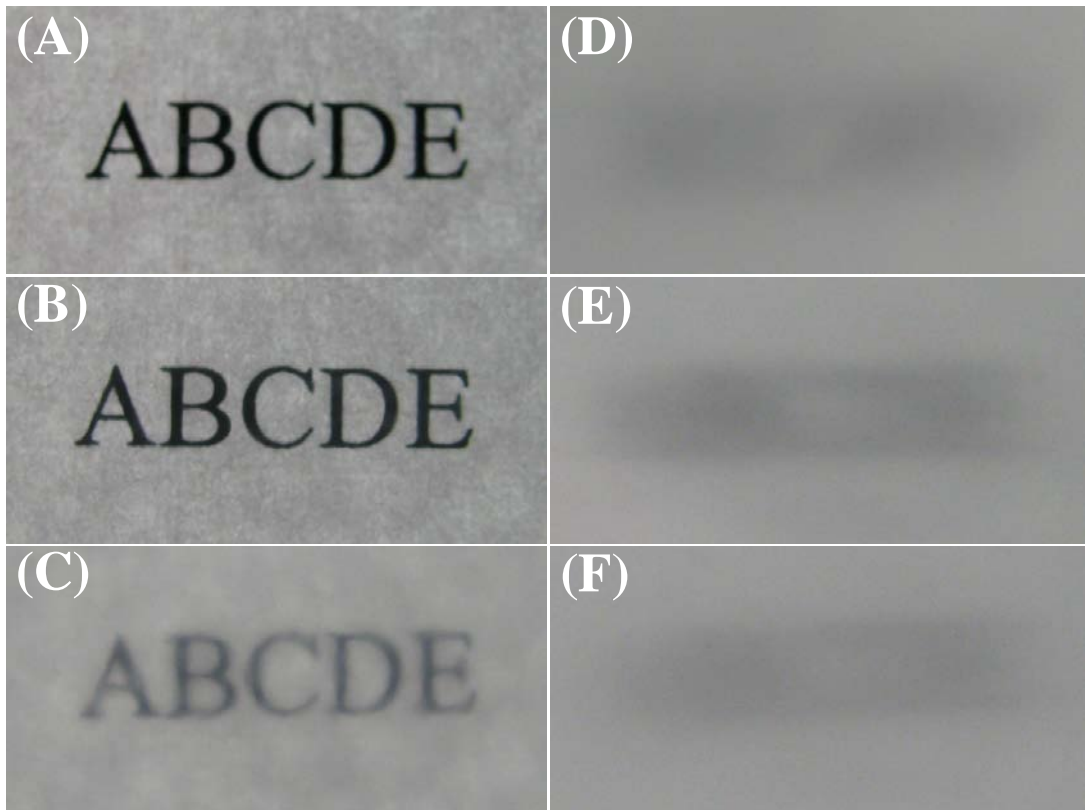


Figure 5-5. Pictures of prepared transparent and translucent composite film samples: (a) PVA, (b) PL, (c) PLCNa, (d) PCNa, (e) PL30B, and (f) P30B

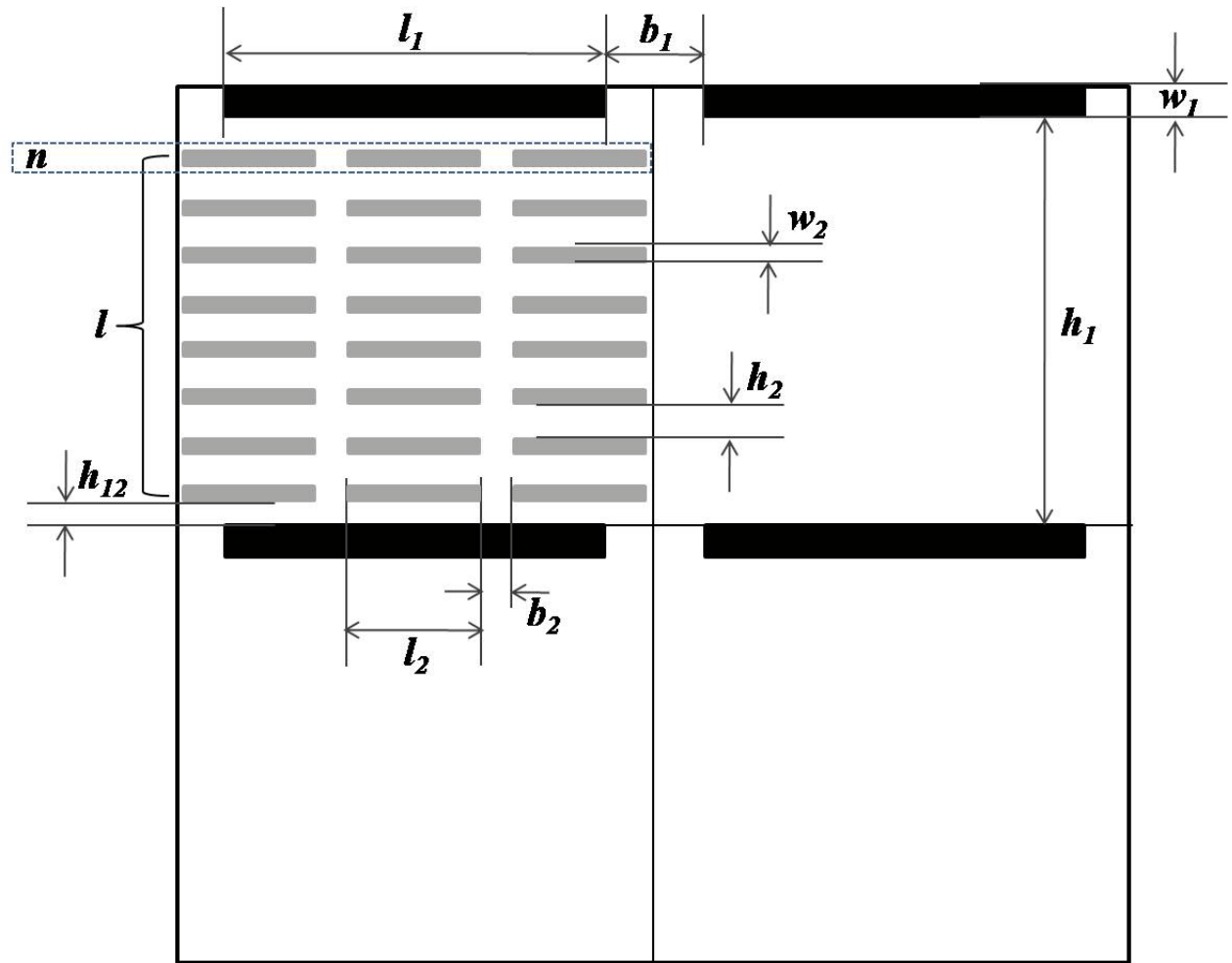


Figure 5-6. Parallel arrangement of two nanoclays in an effective volume: ' n ' is the total number of the smaller platelets which can occupy in a layer in the unit cell and ' l ' is the number of layers in the unit cell. Others are defined in the caption of Figure (5-1) in the Discussion Part.

CHAPTER 6 EFFECT OF POLY(ACRYLIC ACID) ON BARRIER PROPERTIES OF HIGHLY FILLED NANOCOMPOSITE FILMS

Introduction

In order to enhance barrier properties, extending tortuous path a permeant molecule should travel is indispensable to polymer clay nanocomposite (PCN). This has been approached by dispersing impermeable fillers in polymer. Because extending tortuosity is achievable using completely separated and dispersed nanosized clay fillers, researches to lower permeabilities of PCN have been focused on obtaining better dispersion and exfoliation of clay platelets in various polymer matrices [46,53,54,148-151]. However, a PCN in which nanoclays are completely separated and dispersed has not been satisfied for practical barrier applications. Triantafyllidis et al reported a preparation of an epoxy-clay fabric film composite with significant oxygen barrier property enhancements via a partial ion-exchange reaction [9]. Oxygen permeability of resulting specimens was lowered by 2 to 3 orders of magnitude when compared to a pristine polymer film and by 3 to 4 orders of magnitude when compared to a pristine clay film. Because of an intrinsic nature of thermoset epoxy resins, it was difficult to obtain a good film flexibility. Achieving film flexibility and super barrier properties can be obtained by designing a new microstructure of clay platelets using negatively charged organic molecules as a binder additive. As introduced in Chapter 2, Ebina et al [65] successfully prepared flexible transparent clay films with high barrier properties. These films were made based on a hypothesis that significant reduction in barrier properties can be obtained by maximizing tortuous path. Due to highly dense self-laminating microstructures of clay platelets, maximized tortuous path and good flexibility were able to be realized. One challenge for PCN design proposed by Ebina is that clay films can be readily damaged and its shape can be distorted as a result of minor contact under humid conditions due to swelling of natural montmorillonite (MMT) clay by water molecules. Water content in clay

films is important as it will contribute to better flexibility. Therefore a critical quantity of water molecules is required to maintain moderate flexibility of the films.

In this work, existing concept of stratified microstructure reported by Ebina [65,66] was studied and developed to achieve a film for enhanced barrier applications. Effects of polymer loading in clay films on barrier properties and resulting microstructures of clay platelets were investigated. Exterior layers were formed to prevent the swelling of clay films and to promote a better flexibility.

Experiments

Preparation of Highly Filled Nanocomposite Films

Closite Na⁺ (CNa), a natural MMT (Southern Clay Products, Louisville, KY) powder was dispersed slowly in distilled water using a high shear agitator for 3 hours. Poly(acrylic acid) (PAA) with average molecular weight (Sigma Aldrich, St. Louis, MO) of 250,000 was dissolved in distilled water and pH of prepared PAA solution was controlled using aqueous HCl (1 M) or NaOH (1 M) solution. Negatively charged PAA was attained by setting pH of the mixture to basic condition [140,141]. These negatively charged PAA binder molecules will attach to edges of clay platelets. Prepared PAA stock solution was poured into a clay solution and mixed for another 2 hours. Table 6-1 lists corresponding relative amounts of clay and PAA for each sample.

The mixture was degassed in vacuum for 1 hour and then poured onto a Teflon caster, dried in hot oven at 60 °C for 15 – 20 hours. Formed film specimens was detached from the caster and dried at room temperature for several minutes. To prevent swelling of clay films by water molecules, poly(vinyl butyral) (PVB), B60H (Kuraray Inc., Japan) solution dissolved in ethanol with a concentration of 5 wt% was used as an exterior coating. Clay films were dip coated in PVB solution and dried overnight at room temperature. Thicknesses of prepared films were measured using a micrometer and compared with scanning electron microscopy (SEM)

micrographs with error ranges of $\pm 1 \mu\text{m}$. Figure 6-1 represents schematic of experiment procedures for preparing highly-filled PCN film coated with PVB.

Characterizations

Microstructures of clay platelets were characterized by x-ray diffractometer (XRD) (Philips MRD X'Pert System) using $\text{CuK}\alpha$ radiation ($\lambda = 1.54056 \text{ \AA}$) with a range of scanning angle from 2 to 10 degree. Transmission electron microscopy (TEM) (TEM-200CX, Jeol Ltd., Tokyo, Japan) also was used to investigate orientations of clay. An accelerating voltage of 200 kV was used for TEM analysis. Dispersion liquid is dropped directly on a copper grid supported with a collodion membrane. Field emission SEM (FE-SEM) (JEOL JSM-6335F) was conducted on fractured crosssection areas of film specimens as well as film surfaces. Film samples for FE-SEM were sputter coated with gold-palladium alloy (Au-Pd). Submicron-detailed surfaces characteristics were obtained under ambient conditions using atomic force microscopy (AFM) (AFM Dimension 3100, Veeco Co.) by tapping mode within $5 \times 5 \mu\text{m}^2$ areas. Oxygen transmission rate (OTR) value, which is a steady-state rate of transmission of oxygen gas, is widely used as a standard method for estimating barrier properties of a material; it is defined as a quantity of oxygen gas passing through a unit area of parallel surfaces of a plastic film per unit time under conditions of test. OTR of samples were measured using a procedure and instruments (Model OX-TRAN 2/20 MH module, MOCON Co.) described in ASTM D3985-05. Flexibility of obtained film specimen was measured using an intuitive curvature test as shown in Figure 6-2. In a curvature test, three points, A, B and P on a curved line were fixed and r values, radius of curvature at P from a point o, center of curvature for P were measured. Local curvature of k was obtained by taking a reciprocal value of r. Endothermic heat flows of these composites were measured using Differential Scanning Calorimeter (DSC) (MAS-5800, model DSC 200). All

samples were tested in crimped aluminum pans at a heating rate of 25 °C/min under dry nitrogen gas over a temperature range from 25 to 300 °C. Dynamic weight loss tests were conducted by using the same instrument. All tests were performed using sample weights of 10-12 mg at a heating rate of 5°C/min over a temperature range from 30 to 250 °C.

Results and Discussion

Variables Affecting Barrier Properties

In general, it has been reported that barrier properties of polymeric clay nanocomposite materials are improved as weight fraction of embedded fillers increases. However, variances of OTR of highly filled nanocomposite samples resulted in a completely different tendency with that of conventional PCN system where nanoclay loading is usually less than 10 wt%. As observed in Figure 6-3, barrier properties deteriorated as wt% of polymer decreased. Densely arranged unique microstructure of clay platelets and filling voids theory suggested by Beall [112] can be two explanations for this counter tendency. Detour paths of oxygen molecules resulting from randomly dispersed filler particles will not be an important factor for barrier properties of highly filled nanocomposite materials. Rather, it is important to compare morphological features to analyze roles and effects of polymer loading on barrier properties. Morphological feature of clay platelets in nanocomposite film specimens were observed using SEM. Figure 6-4 represents a proposed microstructure of clay platelets and PAA chains schematically with SEM micrographs of prepared film samples. As reported by Ebina, negatively charged PAA chains under basic conditions lead to parallel arrangement by promoting edge-to-edge attachment among clay platelets as shown in Figure 6-4. This arrangement is unlike the ‘house of cards’ structure formed in Laponite JS aqueous solution as observed in Chapter 4. A face-to-face arrangement of CNa is due to high aspect ratio (Aspect ratio is ca. 75-150 nm [85]). CNa clay spontaneously arranges its platelets in a (001) direction [39]. Arrangements of CNa clay platelets

at various polymer loadings were confirmed by SEM micrographs of cross-section area and XRD analysis. For all SEM micrographs of film specimens, intrinsic sinusoidal morphology of clay platelets was observed. A notable difference is a chevron pattern which was observed in Figure 6-5 (a). This pattern disappeared and debris was reduced as PAA loading increased. This indicates that negatively charged PAA chains plays a significant role in determining specimens' brittleness affecting therefore barrier properties. CN3P0 containing no polymer showed more winding features, which produced more microvoids between platelets. In fact, because of highly brittle characteristics of CN3P0 specimen, OTR measurement was not able to be conducted. Use of PAA polymer to organize clay platelet by inducing edge-to-edge arrangement and fill up voids made it possible to improve barrier properties. OTR was lowered when polymer loading exceeded 23 wt%. The lowest OTR value was recorded at 50 wt% of polymer composition.

PAA attached to clay platelets' edge resulting in more curved features and these features were found in (e) and (f) in Figure 6-5. When PAA loading exceeded critical amount which is required to induce clay platelets' edge-to-edge attachment, excess PAA might diffuse into microvoids which were resulted from winding features of clay platelet microstructure. Some microvoids were filled with these PAA chains resulting in dense structure as shown in CN3P70 (e) and CN3P100 (f) of Figure 6-5. Therefore it could be deduced that enhanced barrier properties of CN3P70 and CN3P100 were caused by densely stratified microstructure of clay platelets and polymer-filled voids.

Difference of microstructural features was investigated using X-ray diffraction as illustrated in Figure 6-6 (a). There was no difference in peak positions for all the samples indicating that the polymer chains were not diffused into the intergallery region between clay platelets. Stacked clay platelets were bound to each neighbor by ionic bonds with the aid of

negatively charged PAA chains. Full Width at Half Maximum (FWHM) values were measured to compare a degree of orientation as shown in Figure 6-6 (b). Like that more flattened morphological features of clay platelets were found as polymer loading increased in Figure 6-5 SEM micrographs, FWHM values decreased suggesting improved orientation was obtained at higher polymer loadings. Decreasing FWHM values with increasing polymer loadings also suggested that higher crystallinity was achieved as polymer content was increased. This supported OTR results; lower OTR values were obtained at higher polymer loading as oxygen molecules were blocked more.

DSC results as shown in Figure 6-7 also showed the same crystallinity tendency. Total crystallinity of a polymer is a dominating factor which makes it possible to analyze barrier properties to gas molecules among samples comparatively. However, it should be noted that polymer free volume, and diffusion gas type need also to be considered.

According to a barrier mechanism, a penetration of oxygen molecules initiates with an adsorption on polymer film surfaces prior to diffusion into films' interior. However, if there are some micro- or macro-sized cracks on film surfaces, oxygen molecules will go through the film directly without any adsorption on polymer surfaces. Therefore it is necessary to compare an amount of polymer and cracks on surfaces, and to relate their surface characteristics to barrier properties. Surface characteristics were analyzed by performing SEM and AFM. Figure 6-8 is SEM micrographs of nanocomposite films with various amounts of PAA. Micro-sized cracks on surfaces observed in CN3P0 (a) and CN3P10 (b) resulted from lack of polymer; film surfaces were easily damaged due to low polymer loading. Therefore, OTR values for samples with high polymer content were lower by having less probability of a direct diffusion through cracked

regions into interior regions. Excess polymer enhanced barrier properties by filling cracks on the film surface retarding total diffusion time of gas molecules.

Roles of Poly(vinyl) Butyral Layer

Clay films have several drawbacks in that these films are so brittle and susceptible to water molecules. Highly filled nanocomposite films which were prepared based on spontaneous arrangements of clay platelet also had similar drawbacks with those of clay films. Exterior PVB layers were used to enable PAA/CNa nanocomposite films for use as practical barrier applications. Two main roles of PVB layer were to prevent swelling of clay with water molecules and to improve flexibility of films. As PVB layer was nonsoluble in water, penetration of water molecules was prevented. Degree of physical interlocking which can determine adhesive property between PAA/Clay films and the PVB coating was estimated by examining surface roughness. SEM micrographs of surfaces indicated that high polymer loading contributed to a smoother surface of resulting films. However, surfaces became rough when amount of polymer exceeded 33 wt% (from CN3P30 to CN3P50). A smoother surface returned at 50wt% (CN3P100) of polymer loading as shown in (f) of Figure 6-8. This tendency was confirmed again with RMS data analyzed by AFM as provided in Figure 6-9.

A large RMS value of CN3P10 was caused by weakly attached stacked clay platelets and broken pieces of this brittle specimen, thereby contributing to increased roughness. The largest root mean square (RMS) value was shown in the case of CN3P70. The largest RMS value of CN3P70 might be due to large aspect ratio of CNa clays showing more curved morphological features. At film surfaces some of these clay platelets protruded their surface layer. This effect was also enhanced by large excess in PAA polymer chains which were diffused in microvoids. Increased amount of polymer of CN3P100 lowered RMS value significantly than that of CN3P70. A reason that CN3P100 has a lower RMS value could be due to protruded edges of

curved platelets of tactoids which were covered by polymer making it smoother. This was drawn schematically in Figure 6-10.

To identify excess polymer on surfaces and effects of this excess polymer on roughness specifically, several 3D surface images with two 2D phase contrast images of CN3P10 and CN3P100 and Power spectral density (PSD) were obtained as shown in Figure 6-11 and 6-12, respectively. 3D height contrast images of samples showed a good match with RMS values and SEM surface images. 2D phase contrast images (f) and (g) illustrated well differences in amount of excess polymer on surfaces. A polymer phase which is close to viscoelastic materials exhibits a high phase angle between a cantilever response and that in free air. This corresponds to a brighter region in a phase contrast image. Lower phase angle is usually observed as a darker region which is more elastic. This difference in phase contrast image of tapping mode depending on phase angle was shown in (h) Figure 6-11 [152]. Therefore phase image of (g) CN3P100 was much brighter than (f). PSD is a good indicator to investigate correlation lengths of rough surfaces. Lower frequency region exhibits a macro-sized roughness and higher frequency is a micro-sized roughness which is required to know overall roughness of a sample. All samples showed similar tendency for lower frequency regions as shown in Figure 6-12. However, CN3P70 has higher micro roughness than CN3P100, as excess polymer covered micro-sized rough surfaces.

Flexibilities of obtained specimens were tested using an intuitive curvature test. During sample tests, no visual delamination of PVB layer from surfaces of nanocomposite films was observed proving good adhesion between highly filled nanocomposite film and PVB layer. As shown in SEM micrographs (Figure 6-4 and 6-5) of fractured surfaces of these specific nanocomposite specimens, delaminated layers were observed. Figure 6-13 shows flexibilities of

nanocomposite film specimens before and after PVB coating process. For all samples except CN3P70, flexibilities were improved after PVB coating. Especially, at lower polymer loading, PVB layers contributed to improving flexibility because energy of crack propagation of brittle specimen dissipated into ductile exterior PVB layer. Ductile PVB layer adhered to PAA/CNa nanocomposite film by preventing an initial delamination of brittle clay platelets effectively resulting in much higher curvatures. When amount of PAA increased, effects of PVB layer on flexibility were reduced. Nanocomposite film itself was quite flexible for CN3P10 and CN3P30 and, in fact, they could be folded without any cracking. This is because amount of water molecules existing in PAA linkage molecules to connect clay platelets within structure of clay nanocomposite film is optimum used for CN3P10 and P30 showing a good flexibility. Therefore, it can be concluded that flexibilities of highly loaded nanocomposite films are governed by the extent of hydration of clay platelets as well as the densification of the stratified structure rather than amount of polymer or how the platelets are arranged in this particular case. Even though brittle characteristics of clay platelets were improved by addition of PAA chains as shown in SEM micrographs, flexibilities of specimens were not enhanced by increasing the polymer loading.

PVB coating on both sides of PAA/CNa nanocomposite films contributed to enhanced barrier properties as shown in OTR results in Figure 6-3. PVB layers have its own crystalline structure to prevent diffusion of gas molecules and PVB layers also assist with covering and filling cracks on surfaces of nanocomposite films.

Frequently observed T_g of PAA about 102-109 °C is completely overlapped with endothermic peak from 50 to 150 °C contributing to typical water desorption of MMT [42,153,154,157]. An endothermic peak shown on a curve of CN3P0 which contains no polymer

was due to water desorption of MMT. Heat of fusion for overlapped endothermic peaks for all specimens can be expressed as $\Delta H_{\text{total}} = \Delta H_{\text{PAA}} + \Delta H_{\text{MMT}}$. ΔH_{MMT} dominated over all peaks of CN3P10, P30 and P50. As polymer content increased, peak area increased as well. PAA inherently shows a high degree of intermolecular hydrogen bonding involving “bound water” acquired during polymer preparation process [153,154]. Therefore, in the cases of CN3P70 and P100, increased degree of intermolecular hydrogen bonding caused by excess amount of PAA resulted in a much larger area of heat of fusion. As a result, it can be concluded that when amount of polymer exceeded a certain threshold, endothermic peaks are affected more by intermolecular hydrogen bonding of PAA. Peak position shifted slightly toward lower temperature as amount of polymer increased as indicated as an arrow in Figure 6-7. This phenomenon can be explained by that excess PAA chains, which exist on surfaces or which are not associated to clay platelets, require less energy for an initiation of chain motions. Thermal gravimetric analysis (TGA) thermograms were measured to confirm effects of water on thermal properties of specimens as demonstrated in Figure 6-14. Weight loss attributing to water removal of MMT was identified on a curve of CN3P0. Water molecules contained within PAA polymer chains were bound to clay platelets resulting in retardation of rate and onset of water removal from the composite system. Because small amount PAA polymer chains mainly acts as a linkage molecule to connect between clay platelets in CN3P10 and P30, water molecules within PAA polymer chains or from hydrated clay platelets were not easily removed causing less weight loss than CN3P0 by 220 °C. Final weight loss showed much smaller increment from previous one with similar increment of polymer as amount of polymer increased. It was more difficult to remove water molecules when PAA contents increased because of a much higher degree of intermolecular hydrogen bonding. In fact, based on flexibility tests, the author expected that

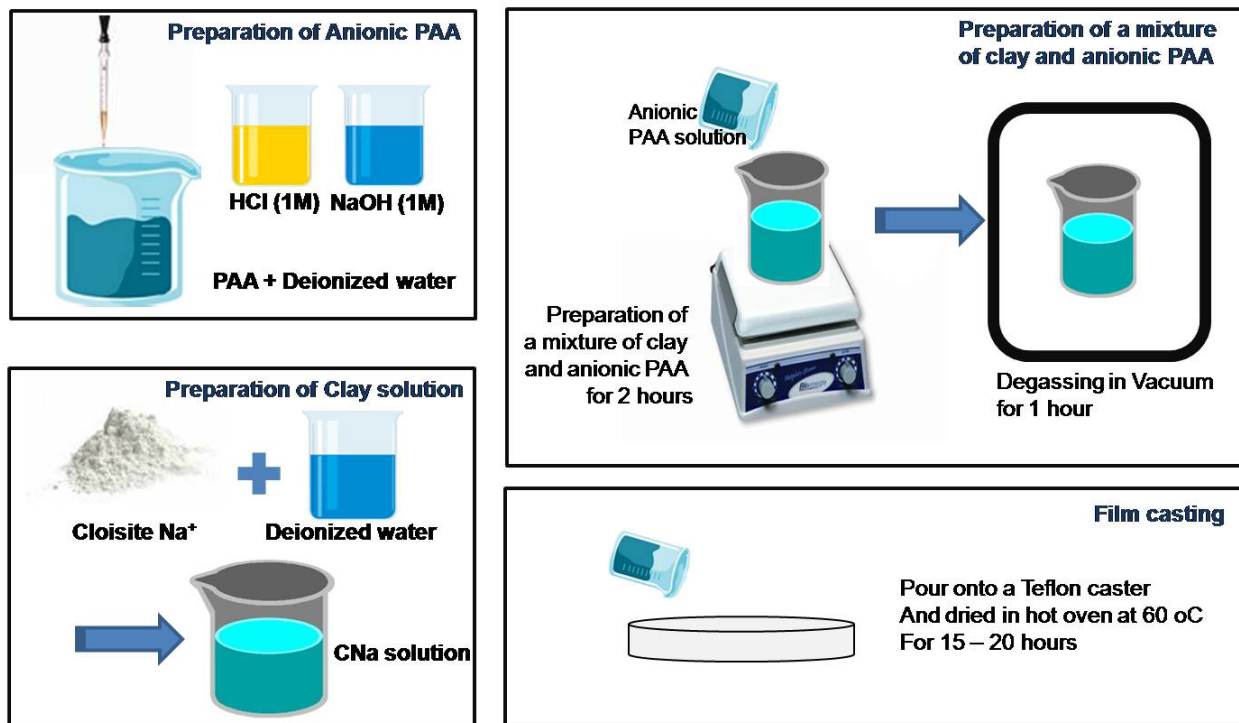
water contents of CN3P10 would be highest while CN3P100 would exhibit poor flexibility due to lower water content. However, results were completely contrary to expectations. Therefore flexibility is determined by amount of water molecules existing in PAA linkage molecules that connects clay platelets within structures of nanocomposite systems, and not by amount of water in complete nanocomposite system. Even though water content of CN3P100 is the largest, a role of water ascribing to flexibility would be reduced as lower quantity of clay used and added PAA increased brittleness of specimens resulting in poor flexibilities. Paralikar et al and Jiang et al. reported that PAA is a typical brittle polymer therefore PAA in composite systems increases brittleness of specimens [155,156]. Critical amount of PAA needed to maintain flexibility has to be determined as exceeding a critical loading will result in a deterioration of macromechanical properties. Large amount of PAA predicted lower oxygen transmission rate. Increased packing density of polymer chains induced by higher degree of intermolecular hydrogen bonding as well as well aligned structures of clay platelets which are flattened showed increased crystallinity as indicated as the largest peak areas in Figure 6-7. Therefore a barrier property of CN3P100 was enhanced more than any other system. It was concluded that optimum range of PAA to achieve good flexibility and barrier property was 30 -35 wt%. It is also important to note that by adjusting pH of PAA, PAA also act as linkage molecules for the clay platelets.

Table 6-1. Corresponding relative amounts of clay and PAA for each sample

Samples	Conc. of clay (wt%)	Amount of PAA (wt%)	Thickness ¹ (μm)	Thickness ² (μm)
CN3P0	3	0	25	N/A*
CN3P10	3	9	28	32
CN3P30	3	23	29	34
CN3P50	3	33	31	33
CN3P70	3	41	33	37
CN3P100	3	50	31	34

1, thickness of clay sample before PVB coating; 2, thickness of clay samples after PVB coating

STEP1: Preparation of PAA/CNa nanocomposite films



STEP2: PVB coating

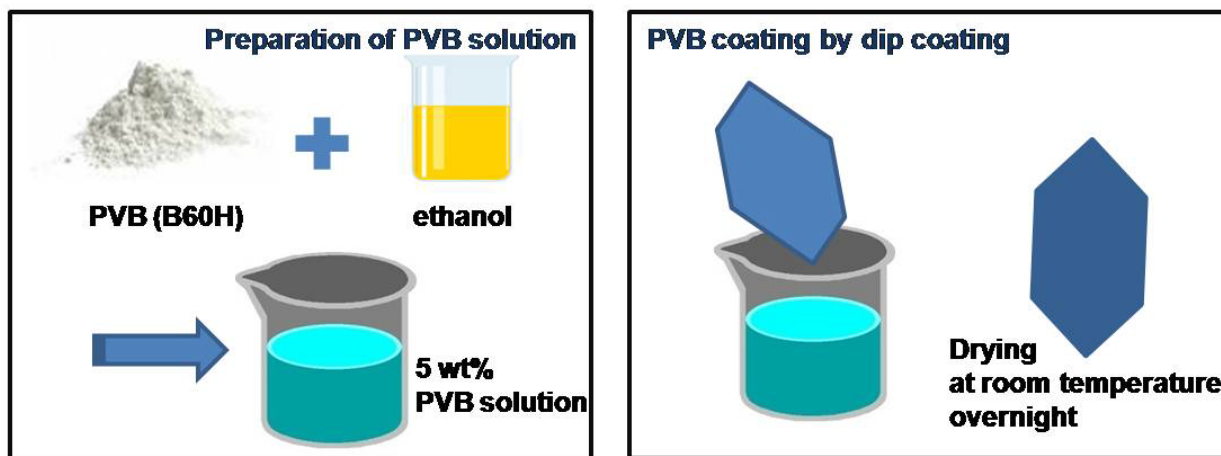


Figure 6-1. Schematically presented experiment procedure for the preparation of PVB-coated PAA/CNa nanocomposite film

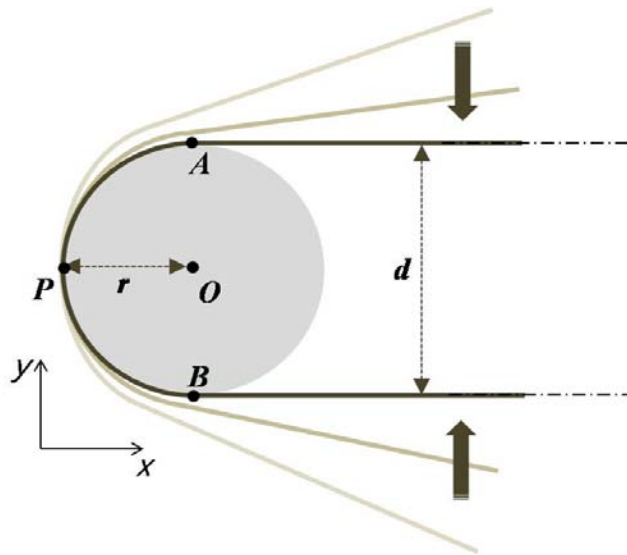


Figure 6-2. Schematic diagram of an intuitive curvature test to measure flexibility of obtained film specimens

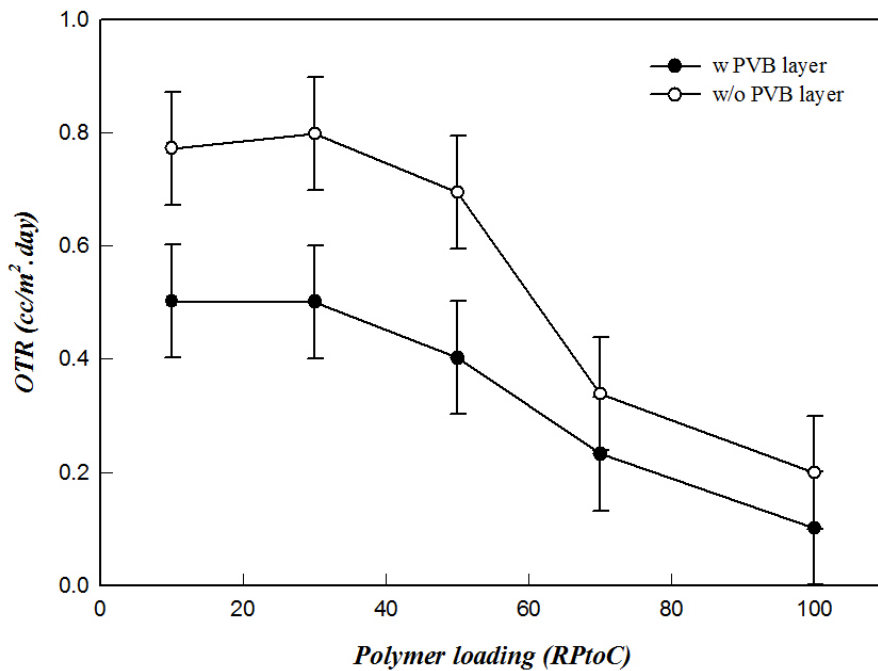


Figure 6-3. OTR values of highly filled nanocomposite film specimens of different polymer loading. OTR values of PVB coated film specimens were also conducted to estimate the contribution of exterior layer on barrier properties. (RPtoC represent the ratio of polymer to clay; refer to table 6-1 for details)

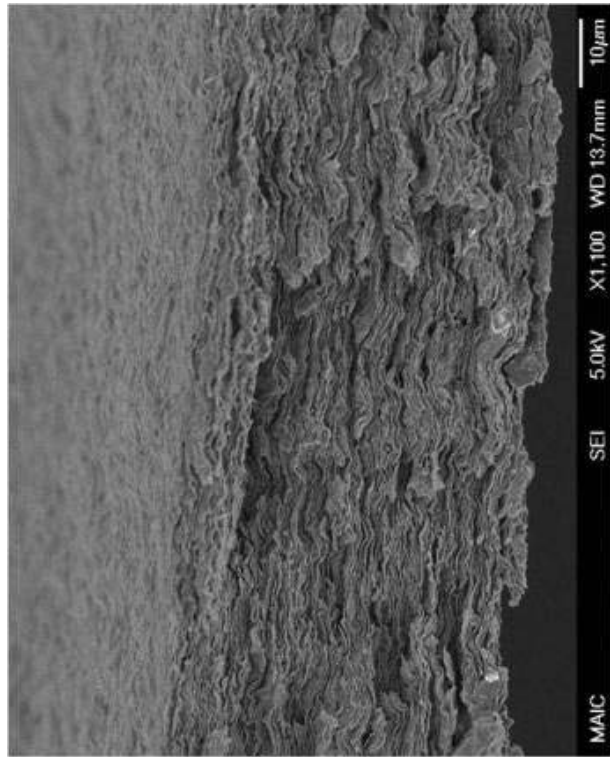


Figure 6-4. Schematic microstructure of clay platelets and PAA chains and corresponding SEM micrographs of prepared film specimen

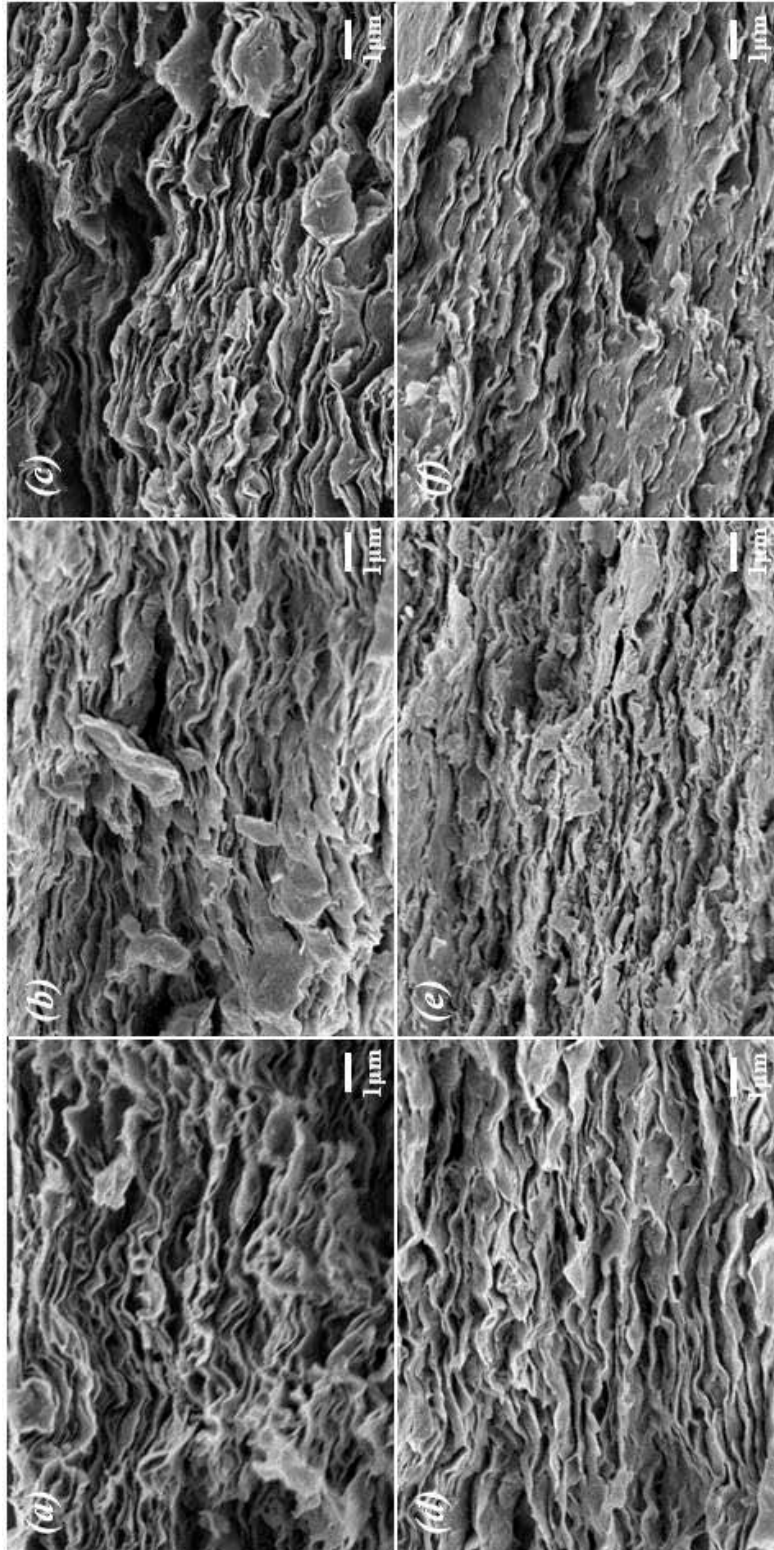
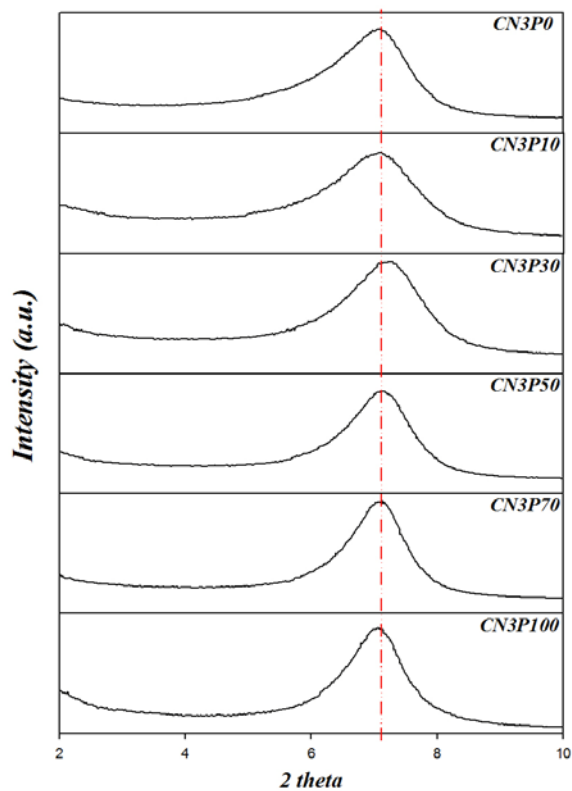


Figure 6-5. SEM micrographs (x 5,000) of cross-section areas of obtained highly filled nanocomposite film specimens (a) CN3P0, (b) CN3P10, (c) CN3P30, (d) CN3P50, (e) CN3P70 and (f) CN3P100

(a)



(b)

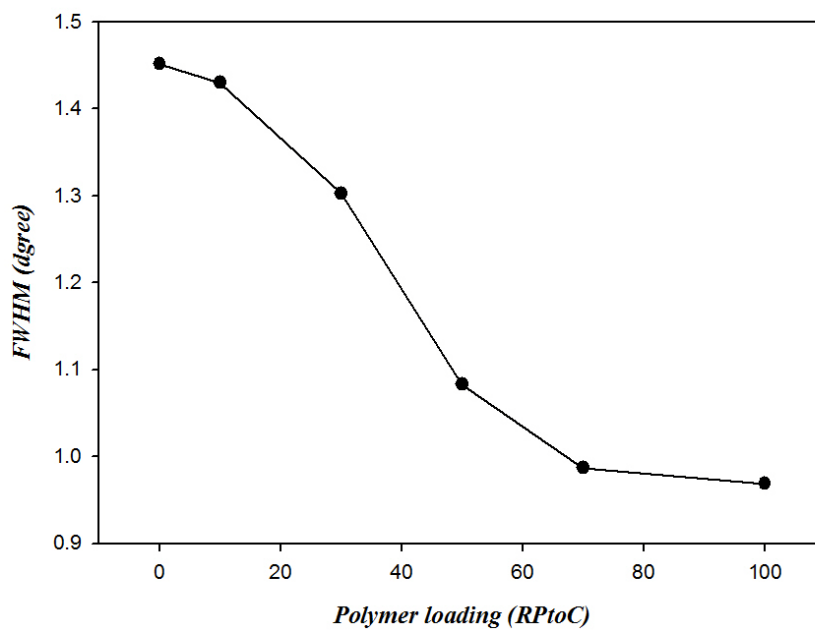


Figure 6-6. (a) X-ray diffraction patterns for CN3P0, P10, P30, P50, P70, and P100; (b) a FWHM as a function of polymer loadings

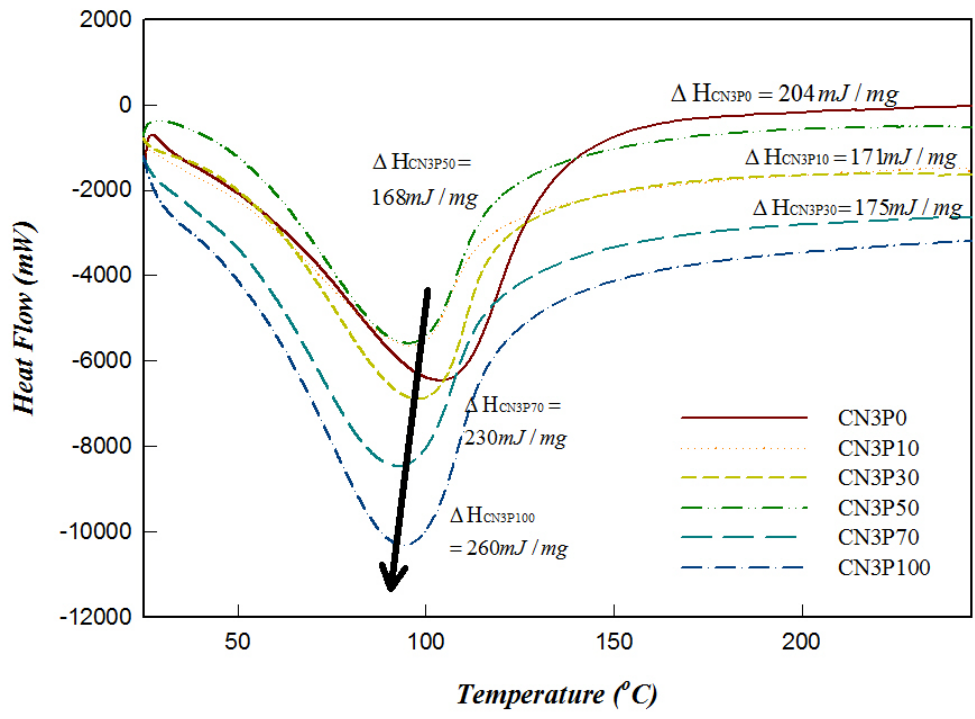


Figure 6-7. DSC thermograms of highly filled nanocomposite films with various amounts of polymer

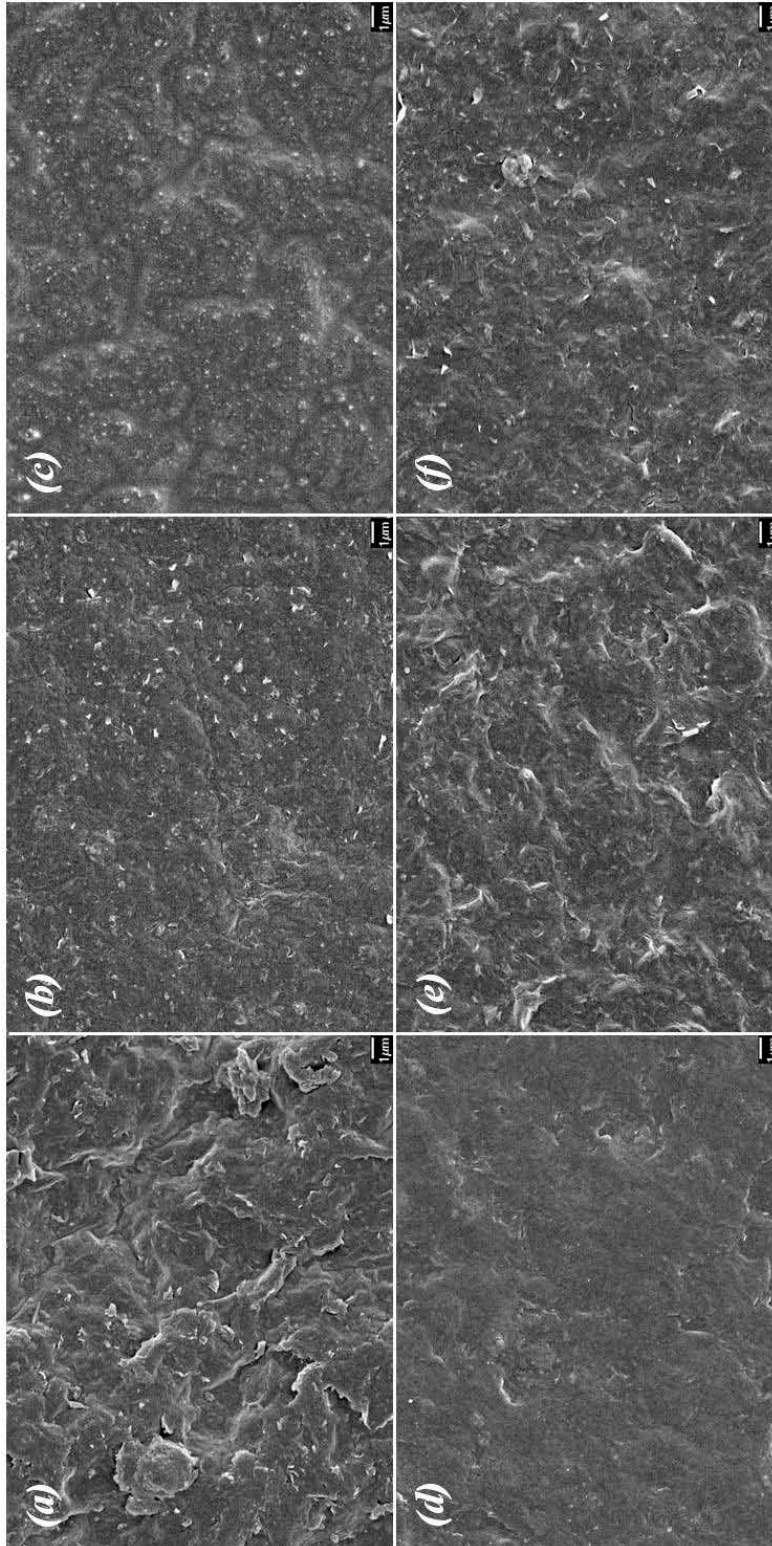


Figure 6-8. SEM micrographs (x 5,000) of surface areas of obtained highly filled nanocomposite film specimens (a) CN3P0, (b) CN3P10, (c) CN3P30, (d) CN3P50, (e) CN3P70 and (f) CN3P100

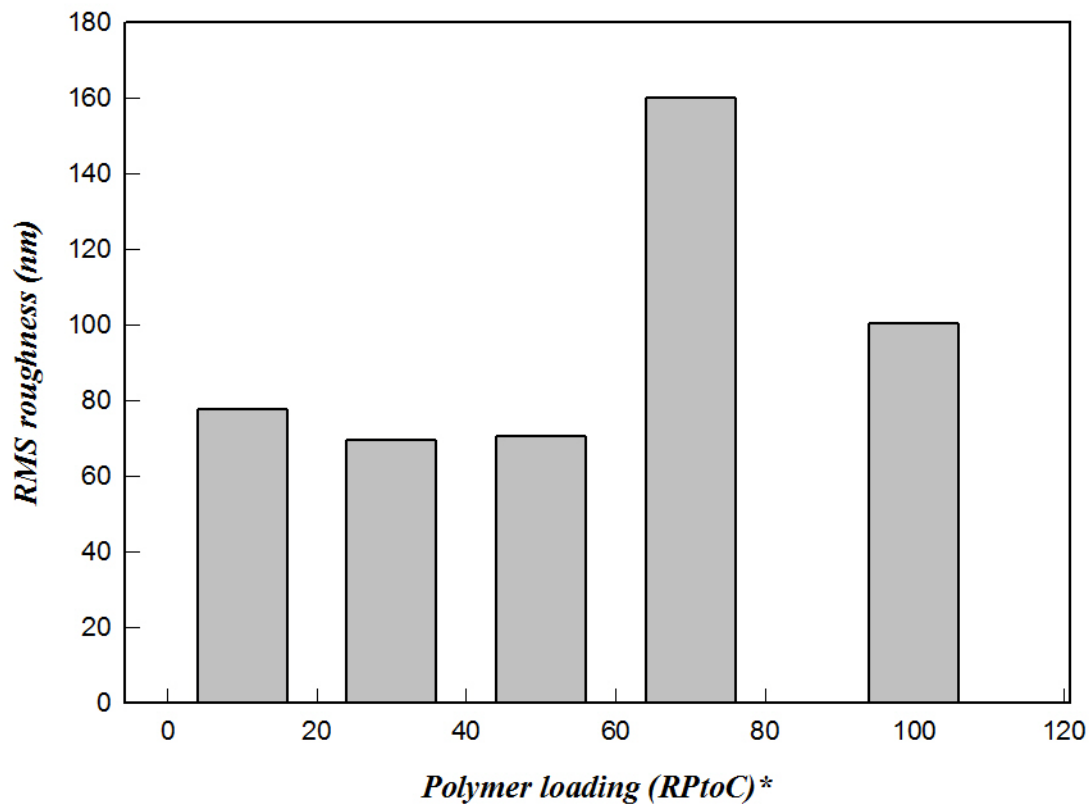


Figure 6-9. Dependence of RMS on the amount of polymer in highly filled nanocomposite films



Figure 6-10. An expected schematic picture of protruded curved edge of tactoids from the surface of CN3P70. Covered region (grey scale) with excess PAA lowered roughness by removing micro roughness on the surface. (Entangled lines and stacked bold lines represent polymer chains and tactoids, respectively)

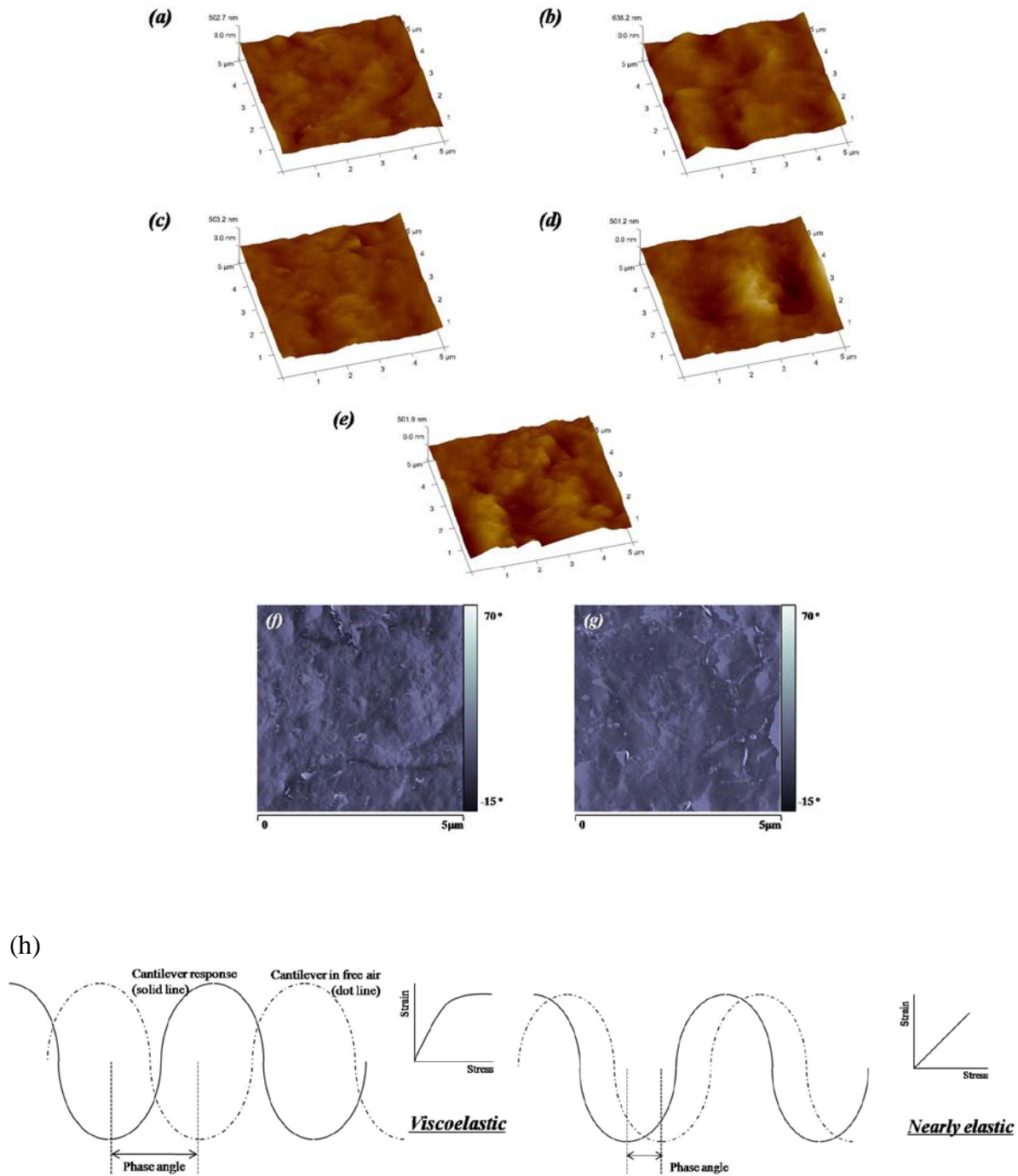


Figure 6-11. 3D height contrast images taken by AFM (tapping mode) on a $5 \times 5 \mu\text{m}^2$ on (a) CN3P10, (b) CN3P30, (c) CN3P50, (d) CN3P70, (e) CN3P100; 2D phase contrast images taken by AFM (tapping mode) on a $5 \times 5 \mu\text{m}^2$ on (f) CN3P10, (g) CN3P100; Schematic diagram to illustrate the definition of phase angle shown in (h) [152]

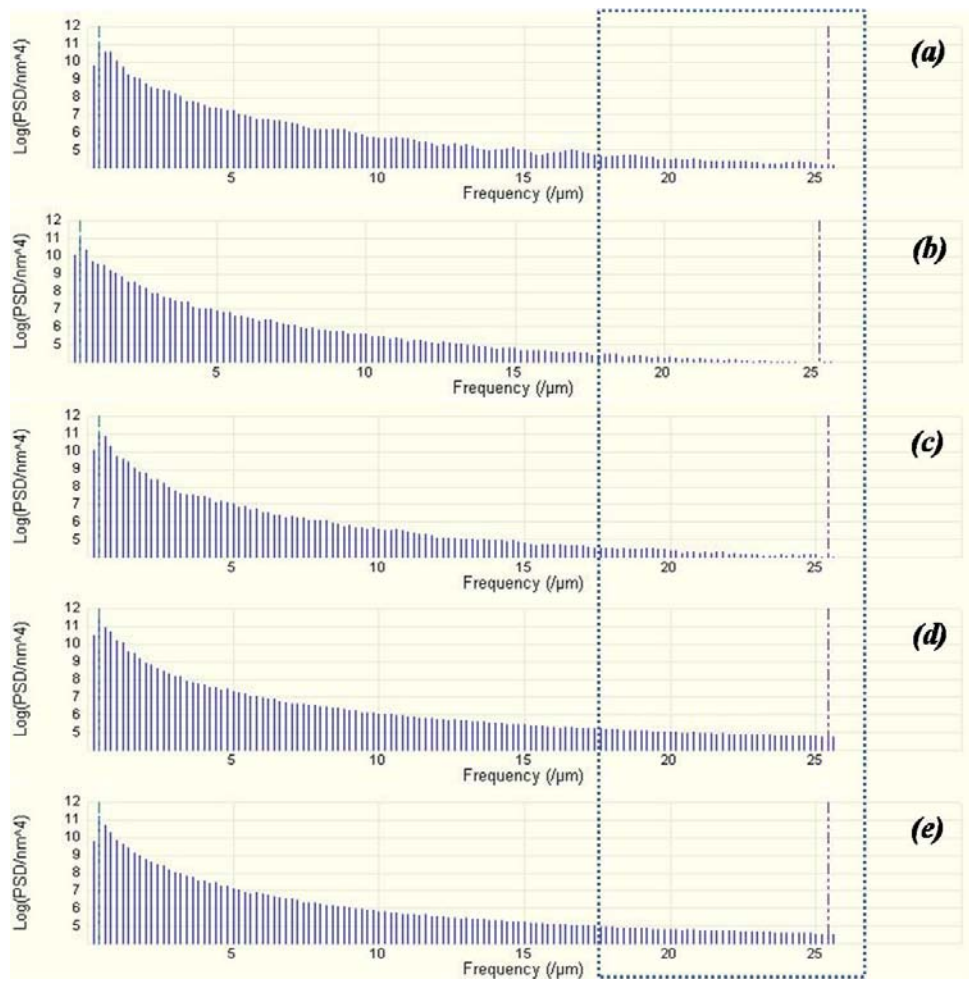


Figure 6-12. Power spectral density diagrams of highly filled nanocomposite samples (a) CN3P10, (b) CN3P30, (c) CN3P50, (d) CN3P70 and (e) CN3P100

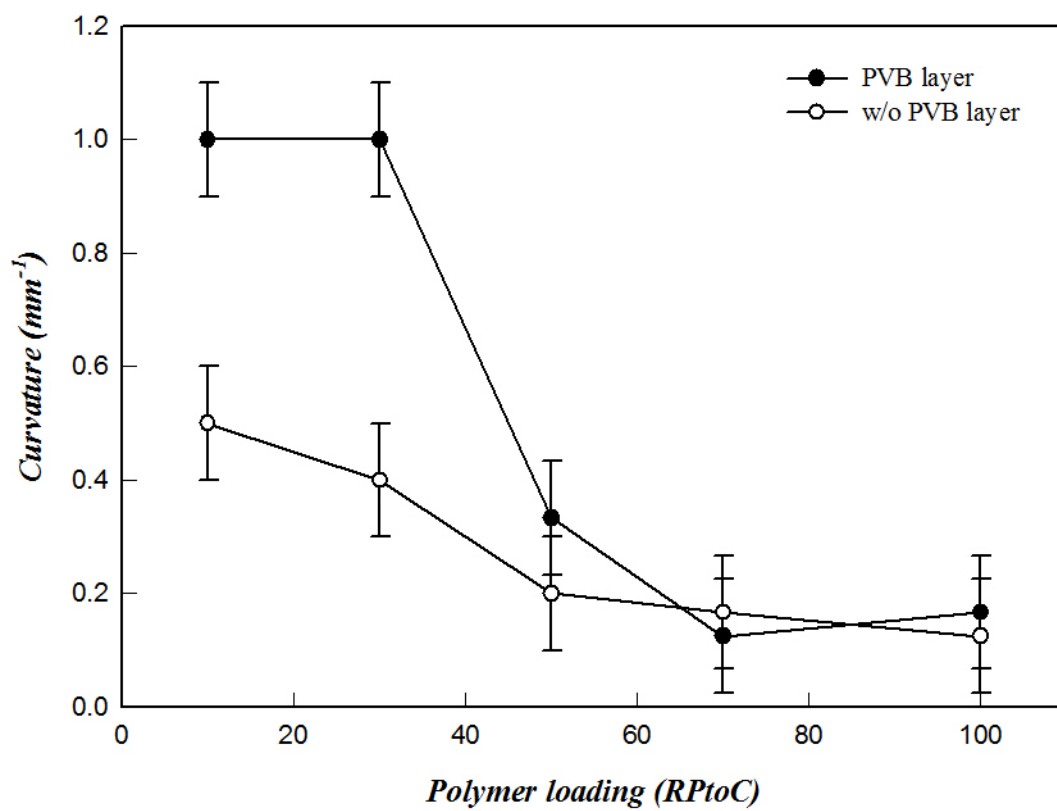


Figure 6-13. Curvature of highly filled nanocomposite films with various amounts of polymer and a picture of a flexible film specimen (CN3P50)

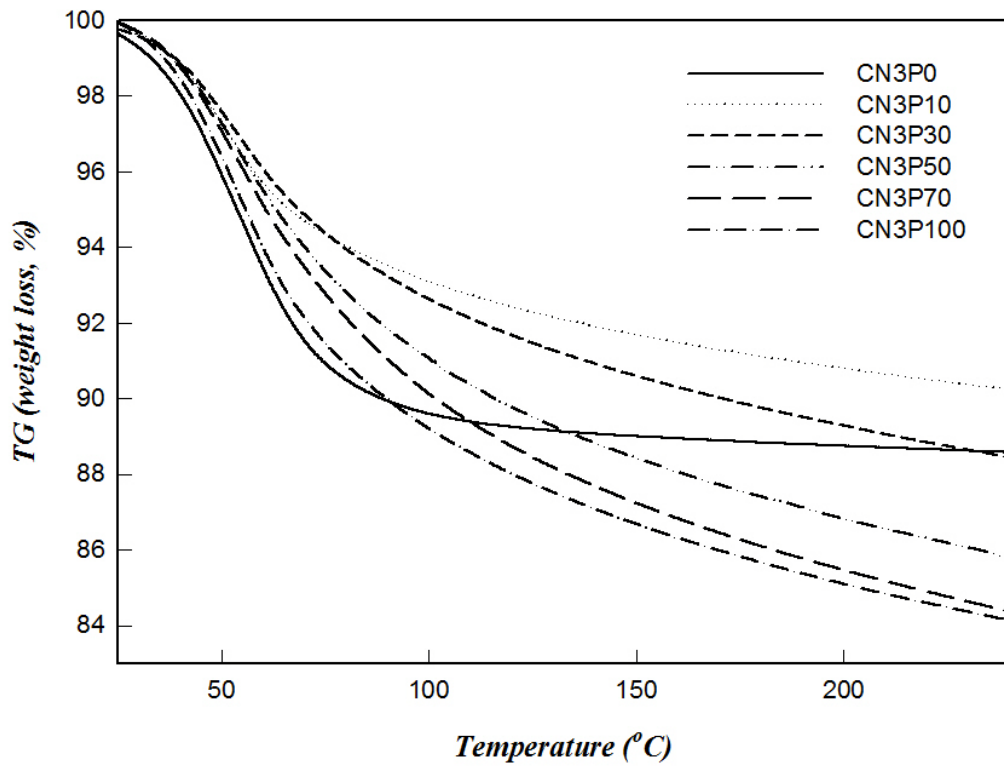


Figure 6-14. TGA thermograms of highly filled nanocomposite films with various amounts of polymer

CHAPTER 7 CONCLUSIONS

The hypothesis and resulting major findings from each section were addressed in this chapter based on the work done so far as following;

Chapter 1:

- Typical three conventional microstructures (phase-separated, intercalated and exfoliated structure) of layered silicate particles in the polymer matrix and their correlations to the barrier property of resulting materials were introduced with the fundamental concept for barrier function of a polymer clay nanocomposite (PCN) material.

Chapter 2:

- Controlling microstructure of filler particles in practical PCN systems is a key factor to achieve an effective barrier material. This chapter has reviewed variables which have effects on the formation of certain microstructure of layered silicate particle in actual PCN systems from the stage of the materials selection to processing parameters.
- To maximize physical properties of PCN material, interplay among three main components, polymer matrix, nanoclays and organic molecules covering these nanoclays and other processing parameters has to be considered.
- A variety of microstructures of PCN have been reported under various actual conditions. A practical PCN material can be defined as a broad mixture of intercalated and exfoliated structure with different ratios and a dominating structure representing whole composite systems determines physical properties of resulting PCN materials.

- Several models have been suggested to design a PCN material with better barrier properties. All existing barrier models are based on Nielsen's detour theory and conform well to results of permeability of practical PCN systems. And there were two common points for all barrier models. First, barrier property was enhanced with increasing total volume fraction of filler particles. Secondly it was noted that the larger aspect ratio promised better barrier properties.

Chapter 3:

- Works in Chapter 3 demonstrated the potential for PCN coatings to enhance barrier performance of packaging materials.
- PCN, which consists of Laponite in poly(vinyl alcohol) (PVA) matrix, coated polypropylene (PP), polyolefin after atmospheric pressure plasma (APP) surface treatment showed a good barrier performance. Oxygen transmission rate (OTR) value of PP was reduced from 150 to 10 cc/m²/day when coated with a PCN solution containing 50 wt% of filler particle.
- As a result of AFM study, it was found that two optimum conditions for the APP treatments promising the highest level of surface roughness and the lowest permeabilities were 18 l/min of nitrogen flow rate and below 20 mm of working distance.
- Through XRD analysis, it was found that an exfoliated structure of PCN sample was obtained after a high shear mixing process. However, when filler content increased above 60 wt%, an intercalated feature was detected because of restacked filler particles in limited volumetric spaces of polymer matrix.

- OTR values showed a general barrier tendency that barrier property is enhanced with increasing volume fraction of filler particle. However, as a result of restacked particles at above 60 wt%, diffusion length of gas molecules was reduced resulting in sharp increase in OTR values.

Chapter 4:

- To obtain better barrier properties and to maintain a good barrier properties under various conditions, an extended tortuous path models using clay platelets as a major component and polymer as a linkage molecules (Highly-filled PCN material) was suggested as a new barrier solution in Chapter 4
- Using a unique ‘A house of cards’ structure of Laponite JS and negatively charged poly(acrylic acid) (PAA), microstructures can approach a densely stratified structures through the face-to-face attachment of clay platelets.
- Identification of ‘a house of cards’ structure of Laponite JS in an aqueous solution was found by forming a clay aerogel through a freezing and drying process. Transmission electron microscopy (TEM) micrographs of a clay aerogel showed well three typical morphological features of the microstructure, which are tilted, edge-standing and paralleled position.
- The behavior of PAA chain in highly filled PCN coating solution depending on pH was examined by EDS test and, in conclusion, PAA chain in the coating solution prepared under pH level of isoelectric point of PAA was entangled each other with the small amount of embedded clay platelets.

- PAA in basic condition played a role as a linkage molecule to realize edge-to-edge contact between clay platelets, the lowest OTR value about 10 cc/m²/day was obtained for negatively charged PAA based-PCN coated PP.
- A significant amount of cracks on the surface were observed by scanning electron microscopy (SEM) when PP was coated with PCN coating solution that were prepared at pH 2 and 4, and these cracks resulted in sharp increase in OTR value to 120 cc/m²/day.

Chapter 5:

- Barrier model to estimate relative permeability (R_p) of PCN containing two different particle types (PC2N) have been proposed in Chapter 5. Initial purpose of this microstructure, PC2N, was to explore the benefits of dispersing smaller platelets between larger sheets such as Cloisite.
- Based on Nielsen's detour theory (Nielsen, 1967), Xu's barrier model (Xu et al., 2006) and a definition of effective volume from Saunder (Saunders et al., 1999), the barrier formula for PC2N microstructure was obtained as following equation:

$$R_p = \frac{2H_1(1-\phi_T)}{\left(L_1 + L_2 \left(\frac{\phi_2}{v_{eff 2}} \right) \right) + 2H_1}, \text{ where, } L_1, L_2 \text{ and } H_1 \text{ can be defined as lateral}$$

length including edge-to-edge distance, (l_1+b_1) and (l_2+b_2) of clay 1 and 2 and vertical length (h_1+w_1) occupied by clay 1 per unit volume, respectively. (Refer to Chapter 5 for specific details)

- However, contrary to initial expectations, it was concluded based on the comparison with actual experimental results that total volume fraction of filler

particles in a composite material determines barrier properties regardless of specific ratio between two particle types.

- Prepared PC2N composite films were beneficial in terms of their relatively light weight and improved optical transmittance by mixing two clay types due to lower density and smaller size particle which is advantageous for elastic light scatterings.
- This work suggested that characteristics of each type of clay particles in the PC2N composite can be manipulated and designed to enhance the physical properties while maintaining good barrier properties.

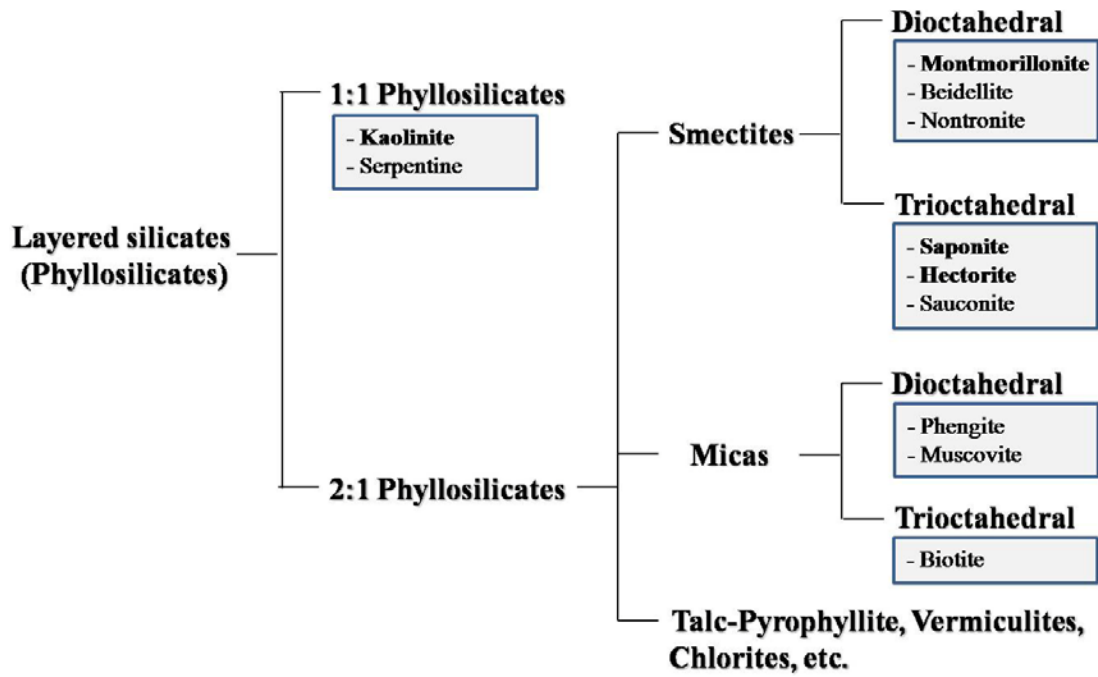
Chapter 5:

- Cloisite Na⁺ platelets form a paralleled oriented microstructure due to their larger aspect ratio and high particle density. Thus it was possible to form a flexible self-supporting highly filled PCN film through edge-to-edge attachments using negatively charged PAA chains
- Barrier tendency with polymer loading of prepared highly filled PCN film samples was opposite to the general barrier tendency of normal PCN material based on Nielsen's detour theory. This is because that different polymer loading resulted in different morphological features varying barrier properties of prepared samples. Morphology of cross sectional area, Crystallinity tendency and microstructure study obtained through SEM, XRD and DSC analysis also conformed well to the barrier tendency with polymer for these samples. Average OTR value of prepared films was 0.5 cc/m²/day and the lowest OTR of 0.1 cc/m²/day was found when PCN film containing 50 wt% of polymer loading was coated with exterior PVB layer.

- To investigate effects of surface morphological feature of PCN films on barrier properties, RMS values and PSD diagram were obtained. As a result of these AFM studies, it was concluded that PCN film containing 41 wt% of PAA showed the highest level of surface roughness and this was because the highest level of microroughness caused by protruded curved edges of stacked clay tactoids.
- Flexible highly-filled PCN film is usually prepared by obtaining densely stratified microstructure and sufficient amount of water molecules in the whole composite system. However, flexibilities of these specific samples were determined by water molecules existing in PAA linkage molecules and clay platelets themselves. Through SEM micrographs, curvature test and thermal analysis, it was found that 23 -33 wt% of PAA loading promised the best flexibility of prepared PCN films.
- Exterior poly(vinyl butyral) (PVB) layer was able to contribute to better barrier properties and flexibility. PVB exterior layer was not delaminated from PCN film proving that PVB layer adhered well to the PCN film by preventing the initial delamination of brittle clay platelets effectively resulting in an increase in curvature and PVB layer also contributed to enhancing barrier property by preventing direct diffusion of gas molecules. For example, CN3P30 showed changes in curvature from 0.4 to 1.0 mm⁻¹ and in OTR values from 0.8 to 0.5 cc/m²/day. And optimum range of PAA contents to achieve good flexibility and barrier property at the same time was 30 -35 wt%.

I hope that these results will be useful to those who want to do research in the fascinating field of PCN materials.

APPENDIX A
CLASSIFICATION OF COMMONLY USED LAYERED SILICATES



APPENDIX B
 COMMERCIALLY AVAILABLE ORGANOCCLAYS AND ORGANIC MOLECULES USED
 FOR THE MODIFICATION OF THE SURFACE OF NANOCCLAYS

Commercial Name	Class	Modifier
Nanofil 757	Natural MMT (MMT-Na ⁺)	NONE
Nanofil 919	Modified MMT	Dimethyl (Benzylmethyl) tallow* quaternary ammonium
Nanofil 804	Modified MMT	bis(2-hydroxyethyl) hydrogenated tallow ammonium
Nanofil 32	Modified MMT	alkylbenzyltrimethylammonium (benzalkonium)
Nanofil 15	Modified MMT	Dimethyl dihydrogenated tallow ammonium
Cloisite Na+	Natural MMT (MMT-Na ⁺)	NONE
Cloisite 15A	Modified MMT	dimethyl,dehydrogenated tallow ammonium
Cloisite 20A	Modified MMT	Dimethyl dihydrogenated tallow ammonium
Cloisite 25A	Modified MMT	dimethyl 2-ethylhexyl (hydrogenated tallow alkyl) ammonium
Cloisite 30B	Modified MMT	methyl tallow bis-2-hydroxyethyl quaternary ammonium
Nanomer-I.44P	Modified MMT	dimethyldialkyl quaternary ammonium
Nanomer-I.30E	Modified MMT	Octadecylamine quaternary ammonium

*tallow represents a mixture of long alkyl homologues with octadecyl the most prominent component.

LIST OF REFERENCES

1. Fornes, T.D., Yoon, P.J., Keskkula, H., and Paul, D.R. (2001). Nylon 6 Nanocomposites: The Effect of Matrix Molecular Weight, *Polymer*, 42: 9929-9940.
2. Yoo, Y., Shah, R.K., and Paul, D.R. (2007). Fracture Behavior of Nanocomposites Based on Poly(ethylene-co-methacrylic acid) Ionomers, *Polymer*, 48: 4867-4873.
3. Kim, D.H., Fasulo, P.D., Rodgers, W.R., and Paul, D.R. (2007). Structure and Properties of Polypropylene-Based Nanocomposites: Effect of PP-g-MA to Organoclay Ratio, *Polymer*, 48: 5308-5323.
4. Kojima, Y., Usuki, A., Kawasumi, M., Okada, A., Fukushima, Y., Kurauchi, T., and Kamigaito, O. (1993). Mechanical Properties of Nylon 6-clay Hybrid, *J. Mater. Res.*, 8: 1185-1189.
5. Podsiadlo, P., Kaushik, A.K., Arruda, E.M., Waas, A.M., Shim, B.S., Xu, J., Nandivada, H., Pumphlin, B.G., Lahann, J., Ramamoorthy, A., and Kotov N.A. (2007). Ultrastrong and Stiff Layered Polymer Nanocomposites, *Science*, 318: 80-83.
6. Lange, J., and Wyser, Y. (2003). Recent Innovations in Barrier Technologies for Plastic Packaging – A Review, *Packag. Technol. Sci.*, 16: 149-158.
7. Osman, M.A., Mittal, V., Morbidelli, M., and Suter, U.W. (2003). Polyurethane Adhesive Nanocomposites as Gas Permeation Barrier, *Macromolecules*, **36**: 9851-9858.
8. Amberg-schwab, S., Hoffmann, M., Bader, H., and Gessler, M. (1998). Inorganic-Organic Polymers with Barrier Properties for Water Vapor, Oxygen and Flavors, *J. of Sol-Gel Sci. and Technol.*, **1/2**: 141-146.
9. Triantafyllidis, K.S., LeBaron, P.C., Park, I., and Pinnavaia, T.J. (2006). Epoxy-clay Fabric Film Composites with Unprecedented Oxygen-Barrier Properties, *Chem. Mater.*, **18**: 4393-4398.
10. Anilkumar, S., Kumaran, M.G., and Thomas, S. (2008). Characterization of EVA/clay Nanocomposite Membranes and Its Pervaporation Performance, *J. Phys. Chem. B*, **112**: 4009-4015.
11. Thomassin, J-M., Pagnouille, C., Caldarella, G., Germain, A., and Jérôme, R. (2006). Contribution of Nanoclays to The Barrier Properties of A Model Proton Exchange Membrane for Fuel Cell Application, *J. of Mem. Sci.*, **270**: 50-56.
12. Duangkaew, P., and Wootthikanokkhan, J. (2008). Methanol Fuel Cell Membranes Based on Sulfonated Poly(vinyl alcohol)-Layered Silicate Nanocomposites, *J. Appl. Polym. Sci.*, **109**: 452-458.
13. Sridhar, V., and Tripathy, D.K. (2006). Barrier Properties of Chlorobutyl Nanoclay Composites, *J. Appl. Polym. Sci.*, **101**: 3630-3637.

14. Choi, W.J., Kim, H.J., Yoon, K.H., Kwon, O.H., and Hwang, C.I. (2006). Preparation and Barrier Property of Poly(ethylene terephthalate)/Clay Nanocomposite Using Clay-Supported Catalyst, *J. Appl. Polym. Sci.*, **100**: 4875-4879.
15. Brulé, B., and Flat, J-J. (2006). High Barrier Polyamide/Polyolefin/Organoclay Nanocomposites, *Macromol. Symp.*, **233**: 210-216.
16. Baughman, R.H., Zakhidov, A.A., and De Heer W.A. (2002). Carbon Nanotubes-the Route Toward Applications, *Science*, **297**: 787-792.
17. Moniruzzaman, M., and Winey, K.I. (2006). Polymer Nanocomposites Containing Carbon Nanotubes, *Macromolecules*, **39**: 5194-5205.
18. Sandler, J.K.W., Kirk, J.E., Kinloch, I.A., Shaffer, M.S.P., and Windle, A.H. (2003). Ultra-Low Electrical Percolation Threshold in Carbon-Nanotube-Epoxy Composites, *Polymer*, **44**: 5893-5899.
19. Bryning, M.B., Islam, M.F., Kikkawa, J.M., and Yodh, A.G. (2005). Very Low Conductivity Threshold in Bulk Isotropic Single-Walled Carbon Nanotube-Epoxy Composites, *Adv. Mater.*, **17**: 1186-1191.
20. Kim, Y.S., Wright, J.B., and Grunlan J.C. (2008). Influence of Polymer Modulus on The Percolation Threshold of Latex-Based Composites, *Polymer*, **49**: 570-578.
21. Alt, V., Bechert, T., Steinrücke, P., Wagener, M., Seidel, P., Dingeldein, E., Domann, E., and Schnettler, R. (2004). An In Vitro Assessment of The Antibacterial Properties and Cytotoxicity of Nanoparticulate Silver Bone Cement, *Biomaterials*, **25**: 4383-4391.
22. Chen, C.Z., and Cooper, S.L. (2000). Recent Advances in Antimicrobial Dendrimers, *Adv. Mater.*, **12**: 843-846.
23. Damm, C., Münstedt, H., and Rösch, A. (2008). The Antimicrobial Efficacy of Polyamide 6/Silver-Nano- and Microcomposites, *Mater. Chem. Phys.*, **108**: 61-66.
24. Koros, W. (1990). Barrier Polymers and Structures: Overview. In: *Barrier Polymers and Structure*, pp 1-21, John Wiley & Sons Ltd, Chichester, UK.
25. Salame, M. (1986). Prediction of Gas Barrier Properties of High Polymers, *Polymer Eng. Sci.*, **26**: 1543-1546.
26. Prasad, T., and Brown, K. (1995). Permachor Method to Predict Diffusivity Coefficients of Organics in Aqueous Solutions in Flexible Membrane Liners, *Waste Management & Research*, **13**: 47-53.
27. Hiltner, A., Liu, R.Y.F., Hu, Y.S., and Bear, E. (2005). Oxygen Transport as A Solid-State Structure Probe for Polymeric Materials: A Review, *J. Polym. Sci. B: Polym. Phys.*, **43**: 1047-1063.

28. Dhoot, S.N. (2004). Sorption and Transport of Gases and Organic Vapors in Poly(ethylene terephthalate), The University of Texas at Austin, Dissertation of Doctor of Philosophy.
29. Jang, J., and Lee, D.K. (2004). Oxygen Barrier Properties of Biaxially Oriented Polypropylene/Polyvinyl Alcohol Blend Films, *Polymer*, **45**: 1599-1607.
30. Petropoulos, J.H., Paul, D.R., and Yampol'ski, Y.P. (1994). In *Polymeric Gas Separation Membranes*. CRC Press, Boca Raton, FL.
31. Nielsen, L.E. (1967). Models for The Permeability of Filled Polymer Systems, *J Macromol. Sci. (Chem)*, **A1**: 929-942.
32. Yu, Y-H., Lin, C-Y., Yeh, J-M., and Lin, W-H. (2003). Preparation and Properties of Poly(vinyl alcohol)-Clay Nanocomposite Materials, *Polymer*, **44**: 3553-3560.
33. Ginzburg, V.V., Singh, C., and Balazs, A.C. (2000). Theoretical Phase Diagrams of Polymer/Clay Composites: The Role of Grafted Organic Modifiers, *Macromolecules*, **33**: 1089-1099.
34. Vaia, R.A., Jandt, K.D., Kramer, E.J., and Giannelis, E. P. (1996). Microstructural Evolution of Melt Intercalated Polymer-Organically Modified Layered Silicates Nanocomposites, *Chem. Mater.*, **8**: 2628-2635.
35. Vaia, R.A., and Wagner, H.D. (2004). Frameworks for Nanocomposites, *Materials Today*, **Nov**: 32-37.
36. Illett, S.M., Orrock, A., Poon, W.C.K., and Pusey, P.N. (1995). Phase Behavior of A Model Colloid-Polymer Mixture, *Phys. Rev. E*, **51**: 1344-1352.
37. Dijkstra, M., and van Roij, R. (1997). Entropy-Driven Demixing in Binary Hard-Core Mixtures: from Hard Spherocylinders Towards Hard Spheres, *Phys. Rev. E*, **56**: 5594-5602.
38. Dijkstra, M., Hansen, J.P., and Madden, P. A. (1997). Statistic Model for The Structure and Gelation of Smectites Clay Suspensions, *Phys. Rev. E*, **55**: 3044-3053.
39. Malwitz, M.M., Lin-Gibson, S., Hobbie, E.K., Butler, P.D., and Schmidt, G. (2003). Orientation of Platelets in Multilayered Nanocomposite Polymer Films, *J. Polym. Sci. B: Polym. Phys.*, **41**: 3237-3248.
40. Mermut, A.R., and Lagaly, G. (2001). Baseline Studies of The Clay Minerals Society Source Clays: Layer-Charge Determination and Characteristics of Those Minerals Containing 2:1 Layers, *Clays and Clay Minerals*, **49(5)**: 393-397.
41. Usuki, A., Kawasumi, M., Kojima, Y., Okada, A., Kurauchi, T., and Kamigaito, O. (1993). Swelling Behavior of Montmorillonite Cation Exchanged for ω -amino Acids by ϵ -Caprolactam, *J. Mater. Res.*, **8**: 1174-1178.

42. Picard, E., Gauthier, H., Gérard, J.-F., and Espuche, E. (2007). Influence of The Intercalated Cations on The Surface Energy of Montmorillonites: Consequences for The Morphology and Gas Barrier Properties of Polyethylene/Montmorillonites Nanocomposites, *J. Colloid and Interface Sci.*, **307**: 364-376.
43. Zhang, W., Chen, D., Zhao, Q., and Fang, Y. (2003). Effects of Different Kinds of Clay and Different Vinyl Acetate Content on The Morphology and Properties of EVA/Clay Nanocomposites, *Polymer*, **44**: 7953-7961.
44. Grunlan J.C., Grigorian, A., Hamilton, C.B., and Mehrabi, A.R. (2004). Effects of Clay Concentration on The Oxygen Permeability and Optical Properties of A Modified Poly(vinyl alcohol), *J. Appl. Polym. Sci.*, **93**: 1102-1109.
45. Demirkol, E.A., and Kalyon, D.M. (2007). Batch and Continuous Processing of Polymer Layered Organoclay Nanocomposites, *J. Appl. Polym. Sci.*, **104**: 1391-1398.
46. Lee, E.C., Mielewski, D.F., and Baird, R.J. (2004). Exfoliation and Dispersion Enhancement in Polypropylene Nanocomposites by In-situ Melt Phase Ultrasonication, *Polym. Eng. And Sci.*, **44**: 1773-1782.
47. Lee, S.S., Hur, M.H., Yang, H., Lim, S., and Kim, J. (2006). Effect of Interfacial Attraction on Intercalation in Polymer/Clay Nanocomposites, *J. Appl. Polym. Sci.*, **101**: 2749-2753.
48. Gerasin V.A., Bakhov, F.N., Merekalova, N.D., Korolev, Yu.M., Zubova, T.L., and Antipov, E.M. (2005). Influence of The Structure of A Modifier Layer on The Compatibility of Polymers with A Modified Montmorillonite, *J Eng. Phys. And Thermophys.*, **78**: 871-877.
49. Osman, M.A., Mittal, V., Morbidelli, M., and Suter, U.W. (2004). Epoxy-Layered Silicate Nanocomposites and Their Gas Permeation Properties, *Macromolecules*, **37**: 7250-7257.
50. Borse, N.K., and Kamal, M.R. (2009). Estimation of Stresses Required for Exfoliation of Clay Particles in Polymer Nanocomposites, *Polym. Eng. And Sci.*, **10**: 641-650.
51. Wagener, R., and Reisinger, T.J.G. (2003). A Rheological Method to Compare The Degree of Exfoliation of Nanocomposites, *Polymer*, **44**: 7513-7518.
52. Chang, J.H., Seo, B.S., and Hwang, D.H. (2002). An exfoliation of organoclay in thermotropic liquid crystalline polyester nanocomposites, *Polymer*, **43**: 2969-2974.
53. Park, J.H., and Jana, S.C. (2003). Mechanism of Exfoliation of Nanoclay Particles in Epoxy-Clay Nanocomposites, *Macromolecules*, **36**: 2758-2768.
54. Fu, X., and Qutubuddin, S. (2001). Polymer-Clay Nanocomposites: Exfoliation of Organophilic Montmorillonite Nanoclays in Polystyrene, *Polymer*, **42**: 807-813.

55. Kwak, J.W., Welt, B., and Beatty, C. (2009). Enhancement of Oxygen Barrier with Polymer Clay Nanocomposite Coatings on Polypropylene Treated with Atmospheric Pressure Plasma, *J Appl. Packag. Res.*, **3**: 39-56.
56. Lepoittevin, B., Pantoustier, N., Devalckenaere, M., Alexandre, M., Calberg, C., Jérôme, R., Henrist, C., Rulmont, A., and Dubois, P. (2003). Polymer/Layered Silicate Nanocomposites by Combined Intercalative Polymerization and Melt Intercalation: A Masterbatch Process, *Polymer*, **44**: 2033-2040.
57. Zerda, A.S., Caskey, T.C., and Lesser, A.J. (2003). Highly Concentrated, Intercalated Silicate Nanocomposites: Synthesis and Characterization, *Macromolecules*, **36**: 1603-1608.
58. Yu, Z.Z., Yang, M., Zhang, Q., Zhao, C., and Mai, Y.W. (2003). Dispersion and Distribution of Organically Modified Montmorillonite in Nylon-66 Matrix, *J. Polym. Sci. B: Polym. Phys.*, **41**: 1234-1243.
59. Hamaker, H.C. (1937). The London-Van der Waals Attraction Between Spherical Particles, *Physica*, **4**: 1058-1072.
60. Koo, C.M., Kim, S.O., and Chung, I.J. (2003). Study on Morphology Evolution, Orientation Behavior, and Anisotropic Phase Formation of Highly Filled Polymer-Layered Silicate Nanocomposites, *Macromolecules*, **36**: 2748-2757.
61. Lin-Gibson, S., Schmidt, G., Kim, H., Han, C.C., and Hobbie, E.K. (2003). Shear-Induced Mesostructure in Nanoplatelets-Polymer Network, *J. Chem. Phys.*, **119**: 8080-8083.
62. Okamoto, M., Nam, P.H., Maiti, P., Kotaka, T., Hasegawa, N., and Usuki, A. (2001). A House of Cards Structure in Polypropylene/Clay Nanocomposites Under Elongational Flow, *Nanoletters*, **1**: 295-298.
63. Bharadwaj, R.K., Mehrabi, A.R., Hamilton, C., Trujillo, C., Murga, M., Fan, R., Chavira, A., and Thompson, A.K. (2002). Structure-Property Relationships in Cross-Linked Polyester-Clay Nanocomposites, *Polymer*, **43**: 3699-3705.
64. Ha, Y.H., Kwon, Y., Breiner, T., Chan, E.P., Tzianetopoulou, T., Cohen, R.E., Boyce, M.C., and Thomas, E.L. (2005). An Orientationally Ordered Hierarchical Exfoliated Clay-Block Copolymer Nanocomposite, *Macromolecules*, **38**: 5170-5179.
65. Ebina, T., and Mizukami, F. (2007). Flexible Transparent Clay Films with Heat-Resistant and High Gas-Barrier Properties, *Adv. Mater.*, **19**: 2450-2453.
66. Tetsuka, H., Ebina, T., Nanjo, H., and Mizukami, F. (2007). Highly Transparent Flexible Clay Films Modified with Organic Polymer: Structural Characterization and Intercalation Properties, *J. Mater. Chem.*, **17**: 3545-3550.

67. Sagitova, E.A., Prokhorov, K.A., Nikolaeva, G.Yu., Pashinin, P.P., Gerasin, V.A., Guseva, M.A., and Antipov, E.M. (2008). Quantitative Characterization of The Orientation of Macromolecules in Intercalated Nanocomposites of Polyolefins/Layered Silicates by Raman Spectroscopy, *Laser Physics*, **18**: 868-881.
68. Russo, G.M., Simon, G.P., and Incarnato, L. (2006). Correlation Between Rheological, Mechanical, and Barrier Properties in New Copolyamide-Based Nanocomposite Films, *Macromolecules*, **39**: 3855-3864.
69. Gopakumar, T.G., Lee, J.A., Kontopoulou, M., and Parent, J.S. (2002). Influence of Clay Exfoliation on The Physical Properties of Montmorillonite/Polyethylene Composites, *Polymer*, **43**: 5483-5491.
70. Famulari, A., Arosio, P., Filippi, S., Marazzato, C., Magagnini, P., Minkova, L., and Meille, S.V. (2007). Clay-Induced Preferred Orientation in Polyethylene/Compatibilized Clay Nanocomposites, *J Macromol. Sci. B: phys.*, **46**: 355-371.
71. Mishra, A.K., Nando, G.B., and Chattopadhyay, S. (2008). Exploring Preferential Association of Laponite and Cloisite with Soft and Hard Segments in TPU-Clay Nanocomposite Prepared by Solution Mixing Technique, *J. Polym. Sci. B: Polym. Phys.*, **46**: 2341-2354.
72. Chen, G., Liu, S., Zhang, S., and Qi, Z. (2000). Self-Assembly in A Polystyrene/Montmorillonite Nanocomposite, *Macromol. Rapid Commun.*, **21**: 746-749.
73. Strawhecker, K.E., and Manias, E. (2000). Structure and Properties of Poly(vinyl alcohol)/Na⁺ Montmorillonite Nanocomposites, *Chem. Mater.*, **12**: 2943-2949.
74. Weon, J.-I., and Sue, H.-J. (2005). Effects of Clay Orientation and Aspect Ratio on Mechanical Behavior of Nylon-6 Nanocomposite, *Polymer*, **46**: 6325-6334.
75. Fischer, H.R., Gielgen, L.H., and Koster, T.P.M. (1999). Nanocomposites from Polymers and Layered Minerals, *Acta Polym.*, **50**: 122-126.
76. Agag, T., and Takeichi, T. (2000). Polybenzoxazine-Montmorillonite Hybrid Nanocomposites: Synthesis and Characterization, *Polymer*, **41**: 7083-7090.
77. Fornes, T.D., Yoon, P.J., Hunter, D.L., Keskkula, H., and Paul, D.R. (2002). Effect of Organoclay Structure on Nylon 6 Nanocomposite Morphology and Properties, *Polymer*, **43**: 5915-5933.
78. Yeun, J.H., Bang, G.S., Park, B.J., Ham, S.K., and Chang, J.H. (2006). Poly(vinyl alcohol) Nanocomposite Films: Thermo-optical Properties, Morphology, and Gas Permeability, *J. Appl. Polym. Sci.*, **101**: 591-596.
79. Sorrentino, A., Tortora, M., and Vittoria, V. (2006). Diffusion Behavior in Polymer-Clay Nanocomposites, *J. Polym. Sci. B: Polym. Phys.*, **44**: 265-274.

80. Chang, J.H., and An, Y.U. (2002). Nanocomposites of Polyurethane with Various Organoclays: Thermomechanical Properties, Morphology, and Gas Permeability, *J. Polym. Sci. B: Polym. Phys.*, **40**: 670-677.
81. Chang, J.H., An, Y.U., and Sur, G.S. (2003). Poly(lactic acid) Nanocomposites with Various Organoclays. I. Thermomechanical Properties, Morphology, and Gas Permeability, *J. Polym. Sci. B: Polym. Phys.*, **41**: 94-103.
82. Deng, Y., Gu, A., and Fang, Z. (2004). The Effect of Morphology on The Optical Properties of Transparent Epoxy/Montmorillonite Composite, *Polym. Int.*, **53**: 85-91.
83. Takahashi, S., Goldberg, H.A., Feeney, C.A., Karim, D.P., Farrell, M., O'Leary, K., and Paul, D.R. (2006). Gas Barrier Properties of Butyl Rubber/Vermiculite Nanocomposite Coatings, *Polymer*, **47**: 3083-3093.
84. Takahashi, S., and Paul, D.R. (2006). Gas Permeation in Poly(ether imide) Nanocomposite Membranes Based on Surface-Treated Silica. Part 1: without Chemical Coupling to Matrix, *Polymer*, **47**: 7519-7534.
85. Property material data, Cloisite® Technical Data Sheets Link. Web address "<http://www.matweb.com/search/GetMatlsByTradename.aspx?navletter=C&tn=Cloisite%20AE>"
86. Dundigalla, A., Lin-Gibson, S., Ferreira, V., Malwitz, M.M., and Schmidt, G. (2005). Unusual Multilayered Structures in Poly(ethylene oxide)/Laponite Nanocomposite Films, *Macromol. Rapid Commun.*, **26**: 143-149.
87. Negrete-Herrera, N., Putaux, J-L., and Bourgeat-Lami, E. (2006). Synthesis of Polymer/Laponite Composite Latex Particles Via Emulsion Polymerization Using Silylated and Cation-Exchanged Laponite Clay Platelets, *Progr. in Solid State Chem.*, **34**: 121-137.
88. Kubies, D., Jrme, R., and Grandjean, J. (2002). Surfactant Molecules Intercalated in Laponite as Studied by C and Si MAS NMR, *Langmuir*, **18**: 6159-6163.
89. Mongondry, P., Tassin, J.F., and Nicolai, T. (2005). Revised State Diagram of Laponite Dispersions, *J. Colloid and Interface Sci.*, **283**: 397-405.
90. Cussler, E.L. (2007). Diffusion Barrier, *Diffusion Fundamentals*, **6**:72.1-72.12.
91. Gusev, A.A., and Lusti, H.R. (2001). Rational Design of Nanocomposites for Barrier Applications, *Adv. Mater.*, **13**: 1641-1643.
92. Fredrickson, G.H., and Bicerano, J. (1999). Barrier Properties of Oriented Disk Composites, *J. Chem. Phys.*, **110**: 2181-2188.
93. Xu, B., Zheng, Q., Song, Y., and Shangguan, Y. (2006). Calculating Barrier Properties of Polymer/Clay Nanocomposites: Effects of Clay Layers, *Polymer*, **47**: 2904-2910.

94. Klute, C.H. (1959). Diffusion of Small Molecules in Semicrystalline Polymers: Water in Polyethylene, *J. Appl. Polym. Sci.*, **1**: 340-350.
95. Saunders, J.M., Goodwin, J.W., Richardson, R.M., and Vincent, B. (1999). A Small-Angle Scattering Study of The Structure of Aqueous Laponite Dispersions, *J. Phys. Chem. B*, **103**: 9211-9218.
96. Bharadwaj, R.K. (2001). Modeling The Barrier Properties of Polymer-Layered Silicate Nanocomposites, *Macromolecules*, **34**: 9189-9192.
97. Balazs, A.C., Singh, C., and Zhulina, E. (1998). Modeling The Interactions Between Polymers and Clay Surfaces Through Self-Consistent Field Theory, *Macromolecules*, **31**: 8370-8381.
98. Kuznetsov, D.V., and Balazs, A.C. (2000). Scaling Theory for End-Functionalized Polymers Confined Between Two Surfaces: Predictions for Fabricating Polymer/Clay Nanocomposites, *J. Chem. Phys.*, **112**: 4365-4375.
99. Krook, M., Albertsson, A.-C., Gedde, U.W., and Hedenqvist, M.S. (2002). Barrier and Mechanical Properties of Montmorillonite/Polyesteramide Nanocomposites, *Polym. Eng. And Sci.*, **42**: 1238-1246.
100. Nah, C., Ryo, H.J., Kim, W.D., and Choi, S.S. (2002). Barrier Property of Clay/Acrylonitrile-Butadiene Copolymer Nanocomposite, *Polym. Adv. Technol.*, **13**: 649-652.
101. Kim, S.H., and Kim, S.C. (2007). Synthesis and Properties of Poly(ethylene terephthalate)/Clay Nanocomposites by In Situ Polymerization, *J. Appl. Polym. Sci.*, **103**: 1262-1271.
102. Choi, W.J., Kim, S.H., Kim, Y.J., and Kim, S.C. (2004). Synthesis of Chain-Extended Organifier and Properties of Polyurethane/Clay Nanocomposites, *Polymer*, **45**: 6045-6057.
103. Swain, S.K., and Isayev, A.I. (2007). Effect of Ultrasound on HDPE/Clay Nanocomposites: Rheology, Structure and Properties, *Polymer*, **48**: 281-289.
104. Thellen, C., Orroth, C., Froio, D., Ziegler, D., Lucciarini, J., Farrell, R., D'Souza, N.A., and Ratto, J.A. (2005). Influence of Montmorillonite Layered Silicate on Plasticized Poly(L-lactide) Blown Films, *Polymer*, **46**: 11716-11727.
105. Wang, Z.F., Wang, B., Qi, N., Zhang, H.F., and Zhang, L.Q. (2005). Influence of Fillers on Free Volume and Gas Barrier Properties in Styrene-Butadiene Rubber Studied by Positrons, *Polymer*, **46**: 719-724.

106. Wang, Y.Q., Wu, Y.P., Zhang, H.F., Zhang, L.Q., Wang, B., and Wang, Z.F. (2004). Free Volume of Montmorillonite/Styrene-Butadiene Rubber Nanocomposites Estimated by Positron Annihilation Lifetime Spectroscopy, *Macromol. Rapid Commun.*, **25**: 19773-19778.
107. Stephen, R., Ranganathaiah, C., Varghese, S., Joseph, K., and Thomas, S. (2006). Gas Transport Through Nano and Micro Composites of Natural Rubber (NR) and Their Blends with Carboxylated Styrene Butadiene Rubber (XSBR) Latex Membranes, *Polymer*, **47**: 858-870.
108. Cabedo, L., Giménez, E., Lagaron, J.M., Gavara, R., and Saura, J.J. (2004). Development of EVOH-Kaolinite Nanocomposites, *Polymer*, **45**: 5233-5238.
109. Lu, C., and Mai, Y.W. (2005). Influence of Aspect Ratio on Barrier Properties of Polymer-Clay Nanocomposites, *Phys. Rev. Lett.*, **95**: 088303(1)-008303(4).
110. Yano, K., Usuki, A., and Okada, A. (1997). Synthesis and Properties of Polyimide-Clay Hybrid Films, *J. Polym. Sci. A: Polym. Chem.*, **35**: 2289-2294.
111. Lape, N.K., Nuxoll, E.E., and Cussler, E.L. (2004). Polydisperse Flakes in Barrier Films, *J. of Mem. Sci.*, **236**: 29-37.
112. Beall, G.W. (2000). *In Polymer-Clay Nanocomposites*; Pinnavaia, T.J., and Beall, G.W. (eds), John Wiley & Sons Ltd, New York.
113. Ray, S.S., Okamoto, K., and Okamoto, M. (2003). Structure-Property Relationship in Biodegradable Poly(butylenes succinate)/Layered Silicate Nanocomposites, *Macromolecules*, **36**: 2355-2367.
114. Hambir, S., Bulakh, N., Kodgire, P., Kalgaonkar, R., and Jog, J.P. (2001). PP/Clay Nanocomposites: A Study of Crystallization and Dynamic Mechanical Behavior, *J. Polym. Sci. B: Polym. Phys.*, **39**: 446-450.
115. Gilman, J.W. (1999). Flammability and Thermal Stability Studies of Polymer Layered-Silicate (Clay) Nanocomposites, *Appl. Clay Sci.*, **15**: 31-49.
116. Kojima, Y., Usuki, A., Kawasumi, M., Okada, A., Karauchi, T., and Kamigaito, O. (1993). Sorption of Water in Nylon 6-clay Hybrid, *J. Appl. Polym. Sci.*, **49**: 1259-1264.
117. Messersmith, P.B., and Giannelis, E.P. (2003). Synthesis and Barrier Properties of Poly(ϵ -caprolactone)-Layered Silicate Nanocomposites, *J. Polym. Sci. A: Polym. Chem.*, **33**: 1047-1057.
118. Utracki, L.A., Sepehr, M., and Boccaleri, E. (2007). Review, Synthetic, Layered Nanoparticles for Polymeric Nanocomposites (PNCs), *Polym. Adv. Tech.*, **18**: 1-37.
119. Ray, S., Quek, S.Y., Eastal, A., and Chen, X.D. (2006). The Potential Use of Polymer-Clay Nanocomposites in Food Packaging, *Intl. J. Food Eng.*, **2**: 5-11.

120. Xu, W.B., Bao, S.P., and He, P.S. (2002). Intercalation and Exfoliation Behavior of Epoxy Resin/Curing Agent/Montmorillonite Nanocomposite. *J. Appl. Polym. Sci.*, **84**: 842-849.
121. Solarski, S., Benali, S., Rochery, M., Devaux, E., Alexandre, M., Monteverde, F., and Dubois, P. (2005). Synthesis of A Polyurethane/Clay Nanocomposite Used as Coating: Interactions Between The Counterions of Clay and The Isocyanate and Incidence on The Nanocomposite Structure, *J. Appl. Polym. Sci.*, **95**: 238-244.
122. Kato, M., Matsushita, M., and Fukumori, K. (2004). Development of A New Production Method for A Polypropylene-Clay Nanocomposite, *Polym. Eng. Sci.*, **44**: 1205-1211.
123. Lyoo, W.S., and Ha, W.S. (1996). Structure and Properties of Microfibrillar Poly(vinyl alcohol) Fibres Prepared by Saponification Under Shearing Force of Poly(vinyl pivalate), *Polymer*, **37**: 3121-3129.
124. Timofiychuk, O.A., Prudnicova, T.I., Mishurov, D.O., Avramenko, V.L., and Shevcovam R.G. (2009). Decomposition of Biodegradable Films Developed on The Basis of Poly(vinyl alcohol) in The Natural Environment, *Phys, Chem and Technol.*, **7**, 61-67.
125. Cendoya, I., López, D., Alegría, A., and Mijangos, C. (2001). Dynamic Mechanical and Dielectrical Properties of Poly(vinyl alcohol) and Poly(vinyl alcohol)-Based Nanocomposites, *J. Polym. Sci. B: Polym. Phys.*, **39**: 1968-1975.
126. Nakane, K., Yamashita, T., Iwakura, K., and Suzuki, F. (1999). Properties and Structure of Poly(vinyl alcohol)/Silica Composites, *J. Appl. Polym. Sci.*, **74**: 133-138.
127. Suzuki, F., Nakane, K., and Pias, J.S. (1996). Formation of A Compatible Composite of Silica/Poly(vinyl alcohol) Through The Sol-Gel Process and A Calcinated Product of The Composite, *J. Mater. Sci.*, **31**: 1335-1340.
128. Lagaly, G. (1986). *Smectitic Clays as Ionic Macromolecules*, Elsevier, London, UK.
129. Lagaly, G. (1999). Introduction: From Clay Mineral–Polymer Interactions to Clay Mineral–Polymer Nanocomposites, *Appl. Clay Sci.*, **15**: 1-9.
130. Tsai, B.C., and Jenkins, B.J. (1988). Effect of Retorting on The Barrier Properties of EVOH, *J. Plast. Film Sheet*, **4**: 63-71.
131. Iwanami, T., and Hirai, Y. (1983). Ethylene Vinyl Alcohol Resins for Gas-Barrier Material, *Tappi J.*, **66**: 85-90.
132. Schaper, E. (1989). Computer-Aided Barrier Design Yields Retortable Food Package, *Modern Plastics*, **66**: 94-99.
133. Tendero, C., Tixier, C., Tristant, P., Desmaison, J., and Leprince, P. (2006). Atmospheric Pressure Plasma: A Review, *Spectrochimica Acta Part B.*, **61**: 2-30.

134. Singh, N.L., Qureshi, A., Mukherjee, S., Rakshit, A.K., Tripathi, A., and Avasthi, D.K. (2007). Surface Modification of Polymeric Blends by Nitrogen Plasma Implantation, *Surface & Coating Tech.*, **201**: 8278-8281.
135. Maiti, M., and Bhowmick, A.K. (2006). New Insights into Rubber-Clay Nanocomposites by AFM Imaging. **47**: 6156-6166.
136. Ishida, H., Campbell, S., and Blackwell, J. (2001). General Approach to Nanocomposite Preparation, *Chem. Mater.*, **12**: 1260-1267.
137. Maiti, P., Nam, P.H., Hasegawa, M.ON., and Usuki, A. (2002). Influence of Crystallization on Intercalation, Morphology, and Mechanical Properties of Polypropylene/Clay Nanocomposites, *Macromolecules*, **35**: 2042-2049.
138. Wan, W., Yu, D., Xie, Y., Guo, X., Zhou, W., and Cao, J. (2006). Effects of Nanoparticle Treatment on The Crystallization Behavior and Mechanical Properties of Polypropylene/Calcium Carbonate Nanocomposites, *J. Appl. Polym. Sci.*, **102**: 3480-3488.
139. Lusti, H.R., Gusev, A.A., and Guseva, O. (2004). The Influence of Platelet Disorientation on The Barrier Properties of Composites: A Numerical Study, *Modelling Simul. Mater. Sci. Eng.*, **12**: 1201-1207.
140. Ogoshi, T., and Chujo, Y. (2005). Synthesis of Anionic Polymer-Silica Hybrids by Controlling pH in An Aqueous Solution, *Mater. Chem.*, **15**: 315-322.
141. Gudeman, L.F., and Peppas, N.A. (1995). pH-Sensitive Membranes from PVA/PAA Interpenetrating Network, *J. of membrane sci.*, **107**: 239-248.
142. Cummins, H.Z. (2007). Liquid, Glass, Gel: The Phases of Colloidal Laponite, *J. Non-Crystalline Solids*, **353**: 3891-3905.
143. Daniel, L.M., Frost, R.L., and Zhu, H.Y. (2008) Edge-Modification of Laponite with Dimethyl-octylmethoxysilane, *J. Colloid and Interface Sci.*, **321**: 302-309.
144. Stefanescu, E.A., Stefanescu, C., Daly, W.H., Schmidt, G., and Negulescu, I.I. (2008). Hybrid Polymer-Clay Nanocomposites: A Mechanical Study on Gels and Multilayered Films, *Polymer*, **49**: 3785-3794.
145. Stefanescu, E.A., Daly, W.H., and Negulescu, I.I. (2008). Hybrid Polymer/Clay Nanocomposites: Effect of Clay Size on The Structure of Multilayered Films, *Macromol. Mater. Eng.*, **293**: 651-656
146. Subramaniyan, A.K., and Sun, C.T. (2006). Enhancing Compressive Strength of Unidirectional Polymeric Composites Using Nanoclay, *Composites: Part A.*, **37**: 2257-2268.

147. Wang, S., Zhang, Y., Ren, W., Zhang, Y., and Lin, H. (2005). Morphology, Mechanical and Optical Properties of Transparent BR/Clay Nanocomposites, *Polymer Testing*, **24**: 766-774.
148. Cui, L., Hunter, D.L., Yoon, P.J., and Paul, D.R. (2008). Effect of Organoclay Purity and Degradation on Nanocomposite Performance, Part 2: Morphology and Properties of Nanocomposites, *Polymer*, **49**: 3762-3769.
149. Yoo, Y., and Paul, D.R. (2008). Effect of Organoclay Structure on Morphology and Properties of Nanocomposites Based on An Amorphous Polyamide, *Polymer*, **49**: 3795-3804.
150. Paul, D.R., and Robeson, L.M. (2008). Polymer Nanotechnology: Nanocomposites, *Polymer*, **49**: 3187-3204.
151. Dasari, A., Yu, Z.-Z., Mai, Y.-W., Hu, G.-H., and Varlet, J. (2005). Clay Exfoliation and Organic Modification on Wear of Nylon 6 Nanocomposites Processed by Different Routes, *Composites Sci. Tech.*, **65**: 2314-2328.
152. Bhushan, B., and Qi, J. (2003). Phase Contrast Imaging of Nanocomposites and Molecularly Thick Lubricant Films in Magnetic Media, *Nanotechnology*, **14**: 886-895.
153. Maurer, J.J., Eustace, D.J., and Ratcliffe, C.T. (1987). Thermal Characterization of Poly(acrylic acid), *Macromolecules*, **20**: 196-202.
154. Caykara, T., and Guven, O. (1998). Effect of Preparation Methods on Thermal Properties of Poly(acrylic acid)/Silica Composites, *J. Appl. Polym. Sci.*, **70**: 891-895.
155. Jiang, S.H., Huang, Y., and Shen, J.R. (2003). Effects of Cholesteric Order on Mechanical Properties of (E-CE)C/PAA Composites, *J. Appl. Polym. Sci.*, **57**: 493-498.
156. Paralikar, S.A., Simonsen, J., and Lombardi, J. (2008). Poly(vinyl alcohol)/Cellulose Nanocrystal Barrier Membranes, *J. Memb. Sci.*, **320**: 248-258.
157. Osman, M.A., Ploetze, M., and Skrabal, P. (2004). Structure and Properties of Alkylammonium Monolayers Self-Assembled on Montmorillonite Platelets, *J. Phys. Chem. B.*, **108**: 2580-2588.

BIOGRAPHICAL SKETCH

Jinwoo Kwak was born in Daegu, Korea, in January 1977. He received his bachelor's degree in textile and polymer chemistry from Yeungnam University, Korea in 2003. After that, he joined advanced polymer lab at the same university and finished courseworks for master's degree there. His research interest in Korea was mainly focused on the preparation of high molecular weight polymer materials with various morphological features. In August 2006, he was admitted to the graduate school of the University of Florida in the Department of Materials Science and Engineering, where he received his master's degree in May 2008. The research throughout his master and doctoral courses was focused on polymer clay nanocomposites.